TECHNICAL UNIVERSITY OF MOLDOVA

JOURNAL OF ENGINEERING SCIENCE

Technical and applied scientific publication founded on 9 February 1995
Alternative title: Meridian ingineresc

2023

Vol. XXX (3)

ISSN 2587-3474
eISSN 2587-3482

TECHNICAL UNIVERSITY OF MOLDOVA (PUBLISHING HOUSE)
„TEHNICA UTM" (PRINTING HOUSE)

According to the Decision of the NAQAER No. 19 from 06.12.2019, JES is classified as B+ journal

Main subjects areas of the Journal of Engineering Science:

A. Industrial Engineering

- Mechanical Engineering and Technologies
- Applied Engineering Sciences and Management
- Materials Science and New Technologies
- Electrical Engineering and Power Electronics
- Energy systems
- Light Industry, New Technologies and Design
- Industrial and Applied Mathematics
- Vehicle and Transport Engineering

B. Electronics and Computer Science

- Electronics and Communication
- Microelectronics and Nanotechnologies
- Biomedical Engineering
- Computers and Information Technology
- Automation

C. Architecture, Civil and Environmental Engineering

- Architecture, Urbanism and Cadaster
- Civil Engineering and Management
- Energy Efficiency and New Building Materials
- Environmental Engineering

D. Food Engineering

- Food Technologies and Food Processes
- Food Industry and Management
- Biotechnologies, Food Chemistry and Food Safety
- Equipment for Food Industries

The structure of the journal corresponds to the classification of scientific publications: ***Engineering, Multidisciplinary.***

How to publish a paper:

1. Send the manuscript and information about the author to the **Editorial Board address:** jes@meridian.utm.md
2. Manuscripts are accepted only in English, by e-mail, in template file (www.jes.utm.md)
3. After a review, you will be notified of the editorial board's decision.
4. After the Journal has been published, we will send it to you immediately by mail.

Editor-in-Chief
Dr. hab. prof. univ. Viorel BOSTAN
Technical University of Moldova
viorel.bostan@adm.utm.md

Editorial Board

Responsible Editor
Dr. hab. Rodica STURZA
Editorial Board address: jes@meridian.utm.md

Editorial Production:
Dr. hab. Aliona Ghendov-Moșanu
Dr. Nicolae Trifan
Dr. Svetlana Caterinciuc
Dr. Rodica Cujba
Zinaida Stratan

CONTENT

A. Industrial Engineering

B. Electronics and Computer Science

C. Architecture, Civil and Environmental Engineering

D. Food Engineering

CUPRINS

Journal of Engineering Science | *Vol. XXX, no. 3 (2023), pp. 7 - 15*
Fascicle *Industrial Engineering* *ISSN 2587-3474*
Topic *Materials Science and New Technologies* *eISSN 2587-3482*

https://doi.org/10.52326/jes.utm.2023.30(3).01
UDC 536.784:539.21

ANALYSIS OF PHONONS BEHAVIOR IN QUASI-ONE-DIMENSIONAL CRYSTALS OF $TTT(TCNQ)_2$ NEAR THE PEIERLS STRUCTURAL TRANSITION IN A 3D APPROXIMATION

Silvia Andronic*, ORCID 0000-0002-7092-6867,
Ionel Sanduleac, ORCID: 0000-0001-7532-1288

Technical University of Moldova, 168 Stefan cel Mare Blvd., Chisinau, Republic of Moldova
*Corresponding author: Silvia Andronic, *silvia.andronic@mt.utm.md*

Received: 08. 12. 2023
Accepted: 09. 05. 2023

Abstract. This research paper focuses on investigating the metal-insulator transition occurring in quasi-one-dimensional organic crystals of $TTT(TCNQ)_2$. The study utilizes a 3D approximation approach and introduces a physical model that incorporates two essential electron-phonon interactions. The first interaction is akin to the deformation potential, while the second interaction follows a polaron type behavior. By employing the random phase approximation, the renormalized phonon spectrum is calculated across different temperatures and various values of the dimensionless Fermi momentum k_F. The findings indicate that the transition exhibits characteristics of the Peierls type, and the critical temperature associated with the Peierls transition is determined. Furthermore, an interesting observation is made that the Peierls critical temperature experiences a notable decrease with an increase in carrier concentration.

Keywords: *Metal-insulator transition; organic materials; quasi-one-dimensional organic crystals; renormalized phonon spectrum; Peierls critical temperature.*

Rezumat. Articolul se concentrează pe investigarea tranziției metal-dielectric care are loc în cristalele organice quasi-unidimensionale de $TTT(TCNQ)_2$. Studiul utilizează o abordare de aproximare 3D și introduce un model fizic care încorporează două interacțiuni esențiale electron-fonon. Prima interacțiune este asemănătoare cu potențialul de deformare, în timp ce a doua interacțiune urmează un comportament de tip polaron. Utilizînd aproximația fazelor aleatorii, spectrul renormat al fononilor este calculat la diferite temperaturi și diferite valori ale impulsului adimensional Fermi k_F. Constatările indică faptul că tranziția prezintă caracteristici de tip Peierls, iar temperatura critică asociată cu tranziția Peierls este determinată. Mai mult, se face o observație interesantă că temperatura critică Peierls înregistrează o scădere notabilă cu o creștere a concentrației purtătorilor.

Cuvinte cheie: *traziție metal-dielectric; materiale organice; cristale organice quasi-unidimensionale; spectrul renormat al fononilor; temperatura critică Peierls.*

1. Introduction

Over the past few years, there has been an increasing focus on studying organic crystals with quasi-one-dimensional (Q1D) properties, driven by their distinct and varied characteristics. These materials have garnered significant interest as they hold potential for application in electronic devices. Theoretical studies [1-4] have demonstrated that, by optimizing certain parameters, these crystals can exhibit significantly improved thermoelectric properties compared to currently known inorganic materials. The utilization of these materials offers several advantages, such as low cost, ecological safety, and relatively inexpensive manufacturing processes. Consequently, they have become a subject of special interest in research. Also, the increased interest in certain Q1D organic materials is due to their high electrical conductivity. For most of the compounds in these categories, it is characteristic that the metallic state manifests itself at temperatures of the order of $T = 300$ K. Another interesting aspect is the presence of the phase transition, specifically a transition from a metal to an insulator at low temperatures, typically occurring around several tens of degrees K. Quasi-one-dimensional systems also exhibit distinctive features such as the periodic arrangement of charge and spin density.

Research on organic conductors marked an intense development since the 1960s, when TCNQ (tetracyanoquinodimethane) molecules were discovered [5]. Then in 1970 TTF (tetrathifulvalene) molecules were discovered [6]. In 1973, the first quasi-one-dimensional organic metal stable at room temperature was synthesized, TTF-TCNQ (tetrathiofulvalinium-tetracyanoquinodimethane) with a partially full conduction band [7, 8]. It was sought to achieve the transition in the superconducting state when the temperature decreased, but the transition in the dielectric state was obtained. This groundbreaking result provided initial experimental evidence of the Peierls transition, a widely observed phenomenon in quasi-one-dimensional systems.

Peierls transition was theoretically predicted in 1955 by the scientist Rudolf Peierls and today this phenomenon bears his name [9]. Peierl's theory suggests that at certain reduced temperatures, a one-dimensional metallic crystal with a conduction band that is half-filled must undergo a transition to a dielectric state where the crystal lattice becomes dimerized. This critical temperature at which this transition occurs is known as the Peierls critical temperature.

The Peierls structural transition has received significant attention in Q1D crystals, as evidenced by numerous studies [10-16]. In the case of TTF-TCNQ crystals, intriguing observations have been made regarding this transition. Specifically, it has been noted that the transition manifests at 54 K in TCNQ stacks and at 38 K in TTF stacks. These transitions coincide with the emergence of band gaps in the electronic spectrum above the Fermi energy and a notable reduction in electrical conductivity. As the temperature decreases, distinct alterations in the phonon spectrum become apparent. Eventually, at a critical temperature, the renormalized phonon frequency reaches zero for a specific phonon wave vector value. This critical temperature corresponds to the occurrence of the Peierls transition [15, 16].

In our research, we have conducted a complete investigation of the transition occurring in TCNQ stacks using a more comprehensive physical model [17]. Our findings indicate that the Peierls transition begins at approximately 59.7 K in isolated TCNQ chains, resulting in a significant decrease in electrical conductivity. However, due to the interchain interactions, the transition is completed at a slightly lower temperature of approximately 54 K. Our study has demonstrated the pivotal role of electron-phonon interaction in this process.

Specifically, it causes a reduction in the renormalized phonon spectrum compared to the initial frequency of free phonons, leading to a decrease in sound velocity across a broad temperature range.

The investigation presented in [18] delved into the Peierls transition occuring in Q1D crystals of TTT_2I_3 type, employing a 2D physical model. The primary focus of the research was to analyze how lattice distortion affects the dispersion of renormalized acoustic phonons. The results revealed that the Peierls transition commences at approximately 35 K in TTT chains. Furthermore, due to the interchain interaction, the transition is finalized at a lower temperature of around 19 K.

The study also demonstrated that the interaction between holes and phonons, along with interactions with the structural defects, contribute to a reduction in the renormalized phonon spectrum and a decrease in the sound velocity over a considerable temperature range.

This paper focuses on studying the behavior of phonons in the vicinity of the Peierls structural transition in quasi-one-dimensional crystals of $TTT(TCNQ)_2$, using a 3D approximation. In Section II we present a comprehensive physical model of the crystal and provide a description of it. Section III is dedicated for examining the renormalized phonon spectrum. Finally, the paper concludes with a summary of findings and conclusions.

2. A 3D approximation of the physical model

The crystals of $TTT(TCNQ)_2$ exhibit a dark - violet needles – like morphology with lengths ranging from 3 to 6 mm. These crystals possess a pronounced quasi-one-dimensional internal structure, consisting of isolated chains of TTT anions and chains of TCNQ cations. The lattice constants for the *x*, *y*, and *z* directions are measured as follows: c = 3.75 Å, b = 12.97 Å and a =19.15 Å [19]. The x – axis aligns parallel to the TCNQ chains along the ***b*** - direction. This compound functions as a charge transfer complex, with the main charge transport occurring through the TCNQ chains. The electron transfer energy between adjacent TCNQ molecules in the x direction is represented as w_1 = 0.125 eV. In the perpendicular directions, w_2 and w_3 are relatively small, and transport primarily relies on the hopping mechanism. The stoichiometric concentration of electrons in $TTT(TCNQ)_2$ crystals is estimated to be $n = 1.1\cdot 10^{21}$ cm^{-3}. In crystals with this stoichiometric concentration, the electrical conductivity ranges from 20 to 160 Ω^{-1}cm^{-1} [19], depending on the purity of the crystal. It has been theoretically demonstrated that there is the possibility of optimizing the thermoelectric properties by increasing the concentration of electrons and by purifying the crystal.

According to [19], the electrical conductivity measured using the microwave method, at a frequency of 10^{10} Hz, varies within the range of 20 $\Omega^{-1}\cdot$cm^{-1} to 160 $\Omega^{-1}\cdot$cm^{-1} at room temperature.

However, when measured using contact in pressed powder, the electrical conductivity ranges from 0.5 $\Omega^{-1}\cdot$cm^{-1} to 1 $\Omega^{-1}\cdot$cm^{-1} [20]. As the temperature decreases, there is an increase in electrical conductivity observed until around T ~ 90 K. However, beyond this point, the metallic behavior diminishes and the crystal undergoes a Peierls transition, transforming into an insulating state at approximately T ~ 35 K in purer crystals [19].

The physical model of the crystal was elaborated in greater detail in [17]. The Hamiltonian of the 3D crystal model was described within the framework of the tight binding and nearest neighbor approximations. It can be represented as folllows:

$$H=\sum_{\boldsymbol{k}}\varepsilon(\boldsymbol{k})a_{\boldsymbol{k}}^{+}a_{\boldsymbol{k}}+\sum_{\boldsymbol{q}}\hbar\omega_{\boldsymbol{q}}b_{\boldsymbol{q}}^{+}b_{\boldsymbol{q}}+\sum_{\boldsymbol{k},\boldsymbol{q}}A(\boldsymbol{k},\boldsymbol{q})a_{\boldsymbol{k}}^{+}a_{\boldsymbol{k}-\boldsymbol{q}}(b_{\boldsymbol{q}}+b_{-\boldsymbol{q}}^{+}). \quad (1)$$

In Eq. (1) - $\sum_{\boldsymbol{k}}\varepsilon(\boldsymbol{k})a_{\boldsymbol{k}}^{+}a_{\boldsymbol{k}}$ corresponds to the energy operator of free electrons in the periodic field of the lattice. This term $\sum_{\boldsymbol{q}}\hbar\omega_{\boldsymbol{q}}b_{\boldsymbol{q}}^{+}b_{\boldsymbol{q}}$ represents the energy operator of longitudinal acoustic phonons, while $\sum_{\boldsymbol{k},\boldsymbol{q}}A(\boldsymbol{k},\boldsymbol{q})a_{\boldsymbol{k}}^{+}a_{\boldsymbol{k}-\boldsymbol{q}}(b_{\boldsymbol{q}}+b_{-\boldsymbol{q}}^{+})$ describes the two most important electron-phonon interactions. The creation and annihilation operators of the electrons are denoted by $a_{\boldsymbol{k}}^{+}, a_{\boldsymbol{k}}$ with a 3D quasi-wave vector $\boldsymbol{k}$ and projections (k_x, k_y, k_z) onto the respective crystal axes. The energy of the electron $\varepsilon(\boldsymbol{k})$ is measured relative to the top of the energy band and can be expressed in the following form:

$$\varepsilon(\boldsymbol{k})=2w_1(1-\cos k_x b)-2w_2(1-\cos k_y a)-2w_3(1-\cos k_z c), \quad (2)$$

where w_1 is the transfer energies of a carrier from one molecule to another in *x* direction (along the chain), while w_2 and w_3 also have the same role, only for the *y* and *z* directions (perpendicular to the chain). In Eq. (1), the creation and annihilation operators of an acoustic phonon are denoted by b_q^{+}, b_q. They are characterized by 3D wave vector $\boldsymbol{q}$ and the frequency $\omega_{\boldsymbol{q}}$. In [21], it was demonstrated that the spectrum of acoustic phonons of a simple one-dimensional chain is described by the following expression:

$$\omega_{\boldsymbol{q}}^2=\omega_1^2\sin^2(q_x b/2)+\omega_2^2\sin^2(q_y a/2)+\omega_3^2\sin^2(q_z c/2). \quad (3)$$

In the given context, ω_1, ω_2 and ω_3 are limit frequencies for oscillations in *x*, *y* and *z* directions, respectively. As mentioned earlier, two most significant mechanisms of electron-phonon interaction are considered: one of the deformation potential type and the other of the polaron type. In the deformation potential interaction, the coupling constants are proportional to derivatives w_1', w_2' and w_3' of w_1, w_2, and w_3 with respect to the intermolecular distances.

These derivatives quantify how the electronic energy is affected by changes in the distances between neighboring molecules. On the other hand, in the polaron interaction, the coupling constant is proportional to the average polarizability of the molecule α_0. This interaction is particularly relevant in crystals composed of large molecules such as TCNQ, so as α_0 is roughly proportional to the volume of molecule.

The square module of matrix element $A(\boldsymbol{k},\boldsymbol{q})$ from Equation (1) has the following form:

$$\begin{aligned}|A(\boldsymbol{k},\boldsymbol{q})|^2 &= 2\hbar w_1'^2(NM\omega_{\boldsymbol{q}})\Big\{\big[\sin(k_x b)-\sin(k_x-q_x,b)+\gamma_1\sin(q_x b)\big]^2+\\ & d_1^2\big[\sin(k_y a)-\sin(k_y-q_y,a)+\gamma_2\sin(q_y a)\big]^2+d_2^2\big[\sin(k_z c)-\sin(k_z-q_z,c)+\gamma_3\sin(q_z c)\big]^2\Big\}.\end{aligned} \quad (4)$$

In Eq. (4), *M* represents the mass of TCNQ molecule; *N* describes the number of TCNQ molecules in the basic region of the crystal; $d_1=w_2/w_1=w_2'/w_1'$; $d_2=w_3/w_1=w_3'/w_1'$; parameters γ_1, γ_2, and γ_3 have the sense of the amplitudes ratio of the polaron-type interaction to the deformation potential one in the *x*, *y*, and *z* directions:

$$\gamma_1 = 2e^2\alpha_0 / b^5 w_1'; \;\; \gamma_2 = 2e^2\alpha_0 / a^5 w_2'; \;\; \gamma_3 = 2e^2\alpha_0 / c^5 w_3'. \quad (5)$$

The renormalized phonon spectrum $\Omega(\boldsymbol{q})$ is determined by the pole of the Green function. It is obtained by solving the transcendent dispersion equation

$$\Omega(\boldsymbol{q}) = \omega_{\boldsymbol{q}} \left[1 - \bar{\Pi}(\boldsymbol{q}, \Omega)\right]^{1/2}, \quad (6)$$

where the principal value of the dimensionless polarization operator takes the form:

$$\mathrm{Re}\,\bar{\Pi}(\boldsymbol{q}, \Omega) = -\frac{\bar{N}}{2\pi^3\hbar\omega_{\boldsymbol{q}}} \int_{-\pi}^{\pi} dk_x \int_{-\pi}^{\pi} dk_y \int_{-\pi}^{\pi} dk_z \left|A(\boldsymbol{k}, -\boldsymbol{q})\right|^2 \times \frac{n_{\boldsymbol{k}} - n_{\boldsymbol{k}+\boldsymbol{q}}}{\varepsilon(\boldsymbol{k}) - \varepsilon(\boldsymbol{k}+\boldsymbol{q}) + \hbar\Omega}. \quad (7)$$

In Eq. (7) $n_{\boldsymbol{k}}$ is the Fermi distribution function, $\hbar$ is the Planck constant and $A(\boldsymbol{k}, \boldsymbol{q})$ is the matrix element of electron-phonon interaction. The integral in Eq. (7) has singularities and must be calculated with a needed accuracy. The Eq. (6) can be solved only numerically. Numerical calculations were performed in the Mathematica package.

3. Results and Discussion

Numerical calculations have been conducted using the following parameters [17, 19]: w_1 = 0.125 eV, w_1' = 0.22 eVÅ^{-1}, c = 3.75 Å, b = 12.97 Å, a =19.15 Å and M = 3.72·10^5 m_e (m_e is the electron rest mass). The sound velocity v_{s1} ≈ 4 ·10^5 cm/s along chains, in c direction, v_{s2} ≈ 2·10^5 cm/s in b direction and v_{s3} ≈ 1·10^5 cm/s in a direction, d_1 = 0.015, d_2 = 0.01, r = 2 (two molecules in an unit cell), γ_1 = 1.7. The parameters γ_2 and γ_3 are determined from the relation: $\gamma_2 = \gamma_1 2^5 b^5/(a^5 d_1)$ and $\gamma_3 = \gamma_1 2^5 b^5/(c^5 d_2)$. The Fermi momentum varies from the value of k_F = 0.56π/2 to the value of k_F = 0.62π/2. These values were chosen in the region of the stoichiometric value of the Fermi momentum for these crystals.

From the information provided, it is evident that the Figures 1-4 depicting the dependence of renormalized phonon frequencies $\Omega(q_x)$ as functions of q_x for various temperatures and different values of q_y and q_z, exhibit several important observations. Firstly, it is observed that the values of $\Omega(q_x)$ are lower (diminished) compared to the frequencies $\omega(q_x)$ in the absence of electron-phonon interaction. This reduction in $\Omega(q_x)$ indicates that the electron-phonon interaction leads to a decrease in the values of the lattice elastic constants.

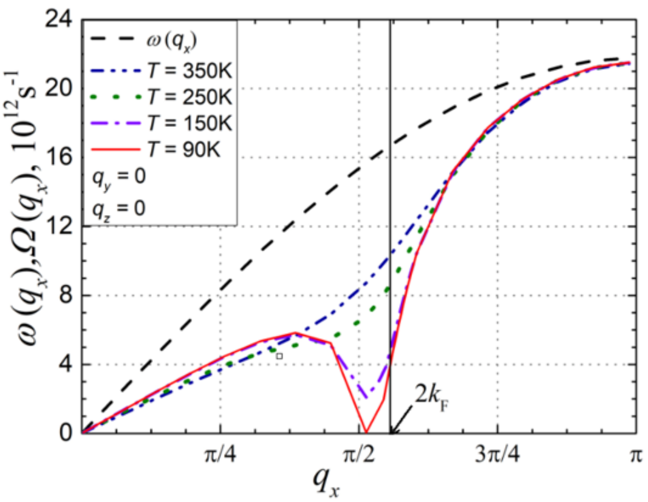

Figure 1. Renormalized phonon spectrum $\Omega(q_x)$ is plotted for various temperatures, with γ_1 = 1.7. The dashed line represents the spectrum of free phonons. The specific value chosen for this plot is: k_F = 0.56π/2.

This phenomenon arises due to the coupling between electrons and lattice vibrations. Secondly, as the temperature T decreases, the curves representing $\Omega(q_x)$ exhibit changes in their shape. Specifically, a minimum appears in the $\Omega(q_x)$ dependencies, and this minimum becomes more pronounced at lower temperatures. This behavior suggests that there is a critical temperature at which $\Omega(q_x)$ reaches zero. However, contrary to the expectation that $\Omega(q_x)$ will attain zero at $q_x = 2\ k_F$, where k_F represents the Fermi wave vector, the figures indicate that $\Omega(q_x)$ attains zero for a value of $q_x \neq 2\ k_F$. The appearance of a minimum in the $\Omega(q_x)$ dependencies with decreasing temperature suggests the possibility of a structural Peierls transition. However, the deviation of $\Omega(q_x)$ reaching zero from $q_x = 2\ k_F$ is due to the deviation of k_F from the expected value of $\pi/4$ in this particular system.

Figure 1 illustrates a scenario where $q_y = 0$, $q_z = 0$ and $k_F = 0.56\pi/2$. In this particular case, the interaction between TCNQ chains is neglected. When the temperature T reaches 90 K, the transition exclusively occurs within the TCNQ chains. This experimental observation is supported by a significant reduction in electrical conductivity. Moreover, the crystal lattice along the TCNQ chains undergoes a transformation from its initial state with a lattice constant c to a new crystalline state with a constant $4c$, that is four times larger. This temperature marks the occurrence of a metal-dielectric phase transition, accompanied by the complete opening of a gap in the carrier spectrum within the 1D conduction band of TCNQ, positioned just above the Fermi energy.

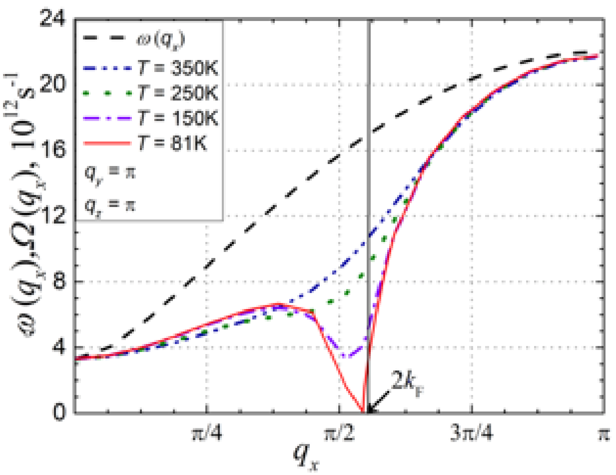

Figure 2. Renormalized phonon spectrum $\Omega(q_x)$ is plotted for various temperatures, with $\gamma_1 = 1.7$. The dashed line represents the spectrum of free phonons. The specific value chosen for this plot is: $k_F = 0.56\pi/2$.

When the interaction between TCNQ chains is considered ($q_y \neq 0$, $q_z \neq 0$), the Peierls critical temperature is reduced. Figures 2 - 4 correspond to 3D physical model with $q_y \neq 0$ and $q_z \neq 0$. These figures illustrate the dependences of $\Omega(q_x)$ on q_x for $q_y = \pi$, $q_z = \pi$, for different values of carrier concentration and different temperatures. Figure 2 represents the case when the Fermi momentum $k_F = 0.56\pi/2$. It is noteworthy that $\Omega(q_x)$ reaches zero at T = 81 K, indicating that the transition takes place at this T.

In Figure 3, the renormalized phonon spectrum $\Omega(q_x)$, for the Fermi momentum $k_F = 0.59\pi/2$ and $q_y = \pi$, $q_z = \pi$ can be observed. In this case the interaction between TCNQ chains is taken into account. As a result, the Peierls transition occurs at T = 57 K. One can see that with an increase in carrier concentration, the Peierls critical temperature decreases more.

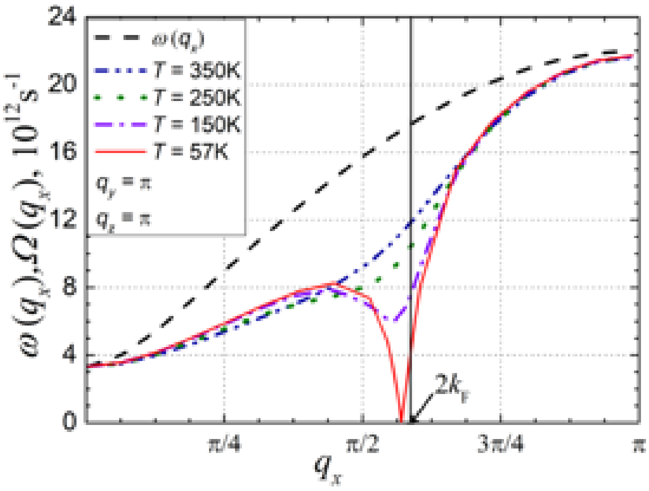

Figure 3. Renormalized phonon spectrum $\Omega(q_x)$ is plotted for various temperatures, with γ_1 = 1.7. The dashed line represents the spectrum of free phonons. The specific value chosen for this plot is: $k_F = 0.59\pi/2$.

Figure 4 exhibits the identical dependencies of the renormalized phonon spectrum $\Omega(q_x)$ as in the previous figures, but with an increased value of the Fermi momentum k_F = $0.62\pi/2$, while maintaining $q_y = \pi$, $q_z = \pi$. This figure showcases different temperatures. It can be observed that the transition temperature further decreases and reaches T = 35.1 K. This observation indicates that as the carrier concentration increases, the Peierls critical temperature continues to diminish.

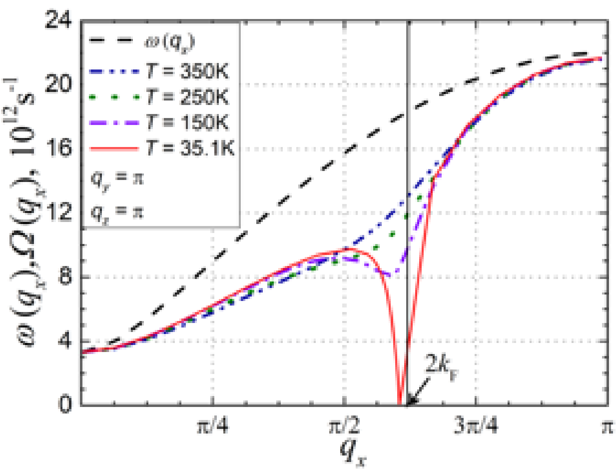

Figure 4. Renormalized phonon spectrum $\Omega(q_x)$ is plotted for various temperatures, with γ_1 = 1.7. The dashed line represents the spectrum of free phonons. The specific value chosen for this plot is: $k_F = 0.62\pi/2$.

4. Conclusions

We have carried out investigations on phonons near Peierls structural transition in quasi-one-dimensional crystals of TTT(TCNQ)$_2$ in the 3D approximation, using a more comprehensive physical model of the crystal. This model incorporates two most significant electron-phonon interactions. The renormalized phonon spectrum has been computed in the random phase approximation. Numerical calculations of the renormalized phonon spectrum, $\Omega(q_x)$, have been performed for various temperatures and different values of q_y and q_z. Our findigs indicate that when the interaction between TCNQ chains is neglected ($k_F = 0.56\pi/2$, q_y = 0, q_z = 0), the Peierls transition initiates in the TCNQ chains alone at T = 90 K. However, when the interchain interaction is taken into account ($q_y = \pi$ and $q_z = \pi$), the transition is completed at $T = 81$ K. Moreover, our calculations demonstrate a significant decrease in the Peierls critical temperature with an increase in carrier concentration. So, for $k_F = 0.59\pi/2$, the transition occurs at $T = 57$ K, and for $k_F = 0.62\pi/2$, the transition takes place at $T = 35.1$ K, respectively. These results were obtained for the case when the interchain interaction is considered. We note that the Peierls transition in $TTT(TCNQ)_2$ crystals was studied first time by us. In other *n*-type crystals, such as those of TTF-TCNQ, the Peierls transition has been studied by several authors, both theoretically and experimentally. It has been shown that the transition starts at $T = 59.7$ K in TCNQ chains alone. When the interaction between the adjacent chains are considered the transition is finished at $T = 54$ K. The electron-phonon interaction diminishes renormalized phonon spectrum $\Omega(q_x)$ with respect to initial frequency $\omega(q_x)$.

Acknowledgments: This work was supported by project **20.80009.5007.08** "Study of optoelectronic structures and thermoelectric devices with high efficiency".

Conflicts of Interest: The authors declare no conflict of interest.

References

1. Casian, A. *Thermoelectric Handbook, Macro to Nano, Ed. by D. M. Rowe, CRC Press*, 2006, cap. 36.
2. Sanduleac, I.; Casian, A.; Pflaum, J. Thermoelectric Properties of Nanostructured Tetrathiotetracene Iodide Crystals in a Two-Dimensional Model. *Journal of Nanoelectronics and Optoelectronics* 2014, 9 (2), pp. 247-252.
3. Jerome, D. Organic Superconductors: When Correlations and Magnetism Walk. *Journal of Superconductivity and Novel Magnetism* 2012, 25, pp. 633-655.
4. Pouget, J. P. Bond and Charge Ordering in Low-Dimensional Organic Conductors. *Physica B* 2012, 407, pp. 1762-1770.
5. Acker, D. S.; Harder, R. J.; Hertler, W. R.; Mahler, W.; Melby, L. R.; Benson, R.; Mochel, W. E. 7,7,8,8-Tetracyanoquinodimethane and its electrically conducting anion-radical derivatives. *Journal of the American Chemical Society* 1960, 82, pp. 6408-6409.
6. Wudl, F.; Smith, G. M.; Hufnagel, E. J. Bis-1,3-dithiolium chloride: an unusually stable organic radial cation. *Chemical Communications* 1970, pp. 1453-1454.
7. Ferraris, J. P.; Cowan, D. O.; Walatka, V.; Perlstein, J. H. Electron transfer in a new highly conducting donor-acceptor complex. *Journal of the American Chemical Society* 1973, 95, pp. 948-949.
8. Coleman, L. B.; Cohen, M. J.; Sandman, D. J.; Yamagishi, F. G; Garito, A. F.; Heeger, A. J. Superconducting fluctuations and the Peierls instability in an organic solid. *Solid State Communications* 1973, 12, pp. 1125-1132.
9. Peierls, R. *Quantum Theory of Solids*. Oxford University Press, London, 1955, pp.108.
10. Jerome, D. Organic Conductors: From Charge Density Wave TTF-TCNQ to Superconducting $(TMTSF)_2PF_6$. *Chemical Reviews* 2004, 104, pp. 5565-5592.
11. Pouget, J. P. The Peierls Instability and Charge Density Wave in One- Dimensional Electronic Conductors. *Comptes Rendus Physique*,2016, 17, pp. 332-356.
12. Streltsov, S. V.; Khomskii, D. I. Orbital-Dependent Singlet Dimers and Orbital-Selective Peierls Transitions in Transition-Metal Compounds. *Physical Review B* 2014, 89 (16), article ID: 161112.
13. Chernenkaya, A.; Medjanik, K.; Nagel, P.; Merz, M.; Schuppler, S.; Canadell, E.; Pouget, J. P.; Schonhense, G. Nature of the Empty States and Signature of the Charge Density Wave Instability and Upper Peierls Transition of TTF-TCNQ by Temperature-Dependent NEXAFS Spectroscopy. *The European Physical Journal B* 2015, 88 (13).
14. Khanna, S. K.; Pouget, J. P.; Comes, R.; Garito, A. F.; Heeger, A. J. X-Ray Studies of $2k_F$ and $4k_F$ Anomalies in Tetrathiafulvalene-Tetracyanoquinodimethane (TTF-TCNQ). *Physical Review B* 1977, 16, 1468.
15. Reitschel, H. The Giant Kohn Anomaly in a Peierls Semiconductor. *Solid State Communications* 1973, 13, 1859.
16. Bulaevskii, L. N. Peierls Structure Transition in Quasi-One-Dimensional Crystals. *Soviet Physics Uspekhi* 1975, 18, pp. 131.
17. Andronic, S.; Casian, A. Phonons near Peierls Structural Transition in Quasi-One-Dimensional in organic crystals of TTF-TCNQ. *Advances in Materials Physics and Chemistry* 2016, 6, pp. 98-104.

18. Andronic, S.; Casian, A. Metal-Insulator Transition of Peierls Type in Quasi-One-Dimensional Crystals of TTT$_2$I$_3$. *Advances in Materials Physics and Chemistry* 2017, 7, pp. 212-222.
19. Buravov, L.; Eremenko, O.; Lyubovskii, R.; Rozenberg, L.; Khidekel, M.; Shibaeva, R.; Shchegolev, I.; Yagubskii, E. Structure and electromagnetic properties of a new high conductivity complex (TTT)$^+$(TCNQ)$_2^-$. *ZhETF Pis. Red.* 1974, 20 (7), pp. 457-461.
20. Shchegolev, I. F.; Yagubskii E. B. Cation-radical salts of tetrathiotetracene and tetraselenotetracene: synthetic aspects and physical properties. *Linear Extendend Chain Compounds* 1982, 2, pp. 385-434. Edited by MILLER, J. S., Plenum Press, New York.
21. Graja, A. Low-dimensional organic conductors. *Word Scientific, Singapore,* 1992.

Citation: Andronic, S.; Sanduleac, I. Analysis of phonons behavior in quasi-one-dimensional crystals of TTT(TCNQ)$_2$ near the Peierls structural transition in a 3D approximation. *Journal of Engineering Science* 2023, 30 (3), pp. 7-15. https://doi.org/10.52326/jes.utm.2023.30(3).01.

Publisher's Note: JES stays neutral with regard to jurisdictional claims in published maps and institutional affiliations.

Submission of manuscripts: jes@meridian.utm.md

https://doi.org/10.52326/jes.utm.2023.30(3).02
UDC 621.833.6:534

PROCESSING OF VIBRO - ACOUSTIC SIGNALS OF PRECESSIONAL PLANETARY TRANSMISSIONS

Stanislav Slobodeaniuc*, ORCID 0009-0002-0865-6701

Technical University of Moldova, 168, Ștefan cel Mare, Chișinău, 2004, Republic of Moldova
*Corresponding author: *Stanislav Slobodeaniuc*, *stanislav.slobodeaniuc@tran.utm.md*

Received: 09. 02. 2023
Accepted: 09. 28. 2023

Abstract. The operation of working machines is accompanied by the constant occurrence of vibrations and shocks, generated by various constructive, kinematic and dynamic factors. The study of the vibro-acoustic aspect of mechanical transmissions and, in particular, of precessional planetary ones is a primary concern for engineers in the field of machine building technologies. The paper presents the research of precessional planetary transmissions under the vibro-acoustic aspect in the anechoic chamber, which is a room, insulated with sound-absorbing material against external noises and isolated anti-vibration. To process the vibro-acoustic signals received as a result of the measurements, the Fourier harmonic series will be applied, a mathematical function that can be used to find the basic frequencies that make up a wave. The final result is the detection of vibration and noise generating sources, the decoding of signals by means of Fourier series and the advancement of constructive-technological solutions to minimize the vibro-acoustic level.

Keywords: *precessional planetary transmission, vibroacoustic signal, transducer, anechoic chamber, harmonic series.*

Rezumat. Funcționarea mașinilor de lucru este însoțită de apariţia în permanență a vibraţiilor şi şocurilor, generate de diverși factori constructivi, cinematici și dinamici. Studiul aspectului vibro-acustic al transmisiilor mecanice şi, în deosebi, al celor planetare precesionale este o preocupare primordială pentru inginerii din domeniul tehnologiilor constructoare de maşini. În lucrare se prezintă cercetarea transmisiilor planetare precesionale sub aspect vibro-acustic în camera anecoică, care reprezintă o încăpere, izolată cu material fonoabsorbant împotriva zgomotelor externe şi izolată antivibratoriu. Pentru procesarea semnalelor vibro-acustice primite în urma măsurărilor vor fi aplicate seriile armonice Fourier, funcție matematică ce poate fi folosită pentru a găsi frecvențele de bază, din care este alcătuită o undă. Rezultatul final este depistarea surselor generatoare de vibraţii şi zgomot, descifrarea semnalelor prin intermediul seriilor Fourier şi înaintarea soluţiilor constructiv-tehnologice pentru minimizarea nivelului vibro-acustic.

Cuvinte cheie: *transmisie planetară precesională, semnal vibro-acustic, traductor, cameră anecoidă, serii armonice.*

1. Sources of noise in planetary precessional transmissions

The operation of working machines is accompanied by the constant occurrence of vibrations and shocks, generated by various constructive, kinematic and dynamic factors. These vibrations and noises create a level of noise pollution, which negatively affects people's health. In the Republic of Moldova, the admissible norms of vibro-acoustic pollution are regulated by HG 589-2016. The shocks and vibrations, to which working machines are subjected, are determined by external and internal causes [1]. Most of the time these causes manifest simultaneously and also generate high dynamic loads, which additionally influence the functionality of the working machines [2].

The dynamic performances of mechanical systems, during operation, can be improved by the appropriate choice of working regimes, by adopting an optimal construction, from the point of view of the stability reserve or by applying some constructive or active control measures. In recent years, there is a tendency to increase the quality and reliability of aggregates, through the use of complex sensory systems, which have monitoring, diagnostic and active control functions.

A common element of most mechanical systems is the mechanical transmission, in most cases geared, which generates vibration and noise. The vibroactivity of reducers depends, in particular, on the exciting forces in the gear. It should be noted that the forces in the gear are generated by execution and assembly errors, as well as by their elastic deformations. In the geometric precessional gear, up to 100% pairs of teeth can be simultaneously in the gear, therefore the determination of the exciting forces is particularly difficult. Therefore, experimental researches are the most appropriate and effective methods for determining the level of vibrations and noise emitted by precessional planetary transmissions. But in this case, the most efficient processing of vibroacoustic spectrograms is particularly important [3].

Each type of mechanical transmission is a medium for generating vibro-acoustic signals, the basic problem of their occurrence usually being:

- incorrect gearing, for example, unevenness in the gearing between the wheels in a transmission can generate vibration and noise. These can be caused by manufacturing errors, damage or wear of the gear teeth;
- wear of bearing bearings, often defective bearings can cause vibration and noise during operation, especially when subjected to excessive loads or when worn;
- an imbalance in transmission components such as flywheels, crankshafts, gears or belts can have an imbalance in their mass, resulting in
of vibration and noise during rotation;
- the occurrence of wear and play of the components or the presence of excessive play can cause uneven movements and fluctuations of the components, generating vibrations and noises;
- overloads and uneven stresses for example incorrect or uneven loads on the transmission can create excessive stresses and vibrations in the transmission components;
- erosion and corrosion as an example damage caused by erosion or corrosion can affect component surfaces and contribute to noise and vibration;
- the occurrence of fluctuations in the engine torque, suppose that the engine torque is not constant or there are significant fluctuations in the transmitted power, this can generate vibrations and noises in the transmission;

- faulty mounting or incorrect assembly such as improper mounting of components or incorrect assembly of the transmission can lead to the generation of vibrations and noises;
- lubrication problems, improper lubrication of components or the lack of it can lead to excessive friction and vibration in the transmission;
- the occurrence of magnetic resonances may cause vibration frequencies that can lead to resonance in transmission components, amplifying vibrations and noise [4].

Magnetic resonance in mechanical transmissions refers to the phenomenon where a variable magnetic field or magnetic source generates vibrations or oscillations in the mechanical components or assemblies around it [5]. There are two main aspects where magnetic resonance can impact mechanical transmissions [6]:

- magnetic torque in gears: In mechanical transmissions involving gears with magnetic components, such as permanent magnets, there is the possibility of magnetic resonance. When two components with varying magnetic fields approach or move relative to each other, a magnetic force of attraction or repulsion between them can occur. If these magnetic forces coincide with the natural frequency of the components, a magnetic resonance can be set up. This phenomenon can lead to unwanted vibrations, which can affect the performance and durability of the gears;
- sub-optimal operating conditions for example a mechanical transmission is used in sub-optimal operating conditions, such as extreme temperatures or contaminated environment, this can lead to the appearance of noises;
- magnetic generators or motors in transmissions: Some mechanical transmissions may contain magnetic generators or electric motors that can generate variable magnetic fields during operation. If the operating frequency of these components coincides with the natural frequency of other mechanical elements in the system, a magnetic resonance can be set up. This can lead to vibrations, noises or even damage to the affected mechanical components.

To avoid or minimize magnetic resonance in mechanical transmissions, it is important to carry out a proper system design, taking into account the magnetic and mechanical interactions between the components involved [7]. Choosing the right materials, balancing components, and careful monitoring of operating frequencies can help reduce or eliminate unwanted vibrations caused by magnetic resonance [8]. Also, the application of techniques to isolate the magnetic components from the mechanical ones and the use of appropriate damping systems can help prevent this phenomenon [9].

Precessional planetary transmissions are a class of mechanical transmissions used to transmit power and torque between different shafts [10]. They are characterized by the use of several planetary gears that rotate around a sun gear and are meshed with a crown wheel. Precessional planetary transmissions have a number of important general aspects:

- *Compact configuration:* Planetary drives have a compact internal configuration, which makes them suitable for applications where space is limited;
- *Variable Gear Ratios:* By adjusting the ratios between the planetary and sun or crown gears, different gear ratios can be obtained, allowing torque and output speed to be adjusted as needed;
- *Torque Splitting Capability:* Planetary transmissions can split torque between multiple planetary gears, making them ideal for applications that require even distribution of power;
- *High efficiency:* Planetary transmissions are known for their high power transmission efficiency, due to their optimized design and the use of quality bearings;

- *Stability under variable loads:* Planetary gears are able to withstand variable loads and shocks, making them suitable for applications with precision requirements under dynamic operating conditions;
- *Durability and reliability:* Due to the fact that the internal components are properly sealed and lubricated, planetary gears have a long life and require less maintenance;
- *Versatility:* Planetary gears can be used in a variety of applications, including robotics, aeronautics, aerospace, medical, machine tools and more;
- *Bidirectional transmission*: Planetary transmissions allow torque to be transmitted in both directions, making them suitable for applications that require reversibility, such as motors and generators;
- *Reduction of vibration and noise:* By proper design and use of suitable materials, planetary gears can reduce vibration and noise during operation [11].

It can be concluded that the sources generating vibrations and noises are to a large extent identical for all types of transmissions, but in the case of precessional transmissions, due to the specific constructive reason, the appearance of the vibro-acoustic sources is longer [12].

2. Recording of vibro-acoustic signals in planetary precessional transmissions

Anechoic chambers are useful in a wide range of applications, including electronic equipment testing, acoustic research, performance testing of telecommunications systems, the study of sounds and vibrations produced by various objects or machines, and many other fields. It is important to note that no anechoic chamber is completely isolated from all acoustic reflections or vibrations, and chamber performance may vary depending on the quality of materials and construction. However, anechoic chambers provide a controlled and isolated environment, essential when recording and analyzing sensitive vibroacoustic signals [13].

The main features of an anechoic chamber include:

Acoustic absorption: The walls, ceiling and floor of the anechoic chamber are covered with acoustic absorbing materials, such as special boards or sound-absorbing material. These materials absorb sound frequencies and minimize reflections and echoes, ensuring that the recorded signal is as pure as possible.

Vibration absorption: In addition to acoustic absorption, an anechoic chamber can also have mechanical isolation systems to prevent the transfer of vibrations from the outside. This ensures that the recorded vibro-acoustic signals are not influenced by unwanted vibrations.

Electromagnetic Isolation: Sometimes anechoic chambers may also have electromagnetic isolation features to protect sensitive signals from external electromagnetic interference.

The anechoic room (Figure 1) from the *„Mechanical and Mechatronic Engineering" Department, „Gheorghe Asachi"* Technical University in Iași is a room, insulated with sound-absorbing material against external noises and anti-vibration isolation, in which sounds are absorbed almost entirely (99%) when incident on adjacent surfaces. The room was built in 1982, with useful dimensions of 10 x 10 x 8 m3 and a wide access door (2 x 1.5 m). The room is wallpapered with clay-based mineral wool prisms, the irregular shape canceling out the reflected acoustic waves. The anti-vibration isolation is almost perfect, the prisms are fixed on a rubber mat, and the foundation of the camera has nothing to do with the foundation of the building. Measurements can be made with great accuracy using Bruel&Kjaer measuring equipment and National Instruments processing

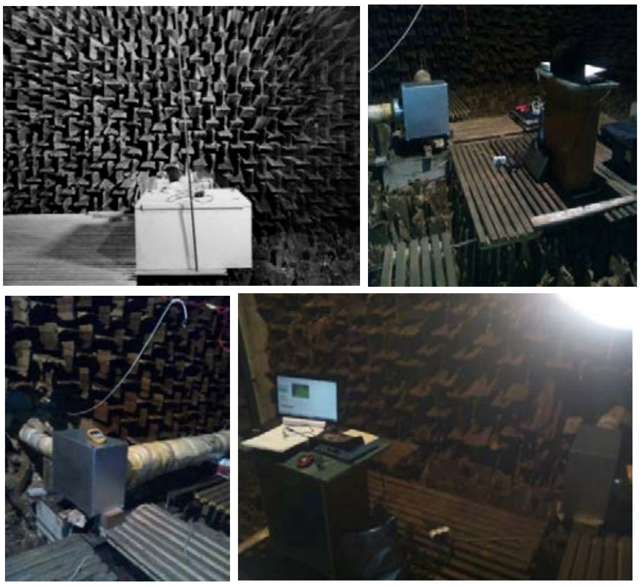

Figure 1. Anechoic chamber.

equipment. The Vibration Laboratory of the Faculty of Mechanics in Iasi uses the camera for the vibroacoustic diagnosis of bearings, gearboxes, some car components, ventilation systems, noise attenuators, calibration of acoustic speakers, etc.

The anechoic chamber shown in (Figure 1) is a specially designed environment to absorb sound waves and minimize acoustic reflections. It is used in a variety of fields and has some distinctive features and key aspects, including:

- *Wall, ceiling and floor covering:* The walls of the anechoic chamber are covered with acoustic absorbing materials, such as acoustic sponges or porous plates, which absorb the incident sound waves. Also, the ceiling and floor are treated in the same way to ensure even absorption;
- *Wall configuration:* The walls of the anechoic chamber may have a special configuration, such as a jagged shape or unusual geometry, to minimize reflections and disperse sound waves;
- *Absence of reflections:* One of the most distinctive aspects of the anechoic chamber is the fact that it minimizes acoustic reflections. This creates an almost totally anechoic environment, where sound waves are largely absorbed and there are no echoes or reverberations;
- *External acoustic isolation:* Anechoic chambers are designed to be acoustically isolated from the external environment, to prevent the entry of unwanted noises and ensure a quiet environment inside;
- *Use in research and testing:* Anechoic chambers are used in various fields such as acoustic research, development of noise-sensitive equipment, testing and calibration of acoustic equipment and testing of absorbent or insulating materials;
- *Specific features:* Anechoic chambers may have certain specific features, such as acoustic windows or special openings to allow testing and measurement inside the chamber without significantly affecting acoustic absorption;
- *Complex design and construction:* Building an anechoic chamber requires complex design and construction to ensure that acoustic absorption is optimized and adequate attenuation of sound waves is achieved;

- *Use in specific studies and research:* Anechoic chambers can be used to study and research different aspects of acoustics, such as evaluating the performance of audio equipment, characteristics of absorbing materials, noise produced by various sources, etc.

Overall, anechoic chambers are a valuable tool in acoustics research and development, providing a controlled and quiet environment for testing and measuring sound waves, as well as for specific studies related to acoustics.

The qualities of the anechoic chamber can be appreciated by the following characteristics:

- the absorption coefficient of the walls (α) is 99% in the frequency band from 150 Hz to 20 kHz. It depends on the characteristics of the sound-absorbing material, the shape and dimensions of the absorbing prisms.
- the deviation from the 1/R law gives indications regarding the nature of the acoustic field in the anechoic chamber, regarding the differences from the conditions of the free acoustic field;
- for sound insulation from the outside, attenuation of 60 ÷ 75dB is recommended, so that the background noise in the room is below the audibility threshold; the background noise falls within the noise curve Cz 25.
- the anti-vibration isolation, on rubber insulators, ensures a low natural frequency (<10Hz).

In recent years, the following have been realized in this room:

- vibroacoustic diagnosis of HVAC equipment (acoustic pressure measurement, FFT analysis, 1/3 octave analysis)
- vibroacoustic diagnosis of noise attenuators (acoustic pressure measurement, FFT analysis, 1/3 octave analysis, acoustic attenuation)
- the study of the acoustic absorption coefficients of different types of sound-absorbing materials (composite, recyclable materials, etc…)

3. Harmonic Fourier analysis of vibro-acoustic waves in precessional transmissions

Harmonic Fourier analysis is a mathematical method used to decompose a complex wave into a series of sinusoidal components of different frequency. This technique is commonly used in the analysis of vibro-acoustic signals to identify and quantify the various frequencies and amplitudes that make up the complex signal. The application of Fourier series in the deciphering of vibroacoustic signals provides an efficient method of analysis and characterization of these complex signals. Fields of applicability include electrical engineering, wave analysis, acoustics. Fourier series are particularly useful in the analysis and deciphering of vibroacoustic signals. These signals can be recordings of vibrations and sounds from various sources, such as cars, engines, mechanical systems or even ambient sounds. By using Fourier series, the frequency components of these signals can be identified and a representation of them in the frequency spectrum can be obtained [14].

In the case of planetary precessional transmissions, Fourier analysis can be used to investigate the vibro-acoustic phenomena associated with the motion and operation of precessional gears. Planetary precessional transmissions type 2K-H consist of two precessional gears, which are formed as a result of the sphero-spatial movement of the satellite block around the precession center – the point of intersection of the straight and inclined axes of the driving crank shaft and the gear teeth generators, which form conical axoids. This complex motion can generate various vibro-acoustic components, including harmonic and interharmonic frequencies, which reflect tooth interactions, tooth movement, and other mechanical phenomena.

A vibro-acoustic spectrogram of a precessional transmission includes several frequencies:

- the rotation frequency of the output shaft, a periodic sinusoidal curve;
- the frequency of engagement of the teeth of the two gears (overlapping on the periodic sinusoidal curve of the driven shaft.

Superimposed on the periodic sinusoid of the output shaft:

- driving shaft rotation frequency;
- tooth engagement frequencies in the two precessional gears;
- frequencies of the bearing elements of the driving and driven shaft, the node of the satellite.

To perform harmonic Fourier analysis of vibro-acoustic spectrograms in precessional planetary transmissions, the following steps can be taken:

Signal recording: The vibroacoustic signal is recorded using specialized sensors or microphones. The recorded signal can be a complex time-varying function.

Signal preprocessing: The recorded signal may contain noise, irrelevant components or artifacts. By applying pre-processing techniques such as filtering and de-noising, the quality of the signal can be improved and the relevant features can be better highlighted.

Fourier series decomposition: Using Fourier series, the preprocessed signal can be decomposed into a sum of complex sinusoidal or exponential components. This involves the calculation of the Fourier series coefficients by integration or specific calculation algorithms.

Spectral Analysis: Identify and analyze the spectral components of signals, such as main frequencies, harmonics, interharmonics, and corresponding amplitudes. By transforming the Fourier series coefficients in the frequency domain, the frequency spectrum of the signal can be obtained. It shows which frequencies are present in the signal and with what magnitude.

Interpretation of results: Analysis of the frequency spectrum allows the identification of the main components of the signal, such as dominant frequencies, harmonics or other specific characteristics. This can help diagnose problems in precessional transmission or understand the origin of vibroacoustic signals. For example, certain harmonic frequencies may suggest problems with gear teeth or precessional motion timing.

This analysis can be particularly useful in diagnosing faults or improving the performance of precessional planetary drives, allowing engineers to better understand the dynamic behavior of the system and identify potential problems before they become critical.

It is important to note that Fourier analysis can be complex and requires advanced mathematical knowledge and signal analysis techniques. Also, harmonic analysis of vibro-acoustic waves in precessional planetary transmissions can be influenced by factors such as lubrication, wear of parts and mechanical loading of the system.

Fourier series have many practical uses, because manipulating and conceptualizing the harmonic coefficients is often easier than working with the original function. Fields of applicability include engineering, wave analysis, acoustics. Fourier series are particularly useful in the analysis and deciphering of vibroacoustic signals. By using Fourier series, one can identify the frequency components of these signals and obtain a detailed representation of them in the frequency spectrum.

Since the vibro-acoustic function of a precessional transmission is periodic, then the most appropriate method of harmonic analysis is the Fourier series decomposition. The presentation of the vibro-acoustic function of the precessional transmission through the Fourier series is dictated by the following advantages:

- unlimited possibilities of presenting the vibro-acoustic function of any real mechanism;
- the simplicity of establishing the causes of vibration and noise generation due to the fact that the form of expression of this function in the form of a trigonometric series corresponds entirely to the nature of vibro-acoustic effects;
- the possibility of decomposing the summary vibro-acoustic function into a series of harmonic components;
- the possibility of establishing the degree of influence of different geometro-kinematic parameters on the summary vibro-acoustic values of the transmission.

The vibro-acoustic function, expressed by the Fourier series in the limits *0 < x > 2,* has the form [15]:

$$F(n) = A_0 + \sum_{k=1}^{n}(a_k \cos kx + b_k \sin kx), \tag{1}$$

where a_k and b_k are the decay coefficients, which best approximate the periodic components. Such values of the coefficients must be found, which will ensure the maximum approximation of the functions *F(n)* and *f(x)*.

According to Eq. (2) we have:

$$a_k = \frac{1}{\pi}\int_0^{2\pi} f(x)\, cos\, kx\, dx;$$
$$b_k = \frac{1}{\pi}\int_0^{2\pi} f(x)\, sin\, kx\, dx; \tag{2}$$
$$A_0 = \frac{1}{2\pi}\int_0^{2\pi} y_2 \sin kx_2\, dx.$$

Using the method of numerical analysis, the Fourier coefficients are approximately determined from the relations:

$$a_k = \frac{2}{N}\sum_{i=1}^{N} y_i\, cos\, kx_i\,;$$
$$b_k = \frac{2}{N}\sum_{i=1}^{N} y_i\, sin\, kx_i\,. \tag{3}$$

The constant component $A_0 = a_0/2$, where a_0 is determined similarly to a_k for $k=0$. Taking into account the peculiarities of *the cos kx* and *sin kx factors,* the number *N* is often taken as equal to *12* or *24* . In case of need for greater precision, *N* is taken equal to *48* .

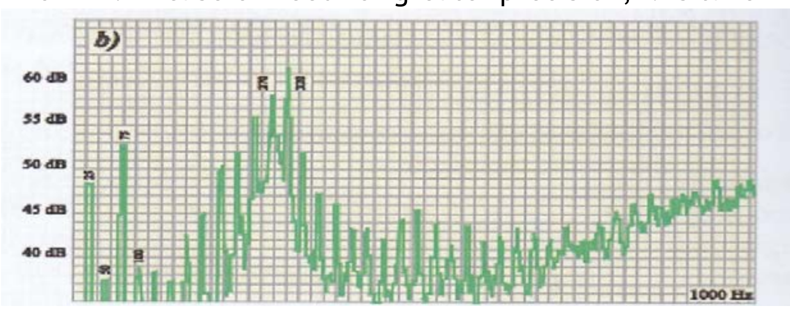

Figure 2. Vibration spectrogram of the 2K-H precessional reducer with the transmission ratio i=-324, n=1500 min $^{-1}$**.**

Since the research of the vibro-acoustic level of precessional transmissions is obtained graphically (vibro-acoustic spectrograms), then the most convenient method of calculating the Fourier coefficients is the template method.

To obtain the probable values of the Fourier coefficients, a sufficient number of records (spectrograms) (e.g. ten) of the same precessional reducer (e.g. Figure 2), recorded in the same operating regimes, must be analyzed. Each diagram is divided into 12 parts. For different measurements y_i at each point for all diagrams the arithmetic mean y_i is determined.

In order to authentically describe the signal, it is necessary to process it, using various existing methods. Using the method described above, the function for determining the kinematic error was obtained. To obtain the probable values of the *Fourier coefficients,* a sufficient number of records were analyzed – ten diagrams, recorded in the reducer control recorder with the transmission ratio *i = 324* at the same operating regimes.

The arithmetic mean of the *Fourier coefficients* for the 10 measurements:

$$\bar{y}_i = \frac{\sum_{j=1}^{10} y_j}{10}, (4)$$

For arithmetic means ***y,*** we determine the mean squared deviation:

$$\sigma = \sqrt{\sum_{j=1}^{10} (y_j - y)/9}. (5)$$

The maximum arithmetic and statistical errors will be:

$$\Delta n(y) = \pm 3\sigma;$$
$$\frac{\Delta n(y)}{\bar{y}} = \pm \frac{3\sigma}{\bar{y}}. (6)$$

Based on the obtained values, templates are made, with which the Fourier coefficients are calculated. The result of the performed harmonic analysis is completed with the elaboration of the vibro-acoustic function, which allows the minimization of the detected vibro-acoustic effects.

Fourier transform. The Fourier transform is a mathematical function that can be used to find the fundamental frequencies that make up a wave. Computers use an algorithm called *the Fast Fourier Transform (FFT)* to quickly calculate any but the simplest signal transforms.

4. Conclusion

The basic goal of researchers in the field is to optimize the constructive part by implementing new solutions to reduce the vibro-acoustic factor. The problem of vibrations and noises in the planetary precessional transmissions is a moment that cannot be avoided due to its specific construction.

The study of sources generating oscillations, the recording of signals and their final deciphering, is of major importance at the stage of designing/updating planetary precessional transmissions. The performed harmonic analysis by calculating of the Fourier coefficients ensure the elaboration of the vibro-acoustic function, which allows the minimization of the detected vibro-acoustic effects.

The anechoic chamber was studied for the execution of experimental measurements in order to establish the sources generating vibro-acoustic signals on a prototype of a precessional planetary reducer and the Fourier series were studied in order to decipher the recorded signals with the aim of proposing and implementing constructive solutions to minimize the vibro-acoustic impact.

Conflicts of Interest: The authors declare no conflict of interest.

References

1. Katznelson, Y. *An introduction to harmonic analysis. Second corrected edition*. Dover Publications, Inc., New York, 1976, 311 p. ISBN 0-486-63331-4.
2. Cordoneanu, D. Smart monitoring and maintenance of a mechatronic system. PhD thesis. Politehnica University, Bucharest, 2022.
3. Vamsi, I.; Sabareech, G.R.; Vaibhav Sh. Integrated Vibro-Acoustic Analysis and Empirical Mode Decomposition for Fault Diagnosis of Gears in a Wind Turbine. In 2nd International Conference on Structural Integrity and Exhibition 2018, 14, pp. 937-944.
4. Malcoci, Iu. Cercetarea nivelului de vibrații și zgomot în transmisiile planetare precesionale. PhD thesis. Technical University of Moldova, Chișinău, 2015.
5. Fedorenko, I. Ya. *Vibration processes and devices in APK*. Altajskogo GAU, Barnaul, 2016, 245 p.
6. Vibrodiagnostika: Vibrodiagnostika defektov mexanicheskix peredach. Available online: https://vibro-expert.ru/vibrodiagnostika-defektov-mexanicheskix-peredach.html (accessed on 06.08.2023).
7. Malcoci, Iu.; Ciobanu, R.; Ciobanu, O. Dynamic systems – vibro-acoustic analysis laboratory guide: case studies. Tehnica UTM, Chisinau, RM, 2017, 94 p.
8. Vibrations and Noises: Research on the Study of Mechanical Vibrations with Data Acquisition Systems, ©2023 [cited 2023-09-01]. Available online: http://stiintasiinginerie.ro/wp-content/uploads/2014/01/104-CERCET%C4%82RI-PRIVIND-STUDIUL-VIBRA%C5%A2IILOR.pdf (accessed on 06.08.2023).
9. Assessment of Vibration and Noise: Aspects of Assessment of Noise and Vibration in Mechanical Transmissions, ©2023 [cited 2023-09-01]. Available online: https://ibn.idsi.md/sites/default/files/imag_file/190-197_8.pdf (accessed on 06.08.2023).
10. Bostan, I. ; Dulgheru, V. ; Malcoci, Iu. Some aspects regarding planetary precessional transmission dynamics. In CoSME'20 IOP Conf. Series: Materials Science and Engineering, 2021, 1009, 012008.
11. Mechanical transmissions: Signal filters used in vibrodiagnosis of mechanical transmissions, 2023. Available online: https://www.ttonline.ro/revista/transmisii-mecanice/filtre-de-semnal-utilizate-in-vibrodiagnoza-transmisiilor-mecanice (accessed on 16.08.2023).
12. Malcoci, Iu., Bodnariuc I. Vibroacoustical diagnosis of planetary precessional kinematical transmission. In IOP Conference Series Materials Science and Engineering, 2016, 147(1), 012003.
13. Anechoic chamber: Acoustic Laboratory, 2023. Available online: http://www.comoti.ro/ro/laboratoare_experimentari_4_2.htm (accessed on 03.08.2023).
14. Fourier transform: Application of the Fourier transform for deciphering vibro-acoustic signals, 2023. Available online: https://ro.alegsaonline.com/art/35911 (accessed on 16.08.2023).
15. Berman, A.F. Kratkij kurs matematicheskogo analyza. Nauka, Moscow, 1973, 720 p.

Citation: A Slobodeaniuc, S. Processing of vibro - acoustic signals of precessional planetary transmissions. *Journal of Engineering Science* 2023, 30 (3), pp. 16-25. https://doi.org/10.52326/jes.utm.2023.30(3).02

Publisher's Note: JES stays neutral with regard to jurisdictional claims in published maps and institutional affiliations.

Submission of manuscripts: jes@meridian.utm.md

Journal of Engineering Science | *Vol. XXX, no. 3 (2023), pp. 26 - 34*
Fascicle | *Industrial Engineering* | *ISSN 2587-3474*
Topic | *Applied Engineering Sciences and Management* | *eISSN 2587-3482*

https://doi.org/10.52326/jes.utm.2023.30(3).03
UDC 656.05

CROSSING SPEEDS OF CARS THROUGH SIGNALIZED INTERSECTIONS

Narciza-Izabela Galusca *, ORCID: 0000-0003-4084-2010,
Silviu-Cristian Iriciuc, ORCID: 0000-0001-8136-7426,
Gelu-Răzvan Gimiga, ORCID: 0000-0002-6798-1793,
Diana-Nicoleta Dima, ORCID: 0000-0002-2217-4330,
Maria-Cristina Scutaru, ORCID: 0000-0002-7077-340X

Gheorghe Asachi Technical University of Iasi-Romania, Department of Transportation Infrastructure and Foundations, 1 Mangeron Blvd, 700050, Iasi, Romania
*Corresponding author: Narciza-Izabela Galusca, *narciza-izabela.galusca@academic.tuiasi.ro*

Received: 07. 12. 2023
Accepted: 08. 22. 2023

Abstract. The article deals with the problem of traffic in three traffic-light intersections in the street network of Iasi city. Usually, the existing traffic lights do not fully take into account the size, structure and parameters of the queue of vehicles waiting at intersections; which in turn affects the traffic capacity of the intersection. In the study, we used a representative set of measurements taken at the three intersections to interpret the variation in the crossing speeds of the traffic light intersection space by the vehicle columns using the linear regression method. We studied several categories of vehicles queuing before the stop line at the intersection. We made a statistical analysis of the time taken to cross three intersections by vehicles in different starting positions. The main results of the research showed estimates in good agreement with observational data as well as a significant reduction in vehicle speed (to 58%) when there are different categories of vehicles queuing at the intersection. This study can be used in the urban traffic diagnosis method, being part of a traffic study together with urban traffic forecasting and therapy.

Keywords: *conflict points, direction, distance, queue, traffic, vehicle.*

Rezumat. Articolul tratează problema traficului în trei intersecții semaforizate din rețeaua de străzi din Iași. Semaforizările existente nu iau în considerare pe deplin dimensiunea, structura și parametrii cozii de vehicule care așteaptă la intersecții; care afectează la rândul său capacitatea de circulație a intersecției. În studiu, s-a folosit un corp reprezentativ de măsurători efectuate în cele trei intersecții pentru a interpreta variația vitezelor de traversare a spațiului intersecțiilor semaforizate de către coloanele de vehicule utilizându-se metoda regresiei liniare. S-a studiat mai multe categorii de vehicule care stau la coadă înaintea liniei de oprire la intersecție. S-a făcut o analiza statistică a timpului necesar traversării unei intersecții de către vehiculele aflate în diferite poziții inițiale. Principalele rezultate ale cercetării au arătat estimări în bună concordanță cu datele rezultate din observații precum și o reducere semnificativă a vitezei vehiculului (la 58%) în cazul în care sunt diverse categorii de vehicule care stau la coadă la intersecție.

Cuvinte cheie: *puncte de conflict, direcție, distanță, coloană, trafic, vehicul.*

1. Introduction

At street intersections, some components of the traffic process influence the functioning of intersections. The management of the traffic flow on the intersection surface, as well as its functioning, depends directly on the space available in the intersection, the existing public transport and the cargo shipment.

Public transport and cargo vehicles are defined by large dimensions, poor maneuverability, slow starting and limited speeds, these vehicles place additional demands on the elements of an intersection, introducing heavy traffic conditions, which must be considered both in the calculation of traffic lights at intersections and in their design and road layout measures and provisions.

In an intersection that can provide sufficient space, management of traffic flows, the dimensioning of traffic storage lanes, the crossing is optimized, and conflict points can be eliminated or their impact on flows reduced.

In an intersection that lacks space (especially when it has built-up frontages), it is not possible to achieve a correct management of traffic flow, certain spaces are given up or others are reduced in size, resulting in difficult traffic processes, with reduced speed and flow of traffic and even increasing the possibility of conflict between vehicles or even traffic accidents [1].

But vehicle delays include many parameters such as signal timing, number of phases, vehicle advances, saturation flow, queuing, etc. [2].

It was also observed that the length of the queue depended on its composition and the associated stop time [3].

The traffic flow through signalized intersections is influenced by a series of factors, among which deserve mention: the time distribution of the traffic, the movement law of the vehicle queues waiting to enter/ cross the intersection, the features of the signal regime, the crossing speed through the intersection [4].

Since other traffic characteristics trough intersections have earlier been studied, an analysis of the variation of the crossing speeds is done in this paper taking into account several parameters as: the vehicle type, its position in the queue, the distance to be passed, the movement direction (through/ left turning) of the cars entering the intersection [5].

2. Measurements of the Crossing Speeds

2.1. Confidence Level

In order to ensure an acceptable level of confidence to the results of measurements [4], the average crossing speeds at a couple of intersections were determined on large amounts of observed vehicles, and taking care to encounter various situations able to reveal the influence of the parameters mentioned in the Introduction.

Intersections: the measurements were performed at: I – intersection Primaverii Bvd Whit T. Vladimirescu (Figure 1), II – Intersection Independentei Bvd. With V. Alecsandri Street (Figure 2), III – Intersection at “Cotnari” (Socola Bvd. With Primaverii Bvd.) (Figure 3) [6].

2.2. Conditions for Performing the Measurements

a) Measurements were performed during periods of most intensive traffic (peak hours of traffic flow).

b) The weather, visibility roadway conditions were normal.

c) The longitudinal roadway declivities were negligible.

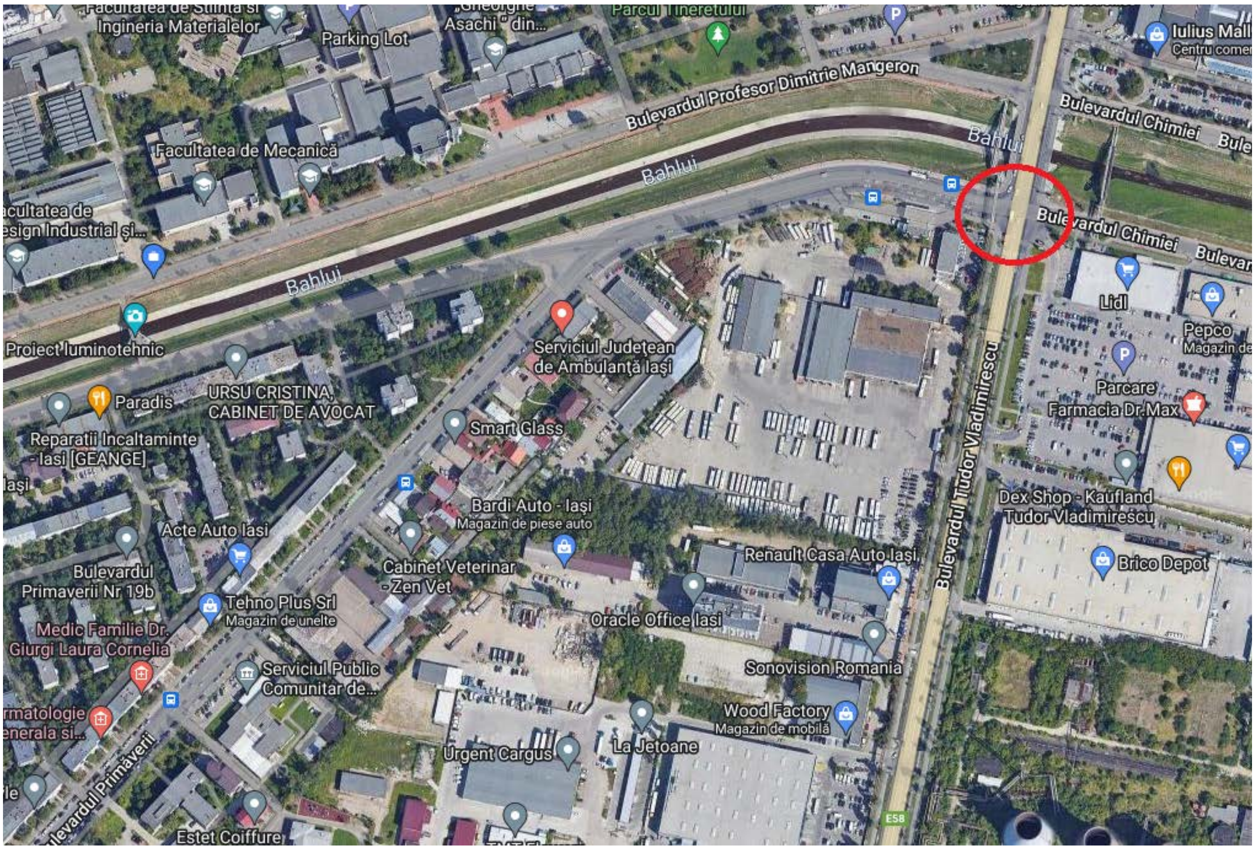

Figure 1. I – Intersection Primaverii Bvd Whit T. Vladimirescu.

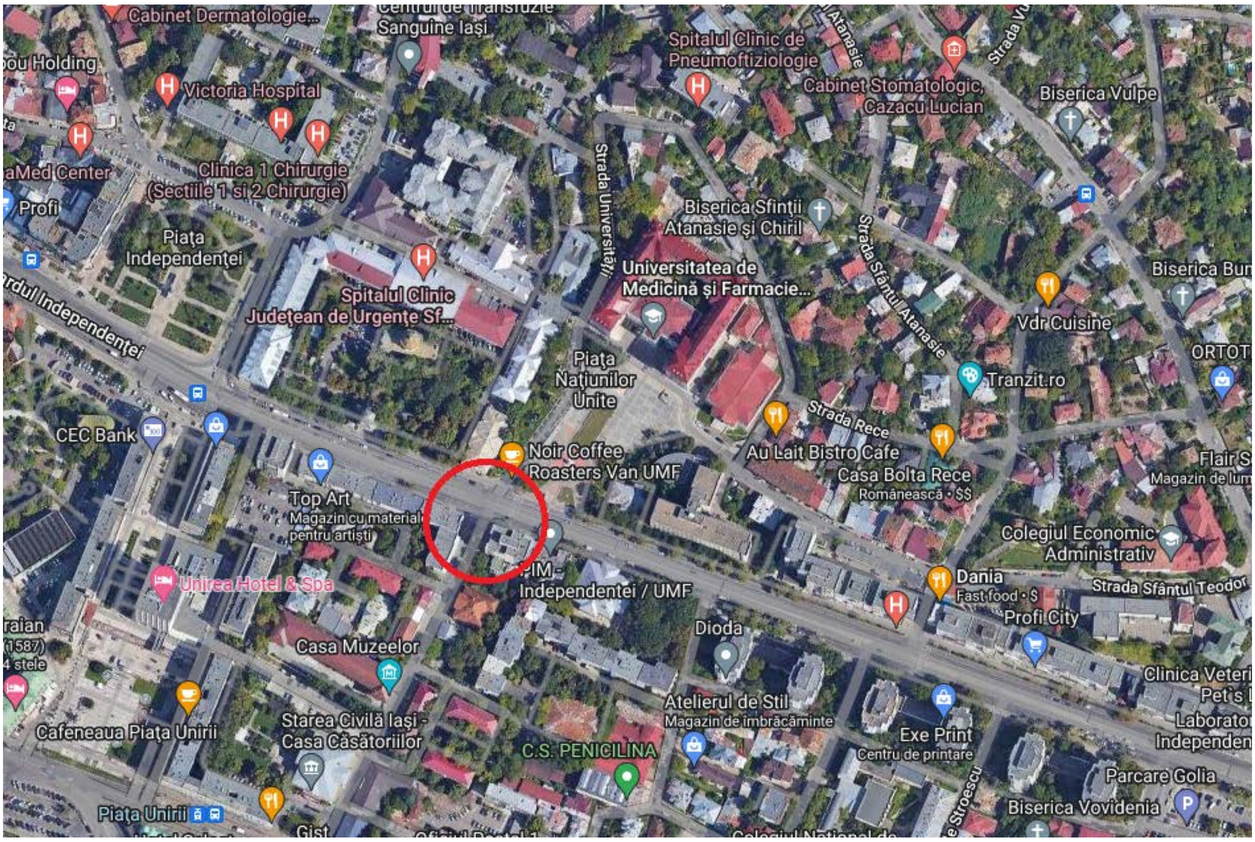

Figure 2. II – Intersection Independentei Bvd. With V. Alecsandri Street.

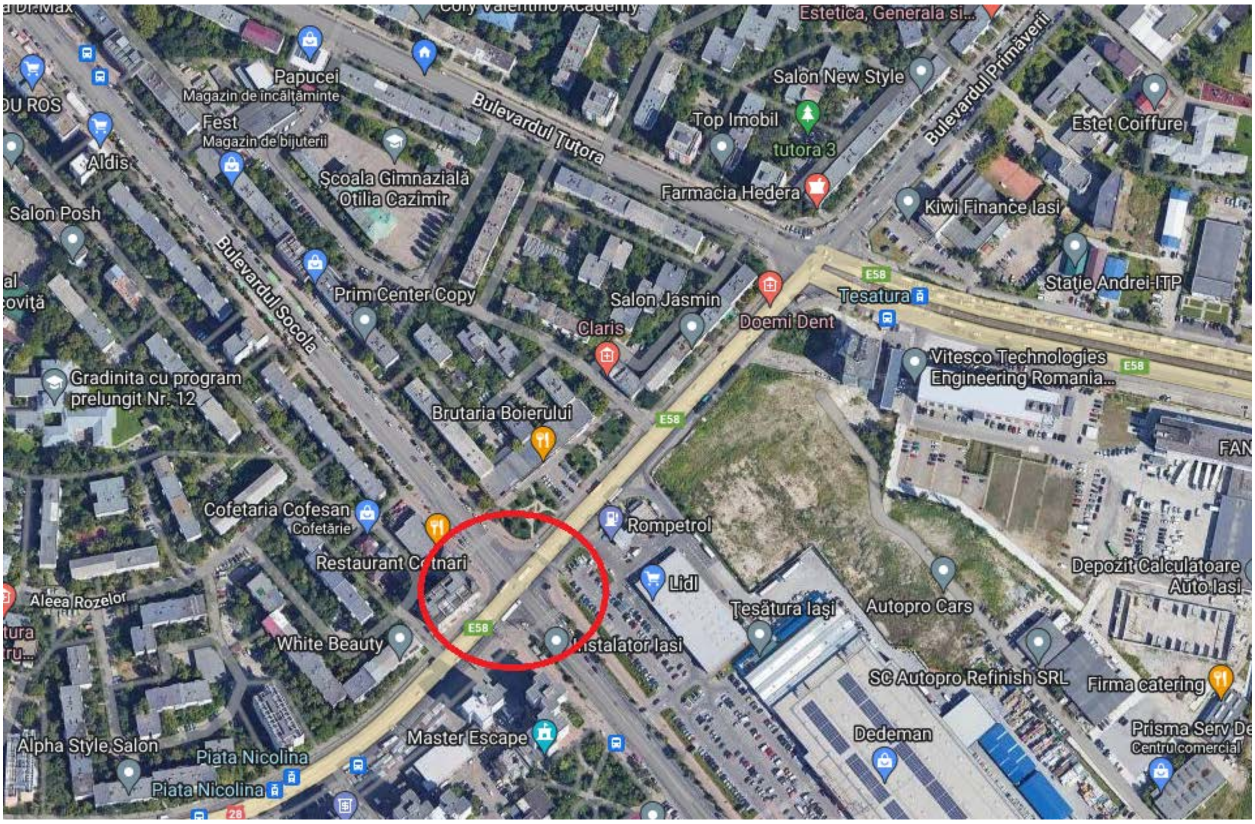

Figure 3. III – Intersection at “Cotnari” (Socola Bvd. With Primaverii Bvd.).

d) The intersections selected for measurements were quite different as regards the traffic features.

e) The crossing speeds were measured from the starting moment of the queue having waited behind the STOP line by the signal.

The average crossing speeds over the distance D (Figure 4) were calculated by use of the Eq. (1) [7-16]:

$$v = \mathrm{D}/\Delta t \tag{1}$$

Where the distances to be crossed were measured in meters and the crossing times (in seconds) were measured by direct observation of the crossing process, using a chronometer. More exactly, $\Delta t = t_2 - t$, where t_1 is the starting moment, while t_2 is the moment at which the vehicle has covered the distance D, (Figure 4) [7-16].

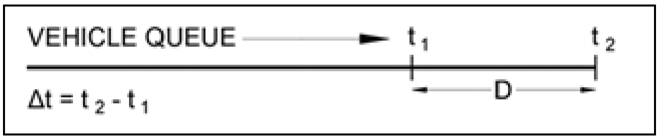

Figure 4. Time interval and distance to be covered for crossing an intersection.

3. Results and Discussion

The present study focuses on *determining the variation of crossing speeds of traffic-light intersections by columns of vehicles* through manually collected data using the linear regression method for three signalized intersections under heterogeneous traffic conditions in the city of Iasi.

Note that crossing speeds are a function of some specific elements such as:

- Intersection crossing direction (forward, left turn) and crossing distance (intersection I forward - 36 m, left turn - 28 m; intersection II forward - 67 m, left turn - 24 m; intersection III forward - 47 m). The greater the distance, the more the column of vehicles can exceed the starting speed stage and enter a normal speed development mode. The speeds developed by vehicles crossing the intersection in the forward direction are higher than the speeds of vehicles in a column turning left, for example.
- Vehicle type (PC - passenger cars, MWV - mid-weight vehicles, B - buses, B3 - 3-axle buses, T - trucks, SV - special vehicles). Lighter and faster vehicles can develop higher crossing speeds than heavier vehicles.

The average values of the crossing speeds determined for the intersections under observation (in this study), also depending on some above mentioned features, are presented in Table 1 and their variation for the through and left turn directions are illustrated in diagrams of Figures 5 and 6.

The shapes of the variation curves of the mean crossing speeds as depending on the vehicle positions in the queue (Figures 5 and 6) clearly suggest that most of them are piecewise almost linear, therefore they may be piecewise approximated by segments of straight lines that together form open polygonal lines. In order to obtain better approximations, the x-axis was divided into several intervals, but these partitions differ from one intersection to another and they also depend on the vehicle type and on moving direction. Thus, the mean crossing speed y depends on the vehicle position in the queue x (which is a positive integer variable) via a linear equation of the form Eq. (2):

$$y = \mathrm{a}_{ij} * x + b_{ijk}, \tag{2}$$

where is related to the intersection and movement direction, j corresponds to the vehicle category (PC – passenger cars, MWV – mid-weight vehicles, B – buses, B3 – 3-axle buses, T – trucks, SV – special (very heavy) vehicles); finally, k corresponds to the current interval in one of the above mentioned partitions (each of them associated to a subscript pair (i, j). The coefficients a_{ijk} and b_{ijk} were estimated based on the statistical data presented in (Table 1), using the method of linear regression.

Table 1

Mean Intersection Crossing Speeds, [m/s]

Inter-section	Direction	Distance	Vehicle type	1	2	3	4	5	6	7	8	9
				Vehicle position in the queue								
I	through	D = 36 m	PC	5.71	6.20	6.50	6.75	7.07	7.52	7.83	8.26	8.72
			MWV	5.45	5.72	5.97	6.23	6.51	6.65	6.92	-	-
			B	4.58	4.79	4.97	5.14	5.35	5.52	-	-	-
			B_3	4.33	4.56	4.72	4.91	5.11	5.26	-	-	-
	left	D = 28 m	PC	5.49	5.79	6.02	6.36	6.75	7.20	7.55	8.00	-
			MWV	5.15	5.38	5.52	5.77	6.00	6.22	-	-	-
			B	4.54	4.91	5.15	5.31	5.40	5.53	-	-	-
			B_3	4.01	4.19	4.42	4.62	4.80	-	-	-	-
			SV	3.78	3.92	4.03	4.16	4.27	4.38	-	-	-
II	through	D = 67 m	PC	7.12	7.40	7.70	7.98	8.27	8.54	8.76	8.93	9.07
			MWV	7.05	7.21	7.40	7.64	7.86	8.09	8.29	-	-
			B	5.58	5.83	6.09	6.43	6.69	-	-	-	-
			B_3	5.45	5.76	5.91	6.09	6.26	-	-	-	-

ContinuationTable 1

	left	D = 24 m	PC	5.02	5.26	5.57	5.70	5.91	6.22	6.54	6.87	7.10
			MWV	4.63	4.93	5.04	5.14	5.23	5.41	5.54	-	-
			B	4.24	4.53	4.77	4.90	5.00	-	-	-	-
			B_3	3.44	3.77	4.05	4.19	4.35	-	-	-	-
III	through	D = 47 m	T	5.26	5.42	5.54	5.66	5.80	5.93	6.06	6.14	-
			SV	3.78	3.92	4.03	4.16	4.27	4.38	-	-	-

The maximum deviations from the estimated values, for each line corresponding to a triple (i, j, k) of subscripts, are listed in the last two columns of (Table 2 and Table 3), while the middle column contains the linear equation of the line segment assigned to each of these triples. These deviations (given in percent, above and under the estimated value, respectively) enable us to remark that the approximation of variation curves of the crossing rates (speeds) with the vehicle position in the queue (and with the other three features) is very accurate: the largest deviation found was equal to 1.6%.

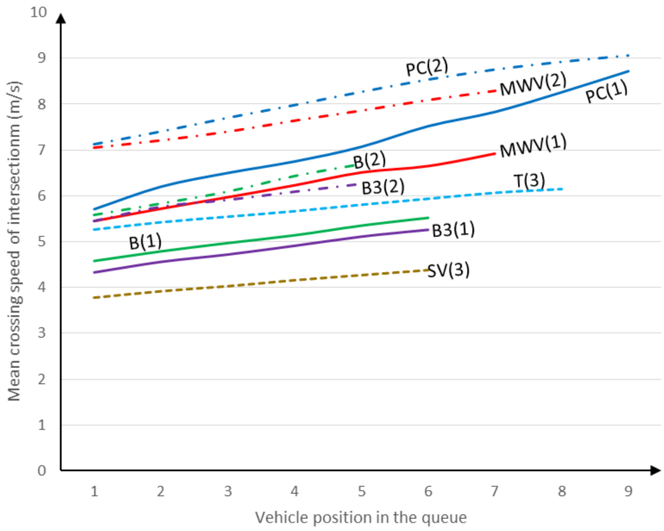

Figure 5. Mean crossing speeds vs. vehicle position in the queue, for through movement and five vehicle types.

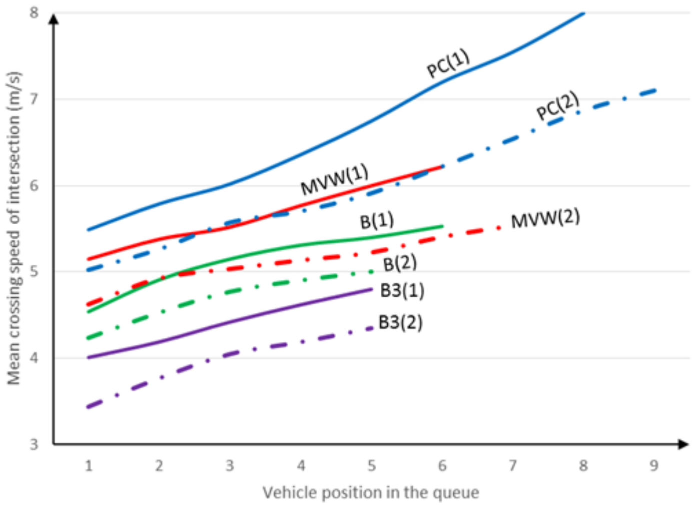

Figure 6. Mean crossing speeds vs. vehicle position in the queue, for LEFT TYRBS movement and four vehicle types.

Table 2

The Equations Modelling the Variation of the Crossing Speeds with the Vehicle Position in the Queue

Intersection, Direction	Vehicle type	Vehicle position	Linear regression equations (including a parabolic equation)	Maximum deviation [%]	
				+	-
I through	PC	1-7	y = 0.340x + 5.450	1.10	1.10
		7-12	y = 0.540x + 4.000	1.60	1.40
	MWV	1-7	y = 0.262x + 5.190	0.10	0.20
		7-12	y = 0.205x + 5.475	0.20	0.20
	B	1-6	y = 0.188x + 4.400	0.20	0.30
	B3	1-6	y = 0.188x + 4.157	0.50	0.60
II through	PC	1-5	y = 0.288x + 6.830	0.10	0.10
		5-9	y = 0.210x + 7.220	0.40	0.80
	MWV	1-3	y = 0.172x + 6.887	0.20	0.10
		3-7	y = 0.227x + 6.712	0.10	0.30
	B	1-5	y = 0.277x + 5.290	0.50	0.50
	B3	1-2	y = 0.310x + 5.140	0.00	0.00
		2-5	y = 0.167x + 5.425	0.30	0.10
III through	T	1-8	y = 0.127x + 5.146	0.40	0.40
	SV	1-6	y = 0.120x + 3.670	0.40	0.30

Table 3

The Equations Modelling the Variation of the Crossing Speeds with the Vehicle Position in the Queue

Intersection, Direction	Vehicle type	Vehicle position	Linear regression equations (including a parabolic equation)	Maximum deviation [%]	
				+	-
I left turns	PC	1-3	y = 0.255x + 5.255	0.40	0.40
		3-8	y = 0.388x + 4.856	0.80	0.50
	MWV	1-3	y = 0.180x + 4.986	0.30	0.60
		3-6	y = 0.233x + 4.827	0.10	0.20
	B	1-4	$y = -0.057x^2 + 0.540x + 4.057$	0.30	0.10
		4-6	y = 0.110x + 4.865	0.30	0.10
	B3	1-5	y = 0.198x + 3.182	0.40	0.40
II left turns	PC	1-5	y = 0.227x + 4.830	0.90	1.10
		5-9	y = 0.295x + 4.490	0.90	0.30
	MWV	1-2	y = 0.300x + 4.330	0.00	0.00
		2-5	y = 0.100x + 4.730	0.00	0.20
		5-7	y = 0.155x + 4.455	0.00	0.40
	B	1-3	y = 0.265x + 3.975	0.00	0.60
		3-5	y = 0.115x + 4.425	0.00	0.30
	B3	1-3	y = 0.305x + 3.135	0.00	0.70
		3-5	y = 0.150x + 3.600	0.20	0.00

4. Conclusions

A couple of conclusions may be drawn from the presented data and the piecewise linear estimations of the mean intersections crossing speeds as functions of the vehicle position in the queue, of the particular intersection observed, of the vehicle type and of the movement direction, using the linear regression method:

1. The crossing speed steadily grows from the first vehicle (on the first position in the queue), because of the delay due to the start from a still state, towards the most remote positions in the queue. The latest vehicles take advantage of the time needed to reach a higher speed until entering the intersection.

2. The lower is the crossing speed, the heavier is the vehicle.

3. The crossing speeds for vehicles moving through are higher than the ones for left-turning vehicles if we compare them for the same vehicle type and position in the queue. This difference is natural because of the difficulties of left turns.

4. The distance D to be covered also influences the crossing speeds, which grow with it since the vehicles can reach a higher speed due to a longer time for acceleration.

5. The composition of the waiting queue is less important for an approach street with several (two or three) lanes, but it is significant for one-lane approaches. The same holds for the percent of left-turning vehicles, which cause delays in the movement of the whole queue.

As a conclusion, it may be appreciated that the mathematical modelling of the crossing speeds through street intersections using *piecewise linear equations* obtained by *linear regression* gives (very) accurate results. Therefore, it may be useful in the analysis (diagnosis) of the urban traffic flow through signalized intersections, and it thus provides a basis for studies aiming at the improvements of traffic signal regimes.

Conflicts of Interest: The authors declare no conflict of interest.

References

1. Popovici, D.; Boboc, V.; Găluşcă N.I. *Transport systems and urban traffic*. "Matei-Teiu Botez" Academic Society, Iasi, Romania, 2004, pp. 183-207. [in Romanian].
2. Murat, Y.S.; Kutluhan, S.; Cakici, Z. Investigation of Cyclic Vehicle Queue and Delay Relationship for Isolated Signalized Intersections. *Procedia Social and Behavioral Sciences* 2014, 111, pp. 252-261.
3. Parmar, D; Gore, N.; Rathva, D.; Dave, S.; Jain, M. Modelling Queuing of Vehicles at Signalized Intersection. *Transportation research* 2020, 45, pp. 557-565.
4. Zarojanu, G.H. *Technical elements of road traffic*. "Matei-Teiu Botez" Academic Society, Iasi, Romania, 2002, pp. 54-79, pp.104-122. [in Romanian].
5. Popovici, D.; Zarojanu, G.H. Urban intersections without traffic lights: Mathematical modeling of vehicle interval frequencies. *Roads and Bridges* 1995 25-26, pp.73-75.
6. https://www.google.com/maps/place (accessed on 05.11.2022).
7. STAS 10795/1-76. Road traffic technique. Traffic investigation methods. Classification.
8. STAS 10144/6-89. Calculation of traffic capacity of street intersections.
9. SR-7348-2001: Equivalence of vehicles for determining driving capacity.
10. STAS 10144/3-91: Geometric elements of streets.
11. Regulations for determining the traffic capacity of public roads PD-189.
12. SR-10795/2-2001: Road traffic technique. Traffic recording equipment.
13. Departmental technical instructions for conducting censuses and developing traffic forecasts in localities and establishing perspective traffic. CD-84.
14. Regulations for the development of traffic studies in localities and the territory of influence" C-242.
15. STAS 1848/4-95: Traffic lights for directing traffic.
16. SR-10144/4-95: Development of street intersections.

Citation: Galusca, N.I.; Iriciuc, S.C.; Gimiga, G.R.; Dima, D.N.; Scutaru, M.C. Crossing speeds of cars through signalized intersections. *Journal of Engineering Science* 2023, 30 (3), pp. 26-34. https://doi.org/10.52326/jes.utm.2023.30(3).03

Publisher's Note: JES stays neutral with regard to jurisdictional claims in published maps and institutional affiliations.

Submission of manuscripts: jes@meridian.utm.md

Journal of Engineering Science *Vol. XXX, no. 3 (2023), pp. 35 - 59*
Fascicle *Industrial Engineering* *ISSN 2587-3474*
Topic *Applied Engineering Sciences and Management* *eISSN 2587-3482*

https://doi.org/10.52326/jes.utm.2023.30(3).04
UDC 621.311.6:629.113-83

DIRECTING THE UNIFORMITY OF THE LEVEL OF PULSE CHARGING OF LI-ION BATTERIES USED IN AUTOMOTIVE INDUSTRY

Oleg Petrov* ORCID: 0000-0003-4791-2384

Technical University of Moldova, 168, Stefan cel Mare Blvd., Chisinau, Republic of Moldova
*Corresponding author: Oleg Petrov, *oleg.petrov@tran.utm.md*

Received: 07. 14. 2023
Accepted: 08. 26. 2023

Abstract. The lithium-ion (Li-ion) battery is widely used in modern electronics, serves as a power source in electric vehicles and for energy storage in renewable energy systems. The strengths of Li-ion batteries are their high energy density. Modern Li-ion batteries can include arrays of cells, the lifetime of which is determined by factors that depend on charge-discharge characteristics. Li-ion batteries connected in series have different aging rates due to different capacities. The capacity deviation increases as the battery has been used, generating an increase in compensation current, which continues to increase until ignition. To solve this problem, a pulse device and a charging method in a charge equalization battery were proposed in this paper. A numerical simulation of how to charge real Porsche Taycan car batteries was performed. The results obtained confirmed the effectiveness, the energy losses did not exceed 2% of the battery capacity. A bench diagram was developed for studying and programming the operating modes of battery control units for hybrid and electric cars.

Keywords: *lithium-ion battery charging, current pulses, charge equalization, resistive voltage divider, testing charging systems.*

Abstract. Bateria litiu-ion (Li-ion) este utilizată pe larg în electronicele moderne, servește drept sursă de energie în vehiculele electrice și pentru stocarea energiei în sisteme cu surse regenerabile. Punctele forte ale bateriilor Li-ion sunt densitatea lor mare de energie. Bateriile moderne Li-ion pot include rețele de celule, a căror durată de viață este determinată de factori care depind de caracteristicile de încărcare-descărcare. Bateriile conectate în serie au rate diferite de îmbătrânire din cauza capacităților variate. Abaterea capacității crește pe măsură ce bateria a fost utilizată, generând o creștere a curentului de compensare, care continuă să crească până la aprindere. Pentru a rezolva această problemă, în lucrare au fost propuse un dispozitiv de impuls și o metodă de încărcare într-o baterie cu egalizare de încărcare. A fost efectuată o simulare numerică a modului de încărcare a bateriilor auto Porsche Taycan real. Rezultatele obtinute au confirmat eficacitatea, pierderile de energie nu au depasit 2% din capacitatea bateriei. A fost dezvoltată o schemă de banc pentru studiul și programarea modurilor de funcționare a unităților de control a bateriei pentru mașini hibride și electrice.

Cuvinte cheie: *încărcare baterii litiu-ion, impulsuri de curent, egalizarea încărcării, divizor rezistiv de tensiune, testare sisteme de încărcare.*

1. Introduction

Most new electric vehicles are equipped with lithium-ion batteries. Batteries account for about 40% of the cost of electric vehicles and 60% of the cost of high-capacity energy storage [1]. The energy of charged batteries in an electric car is mainly used to power electric drives of cars with a voltage of up to 400 V. A separate battery has a low electromotive force (EMF), therefore, to obtain a high voltage, these batteries are connected in series into a battery.

At the same time, the characteristics of the elements of these batteries must be strictly the same. However, it is known that no two batteries are the same, even if they are made by the same manufacturer and have the same model. Small changes in the characteristics of each cell will still take place, whether it be the state of charge (SoC), equivalent series resistance (ESR), capacity or temperature characteristics. When cells are connected to each other to form a battery, changes in characteristics result in an imbalance in cell voltages. For example, if one cell has a slightly lower capacity, it will continue to discharge, and each time it is charged, it will experience a slight overvoltage. Over time, this will lead to a decrease in its capacity and service life. In a study by Sang-Sun Yun and Seok-Cheol Kee, 2022, [2], it was confirmed that the capacity deviation increased as the battery was used, resulting in an increase in the total amount of compensation current. The total value of the compensating current continues to increase until ignition occurs.

This phenomenon makes equalizing the charge of individual battery cells an indispensable procedure. The process of balancing voltages and SoCs between cells when they are connected and fully charged is called cell balancing.

Bortecene Yildirim et al. 2019 [3] investigated the following types of battery cell balancing:

a. Passive balancing.
b. Active balancing.
c. Runtime balancing.
d. Lossless balancing.

Passive Balancing This is a simple form of balancing by switching a resistor between cells. The energy loss to heat the balancing resistors (typically 30 to 40 Ω) allows overcharged cells to be discharged. This type is acceptable when balancing requirements are low. However, as cells age, the amount of balancing required to optimize energy increases. As a result, the amount of energy lost to heat increases and the charging time increases.

Active Balancing The idea here is to redistribute energy throughout the cells. Power from the cells with the highest SoC is transferred to the cells with the lowest SoC. This is the ideal approach to cell balancing. However, this means that the system must be able to move energy between cells in the battery, so many wires and switches are needed, which means more weight, complexity, and cost.

Runtime Balancing Each cell is connected to a separate low power direct current into direct current (DC-DC) converter, then each converter is connected in series. This then allows full control of the power supplied and received by each cell, depending on their capabilities. This system can provide a much higher level of reliability, but comes at a significant cost increase.

Lossless Balancing This approach turns cells on and off during charging. This means we have a lot of switches and these switches must be rated for full current.

Bortecene Yildirim et al. 2019 [3] showed that the main disadvantage of Active Balancing, by redistributing energy with the help of capacitances, is voltage balancing, which limits the speed and accuracy of balancing.

However, Active Balancing using capacitors can be improved to increase balancing accuracy and reduce time costs by using a pulse charging method.

This article is devoted to the development and research of a new device and method of charging with leveling the charge level of the cells in the battery at the second stage of charging (application for invention No. c20230044 dated 24.05.23, AGEPI R. Moldova) of a high-voltage lithium-ion automotive battery Porsche Taycan and the development of a test bench to investigate the effectiveness of this device.

In the process of research, methods of mathematical, structural and simulation modeling of instantaneous circuits of the charging device and leveling the level of battery charging were used. The calculations were performed using the Microsoft Office Excel 2007 program.

The main elements of the device are:

The list of designations of the main elements presented in figures 1, 2, 13:

$\boldsymbol{B_{11}, B_{12}, ..., B_1n ; B_{21}, B_{22}, ..., B_2n}$ – accumulators of the high-voltage battery;

C_1, C_2, ..., Cn - electrical energy storage devices, in particular capacitors;

R_1, R_2, ..., Rn – voltage divider resistors;

S_1, S_2 - electronic switches for switching on battery cells and energy storage devices;

BS_1, BS_2, ..., BSn - electronic switches for connecting batteries to drives;

RS_1, RS_2, ..., RSn - electronic switches for connecting voltage divider resistors to energy storage devices;

S – voltage sensor;

BSM - battery control unit;

DC-DC - power supply for charging batteries with direct current (DC);

GND - grounding of electrical circuits;

K - the point of connection of the power source to the device for charging and equalizing battery charges.

The main effective electrical quantities in the device are

$\boldsymbol{E_{B11}, E_{B12}, ..., E_{B1n}, E_{B21}, E_{B22}, ..., E_{B2n}}$ - Electromotive force (EMF) of high-voltage batteries;

$\boldsymbol{i_{Bch1}, i_{Bch2}}$ – battery charging current;

$\boldsymbol{i_{Bcv}}$ is the equalizing current of accumulator charging from storage devices;

$\boldsymbol{i_{Cch}}$ – storage current charging;

$\boldsymbol{i_{Scv}}$ - equalizing current of storages and voltage divider for equalization of voltage of storages;

$\boldsymbol{U_{CC}}$ is the voltage of the DC-DC power converter at the stage of charging batteries with constant current (CC);

$\boldsymbol{U_{CV}}$ is the voltage of the DC-DC power converter at the stage of charging batteries at a constant voltage (CV);

$\boldsymbol{U_{R1}, U_{R2}, ..., U_{Rn}}$ – voltage of voltage divider resistors;

$\boldsymbol{U_{C1}, U_{C2}, .., U_{Cn}}$ – energy storage voltage;

$\boldsymbol{E_{B1}, E_{B2}, .., E_{Bn}}$ – EMF of the batteries.

2. Battery leveling device

The proposed Device (1) for equalizing the level of charge of batteries (2) of rechargeable batteries (B_{11}, B_{12}, ..., B_1n; B_{21}, B_{22}, ..., B_2n) Management System (BMS) and consists of: n energy storage devices connected in series in a circuit, which can be capacitors (C_1, C_2, ..., Cn); electronic switches (S_1) and (S_2) for connecting to a direct current source (DC-

DC) circuits: n rechargeable batteries (B_1, B_2, ..., Bn) and n energy storage devices (C_1, C_2, ..., Cn), respectively; n-series connected via electronic switches (RS_1, RS_2, ..., RSn) into a chain of resistors (R_1, R_2, ..., Rn), one output of each of the resistors (R_1, R_2, ..., Rn) is connected by an electrical jumper to the corresponding output of the drive energy (C_1, C_2, ..., Cn), in turn, one output of each of the energy storage devices (C_1, C_2, ..., Cn) is connected by an electrical jumper through electronic switches (BS_1, BS_2, ..., BSn) with the corresponding output connected in series in rechargeable battery circuit (B_{11}, B_{12}, ..., B_1n; B_{21}, B_{22}, ..., B_2n); to the analog input of the control unit (BMS) through a voltage sensor (S) connect the input output of the drive C_{11} to control the voltage of the drives. The connection diagram of the device is shown in fig. 1 where n and i are positive integers, **n** is greater than 1 and $1 \leqslant i \leqslant n$.

3. Battery equalization method

Lithium-ion batteries are known to require 2 stages to properly charge: constant current charging (CC mode) followed by constant voltage charging (CV mode). At the first stage, the current value is 0.2-0.5 C (where C is the battery capacity). For an accelerated charge, it is allowed to increase the current up to 0.5-1.0 C [4]. The high-voltage lithium-ion battery system of the Porsche Taycan consists of 5000 mAh battery cells [5]. The rated charging current at the first stage (CC mode) is 1000 - 2500 mA, and with accelerated charging it can reach 2.5-5 A. In this mode, the battery is charged up to the level of SoC = 80 %. Next, a charge is made with a constant voltage (PV), at which the charging current gradually decreases. When the current drops to a minimum, charging is completed and the current is turned off. When using the proposed technical solution (Figure 1a), the first stage differs in that, together with the battery cells (under the control of the BMS program), up to the cell voltage level. At the second stage of charging the battery in the proposed technical solution, first, a chain of pre-charged capacitors (C_1, C_2, ..., Cn) is connected to the battery charging current source for a time equal to 3τ and charged to a voltage level corresponding to the voltage specified by the manufacturer for A battery is made up of a number of cells connected in series. Such a charging protocol can be referred to as a constant current-pulsed charging current at constant voltage (CC-PCCCV) protocol. Not to be confused with (CC-PCC) [6].

Due to the fact that capacitors manufactured by the industry have a wide range of parameters (up to 20%), the voltages of the capacitors (C_1, C_2, ..., Cn) are equalized using voltage divider resistors (R_1, R_2, ..., Rn).

To this end, at the end of the capacitor charging time for a time of 1τ, a chain of resistors is connected in parallel, each resistor to its own capacitor in the chain of capacitors (C_1, C_2, ..., Cn). Next, the capacitors (C_1, C_2, ..., Cn) are connected in parallel to the battery cells (B_{11}, B_{12}, ..., B_1n; B_{21}, B_{22}, ..., B_2n) and transfer energy to the latter. Resistors (R_1, R_2, ..., Rn) are selected with a parameter spread of no more than 1%. Thus, the cells (B_1, B_2, ..., Bn) are charged with current pulses, the voltage of which corresponds to the level set by the battery manufacturer. The process is repeated until the EMF of each battery is equal to the voltage of the charged storage (Fig. 2). A distinctive feature of the proposed technical solution is that. That the charging current in the second stage does not flow through the rechargeable battery cells (Fig. 2**).**

At the second stage of charging batteries (B_1, B_2, ..., Bn) from a power source (DC-DC) in the constant voltage mode ***Ucv***, in order to prevent the flow of charging current through the series circuit of batteries (B_1, B_2, ..., Bn), they are charged by multiple parallel connection to the appropriate energy storage devices (C_1, C_2, ..., Cn), which, before each connection, are charged to the voltage set by the battery manufacturer:

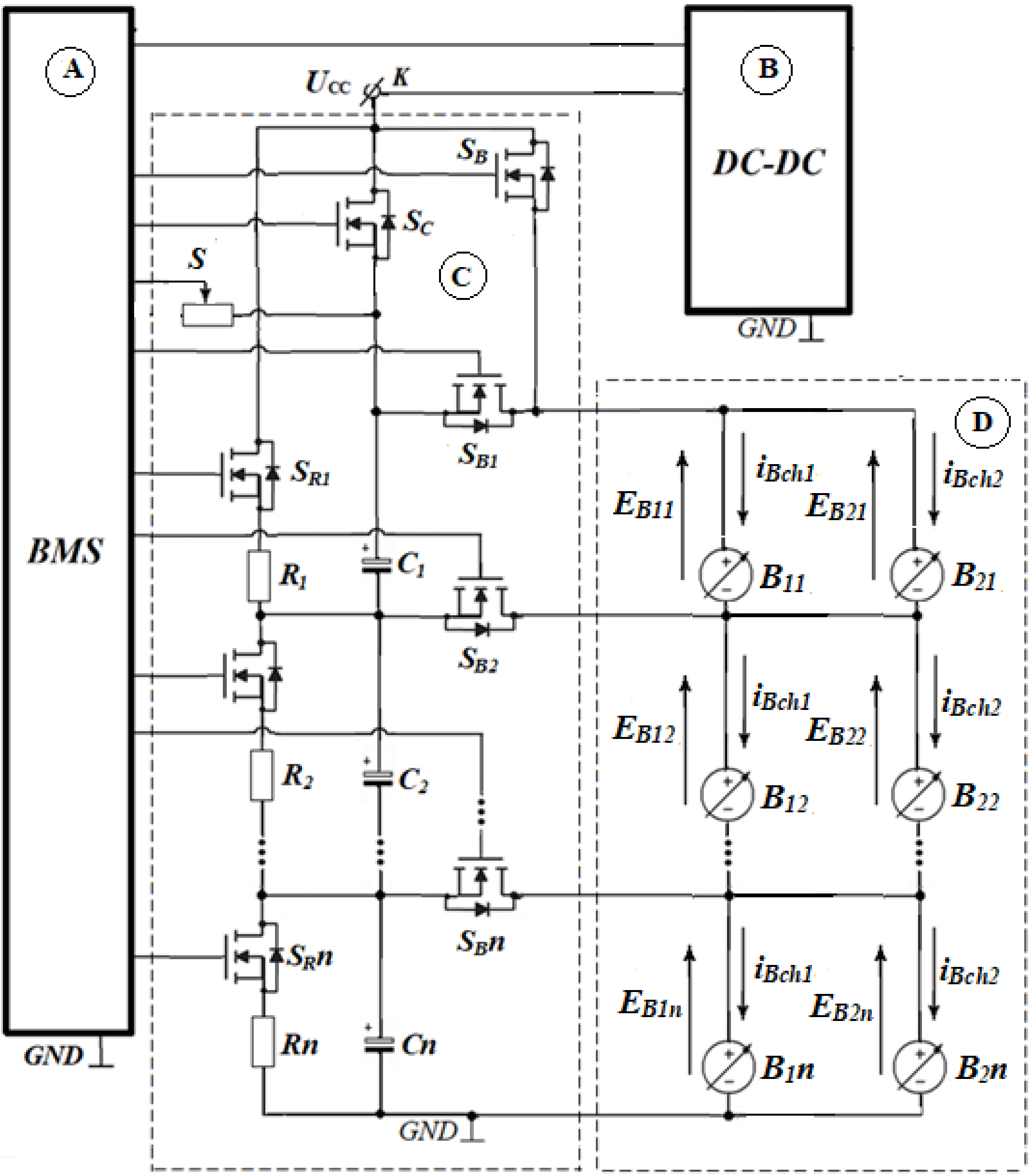

Figure 1. Schematic diagram of the steering device a of the charge level of Lithium-ion batteries at Porsche Taycan model:

A - Porsche Taycan battery management system (BSM);

B - Direct current converter (DC-DC);

C - Battery cell charger and equalizer;

D - Porsche Taycan lithium-ion battery system.

- phase 1.1 of the state of the circuit (see Figure 2 B) of the proposed device, is characterized by the fact that for 2τ (τ is the time constant of the accumulator), the voltage ***Ucv*** is applied to the chain of energy accumulators (C_1, C_2, ..., Cn) for additional charging drive (C_1, C_2, ..., Cn) up to SoC = 99% of drives;

- phase 1.2 of the state of the device circuit (see Fig. 2 C) is characterized by the fact that for a time of 1τ a resistor (R_1, R_2, ..., Cn) is connected in parallel to each storage device (C_1, C_2, ..., Rn) and cause the flow of an equalizing current i_{Scv} to equalize the voltage (U_{C1}, U_{C2}, .., ***Ucn***) on each drive to the voltage specified by the manufacturer, since a chain of series-connected resistors of the same resistance (R_1, R_2, ..., Rn) divides the source voltage (DC-DC) for voltages specified by the battery manufacturer (B_1, B_2, ..., Bn);

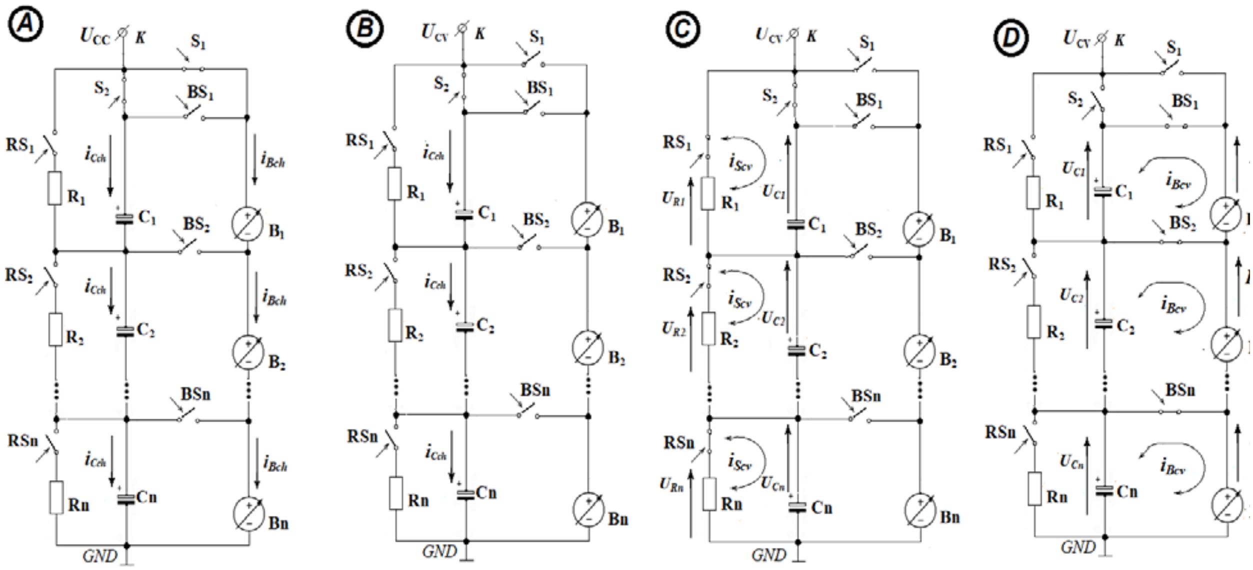

Figure 2. Electrical circuits for switching on the device for charging and equalizing the charge of battery cells for modes:

A - charging of battery cells to the level of SoC = 80% and capacitors to the level of SoC = 91.67% at a constant current value CC;

B - charging capacitors to the level of SoC=99.5%;

C - voltage equalization of capacitors by a voltage divider;

D - transfer of capacitors energy by pulses to battery cells.

- phase 1.3 of the state of the circuit of the proposed device, is designed to measure the total voltage ($\boldsymbol{U_{C1}, U_{C2}, .., U_{Cn}}$) of drives ($C_1$, C_2, ..., Cn), which is read from the sensor **S** and entered into the memory of the BMS device;

- phase 1.4 of the state of the circuit (see Fig. 2 D) of the proposed device, serves to charge batteries (B_1, B_2, ..., Bn) with an equalizing current $\boldsymbol{i_{Bcv}}$, which flows when the storage devices (C_1, C_2, ..., Cn) and batteries are connected in parallel (B_1, B_2, ..., Bn). The peculiarity of this charging method is that when the EMF EB of the batteries (B_1, B_2, ..., Bn) is equal to the voltage UC of the storage devices (C_1, C_2, ..., Cn), the equalizing current $\boldsymbol{i_{Bcv}}$ between these pairs will not flow, and for those batteries , for which the EMF $\boldsymbol{E_B}$ has not reached the voltage level determined by the manufacturer, the equalizing current $\boldsymbol{i_{Bcv}}$ from the storage devices will flow and their voltage will decrease, therefore the total voltage ($\boldsymbol{U_{C1}, U_{C2}, .., U_{Cn}}$) of the storage devices (C_1, C_2, ..., Cn) is also at the end charging will go down;

- phase 1.5 of the state of the circuit of the proposed device, is designed to measure the residual voltage UCV' of storage devices (C_1, C_2, ..., C_1n) which is read from the sensor S and entered into the memory of the BMS device;

- phase 1.6 of the circuit state is designed to compare the residual voltage $\boldsymbol{U_{CV}'}$ with the value stored in the memory of the BMS device. If the voltage values $\boldsymbol{U_{CV}' = U_{CV}}$ are equal, the second stage of charging the batteries (B_1, B_2, ..., Bn) is stopped, and if the residual voltage $\boldsymbol{U_{CV}}'$ is less, that is, part of the storage energy is spent on charging the batteries, then go to phase 1.1 and repeat the charging process.

Thus, the charging of each battery separately will be performed by current pulses of the corresponding storage device until the battery EMF is equal to the storage voltage.

The operation algorithm of the device (1) for metered charging of the battery cells by parallel connection of energy storage devices to them in order to equalize the charges, preventing the flow of current through the charged cells, is shown in Figure 3.

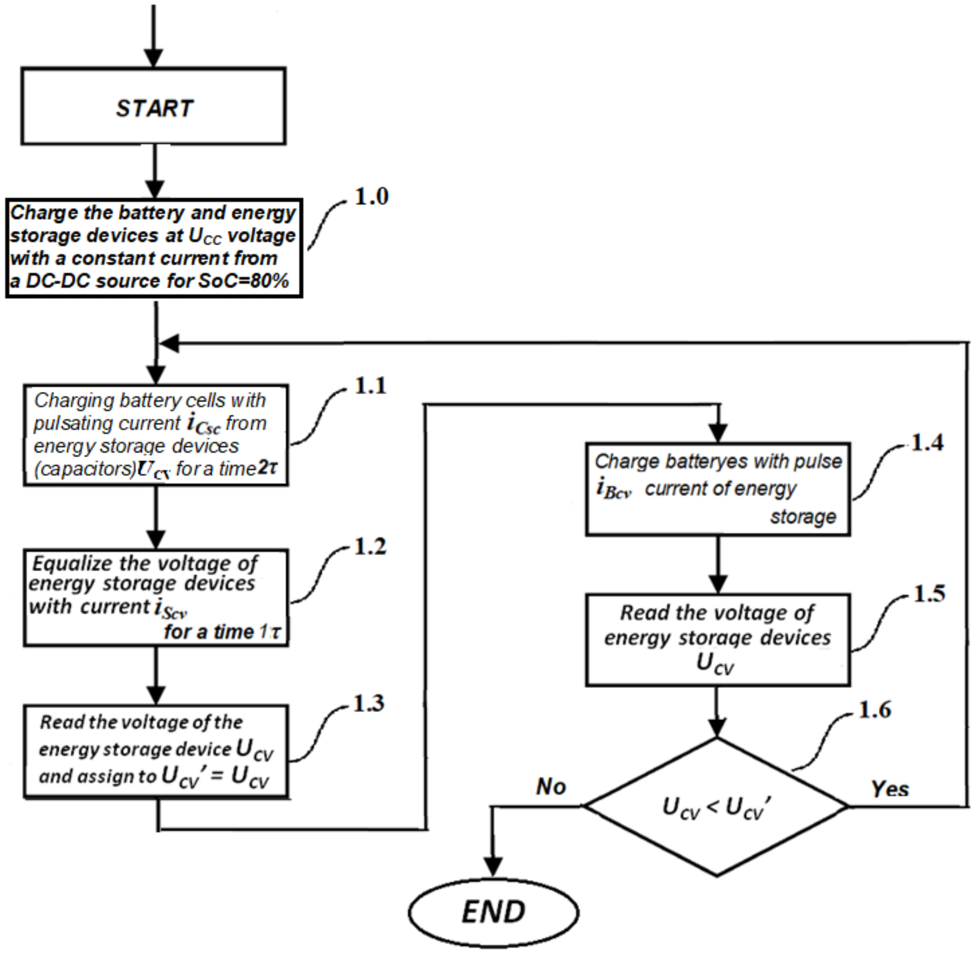

Figure 3. Battery charging algorithm with charge equalization.

3. Porsche Taycan Car Battery Charger Workflow Parameters

To analyze the effectiveness of the proposed device and confirm the possibility of implementing the invention, we will carry out an approximate calculation of the elements of the device and the parameters of the Porsche Taycan battery charging process [5].

Table 2

Parameters High-voltage lithium-ion car battery Porsche Taycan

Specification	Parameter
Nominal voltage	800V
Number of battery cells with nominal voltage	396 cells with U_{BA} = 3.7V
Cell modules	33 modules
Number of elements (in series)	n_A = 198 cells in battery
Battery cell capacity	5.0 Ah = 5000 mA/h
Usable capacity	E_{AB} = 93.4 kWh (336.2 · 10^6 J)
Rated capacity of one cell in a battery	E_A = 18 · 10^3 J
The internal resistance of a cell in a battery	Ra = 20 mΩ

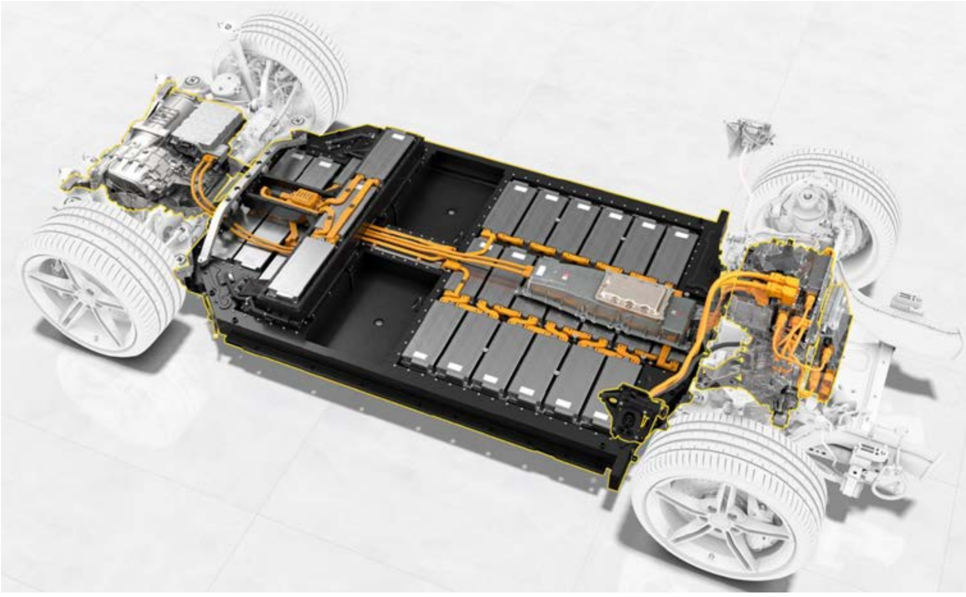

Figure 4. Porsche Taycan high-voltage battery and location of its modules [5].

The Taycan is the first mass-produced vehicle to offer 800 volts instead of the usual 400 volts for electric vehicles. This ensures consistent high performance, reduces charging times and reduces weight and cable management space [5].

The Performance Plus bi-level battery used in the Taycan Turbo S and Taycan Turbo contains 33 cell modules with 12 individual cells each (396 in total). The total power is 93.4 kWh. Each module has an internal control unit for voltage and temperature control and is connected to each other by bus bars [5].

Battery modules consist of battery cells and are connected in series. In each module, two cells are connected in parallel, and then these pairs are connected in series. This solution helps equalize the voltage of two battery cells connected in parallel and reduces the influence of low capacity cells on the resulting battery voltage but does not eliminate the problem of different cell aging rates.

In our case, we will take an electrolytic capacitor manufactured by Jb Capacitors Company (Table 3) with an internal resistance ***Rc*** = 9 mΩ [7]. However, commercially available capacitors have a wide range of parameters: the capacitance of two identical capacitors can differ by +/- 20%.

Table 3

Parameters of electrolytic capacitors

Specification	Parameter
Capacitor type	Aluminum electrolytic JNK
Capacity	*Cc* = 56 000 uF ± 20%
Working voltage	10 B DC (for 4.2 Reserved 135%)
Working temperature	-40°C ~ +105°C
Resistance Type ESR 20°C, 120Hz	*Rc* = 9 mΩ = 0.009 Ω

Therefore, in charging mode 1.1 (see Figure 3), the constant voltage from the DC-DC source will be distributed unevenly across the capacitor circuit. To eliminate this disadvantage of capacitors, in the proposed technical solution, after charging the capacitors, they are briefly connected to the voltage divider of the DC-DC source and the voltages are equalized, since the divider is created from the same resistors (RS_1, RS_2, ..., RSn), the deviation of the electrical resistance of which is not more than +/-1%. For example, for the High-voltage lithium-ion battery Porsche Taycan, a metal film resistor with a resistance of ***Rr*** = 1 Ω was chosen with a manufacturing accuracy of +/-1% (Table 4).

Table 4

Parameters of voltage divider Metal Film Resistor [8]

Specification	Parameter
Tip:	Wire Wound Resistor
Manufacturer	ABECO ELECTRONIC CO., LTD
Model:	CSR NEW MELF
Putere nominală	5 W
Resistance, Rsh:	1 Ω
High Precision:	0.1%

For electronic switch S_1, S_2, BS_1, BS_2, ... , BSn; RS_1, RS_2, ... , RSn accept NPN Silicon Epitaxial Transistor Bipolar (see Table 5).

Table 5

Parameters of electronic switch [9]

Specification	Parameter
Marking	FGA25N120
Collector−Emitter Voltage	VCC = 1200 Vdc
Collector Current	IC = 25 A
Maximum power dissipation	125 W

On Fig. 5 shows the degree of completion of the process (as a percentage) of the time of the process (charge or discharge) (see Figure 6) [10]. The first stage of charging ends when the battery charge reaches SoC=80%. At the first stage of charging the battery (2), its batteries (B_1, B_2, ..., Bn), for example, lithium-cobalt oxide batteries ($LiCoO_2$) and storage devices connected to them in parallel, in this case electrolytic capacitors (C_1, C_2, ..., Cn) will be charged to a voltage of U_C = 3.9 V. DoD (Depth of Discharge) is a numerical compliment at DoD =20%, the value of SoC= 80% (see Figure 5) [10].

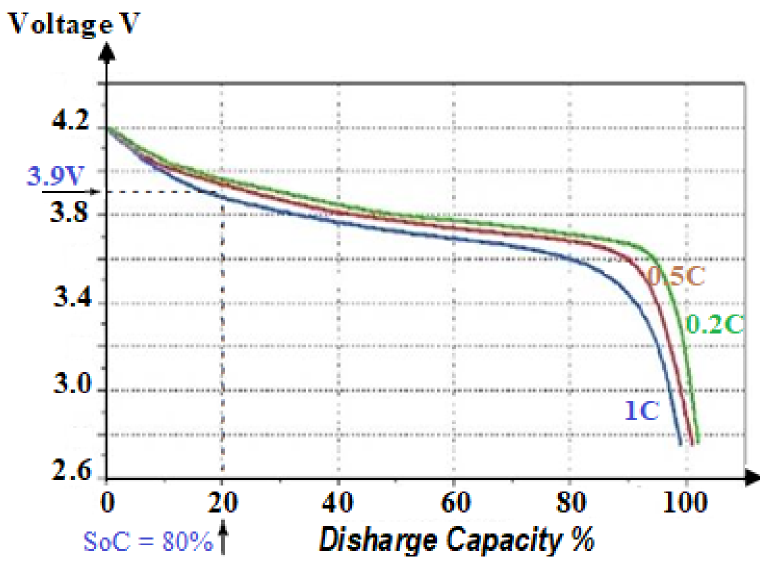

Figure 5. Lithium ion battery voltage and remaining energy [10].

If there is an imbalance of +/-10% battery charge, the individual batteries of the battery will be charged to a voltage of U_C = 3.85 V (Figure 6).

At the second stage of charging, the proposed technical solution is used as follows: in charging mode ***1.1***, turn off the electronic switches (BS_1, BS_2, ..., BSn; RS_1, RS_2, ..., RSn) and to power the capacitor bank (C_1, C_2, ..., Cn) turns on the electronic switch S_2 and supplies a constant voltage U_{CV} from a DC-DC source to a chain of n_C = 99 capacitors.

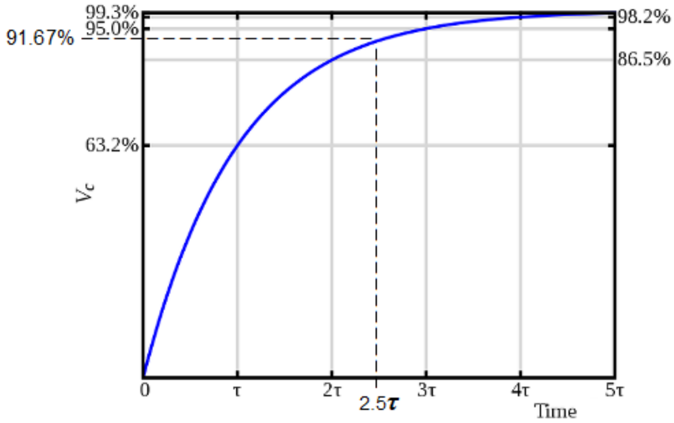

Figure 6. Capacitor charge and discharge [11].

Each capacitor must receive a voltage ***Uash (i)*** = 4.20 V. To charge a chain of n_A = 198 by two parallel-connected cells of the High-voltage lithium-ion battery Porsche Taycan [5], the voltage U_{CV} of the DC-DC source, for charging at a constant voltage, must be equal to:

$$U_{CV} = Uash\,(i) \cdot n_A \quad (1)$$
$$U_{CV} = 4.20 \cdot 198 = 832\ \text{B}$$

The total resistance of internal resistances Rc of series-connected capacitors (C_1, C_2, ..., Cn) with a number n_C, equal to the number of batteries n_A and will be:

$$R_{CS} = Rc \cdot n_C / 2 \quad (2)$$
$$R_{CS} = 0.009 \cdot 198 / 2 = 0.891\ \Omega$$

Therefore, when connected to the U_{CV} voltage, the initial charging current of the capacitors can be:

$$i_{Sch} = U_{CV} / R_{CS} \quad (3)$$
$$i_{Sch} = 832 / 0.891 = 933.8\ \text{A}$$

In order to prevent the capacitors from burning out from such a current, in the proposed technical solution, the capacitor banks are charged together with the batteries at the first stage of charging at a constant current value, therefore, at the end of the first stage, the capacitors will also be charged to a voltage of ***U'a(i)*** = 3.9 V , and some, due to imbalance, will be charged up to U_{DC} = 3.85 V. For capacitors, this voltage value is 91.67% (of 4.2V), which for capacitors is equivalent to a charge time of 2.5τ (see Figure 6) [11].

Therefore, at the second stage of charging the batteries, to charge the energy storage (capacitors), there will be enough time 3τ for the capacitor voltage to be slightly more than 4.18 V (99.5% of 4.2 V) (see Figure 6) [11]. The total charge of the capacitor C(i) is calculated by the formula:

$$E = U^2 \cdot C / 2 \quad (4)$$

Let's take the EMF level at the beginning of the second stage of battery charging ***Ea'*** and at the end of ***Ea''*** based on the materials of Isabelle Sourmey 2022 [4]. In this case, one storage capacitor C(i) can transfer energy to the accumulator B(i) at the beginning of the second stage with ***Uash (i)*** and:

$$\Delta Ecstart = (Uash\ (i))^2 - E_1a^2) \cdot C/2 \quad (5)$$
$$\Delta Ecstart = (4.2^2 \cdot 3.85^2) \cdot 0.056 / 2 = 0.079\ J$$

Figure 7 gives reason to take E_2a = 4.1 V. Therefore, at the end of the second stage, this capacitor can transfer energy to the battery cell:

$$\Delta Ecend = (Uash\ (i)\ ^2 - E_2a^2) \cdot C/2 \quad (6)$$
$$\Delta Ecend = (4.2^2 - 4.1\ ^2) \cdot 0.056 / 2 = 0.0232\ J$$

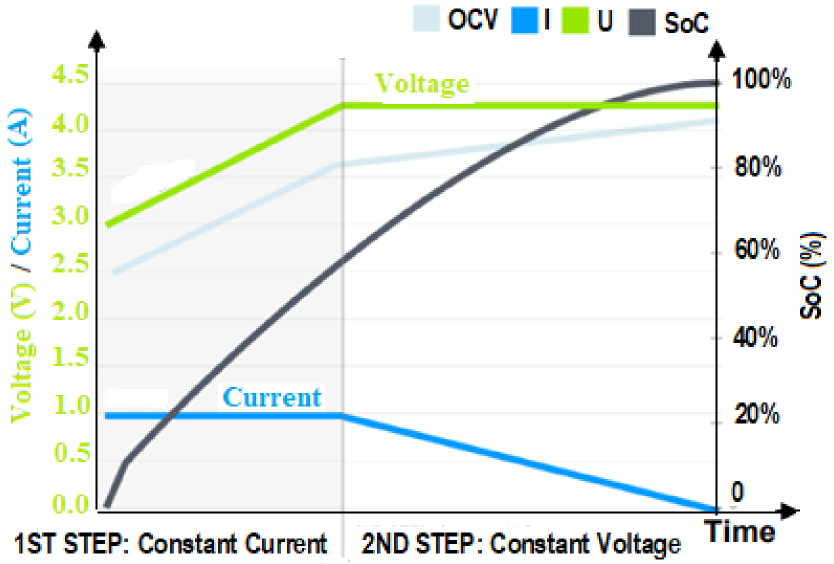

Figure 7. Li-Ion charging progress CC/CV [4].

For one cycle of connecting the capacitor to the battery cell during the second stage, on average, you can transfer:

$$\Delta Ec = (\Delta Ecstart + \Delta Ecend) / 2 \quad (7)$$
$$\Delta Ec = (0.079 + 0.0232) / 2 = 0.0511\ J$$

Charging batteries at the second stage using the proposed technical solution with an imbalance in the charge level of +/-10% means that if the battery cells after the first stage can have a charge of about 80% [4], then individual cells can have 70% or 90%. The calculation of the energy required for charging and equalization, which the capacitor must transfer, is carried out for the case of an incomplete charge of 70%. In this case, it must be taken into account that these cells can be paired. Therefore, the missing energy that must be added with the help of a capacitor at the second stage of charging will be about ***ΔEp***=60% of the total energy reserve of one cell E_A:

$$E_A''\ (i) = E_A\ (i) \cdot \Delta Ep / 100 \quad (8)$$
$$E_A''\ (i) = 18 \cdot 10^3 \cdot 60 / 100 = 10.8 \cdot 10^3\ J$$

The number of cycles to transfer energy using capacitors to cover the imbalance of a pair of cells in the module ***ΔEp*** = 60% of the energy of one cell to charge to $E_A''(i)$:

$$E_A''\ (i) = E_A\ (i) \cdot \Delta Ep / 100 \quad (8)$$
$$E_A''\ (i) = 18 \cdot 10^3 \cdot 60 / 100 = 10.8 \cdot 10^3\ J$$

The maximum number of cycles to transfer with the help of capacitors is still ΔEp = 60% of the energy to charge up to $E_A''(i)$:

$$N\,cycle = E_A''(i) / \Delta Ec \tag{9}$$

$$N\,cycle = 10.8 \cdot 10^3 / 0.0511 = 551.9 \cdot 10^3$$

Let us determine the charging time of the capacitors (C_1, C_2, ..., Cn) at the second stage. The duration of the process of charging the capacitor depends on two values: on the electromotive force of the source - U_{CV} and on the time constant - τ.

The time constant of charging / discharging the capacitor τ is determined by the product of the resistance and the capacitance of the capacitor [12], therefore,

$$\tau_C = R_C \cdot C_C\,, \tag{11}$$

where:

τ_C - time constant, s;

R_C - resistance, Ω;

C_C - capacitance, F.

$\tau_C = 0.009 \cdot 0.056 = 0.504 \cdot 10^{-3}$ s

Charging capacitors (C_1, C_2, ..., Cn) to a value of 99.3% capacity, that is, up to a voltage of 4.2 V, to transfer this charge to the batteries, with an average capacitor voltage of U_C = 3.93 V, will require at least 3τ of time. It will take time to charge the capacitor t_C:

$$t_C = -\ln(1 - UD_C / Uash\,(i)) \cdot 3\tau'_C \tag{12}$$

$$t_C = -\ln(1 - 3.85 / 4.20) \cdot 3 \cdot 0.513 \cdot 10^{-3} = 3.75 \cdot 10^{-3}\ \text{s}$$

The total time spent on multiple refueling of the energy storage (capacitor) before transferring energy to the batteries will be:

$$\sum t'_C = t_C \cdot N\,cycle \tag{13}$$

$$\sum t'_C = 3.75 \cdot 10^{-3} \cdot 551.9 \cdot 10^3 = 2069.6\ \text{s} = 34.5\ \text{min} = 0.57\ \text{hour}$$

In the process of charging the capacitors, in state phase 1.1, the circuits of the device (1) after 2τ pass into the state phase ***1.2*** (capacitor charging with voltage equalization). This phase lasts for another 1τ, that is, one third of t'_C, which is:

$$t'd = 3.75 \cdot 10^{-3} / 2 = 1.875 \cdot 10^{-3}\ \text{s} \tag{14}$$

The charging time of the capacitors for power transfer in the second stage is much less than the time required to charge the lithium-ion battery. To charge a lithium-ion battery to a level of 99%, on average, it will take t_{2A} = 100 minutes (6000 s). These data are accepted from Rahul Bollini 2022 [13], and from Battery University BU-409 [14].

Therefore, if we neglect the time spent on switch switching, then the total time spent by the device on charging the Porsche Taycan High-voltage lithium-ion battery is from 80% to 99%, with a battery charge imbalance of 20% (see Table 2) will be:

$$\sum t_{CA} = t_C' + t_{2A} \tag{16}$$

$$\sum t_{CA} = 34.5 + 100 = 134.5\ \text{min} = 2.24\ \text{hour}$$

Let's calculate the frequency of the battery charging current pulses. Assuming that the charge time at the second stage of the battery charge is equal to the sum of the time of all pulses, we determine the duration of one charge pulse - t_p:

$$t_p = t_{2A} / N\ cycle \tag{17}$$

$$t_p = 6000 / 551.9 \cdot 10^3 = 0.0109\ s$$

If we neglect the time spent on switching switches, then the total time of one cycle ***T***, that is, the period will be equal to (Figure 7):

$$T = t_p + t_C$$

$$T = 0{,}0109 + 3.75 \cdot 10^{-3} = 0{,}01465\ s \tag{18}$$

Therefore, the pulse frequency will be:

$$f = 1 / T \tag{19}$$

$$f = 1 / 0.01465 = 68\ Hz$$

Fig. 8 and 9. Schematic representation of a current pulse profile and definition of related parameters. The continuous line represents the current pulse profile and the dotted line represents the associated reference current profile.

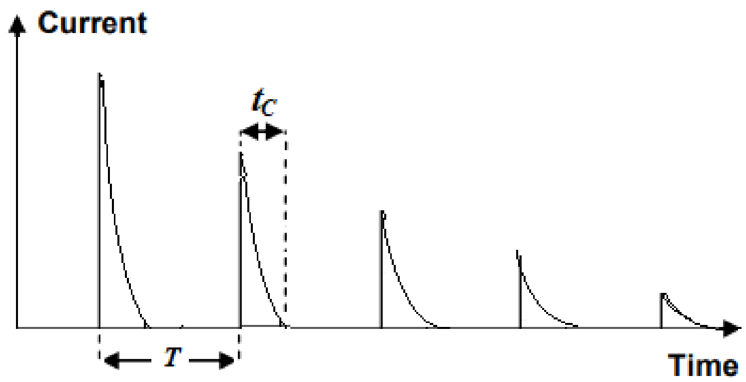

Figure 8. Capacitor current at constant voltage of the voltage divider:
T- Time of one cycle; t_C - the duration of charge of capacitors.

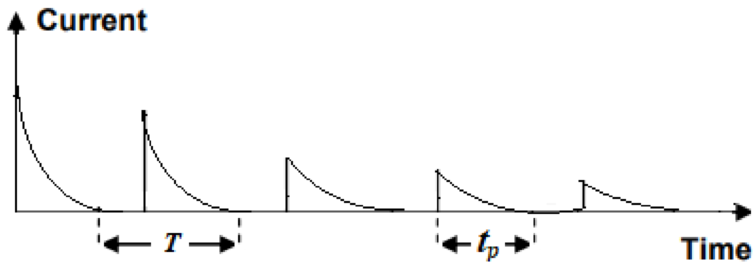

Figure 9. Charging current pulses of battery cells from a capacitor:
T- Time of one cycle t_p - the duration of one pulse.

Makeen P. et al., 2022 [6] concluded that the charging current frequency of less than 6 kHz and more than 50 kHz increases the charging time, and energy losses are minimized. In the considered application of the proposed device, the calculated pulse frequency f = 68 Hz, i.e. less than 6 kHz, therefore, the current pulses generated by the proposed device for charging the Porsche Taycan electric vehicle battery should minimize energy losses in the battery.

Additional time costs will be $\sum t'_C$ = 34.5 (min) = 0.57 (hour). However, relative to the total charging time of lithium-ion batteries, which is 180 minutes [14], the additional time for charging using the proposed method will increase by no more than 20%.

5. Calculation of the efficiency of the proposed equalization charger

It is of practical interest to determine the resistance value of the voltage divider resistors, the energy loss dissipated by the resistors, the voltage deviation of charged storage devices and the time spent on charging at the second stage with the battery voltage equalization.

Using a voltage divider across resistors to equalize the voltage of the capacitors before charging the batteries will cause energy wastage. To calculate the losses, the operation of the proposed device was simulated in relation to the High-voltage lithium-ion battery of Porsche Taycan (Table 2). The calculation of the instantaneous capacitor charging circuit at the moment of time corresponding to the charge time of the time constant **4τ** at the moment the voltage divider is turned on to equalize the voltages of the storage capacitors is performed. The charge time corresponding to the time constant **4τ** was chosen because the capacitors have already passed the time **2τ** when charging together with the batteries. This circuit will make it possible to select the value of the resistances of the resistors to equalize the voltages of the capacitors.

For a more compact representation of the calculated data, 198 pairs of parallel-connected cells that are connected in series into a battery, for the convenience of calculation and presentation of results, we will divide into groups into groups: ***nga*** = 11 groups, ***nag*** = 18 pairs of cells in each group and, accordingly: ***ngc*** = 11 groups of capacitors from Cg1 to Cg11 and ***ncg*** = 9 capacitors per group. The calculation scheme is shown in figure 12. The rated voltage ***Ua*** = 4.2 V is taken in accordance with the battery charging voltage of the battery Porsche Taycan (Table 2).

The disbalance of storage capacitors capacitances is set by the coefficient of difference between the internal resistances of the group capacitors: ***Disb of Resrg(i).***

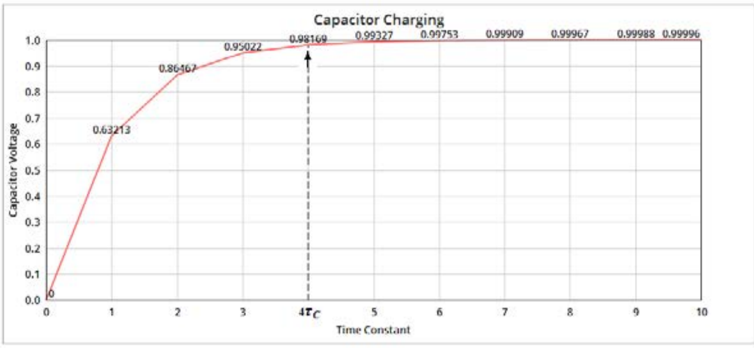

Figure 10. Capacitor charging voltage slope [12].

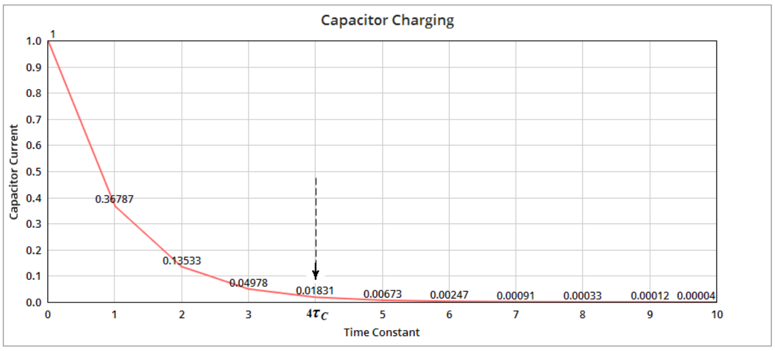

Figure 11. Capacitor charging current slope [12].

To simplify the calculation of the internal resistance of capacitors (energy storage) ***Resr'(i),*** we express in terms of data on the values (expressed as a percentage) of voltage (Voltage) and current (Current), depending on the charge of the capacitor [12]:

$$Resr'(i) = Resr(i) \cdot Voltage/Current \quad (20)$$

The equivalent resistance of the shunt resistor of the voltage divider and the internal resistance of the storage capacitor is determined by the formula:

$$Requiv'(i) = Resr'(i) \cdot Rsh/(Resr'(i)+Rsh) \quad (21)$$

The equivalent resistances of each group of series-connected resistors and capacitors are determined by the formula:

$$Rgequiv'(i)= Re'(i) \cdot nag \quad (22)$$

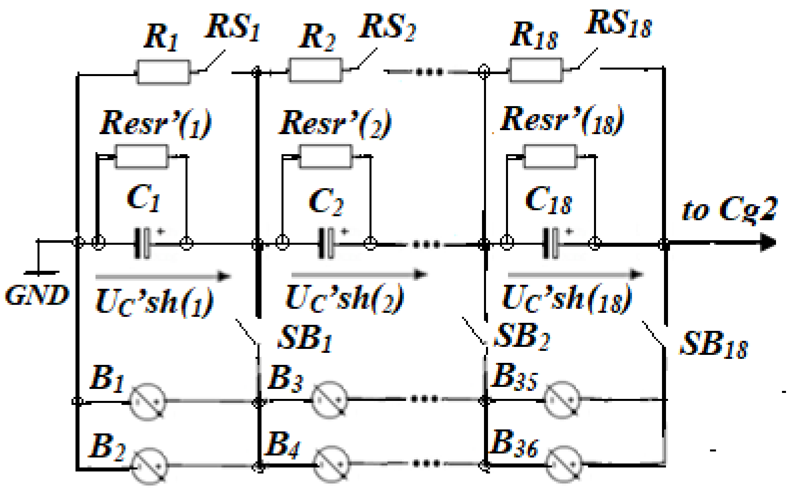

Figure 12. Connection diagram of capacitors and a voltage divider of a group of batteries of the Sg1 battery for calculating the voltage equalization on the capacitors before connecting to the batteries of the group.

The value of the nominal EMF of the capacitor as the product of the battery charging voltage determined by the manufacturer and the correction factor [12] is determined by the formula:

$$EMFc' = Uc \cdot Voltage/100 \quad (23)$$

The value of the rated charging current of the capacitor as the product of the charging current at the battery charging voltage determined by the manufacturer and the correction factor [12] is determined by the formula:

$$Ic' = Idc\text{-}dc \cdot Current/100 \quad (24)$$

The value of the charging current of capacitors with voltage equalization from a DC-DC source is determined by the formula:

$$I_{dc\text{-}dc}' = U_{dc\text{-}dc} / \sum_{i=1}^{i=ngc} Rgequiv'(i) \quad (25)$$

Electromotive force of a group of capacitors:

$$EMFcg' = Ecg \cdot Voltage/100 \quad (26)$$

Power loss to shunt resistors:

$$\Sigma Ploss\ instant' = \sum_{i=1}^{i=ngc} (Ucg'(i) \cdot Ishg'(i)) \tag{27}$$

Energy loss for shunt resistors:

$$\Sigma Eloss\ instant' = \sum Ploss\ instant' \cdot Ncycle \cdot td' / 3600 \tag{28}$$

Equivalent resistance of a group of shunted capacitors:

$$Resrg'(i) = \Sigma Rcesrg \cdot (Voltage / Current) \cdot Disb\ of\ Resrg(i) \tag{29}$$

Equivalent resistance of a group of shunted capacitors:

$$Rgequiv'(i) = Rshg \cdot ncg \cdot R'esrg(i) / (Rshg \cdot ncg + Resrg'(i)) \tag{30}$$

Capacitor group voltage:

$$Ucg'(i) = Rgequiv'(i) \cdot Idc\text{-}dc' \tag{31}$$

Capacitor group charging current:

$$Icg'(i) = Ucg'(i) / Resrg'(i) \tag{32}$$

The current of a group of resistors shunting capacitors:

$$Ishg'(i) = Ucg'(i) / (Rshg \cdot ncg) \tag{33}$$

Power loss on groups of shunt resistors:

$$Pc(i) = Ucg'(i) \cdot Icg'(i) \tag{34}$$

Energy loss on groups of shunt resistors:

$$Plossg'(i) = Ucg'(i) \cdot Ishg'(i) \tag{35}$$

Voltage applied to shunted capacitor:

$$Uc'sh(i) = Ucg'(i) / ncg \tag{36}$$

Voltage applied to capacitors:

$$Uc'sh\ less\ (i) = Udc\text{-}dc / \sum_{k=1}^{k=ngc} Resrg'(k) \cdot Resrg'(i) / ncg \tag{37}$$

The calculation was made for the case of using capacitors with a typical capacitance deviation of +/- 20% (parameters in Table 3), used as energy storage devices for pulsed energy transfer to batteries and divider resistors (parameters in Table 4).

The resistors of the charging voltage divider U_{CV} used to equalize the voltage of the capacitors made it possible to equalize the voltage to the limits that allow charging the batteries at the second stage of charging without exceeding the allowable limit of 4.25 V (see Figure 5 and Table 7).

Table 6

Initial parameters of the energy storage voltage equalization mode

Initial data		Data adapted to Time Constant τ=4	
Uc = Ua charging, V	4.2	t'd (c) equalizat. time	0.001875
ncg	18	N cycle	551900
ngc	11	Voltage, %	98.16
Resr nom, Ω	0.009	Current, %	0.02

Continuation Table 6

Σrcesrg, Ω	0.16	EMF' c, V	4.12
Rsh nom, Ω	1.00	I'c, A	0.09
Rshg, Ω	54.00	I'dc-dc, A	4.29
EMFcg, V	75.60	EMF'cg, V	74.21
U dc-dc nom, V,	831.60	ΣP'loss instant, Wt	3492.75
I dc-dc by τ=0, A	466.67	ΣE'loss instant,Wth	1003.99
Usable capacity, kWh	93.4	ΣE'loss in % of usable capacity	1.2%

Table 7

Expected parameters of the energy storage voltage equalization mode

	Cg1	Cg2	Cg3	Cg4	Cg5	Cg6	Cg7	Cg8	Cg9	Cg10	Cg11
Disb of Resrg(i)	1	1.2	1	0.8	1	0.8	1	1.2	1	0.8	1.2
R'esrg(i) (Ω)	868.5	1042.2	868.5	694.8	868.5	694.8	868.5	1042.2	868.5	694.8	1042.2
R'gequiv(i)(Ω)	17.63	17.69	17.63	17.55	17.63	17.55	17.63	17.69	17.63	17.55	17.69
U'cg(i) (V)	75.63	75.89	75.63	75.25	75.63	75.25	75.63	75.89	75.63	75.25	75.89
I'cg (i) (A)	0.09	0.07	0.09	0.11	0.09	0.11	0.09	0.07	0.09	0.11	0.07
I'shg (i) (A)	4.20	4.22	4.20	4.18	4.20	4.18	4.20	4.22	4.20	4.18	4.22
Pc (i) (Wt)	6.59	5.53	6.59	8.15	6.59	8.15	6.59	5.53	6.59	8.15	5.53
P'lossg(i) (Wt)	317.81	319.97	317.81	314.60	317.81	314.60	317.81	319.97	317.81	314.60	319.97
Uc'(i) shunt (V)	4.20	4.22	4.20	4.18	4.20	4.18	4.20	4.22	4.20	4.18	4.22
Uc'(i)without(V)	4.20	5.04	4.20	3.36	4.20	3.36	4.20	5.04	4.20	3.36	5.04

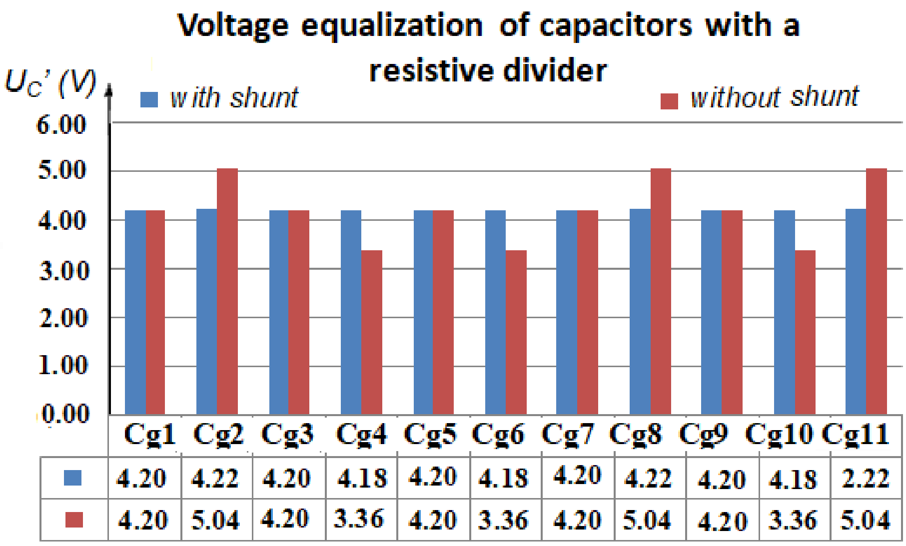

Figure13. Capacitor voltage in storage groups equalized by a resistive divider.

The voltage of capacitors in battery groups (Cg1, ..., Cg11), balanced by a resistive divider, does not exceed the allowable limits for charging cells equal to 4.25 V. At the same time, the diagram in Figure 13 shows how large the voltage spread is when the internal resistances of the capacitors deviate. A similar deviation can also occur in battery cells with a spread in the parameters of the cells, similar to the spread in the parameters of a capacitor.

6. Stand for research and modes of operation of lithium-ion battery cells

Any technical solution must be preliminarily calculated, designed and created in the form of a sample. Before being handed over to the user for use, the sample must be tested and carefully examined.

As for the proposed device (application for invention No. c20230044 dated May 24, 23, AGEPI R. Moldova), calculations were made and the elements of the device for equalizing the charge of the battery cells were selected: for the Audi Q5 hybrid Quattro hybrid car (the report was sent to the ESFA 2023 congress committee); for the e-GOLF electric car (report sent to the IMANEE 2023 international conference committee). Discussions with experts will help improve the proposed technical solution. The next step is to create and test a sample. Due to the technical features of the proposed solution, which consists in the ability to change the battery charging modes, the proposed device can be used to study battery charging modes; it can become the basis of the stand. To do this, a device for charging and equalizing the voltage of lithium-ion batteries must be equipped with measuring instruments: to control the temperature of the battery cells; to measure the internal resistance of battery cells; for measuring voltage, charging current, power consumption and charge time of lithium-ion battery cells.

To control the operation of the stand, a control processor device is required, which will perform the functions of the BMS battery charging management system and collect information about the progress of the charging process. The control device must be programmable for research and laboratory applications.

For this purpose, the Arduino Uno R3 controller is suitable (Fig. 14 (I)) [15,16], which can be used as a control device to control the operating modes of the charger, perform BMS functions, and collect information about the stand. operating modes. The Arduino Uno R3 controller has 14 digital inputs/outputs, 6 of which can be used as PWM outputs (PWM), 6 analog inputs (ADC), a 16 MHz crystal, a USB connector, a power connector, an in-circuit programming connector (ICSP) and a reset button. The Arduino Uno is programmed using the free Arduino software. The ATmega328 microcontroller in the Arduino Uno comes with a firmware uploader that allows you to upload new programs to the microcontroller without the need for an external programmer. In addition, a personal computer can be connected to the USB port (Fig. 14(A)) and perform both experiment management tasks and preparation of programs for testing various battery charging methods.

On fig. 14(B) is a circuit diagram of a battery cell equalization charger (FIG. 14(B)). The charger circuit pins are labeled according to the Arduino Uno R3 PWM outputs (Figure 14(I)): ~3, ~5, ~6, ~9, as well as analog inputs: A1 and A3. Up to 14 pcs. 18650 type batteries (Fig. 14(C)) are connected to the charger to charge and equalize the battery cells based on the proposed technical solution (Fig. 14(B)).

For testing and preparation of batteries, it is advisable to equip the stand with a lithium battery capacity tester 18650, (for four batteries) and a battery charge detector 18650, type C (Fig. 14(D)) [17]. The tester has an operating voltage of 5V DC and is suitable for all batteries that meet the requirements for stopping the discharge at a voltage of 2.5~3.5V and an initial voltage of 2.8V to 4.2V. The tester has the following options:

- Power interface: Two Type-C power interfaces.
- System language: English.
- Number of tests: 4-way measurement of charging and discharging.

• Internal resistance measurement: The two-wire DC method is used to measure internal resistance.

• Charging function: automatic charging shutdown when fully charged.

• Discharging function: automatic stop when conditions are met, discharging current is not adjustable.

• Automatic charging and discharging: supported. The battery is fully charged at the end of automatic mode.

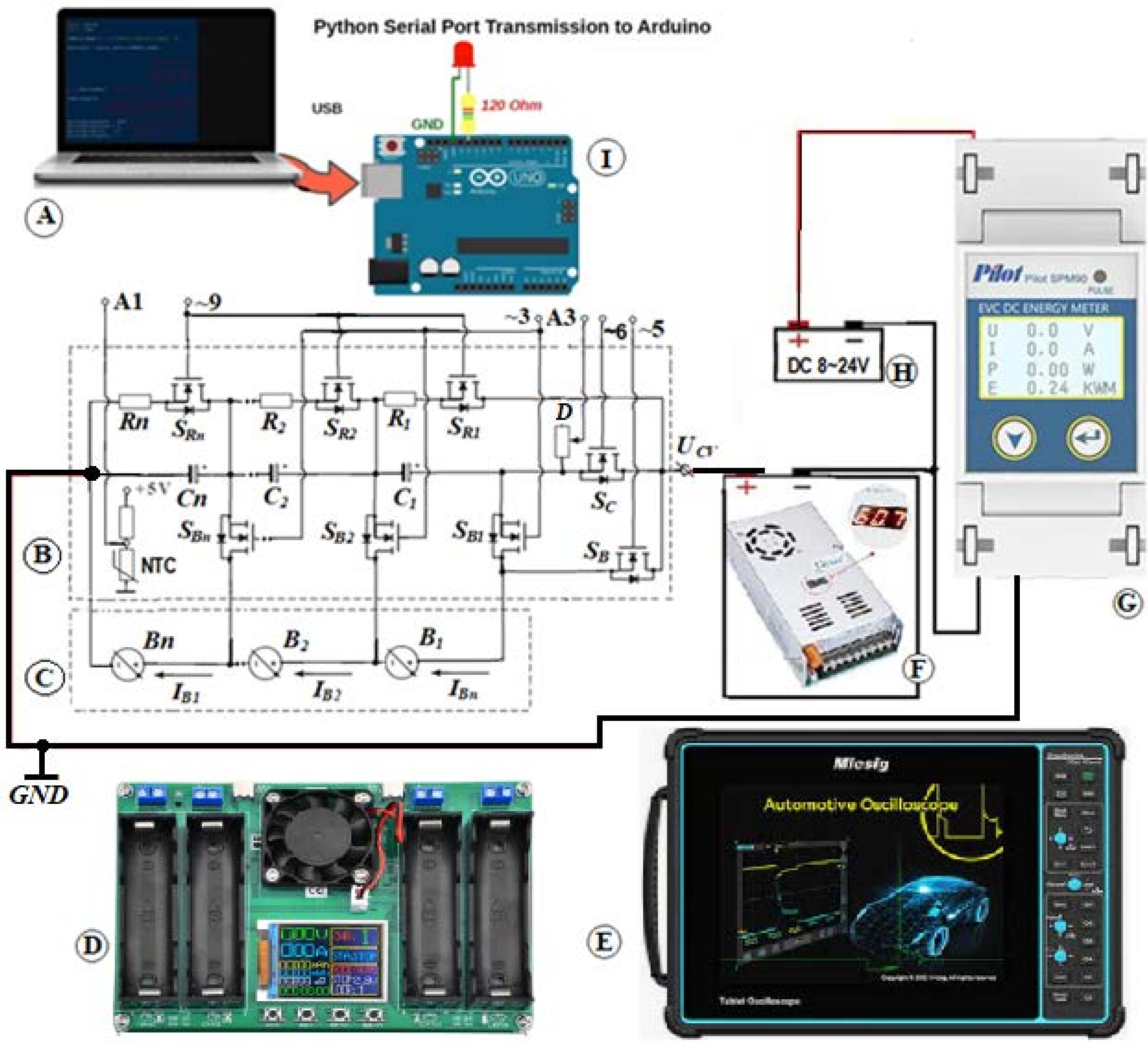

Figure 14. Stand for research and modes of operation of lithium-ion battery cells:

A - Phyton Script Transmits PC [25];

B - Pulsed battery charger with cell equalization;

C -Li-ion batteries type 18650

D -18650 Lithium Battery Capacity Tester [17];

E - Micsig ATO2004 automotive oscilloscope [18].

F - DROK 60V Power Supply [19];

G - Direct current meter SPM90 [20];

H - Energy meter power supply SPM90 [20];

I - Arduino Uno R3 Device to control the stand and perform BMS functions [15].

• Cyclic charge and discharge: supported only in automatic mode, adjustable from 1 to 9 cycles.

• Cooling mode: active fan cooling.

• Discharge stop voltage: 2.5V, 2.6V, 2.7V, 2.8V, 2.9V, 3.0V, 3.1V, 3.2V, 3.3V, 3.4 V, 3.5 V. Total 11 adjustable gears.

• Discharge current: the maximum current is about 1A.

• Charging voltage: controlled by a special battery charging chip, with a maximum charge of about 1A and a full charge voltage of 4.2V [17].

Table 8

Stand for research of batteries of electric vehicles

Nr	Name of elements	Brand	Quantity	Unit price	Price
1	Arduino controller	Arduino Uno R3	1	€29.99 + €6.70	€36.69
2	4-channel oscilloscope from Micsig specially made for the automotive industry	Micsig ATO2004 automotive oscilloscope	1	€950.41+ €50	€1000.41
3	18650 Lithium Battery Capacity Tester Module MAh Digital Type-C Four Batteries 18650 Battery Power Detector Capacity Tester, Mainland China	Battery Capacity Tester	1	€11,33 + €10	€21.33
4	n - channel MOSFET or IGBT transistors	FGA25N120	26	€1,26	€32.76
5	Resistor R1 = 100 Ω	C5-35B-50 100	26	$3.59	€93.34
6	Resistor R2 = 10 kΩ		29	€19.03 (for 100 units)	€19.03
7	Voltage divider resistors Rd = 1, 3, 5 Ω ± 1% , 5 W		36	€5.30	€190.80
8	Aluminum Electrolytic Capacitor JNK	56 000 µF ± 20% 10 B DC	12	€4,80	€57.60
9	830 dot solderless breadboard	MB-102	3	€3,28	€9.84
10	DC voltage source DROK 60V Power Supply, AC 220V to DC 0-60V 0-8A 480W	DROK 60V Power Supply	1	€36.89+ €25	€ 61,89
11	Film temperature sensor	Selco TF-F010K-1-2	3	€1.44	€4, 32
12	SPM90 - DIN rail DC meter and current shunt		1	€103	€103.00
13	Battery Samsung 18650 20A INR18650-25R	INR18650-25R	12	€7,75	€ 93.00
	Total				**€1724.01**

An oscilloscope must be included in the stand to observe and record the forms of capacitor current pulses for charging batteries. An automotive digital oscilloscope Micsig ATO2004, 200 MHz, 220 Mbps is suitable for this purpose [18]. This portable oscilloscope has a touch screen and can be used to diagnose the electrical and electronic equipment of vehicles (Fig. 14(E)). The choice of this oscilloscope model is due to the characteristics of this model, which allow it to be used not only to study electrical processes in the model of the proposed technical solution, but also to conduct laboratory work on diagnosing a Skoda Fabia car in the Laboratory of the Department of Transport. The ATO2004 model has: 200 MHz bandwidth; analog channels - 4; sample rate (max.) 2 GS/s; memory depth 220Mpts; acquisition rate (max.) 300 000 wfms/s; segmented storage for recording up to 10 000 events.

The oscilloscope Micsig ATO2004 model supports testing procedures for charging/starting circuits, sensors, actuators, ignition, network (CAN L/H, CAN FD, LIN, Flexray, K line) of vehicles. Model ATO2004 allows you to perform combined tests of vehicle electrical equipment and is equipped with an Industrial 10.1" TFT-LCD (1280x800) display [18].

The proposed device is powered by 600W digital display switching power supply Adjustable voltage 0-12V 24V 36V 48V 60v 80V AC 110/220V to DC SMPS LED POWER SUPPLY.

Single Display 60V Power Supply, AC 220V to DC 0-60V 8A 480W Buck Converter (Fig. 14(F)), Voltage Adjustable: 5V 12V 24V 30V 36V 48V 60Volt Transformer 3A 5A 8Amp Charger for Lab CCTV [19]. This device allows you to adjust the voltage up to 60 V when charging battery cells with direct current. This is enough to power up to 14 cells, in particular the 18650 size, connected in series by a chain into a battery. The Single Display 60V Power Supply, with an input voltage of 220V, allows you to adjust the output voltage in a wide range: 0-60V DC. The device is easy to operate and can be used to adjust the output voltage directly with a potentiometer. The voltage adjustment accuracy is 0.1V. The maximum current is 8A. This buck converter is equipped with an LED screen and a cooling fan. When the working power is high, the cooling fan will activate automatically.

The converter has overload protection, overvoltage protection, short circuit protection, which can protect your device from damage. The input voltage is 220V.

The SPM90 DC meter is designed to measure DC electricity consumption and to be installed in electric vehicle charging equipment on a 35mm DIN rail.

SPM90 is equipped with RS-485 interface with ModBus RTU protocol, pulse output and accuracy class 0.5.

The SPM90 DC electricity meter measures voltage, current and power in the DC circuit with high accuracy in real time.

The SPM90 meter belongs to the accuracy class of 0.5 electricity meters for all technical parameters. A current measuring shunt is included with the SPM90 DC electricity meter to measure the total amount of electricity kWh used to charge the battery.

The selected equipment and other necessary details for the creation of the stand are shown in Table 8. It is planned to assemble the stand by the staff and graduate students of the Department of Transport. The stand will allow you to check the effectiveness of the proposed device for charging and equalizing the voltage of battery cells at the second stage of charging these cells. The design of the device uses capacitors to charge the cells, so using capacitors of different capacities; you can change the frequency and power of the current pulses that charge the battery cells. Due to the presence of the Arduino control controller, it is possible to programmatically control the battery cell power switch and charge the battery cells with PWM current pulses at the first stage of their charging. Only a smoothing filter is required so that the supply voltage does not exceed the allowable limit. The measuring equipment of the stand allows monitoring the charging processes and investigating the effect of various mode parameters on the efficiency of the battery cell charging process. These studies are currently of interest to improve methods for charging lithium-ion batteries, the use of which is growing rapidly. Regarding the use of the stand for laboratory work, the topic of work related to the study of lithium-ion batteries is relevant for the Department of Transport due to the enormous increase in the number of electric and hybrid vehicles in Moldova.

6. Results

A new technical solution to the problem of charging a battery of batteries with the equalization of battery charges using energy storage devices is proposed. A device and a method for charging batteries connected in series are described, which excludes the flow of current through batteries that have reached the level of full charge, when charging batteries that have not reached this level.

By calculating the instantaneous circuit at the second stage of voltage equalization and charging of storage devices with the expected spread of storage parameters, it is shown that charging lithium-ion batteries using the proposed device and the proposed method using the High-voltage lithium-ion battery of Porsche Taycan as an example, allows charge lithium-ion batteries with current pulses generated by capacitive storage devices at the second stage, at a constant charging voltage close to the nominal value, preventing current from flowing through charged batteries and without exceeding the permissible level of battery charging voltage.

The charging time of the considered high-voltage battery with the elimination of 15% of the imbalance of the batteries will last up to 139 minutes (2.31 hours).

To equalize the charges of the High-voltage lithium-ion battery Porsche Taycan using capacitive storage devices in this example, additional energy costs $\Sigma E'_{loss}$ = 334.7 Wh will be required, which is 1.2% of the usable capacity of the battery (93.4 Wh).

The cost of creating a stand will require costs up to €2000, since not all companies have presented the cost of delivery to the Republic of Moldova and the cost of customs costs should be taken into account.

7. Discussion

The article discusses the operating modes and selects the parameters of a device that provides capacitor voltage equalization by resistive dividers for pulsed, individual charging of lithium-ion batteries at the final stage of charging (in constant voltage mode). An original method for calculating instantaneous voltage equalization circuits by resistive dividers is applied. However, the effect of pulse charging on Li-ion batteries, charging time and service life of Li-ion batteries has always been a bottleneck in the application of electric vehicles [21]. The discussion about the efficiency of charging batteries with current pulses continues, some authors believe this mode is effective and develop power supplies for pulsed charging [22]. Others report positive effects in terms of charging efficiency, charge time, and battery degradation, but feel the results are mixed [23]. To analyze the behavior of lithium-ion batteries, models based on linear regressions, manufacturer characteristics and integration of equations into an electrical model of electrochemical phenomena are proposed [24]. The Department of Transport of the Technical University of Moldova lacks scientific personnel and funding to conduct research of this level, therefore, the creation of a stand for studying the charging modes of real batteries using modern measuring equipment will contribute to obtaining new scientific results. With the help of the stand it will be possible to bring the proposed technical solution to implementation. The expected type of change in the voltage and current of the battery charging using the proposed device for charging and equalizing the voltage of the battery cells is shown in Figure 8 and 9. The author wants to present this graph to students using an oscilloscope on the stand.

A good indication of the cost savings of setting up a stand in the Department of Transportation is that researchers Xinrong Huang and others 2021 [22] to study various modes of charging with a pulsed current of lithium-ion batteries, the frequency and shape of the current pulses were reproduced using an expensive KEPCO BOP 100-10 device MG bidirectional programmable power supply worth $10 614.10. In our case, the principle of the proposed device is to generate charging current pulses for charging lithium-ion batteries, and the presence of a controller as part of the designed stand will allow: to change the frequency of the pulses. The selection of capacitors will allow you to change the duration of the pulses and conduct similar studies at a lower cost.

The possibility of using the selected brand of oscilloscope not only for research and laboratory work, but also for diagnosing automotive sensors and devices is also a good argument in favor of creating a stand with the costs shown in Table 8.

The stand will make it possible to study the effect of charging modes with pulsed current at different frequencies, amplitudes, and duty cycles on the battery life but will also allow using the stand for laboratory work in such disciplines as "Electrical and electronic equipment of cars", "Electric and hybrid cars".

8. Conclusions

The proposed device for equalizing the level of charge of batteries when charging batteries can be created on the basis of commercially available electronic components and can be used to equalize the charges of high-voltage batteries used in the automotive industry, as well as to charge batteries from renewable energy sources.

The proposed method of levelling the charge level of the batteries in the battery allows you to:

- increase the service life of batteries by eliminating the flow of current through fully charged batteries, that is, preventing them from overcharging and overheating;
- reduce energy losses for heating balancing resistors, as they turn on for a short time in the voltage equalization phase on the capacitors;
- get rid of the need to control the voltage of each battery cell separately.
- to provide improved performance and longer service life of lithium-ion batteries by pulse charging of the proposed device.

Numerical simulation of the preparation mode of the proposed device for charging a real car battery of the Porsche Taycan electric car was carried out, which made it possible to determine the technical parameters of the proposed device.

Obtained results confirmed the effectiveness of the technical proposal, energy losses do not exceed 2% of the useful battery capacity of the Porsche Taycan electric vehicle, and the time spent on charging using the proposed device and charging method will increase by no more than 20% relative to the average charging time of lithium-ion batteries. batteries, which is 180 minutes.

To continue the study, a bench scheme was developed to study the effect of the operating modes of the proposed device and the charging method on the charging efficiency of lithium-ion batteries, and the equipment necessary for research was selected. This stand can be used not only for scientific research, but also for laboratory work on car mechatronics and programming control units for charging batteries of hybrid and electric vehicles.

Conflicts of Interest: The author declares no conflict of interest.

References

1. Ryan, A. Tackling the rising cost of electric vehicle batteries. Available online: https://www.fleetnews.co.uk/electric-fleet/costs-and-incentives/tackling-the-rising-cost-of-electric-vehicle-batteries (accessed on 20.07.2022).
2. Yun, S.-S.; Kee, S.-C. Effect of Capacity Variation in Series-Connected Batteries on Aging. *Batteries* 2023, *9*, 22.
3. Yildirim, B.; Elgendy, M.; Smith, A.; Pickert, V. Evaluation and Comparison of Battery Cell Balancing Methods IEEE. Available online: https://eprints.ncl.ac.uk/file_store/production/261931/F4ADEC30-2EDD-4881-A81A-AC0BFDE3D9EB.pdf, (accessed on 12.02.2023).
4. Sourmey, I. Charging your lithium-ion batteries: 5 expert tips for a longer lifespan. Saft Connected Energy Division. Available online: https://www.saft.com/energizing-iot/charging-your-lithium-ion-batteries-5-expert-tips-longer-lifespan (accessed on 13.01.22).
5. Gudkov, N. We disassemble the 800-volt Porsche Taycan sedan by electron. Available online: https://www.drive.ru/kunst/porsche/5d6fc320ec05c48e5300013c.html (accessed on 04.09.2019).
6. Makeen, P.; Ghali, H.A.; Memon, S. A Review of Various Fast Charging Power and Thermal Protocols for Electric Vehicles Represented by Lithium-Ion Battery Systems. *Future Transp.* 2022, 2, pp. 281–299.
7. Jb Capacitors Company. Available online: https://www.jbcapacitors.com/pdf/JNK-5000H-at-105-Snap-in-Aluminum-Electrolytic-Capacitor.pdf (accessed on 4.07.2023).
8. Rf parts company. Available online: https://www. rfparts.com/rs5-1-dale-wirewound-resistor-1-ohm-5-watt-1-tolerance.htm (accessed on 04.07.2023).
9. NdFT Company. Available online: https://ndft.com.ua/product-category/semiconductor-devices/tranzistory-i-drugie-aktivnye-komponenty/silovye-tranzistory-bipolyarnye/ (accessed on 4.07.2023).
10. McEwen, R. Voltage Vs remaining energy of Lithium Ion batteries. Available online: https://meloyelo.nz/knowledge-base/voltage-vs-remaining-energy-of-lithium-ion-batteries/ (accessed on 14.07.2020).
11. Zaread i razread condensatora. Ingenernye sistemy cvartiry i doma. Available online: http://ingsvd.ru/main/polza/1147-zaryad-i-razryad-kondensatora.html (accessed on 4.07.2023).
12. Simple Equation for Capacitor Charging with RC Circuits. Wira Electrical. Available online: https://wiraelectrical.com/equation-for-capacitor-charging/ (accessed on 04.07.2023).
13. Bollini, R. Understanding Charge Discharge Curves of Li-ion Cells. EVreporter Magazines. Available online: https://evreporter.com/understanding-charge-discharge-curves-of-li-ion-cells/, (accessed on 04.01.2022).
14. BU-409: Charging Lithium-ion. Available online: https://batteryuniversity.com/article/bu-409-charging-lithium-ion (accessed on 25.10.2021).
15. Arduino Uno R3 Specifications/Functions, 2022-12-11. Available online: https://spiceman.net/arduino-uno/ (accessed on 11.12.2022).
16. Arduino Uno Rev3 Entwicklungsboard Development Board, ATmega328, UNO R3, A000066, 2023. Available online: https://www.ebay.de/p/2254348831?iid=252313246890 (accessed on 7.07.2023).
17. Aliexpress 18650 Lithium Battery Capacity Tester, 2023, Available online: https://aliexpress.ru/item/1005004862750518.html?gatewayAdapt=glo2rus&sku_id=12000031144439656 (accessed on 7.07.2023).
18. Micsig ATO2004 automotive oscilloscope. Available online: https://eleshop.eu/micsig-ato2004-oscilloscope.html, (accessed on 7.07.2023).
19. Signle Display 60V Power Supply, AC 110V 220V to DC 0-60V 8A 480W Buck Converter. Available online: https://www.droking.com/DROK-60V-Power-Supply-AC-110V-220V-to-DC-0-60V-8A-480W-Buck-Converter-Adjustable_1 (accessed on 20.07.2023).
20. Energometrika. Available online: https://www.energometrika.ru/catalog/spm90-schetchik-postoyannogo-toka-na-din-reyku.html (accessed on 20.07.2023).

21. What Is Pulse Charging For Lithium-Ion Batteries? What Is The Impact Of Pulse Charging On Lithium-Ion Batteries? Available online: https://www.linkedin.com/pulse/what-pulse-charging-lithium-ion-batteries-impact-bruce-feng (accessed on 27.02.2023).
22. Huang, X.; Liu, W.; Acharya, A. B.; Meng, J.; Teodorescu, R.; Stroe, D-I. Effect of Pulsed Current on Charging Performance of Lithium-ion Batteries. *IEEE Transactions on Industrial Electronics* 2022, 69(10), pp. 10144-10153.
23. Vermeer, W.; Stecca, M.; Mouli, G. R.C.; Bauer, P. A Critical Review on The Effects of Pulse Charging of Li-ion Batteries. In: *19th International Power Electronics and Motion Control Conference (PEMC),* Gliwice, Poland, 2021, pp. 217-224.
24. Camas-Náfate, M.; Coronado-Mendoza, A.; Vega-Gómez, C.J.; Espinosa-Moreno, F. Modeling and Simulation of a Commercial Lithium-Ion Battery with Charge Cycle Predictions. *Sustainability* 2022, 14, 14035.
25. Sreedharan, R. Cross Platform serial communication using Python (PySerial) and Arduino. Available online: https://www.xanthium.in/Cross-Platform-serial-communication-using-Python-and-PySerial (accessed on 24.06.2022).

Citation: Petrov, O. Directing the uniformity of the level of pulse charging of Li-ion batteries used in automotive industry. *Journal of Engineering Science* 2023, 30 (3), pp. 35-59. https://doi.org/10.52326/jes.utm.2023.30(3).04

Submission of manuscripts: jes@meridian.utm.md

https://doi.org/10.52326/jes.utm.2023.30(3).05
UDC 621.311.014:621.316(478)

OPPORTUNITY OF USING A MIXED NEUTRAL TREATMENT SOLUTION IN THE DISTRIBUTION ELECTRICAL NETWORKS OF THE REPUBLIC OF MOLDOVA

Ina Dobrea*, ORCID: 0009-0001-2243-1149,
Adrian Rotaru, ORCID: 0009-0005-9970-7579,
Ion Stratan, ORCID: 0009-0001-7333-5982

Technical University of Moldova, 168 Stefan cel Mare Blvd., Chisinau, Republic of Moldova
*Corresponding author: Ina Dobrea, *ina.dobrea@ee.utm.md*

Received: 08. 12. 2023
Accepted: 09. 06. 2023

Abstract. The optimal solution selection for the treatment of the neutral point in distribution networks (6-35 kV) holds significant practical importance as it directly or indirectly affects the continuity and reliability of supplying electrical energy to consumers, the behavior of medium-voltage electrical networks under single-phase fault conditions, and its impact on the quality of the power distribution service (duration and frequency of power interruptions). It also affects resulting overvoltages, adopted technical solutions, level of electrical security assurance, investments, and so forth. Developing a mathematical model for various methods of treating the neutral point in distribution networks allows for the calculation and analysis of these operating conditions, identifying the optimal one, thus avoiding experimental attempts that are limited by the advanced wear of equipment within the electrical networks of the Republic of Moldova. Based on the developed mathematical model, comparative calculations are performed regarding the feasibility of implementing the combined neutral regime.

Keywords: *combined (mixed) neutral, overvoltage, neutral voltage displacement, arc suppression coil (ASC), resistor.*

Rezumat. Alegerea soluției optimale de tratare a neutrului rețelelor de distribuție (6-35) kV are o importanță practică deosebită care se repercută, direct sau indirect, asupra continuității și fiabilității în alimentarea consumatorilor cu energie electrică, asupra comportării rețelelor electrice de medie tensiune în regim de defect monofazat și impactul acestuia asupra calității serviciului de distribuție a energiei electrice (durata și frecvența întreruperilor alimentării cu energie electrică), supratensiunilor rezultate, soluțiilor tehnice adoptate, nivelului de asigurare a securității electrice, investițiilor, etc. Elaborarea modelului matematic pentru diferite modalități de tratare a neutrului rețelelor electrice de distribuție permite calculul și analiza acestor regimuri, identificarea celui optimal evitând încercările experimentale, limitate de uzura avansată a echipamentelor din cadrul rețelelor electrice din Republica Moldova. În baza modelului matematic dezvoltat în lucrare sunt realizate calcule comparative privind oportunitatea implementării regimului neutrului combinat.

Cuvinte cheie: *neutru combinat (mixt), supratensiuni, deplasarea neutrului, bobină de stingere a arcului electric (BSA), rezistor.*

1. Introduction

Ensuring the electricity demand nationwide is the main task of the National Power System (NPS), which is divided into specialized segments - generation, transmission, distribution, and supply of electric energy. The 6-35 kV distribution electrical networks and their associated technologies represent one of the most dynamic development areas in the power sector. Until the end of the 20th century, the power system evolved towards expansion and centralization, benefiting from the quantitative advantages offered by the "economies of scale" in technical systems [1]. During this period, distribution electrical networks played a role in providing complete coverage to the served territories and in the "top-down" distribution of electric energy, using simple and reliable schemes. In the early 21st century, continuous improvements in equipment, technologies, and materials have allowed a change in the approach to constructing distribution networks, revising the principles of organizing the consumer power supply system, and necessitating major changes.

The main trends in the development of distribution electrical networks (DENs), which will influence their long-term evolution, are as follows:

- Increasing electricity demand and ensuring the enhancement of the existing DENs' transport capacity. According to the International Energy Agency (IEA) Report [2], global electricity demand will rise from 2.6% in 2023 to an average of 3.2% in 2024-2025.
- Improving energy efficiency in distribution networks (including reducing technical and non-technical losses), enhancing management, and electrical security.
- Implementing innovative technologies, such as smart grids and advanced energy storage.
- Integrating renewable energy sources and distributed generation into the distribution electrical networks.
- Rising electrical load density, driven by the increased height of residential and utility buildings, as well as the growth in power ratios and the compactness of modern production systems.

Among the known technical measures, the treatment mode of the neutral point in distribution networks holds significant practical importance, which directly or indirectly impacts the continuity and reliability of supplying electric energy to consumers. It also affects the behavior of medium-voltage electrical networks under single-phase fault conditions and its impact on the quality of the power distribution service (duration and frequency of power interruptions), electrical installations, and their operation, adopted technical solutions, and the level of electrical security assurance, among others.

In accordance with the foreign country classification based on standard [3], there are five modes of neutral treatment. Specifically, in global practice, concerning medium-voltage networks (1 – 69 kV), unlike high-voltage networks (110 kV and above), the following neutral treatment solutions are observed in MT electrical networks [4-7]:

1. *Isolated Neutral:* Widely applied in post-Soviet countries such as Russia, Belarus, Ukraine, as well as in Italy, Spain, China, and some areas in Germany, Romania, and Finland (for 20 kV overhead networks). However, this method of neutral treatment in 1-69 kV networks possesses too many disadvantages, leading to its elimination from operation in the 1940s-1950s in most European, Australian, North and South American countries.

2. *Compensated Neutral (earthed through an arc suppression coil):* Applied in most European countries, China, and Russia.
3. *Neutral earthed through a low or high-value resistor:* Found in France, some areas in Germany, Bulgaria, Hungary, and Russia. In recent years, this neutral treatment method has been implemented in Romania, Belarus, and Ukraine.
4. *Combined Neutral or Mixed Solution (combining variants 2 and 3):* Applied in Germany, the Czech Republic, and Russia.
5. *Directly Earthed Neutral:* The method of neutral treatment used in the United Kingdom and the USA, Canada (the Anglo-Saxon Solution).

In the Republic of Moldova, the medium-voltage (MV) electrical networks, ranging from 6 to 35 kV, are managed by the companies ÎCS "Premier Energy Distribution" SA, RED Nord SA, and ÎS Moldelectrica. The 6-10 kV electrical networks, approximately 22 thousand km in length, are mostly overhead (88.6%), with 11.4% consisting of cable networks. The 35 kV electrical networks, approximately 1300 km in length, are exclusively overhead.

Currently, within the RM's Distribution Electrical Networks, there are two neutral treatment solutions regulated by the Rules of Electrical Installations Design (REID) [8], implemented over time as follows:

1. Isolated Neutral.
2. Neutral treated through an arc suppression coil (ASC), with manual or automatic adjustment.

These treatment systems are dedicated to specific network configurations and have advantages and disadvantages, which necessitate continuous improvement. Most of the distribution networks at the mentioned voltages operate in a mode of compensating capacitive current through the ASC. There is also a small number of stations where the neutral is isolated, but only in cases where the distribution networks are short, and the capacitive currents at the station have low values (below 10 A).

Studies and research conducted in the last 15 to 20 years [5, 6, 9] confirm the impossibility of obtaining a specific technical or techno-economic criterion for selecting the optimal neutral treatment solution in medium-voltage (MV) electrical networks. Thus, the choice of the optimal neutral treatment mode must be made in relation to a specific electrical network, under the conditions of a particular country.

Currently, in the Republic of Moldova, there are no studies and research for implementing resistive or combined neutral treatment. Additionally, there are no regulations or guidelines regarding the application of possible solutions or methods for compensating capacitive currents in earth connections. The purpose of this study is to analyze the potential for implementing combined neutral treatment in DENs of the Republic of Moldova, with the objectives being: analyzing the normal and single-phase fault conditions in MV electrical networks, identifying the fundamental criteria for choosing the appropriate solution, estimating the feasibility of implementing combined neutral treatment under the conditions of the Republic of Moldova.

The research hypothesis is focused on improving the existing modes of neutral treatment in RM's distribution networks or implementing new solutions that will contribute to the following: reducing overvoltages in the case of single-phase earth connections, reducing the number of disconnections and improving distribution service performance indicators [10], eliminating the evolution of single-phase faults into polyphase short circuits, enhancing the reliability of electricity supply to end consumers.

2. Materials and Methods

2.1. Expressions of network state variables during a single-phase fault

In distribution networks with voltage levels of 6-35 kV, single-phase faults constitute 75-80% of the total fault occurrences. Metallic ground connections account for approximately 10-15%, while the rest are accompanied by electric arcs at the fault location. The probability of arc self-extinction, burning duration, intermittent nature of the arc, and the value of the grounding current determine the overvoltages on the healthy phases, which can reach values of 3-3.5 times the phase voltage (U_f). Additionally, the consequences of these overvoltages include insulation breakdown in the weakest points of the electrical network and the transformation of single-phase faults into polyphase short circuits. The thermal action of the earth fault current may also cause fires.

To avoid or reduce the consequences of single-phase faults and the accompanying overvoltages, it is necessary to create conditions in which the electric arc at the fault location will self-extinguish or burn stably, and the grounding current will be limited to non-hazardous values.

The state of the electrical network in a steady-state single-phase fault condition is characterized by the values of certain quantities known as state variables, including:

- Phase voltages,
- Neutral-to-ground voltage,
- Fault current.

To obtain the analytical relationships of the state variables of the electrical network that characterize the steady-state condition of a single-phase fault, an equivalent calculation scheme will be used. The structure of this scheme is derived based on the relationships between the symmetrical components of voltage and current, considering the specific conditions of this fault and their validity at the fault location [11] (Figure 1).

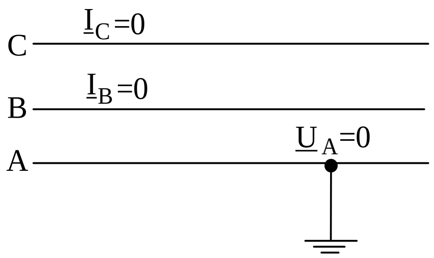

Figure 1. A single-phase fault.

If the currents due to consumers connected to the line are not taken into account, the presence of the fault can be expressed through the following relationships:

$$\left.\begin{aligned} \underline{I}_B = \underline{I}_C = 0; \\ \underline{U}_A = 0. \end{aligned}\right\}, \tag{1}$$

where: $\underline{I}_B$ is the current in phase B; $\underline{I}_C$ - the current in phase C; $\underline{U}_A$ - the voltage on phase A.

Taking into account the decomposition into symmetrical components of voltages and currents, assuming phase A as the reference, the following relationships can be written:

$$\left.\begin{aligned} \underline{I}^h + \underline{a}^2 \cdot \underline{I}^d + \underline{a} \cdot \underline{I}^i = 0; \\ \underline{I}^h + \underline{a} \cdot \underline{I}^d + \underline{a}^2 \cdot \underline{I}^i = 0, \end{aligned}\right\} \tag{2}$$

where $\underline{a} = -\frac{1}{2} + j\frac{\sqrt{3}}{2}$; $\underline{a}^2 = -\frac{1}{2} - j\frac{\sqrt{3}}{2}$.

From (2) it follows:

$$\underline{I}^h + \underline{a}^2 \cdot \underline{I}^d + \underline{a} \cdot \underline{I}^i = \underline{I}^h + \underline{a} \cdot \underline{I}^d + \underline{a}^2 \cdot \underline{I}^i, \quad (3)$$

or

$$(\underline{a}^2 - \underline{a}) \cdot \underline{I}^d = (\underline{a}^2 - \underline{a}) \cdot \underline{I}^i, \quad (4)$$

so:

$$\underline{I}^d = \underline{I}^i, \quad (5)$$

By substituting this result into one of the equations (2) for decomposing the current from the healthy phases, we obtain:

$$\underline{I}_B = \underline{I}^h + \underline{a}^2 \cdot \underline{I}^d + \underline{a} \cdot \underline{I}^i = \underline{I}^h + (\underline{a}^2 + \underline{a}) \cdot \underline{I}^d = \underline{I}^h - \underline{I}^d = 0,$$

as a consequence:

$$\underline{I}^h = \underline{I}^d = \underline{I}^i. \quad (6)$$

Conditions (1) and (6) allow the preparation of the equivalent calculation scheme (Figure 2). In this scheme, D, I, and H represent the equivalent networks of the system with respect to the fault location, valid for the three symmetrical components: positive sequence, negative sequence, and zero sequence [7].

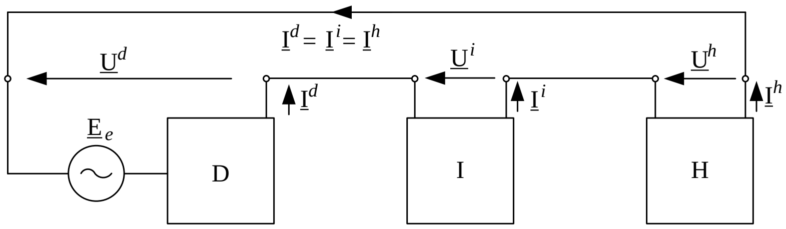

Figure 2. Schema echivalentă pentru defectul monofazat.

The three schemes are connected in series. In the positive sequence diagram, the considered source is included, assumed to provide a system of three voltages with equal magnitudes and 120° phase displacement, forming a positive sequence system of voltages. There are no electromotive forces (e.m.f) in the negative sequence and zero sequence components.

For the symmetrical components of voltage, the following can be written:

$$\left.\begin{aligned} \underline{U}^d &= \underline{E}_e - \underline{I}^d \cdot \underline{Z}^d; \\ \underline{U}^i &= -\underline{I}^i \cdot \underline{Z}^i; \\ \underline{U}^h &= -\underline{I}^h \cdot \underline{Z}^h. \end{aligned}\right\} \quad (7)$$

Similarly, for the symmetrical components of current, the relationship is valid:

$$\underline{I}^d = \underline{I}^i = \underline{I}^h = \frac{\underline{E}_e}{\underline{Z}^d + \underline{Z}^i + \underline{Z}^h}. \quad (8)$$

The single-phase to ground faults current is determined using the relationship:

$$\underline{I}_{PP} = \underline{I}^d + \underline{I}^i + \underline{I}^h. \quad (9)$$

The voltages on the phases of the network in the steady-state condition of a single-phase fault are determined as follows:

- for phase A (fault which occurs at A-Phase)

$$\underline{U}_A = \underline{U}_A^h + \underline{U}_A^d + \underline{U}_A^i = (-\underline{I}^h \cdot \underline{Z}^h) + (\underline{E}_e - \underline{I}^d \cdot \underline{Z}^d) + (-\underline{I}^i \cdot \underline{Z}^i) =$$
$$= \underline{E}_e - \underline{I}^d \cdot (\underline{Z}^h + \underline{Z}^d + \underline{Z}^i) = \underline{E}_e - \frac{\underline{E}_e}{\underline{Z}^h + \underline{Z}^d + \underline{Z}^i} \cdot (\underline{Z}^h + \underline{Z}^d + \underline{Z}^i) = 0;$$

- for phase B:

$$\underline{U}_B = \underline{U}^h + \underline{a}^2 \cdot \underline{U}^d + \underline{a} \cdot \underline{U}^i = -\underline{I}^h \cdot \underline{Z}^h + \underline{a}^2 \cdot (\underline{E}_e - \underline{I}^d \cdot \underline{Z}^d) + \underline{a} \cdot (-\underline{I}^i \cdot \underline{Z}^i);$$

- for phase C:

$$\underline{U}_C = \underline{U}^h + \underline{a} \cdot \underline{U}^d + \underline{a}^2 \cdot \underline{U}^i = -\underline{I}^h \cdot \underline{Z}^h + \underline{a} \cdot (\underline{E}_e - \underline{I}^d \cdot \underline{Z}^d) + \underline{a}^2 \cdot (-\underline{I}^i \cdot \underline{Z}^i).$$

For electric power transmission and distribution networks composed only of passive elements (without generators), it can be considered that:

$$\underline{Z}^d = \underline{Z}^i.$$

Thus:

$$\underline{U}_B = -\underline{I}^d \cdot \underline{Z}^h + \underline{a}^2 \cdot \underline{E}_e - (\underline{a}^2 + \underline{a}) \cdot \underline{I}^d \cdot \underline{Z}^d = \underline{a}^2 \cdot \underline{E}_e + (\underline{Z}^d - \underline{Z}^h) \cdot \underline{I}^d;$$
$$\underline{U}_C = -\underline{I}^d \cdot \underline{Z}^h + \underline{a} \cdot \underline{E}_e - (\underline{a}^2 + \underline{a}) \cdot \underline{I}^d \cdot \underline{Z}^d = \underline{a} \cdot \underline{E}_e + (\underline{Z}^d - \underline{Z}^h) \cdot \underline{I}^d.$$

By introducing, in the obtained expressions, the relationship (8) of the current in the positive sequence, we obtain:

$$\underline{U}_B = \underline{a}^2 \cdot \underline{E}_e + (\underline{Z}^d - \underline{Z}^h) \cdot \frac{\underline{E}_e}{2 \cdot \underline{Z}^d + \underline{Z}^h} = \underline{E}_e \cdot \left(\underline{a}^2 + \frac{\underline{Z}^d - \underline{Z}^h}{2 \cdot \underline{Z}^d + \underline{Z}^h} \right) = \underline{k}_B^{def} \cdot \underline{E}_e; \quad (10)$$

$$\underline{U}_C = \underline{a} \cdot \underline{E}_e + (\underline{Z}^d - \underline{Z}^h) \cdot \frac{\underline{E}_e}{2 \cdot \underline{Z}^d + \underline{Z}^h} = \underline{E}_e \cdot \left(\underline{a} + \frac{\underline{Z}^d - \underline{Z}^h}{2 \cdot \underline{Z}^d + \underline{Z}^h} \right) = \underline{k}_C^{def} \cdot \underline{E}_e; \quad (11)$$

$$\underline{k}_B^{def} = \underline{a}^2 + \frac{\underline{Z}^d - \underline{Z}^h}{2 \cdot \underline{Z}^d + \underline{Z}^h}; \qquad \underline{k}_C^{def} = \underline{a} + \frac{\underline{Z}^d - \underline{Z}^h}{2 \cdot \underline{Z}^d + \underline{Z}^h}, \quad (12)$$

where: $\underline{k}_B^{def}$, $\underline{k}_C^{def}$ are the voltage coefficients for a single-phase fault.

These coefficients are complex numbers, and their modulus represents the multiple of increase in voltages on the healthy phases during a single-phase fault compared to the phase voltage at the corresponding section without a fault. In other words, this is the phase voltage of phase A.

The voltage on the *electrical neutral* of the network (physical neutral may be absent – when the secondary winding of the transformer is connected in a delta configuration) will always be equal to the homopolar voltage, as the positive and negative sequence systems do not result in neutral displacement:

$$\underline{U}_N = \underline{U}^h. \quad (13)$$

At the appearance of the homopolar system, the neutral undergoes a potential change from 0 to $\underline{U}^h$.

2.2. Transient processes at single phase-to-ground faults in medium-voltage networks with the neutral treated by ASC

In addition to reducing the industrial frequency component of the earth fault current and extinguishing the electric arc, the ASC also plays a significant role during the transient process. It reduces the rate of change of voltage on the network neutral and, consequently, on the phases, leading to a considerable reduction in the amplitudes of the free components and, thus, to a decrease in overvoltages in the network.

To analyze the transient processes during the ignition and extinction of the electric arc when the neutral is treated by the ASC, the following scheme will be used (Figure 4).

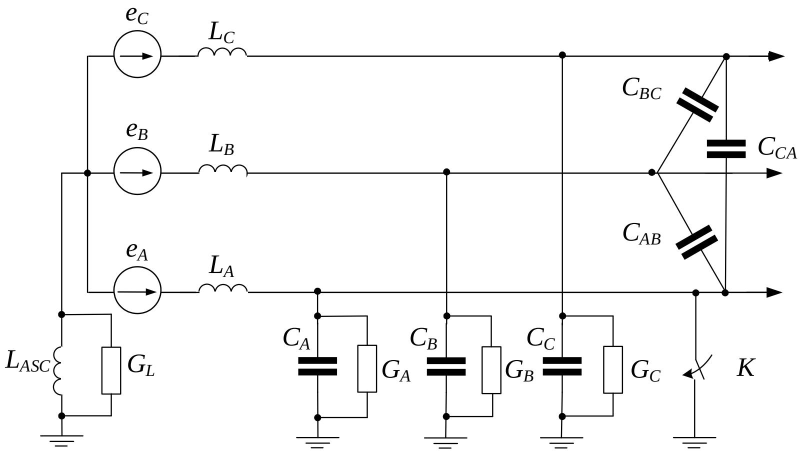

Figure 4. The equivalent schematic of the electrical network with the neutral treated through the arc suppression coil.

It is worth mentioning that the resistances of the phases were not included in the schematic since they are contained within the equivalent resistance, which includes the current return path resistance and the resistance of the fault arc grounding.

This resistance can vary within wide limits and can be different for different stages of the transient process. For instance, for the free components with higher frequencies than the industrial frequency, the skin effect is more pronounced, resulting in a higher resistance. Due to these considerations, the attenuation coefficient, denoted as k_δ, is used in practice, which is obtained from practical experience gained during the operation of medium-voltage networks [12].

Just like in the case of isolated neutral, during the ignition of the fault arc, the non-fault phases' capacitances are charged up to the line voltage. This process exhibits oscillatory behavior with attenuation. The ASC practically does not influence the amplitude or frequency of the free component, as it is shunted by the inductance of the faulty phase, which is much smaller than the inductance of the ASC. Therefore, during the initial breakthrough, the ASC does not affect the transient process parameters, and it behaves analogously to an isolated neutral [13].

From Figure 5, it can be observed that when phase A is grounded, the ASC is connected to the e.m.f. of phase A, which triggers a transient process of current modification in the ASC. Considering that $L_f \ll L_{ASC}$, the inductance of the faulty phase can be neglected, as it does not affect the transient process occurring in the ASC. The schematic representation of this transient process will look like this:

For the Figure 5 circuit, three equations can be formulated according to Kirchhoff's laws:

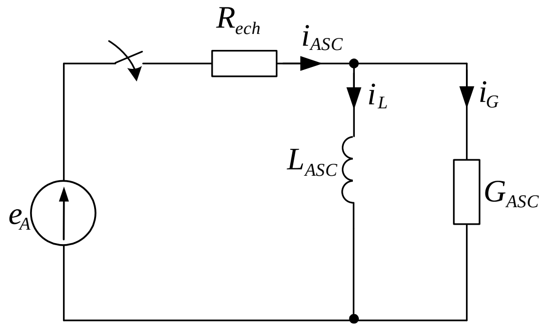

Figure 5. The equivalent circuit for analyzing the transient process in ASC during the first insulation breakdown.

$$\begin{cases} i_{ASC} = i_L + i_G; \\ R_{ech} \cdot i_{ASC} + L_{ASC} \cdot \dfrac{di_L}{dt} = e_A; \\ \dfrac{i_G}{G_{ASC}} - L_{ASC} \cdot \dfrac{di_L}{dt} = 0. \end{cases} \quad (14)$$

If this system is solved for the current i_L, the differential equation of the transient process is obtained:

$$(R_{ech} \cdot G_{ASC} + 1) \cdot L_{ASC} \cdot \frac{di_L}{dt} + R_{ech} \cdot i_L = e_A. \quad (15)$$

The solution of this differential equation will be:

$$i_L = i_{Lfr} + i_{Llb}. \quad (16)$$

The forced component will be expressed as follows:

$$i_{Lfr} = I_m \cdot \sin(\omega t + \psi_{st} - \varphi), \quad (17)$$

where: $I_m = \dfrac{E_m}{\sqrt{R_{ech}^2 + \omega^2 \cdot L_{ASC}^2}}$ (if the ASC conductance is neglected); $\psi_{st} \approx 90°$ – it is the phase of the voltage at which the insulation breakdown occurs (assuming that the breakdown occurs when the voltage on the non-fault phase reaches its peak value), which is why the initial phase of the current corresponds to the phase of the voltage at the time of breakdown); φ – the phase difference between the voltage across the coil and the forced component of the current.

The free component will be:

$$i_{Llb} = A \cdot e^{-\frac{t}{\tau}}, \quad (18)$$

where: A is the integration constant, determined from the initial conditions, i.e. $i_L=0$, or $I_m \cdot \sin(\psi_{st} - \varphi) + A = 0$, which yields: $A = -I_m \cdot \sin(\psi_{st} - \varphi)$; τ – the time constant. The time constant can be determined from the equation (15):

$$\tau = L_{ASC} \cdot \left(G_{ASC} + \frac{1}{R_{ech}} \right). \quad (19)$$

From the above-explained details, the relationship for the current in ASC during arc ignition can be obtained:

$$i_L = I_m \cdot \sin(\omega t + \psi_{st} - \varphi) - I_m \cdot \sin(\psi_{st} - \varphi) \cdot e^{-\frac{t}{\tau}}. \quad (20)$$

Angle $\varphi \approx 90°$, since R_{ASC} >> L_{ASC}, implies $\psi_{st} - \varphi \approx 0$, which means that the free component is negligibly small. Therefore, the conclusion can be drawn that in the compensated network, the transient process during the first insulation breakdown does not differ from the transient process that occurs in the network with an isolated neutral.

After arc extinction, the ASC decisively influences the transient process. This is due to the fact that the ASC significantly alters the network's admittance to ground, facilitating the discharge of electric charges to the ground. Moreover, the considerable inductance of the ASC prevents sudden voltage rise on the network's neutral and phases, thereby limiting the level of overvoltage.

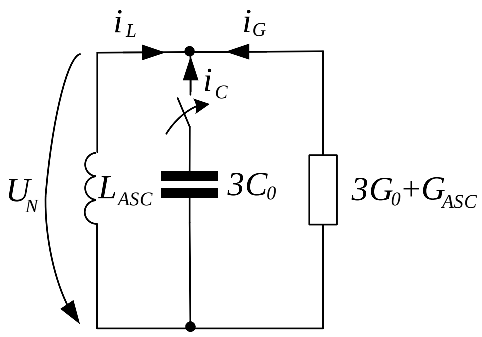

Figure 6. The equivalent circuit for the transient process that occurs after arc extinction.

In Figure 6 the phase-to-ground conductance is denoted by G_0.

The diagram (Figure 6) represents an oscillating circuit in which the transient process can be described by the following relationships:

$$i_L = \frac{1}{L_{ASC}} \cdot \int U_L \cdot dt; \quad (21)$$

$$i_C = 3C_0 \cdot \frac{dU_C}{dt}; \quad (22)$$

$$i_G = (3 \cdot G_0 + G_{ASC}) \cdot U_G; \quad (23)$$

$$i_C + i_G + i_L = 0. \quad (24)$$

If we substitute equations (21), (22), and (23) into equation (24), considering the equality U_N=U_C=U_G=U_L, we obtain:

$$3C_0 \cdot \frac{dU_N}{dt} + (3 \cdot G_0 + G_{ASC}) \cdot U_N + \frac{1}{L_{ASC}} \int U_N \cdot dt = 0. \quad (25)$$

If equation (25) is divided by $3C_0$ and then differentiated with respect to time, the resulting differential equation describes the neutral voltage during the transient process when the electric arc is extinguished.:

$$\frac{dU_N^2}{dt^2} + \frac{(3 \cdot G_0 + G_{ASC})}{3C_0} \cdot \frac{dU_N}{dt} + \frac{1}{3C_0 \cdot L_{ASC}} \cdot U_N = 0. \quad (26)$$

For a more simplified and clear analysis of this relationship, the following coefficients are introduced:

- Coefficient of deviation from complete compensation:

$$\upsilon = 1 - \frac{I_{L1}}{I_{C1}} = 1 - \frac{E_f \cdot \dfrac{1}{\omega L_{ASC}}}{E_f \cdot 3\omega C_0} = 1 - \frac{1}{3\omega^2 C_0 L_{ASC}} = 1 - \frac{\omega_0^2}{\omega^2}, \tag{27}$$

where: I_{L1}, I_{C1} represent the inductive currents through the ASC and the corresponding capacitive ground-fault current at the industrial frequency; $\omega_0 = \frac{1}{\sqrt{3C_0 L_{ASC}}}$ – frequency of resonance of the oscillating circuit of the ASC; C_0 – the phase capacitances; ω – the angular frequency corresponding to the industrial frequency.

When compensation is complete, then $I_{L1} = I_{C1}$ and $\upsilon = 0$; when $I_{L1} < I_{C1}$ subcompensation occurs and $\upsilon > 0$, when $I_{L1} > I_{C1}$ overcompensation occurs and $\upsilon < 0$.

- The attenuation coefficient that characterizes the active component of the ground-fault current:

$$\partial = \frac{I_{a1}}{I_{C1}} = \frac{E_f \cdot (3G_0 + G_{ASC})}{E_f \cdot 3\omega C_0} = \frac{3G_0 + G_{ASC}}{3\omega C_0}, \tag{28}$$

where I_{a1} is composed of two components, the first one is determined by current leakage on the insulator surfaces and constitutes 2 - 3% of the capacitive current of the network, but the second component is determined by losses in the ASC and constitutes approximately 2% of the inductive component of the current in the ASC, For the given data, the attenuation coefficient has the value of 0,05 [12-14]; I_{C1} – the capacitive ground-fault current at the industrial frequency.

Taking into consideration equations (27) and (28), equation (26) becomes:

$$\frac{dU_N^2}{dt^2} + \partial\omega \cdot \frac{dU_N}{dt} + \omega^2 \cdot (1-\upsilon) \cdot U_N = 0. \tag{29}$$

The roots of this equation are expressed as follows:

$$p_{1,2} = \left[-\frac{\partial}{2} \pm \sqrt{\left(\frac{\partial}{2}\right)^2 - (1-\upsilon)} \right] \cdot \omega. \tag{30}$$

Since $\left(\frac{\partial}{2}\right)^2$ << $1-\upsilon$ the roots of the equation will be complex conjugates, indicating that the discharge will exhibit an oscillatory character.

The solution of equation (25) will have the following form:

$$u_N(t) = U_{Nm} \cdot e^{-\frac{\partial}{2}\cdot\omega t} \cdot \sin(\omega_{st} t + \varphi_{N0}), \tag{31}$$

where $\omega_{st} = \omega \cdot \left| \sqrt{\left(\frac{\partial}{2}\right)^2 - (1-\upsilon)} \right|$ – is the angular frequency of the free oscillations of the transient process of neutral voltage modification; U_{Nm}, φ_{N0} – are the initial amplitude and initial phase of the free component of the neutral voltage. These quantities are determined from the initial conditions, i.e., they depend on the values taken by $u_N(0)=u_C(0)$ și $i_L(0)$, , thus, on the moment of arc extinction.

After the electric arc is broken, the free component of the voltage u_N overlaps with the phase voltages. In this case, the voltage on the faulty phase can be expressed as follows:

$$u_A(t)=e_A(t)+u_N(t)+U_{Am}\cdot e^{-\delta_2\cdot(t-\frac{T_1}{2})}\cdot\cos\omega_2(t-\frac{T_1}{2})=E_m\cdot\sin\left[\omega\cdot(t-\frac{T_1}{2})+\frac{3\cdot\pi}{2\cdot\omega}\right]+$$
$$+U_{Nm}\cdot e^{-\frac{\partial}{2}\cdot\omega(t-\frac{T_1}{2})}\cdot\sin(\omega_{st}t+\varphi_{N0})+U_{Am}\cdot e^{-\delta_2\cdot(t-\frac{T_1}{2})}\cdot\cos\omega_2(t-\frac{T_1}{2}). \quad (32)$$

In equation (32), the free component resulting from the process of restoring the voltage on the faulty phase is included. This process is characterized by the amplitude U_{Am}, attenuation coefficient δ_2 and angular frequency ω_2, while T_1 is the period of the free component for the transient process that occurs after arc ignition. It is assumed that the arc extinguishes at the first passage through zero of the free component of the current, which happens after a time equal to $\frac{T_1}{2}$. Time $t=0$ is considered at the moment of breakthrough, when the voltage on the faulty phase reaches the value of E_m.

For capacitive current, the relationship is valid:

$$i_C(t)=3C_0\cdot\frac{du_C}{dt}=3C_0\cdot\frac{du_N}{dt}. \quad (33)$$

If we take into consideration that $\frac{1}{\omega_{st}L_{BSA}}\gg 3G_0+G_{BSA}$, then it can be considered that $i_G(t)\approx 0$ and $i_L(t)\approx i_C(t)$.

In such a way, if $t=0$ is considered as the beginning of the transient process, then equations (22) and (33) take the following form:

$$u_N(0)=U_{Nm}\cdot\sin\varphi_{N0};$$
$$i_L(0)=3C_0\cdot\frac{du_N}{dt}\Big|_{t=0}=3C_0\cdot\omega_{st}\cdot U_{Nm}\cdot\cos\varphi_{N0}. \quad (34)$$

The solutions of this system will be as follows:

$$U_{Nm}=\sqrt{(u_N(0))^2+\left(\frac{i_L(0)}{3C_0\cdot\omega_{st}}\right)^2};$$
$$tg\varphi_{N0}=3C_0\cdot\omega_{st}\cdot\frac{u_N(0)}{i_L(0)}. \quad (35)$$

In such a way, the initial conditions for solving the differential equation are different depending on the moment in time when the arc extinguishes. If we assume that the electric arc will extinguish at the first zero crossing of the free component of the grounding current, then the current through the ASC will be approximately equal to zero ($i_L(0)\approx 0$), because one half-period of the free component ($\frac{T_1}{2}$) is much smaller than the time constant of the ASC and the current in the ASC does not show any significant changes. In such a way, considering $i_L(0)=0$, from (35) we obtain: $U_{Nm}=u_N(0);\ \varphi_{N0}=90°$. Therefore, the neutral voltage will change according to the law:

$$u_N(t)=u_N(0)\cdot e^{-\frac{\partial}{2}\cdot\omega t}\cdot\sin(\omega_{st}t+90°)=u_N(0)\cdot e^{-\frac{\partial}{2}\cdot\omega t}\cdot\cos\omega_{st}t\,. \tag{36}$$

As mentioned above, since in the general case $e_A(t)+u_N(t)\neq 0$, a process of restoring the voltage on the faulty phase will occur with an angular frequency ω_2 there will be a voltage peak during the restoration of the voltage on the faulty phase. If the electrical stiffness of phase A at the defect location is higher than this threshold voltage (u_{pr}), then the voltage on the faulty phase will change according to the relationship:

$$\begin{aligned}u_A(t)&=e_A(t)+u_N(t)=E_m\cdot\sin\left(\omega\left(t-\frac{T_1}{2}\right)+\frac{3\pi}{2\omega}\right)+\\&+u_N(0)\cdot e^{-\frac{\partial}{2}\cdot\omega\left(t-\frac{T_1}{2}\right)}\cdot\cos\omega_{st}\left(t-\frac{T_1}{2}\right)+U_{Am}\cdot e^{-\delta_2\cdot t}\cdot\cos\omega_2(t-\frac{T_1}{2})=\\&=-E_m\cdot\cos\omega\left(t-\frac{T_1}{2}\right)+u_N(0)\cdot e^{-\frac{\partial}{2}\cdot\omega\left(t-\frac{T_1}{2}\right)}\cdot\cos\omega_{st}\left(t-\frac{T_1}{2}\right)+U_{Am}\cdot e^{-\delta_2\cdot t}\cdot\cos\omega_2(t-\frac{T_1}{2}).\end{aligned} \tag{37}$$

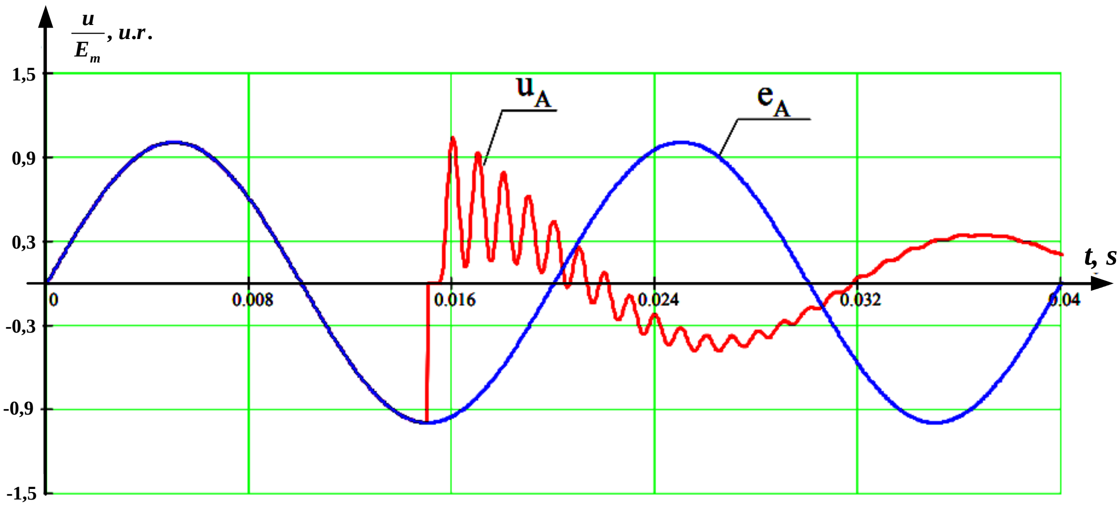

Figure 7. The voltage on the faulty phase during the extinction of the electric arc over the course of two periods of industrial frequency.

Result $u_N(0)=1,48\cdot E_m$. If the following parameters of the transient process are accepted: $\partial=0,05$, $\omega_1=\omega_2=2\pi 1000$, δ_2=200, then the voltages on the faulty phase and on the neutral will take the form presented in Figure 7 (the voltage values are reported relative to the amplitude value).

In the case when the electric arc extinguishes at the zero crossing of the forced component, from equations (27) and (28), it can be observed that the quantities representing the reactive and active components of the grounding current, relative to this current, i.e.:

$$\upsilon=1-\frac{I_{L1}}{I_{C1}}=\frac{I_{C1}-I_{L1}}{I_{C1}}=\frac{I_{r1}}{I_{C1}};\ \partial=\frac{I_{a1}}{I_{C1}}, \tag{38}$$

Here, index *1* indicates the fundamental harmonic; I_{r1} – the residual current.

The forced component of the grounding current can be expressed as the active and reactive components:

$$i_{pp}=-E_m\cdot 3\omega C_0\cdot(\partial\cdot\sin\omega t+\upsilon\cdot\cos\omega t). \tag{30}$$

At the moment of arc extinction, the current passes through zero ($i_{pp}=0$), from which it follows that:

$$\partial \cdot \sin \omega t + \upsilon \cdot \cos \omega t = 0 \quad sau \quad \varphi_{st} = \omega t_{st} = arctg\left(-\frac{\upsilon}{\partial}\right), \tag{40}$$

where t_{st} is the time interval between the moment of zero crossing of the e.m.f. of the faulty phase and the grounding current, and φ_{st} is the phase angle corresponding to this time.

Since, until the zero crossing of the forced component of the grounding current, the transient process initiated at the arc ignition practically diminishes, the neutral voltage at the moment of extinction will be $u_N(t) = -e_A(t)$, hence $e_A(t) + u_N(t) = 0$. This means that the high-frequency component, which was present when the arc extinguished at the first zero crossing of the free component, will be absent in this case. The voltage restoration process is described by the relationship:

$$u_A(t) = u_{Afr}(t) + u_{Alb}(t) = E_m \cdot \left(\sin\left(\omega \cdot t + \varphi_{st}\right) - e^{-\frac{\partial}{2}\cdot\omega\cdot t} \cdot \sin(\omega_{st} t + \varphi_{st}) \right), \tag{41}$$

where: $u_{Afr}(t) = E_m \cdot \sin\left(\omega \cdot t + \varphi_{st}\right)$ – the forced component, s equal to the e.m.f. of phase A, but with the initial phase that $e_A(t)$ has at the moment of arc extinction, in other words φ_{st};

$u_{Alb}(t) = u_N(t) = E_m \cdot e^{-\frac{\partial}{2}\cdot\omega\cdot t} \cdot \sin(\omega_{st} t + \varphi_{st})$.

The presence of ASC significantly reduces the speed of voltage restoration on the faulty phase, but it plays a positive role because it provides a longer time for deionizing the faulty location and reduces the probability of re-ignition of the electric arc.

2.3. Transients during a single-phase to ground fault in medium voltage networks with the neutral treated by ASC and resistor

Treating the neutral through the ASC in parallel with a resistor is called combined treatment. The processes that occur when grounding a phase in this case do not fundamentally differ from the case of treating the neutral only through ASC. This is because the presence of the resistor only changes the conductance between the neutral and the ground (Figure 8), which means that the relationships deduced for the case of treating the neutral through ASC alone are valid in this case as well, with the addition of the resistor's conductance (G_R) in the appropriate places.

In other words, the resistor will affect the attenuation coefficient:

$$\partial = \frac{3G_0 + G_{ASC} + G_R}{3\omega C_0}. \tag{42}$$

And, to a negligible extent, the frequency of free oscillations of the transient process:

$$\omega_{st} = \omega \cdot \left| \sqrt{\left(\frac{\partial}{2}\right)^2 - (1-\upsilon)} \right|. \tag{43}$$

The use of this neutral treatment scheme is relevant for overhead lines where there is an asymmetry in phase-to-ground capacitances. In such cases, tuning the ASC to resonance or with a small deviation from resonance leads to the neutral shift in normal operation. If the asymmetry is pronounced, a displacement voltage appears on the neutral that exceeds the permissible voltage of $0.15 \cdot U_{f.nom}$ [14, 15].

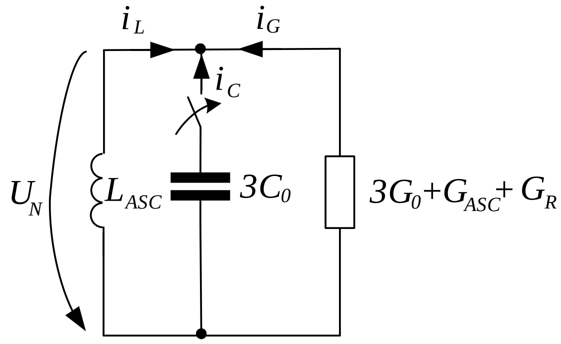

Figure 8. The simplified equivalent circuit of a medium-voltage network with the neutral treated by an ASC in parallel with a resistor.

To ensure this voltage, in some cases, it is necessary to detune the ASC by not less than 20% [16], which reduces the effectiveness of the ASC in both stabilized grounding operation and transient operation. An alternative solution to this problem is connecting a resistor in parallel with the ASC, which, when chosen correctly, allows tuning the ASC close to resonance while keeping the neutral voltage within the required limits.

In some studies, for example in [17], it is proposed to use the resistor in parallel with the ASC in all cases, even when the phase-to-ground capacitances are equal, with the aim of reducing overvoltages during grounding through electric arc. This is justified by the fact that installing the resistor is more economically convenient than installing ASC with automatic fine-tuning capability.

In this case, the value of the resistor must be chosen based on two conditions:

- to ensure that the neutral displacement voltage in normal operation does not exceed $0.15U_{f.nom}$;
- to limit overvoltages during single-phase fault with intermittent electric arc, in case of the maximum possible detuning of the ASC that may occur in practical operation.

Derived from the first condition, the value of the resistor will be chosen according to the condition:

$$U_N \leqslant 0.15U_{f.nom}. \tag{44}$$

The neutral voltage is determined using the relationship:

$$U_N \approx U_{N\ m.g.} \cdot q, \tag{45}$$

where: $U_{N\ m.g.}$ is the voltage that arises due to the asymmetry between the phase-to-ground capacitances of the network:

$$\begin{aligned}\underline{U}_{N\ m.g.} &= \frac{\underline{E}_A \cdot j\omega \cdot C_{0A} + \underline{E}_B \cdot j\omega \cdot C_{0B} + \underline{E}_C \cdot j\omega \cdot C_{0C}}{j\omega \cdot (C_{0A} + C_{0B} + C_{0C})} = \\ &= \frac{\underline{E}_A \cdot C_{0A} + \underline{E}_B \cdot C_{0B} + \underline{E}_C C_{0C}}{C_{0A} + C_{0B} + C_{0C}}.\end{aligned} \tag{46}$$

$q = \dfrac{X_{ASC}}{R_{ASC} + R_N} = \dfrac{B_{ASC}}{G_{ASC} + G_R}$ is the quality factor of the ASC, and it can reach high values: *q=20..200*.

Taking into consideration (44) and (45), we can write:

$$U_{N\ m.g.} \cdot q \le 0.15 U_{f.nom}. \tag{47}$$

Or:

$$U_{N\ m.g.} \cdot \frac{B_{ASC}}{G_{ASC} + G_R} \le 0.15 U_{f.nom}. \tag{48}$$

From (48), the conductance of the resistor can be determined:

$$G_R \ge \frac{U_{N\ m.g.} \cdot B_{ASC}}{0{,}15 U_{f.nom}} - G_{ASC}, \tag{49}$$

and the resistance of the resistor:

$$R_N = \frac{1}{G_R} \le \frac{0.15 \cdot U_{f.nom}}{U_{N\ m.g.} \cdot B_{ASC} - 0.15 U_{f.nom} \cdot G_{ASC}}. \tag{50}$$

3. Results and discussion

For the "Central 110/10 kV Substation Balți" state variables will be calculated in a stabilized state for single-phase-to-ground faults, considering the treatment of the neutral through ASC in parallel with a high-value resistor.

At the Substation two power transformers of ТДН-16000/110/11 type are installed, with the parameters: ΔPsc=85 kW, Usc=10.5% and the connection scheme Y0/Δ-11; Additionally, each bus section is connected to a transformer for creating an artificial neutral (TNA) of ТМПС-630/10.5/0.23 type with the parameters: ΔPsc=8.63 kW, Usc=5.5%, ΔP0=0.997 kW, I0%=0.49%, I1n=34.6 A and the connection scheme Y0/Δ-11; In the neutral of each TNA two ASCs are connected, of type: РЗДСОМ-380/10 and РЗДПОМ-480/10.

The calculated total capacitances are as follows: for section 1– C_{01}=13.34 μF; and for section 2 – C_{02}=13 μF, the grounding current is I_{pp} =73 A.

The calculation will be performed for section 1, feeder number 2. The feeder number 2 diagram and the grounding location are indicated in (Figure 9).

For the analyzed power station, the treatment of the neutral through the combined ASC with a high-value resistor is examined. Considering that the ASC operates in over-compensation mode (*k=1.1*), it follows that the capacitive current will not exceed 8 A.

From the catalog, a resistor with a resistance value of R_n=500 Ω is selected so that the current through it does not exceed 10 *A*.

The impedance of the resistor with a resistance value of $R_N = 500\ \Omega$:

$$\underline{Z}_N = \frac{\underline{Z}_{ASC} \cdot R_N}{\underline{Z}_{ASC} + R_N} = \frac{(1.033 + j76.426) \cdot 500}{(1.033 + j76.426) + 500} = 12.377 + j74.38\ \Omega.$$

According to the deduced expressions, the operating parameters are calculated for the variant with the neutral treated with ASC and the neutral combined with ASC in parallel with a high-value resistor. The obtained results are presented in Table 1.

The obtained results demonstrate that the combined treatment of the neutral using ASC in parallel with a 500 Ω resistor leads to a reduction in the neutral voltage (in normal operation) by approximately 3.5 times. This creates a more favorable operating condition for the network and allows integration within the limits of the neutral displacement voltage values specified by the current regulations [18] (p.542).

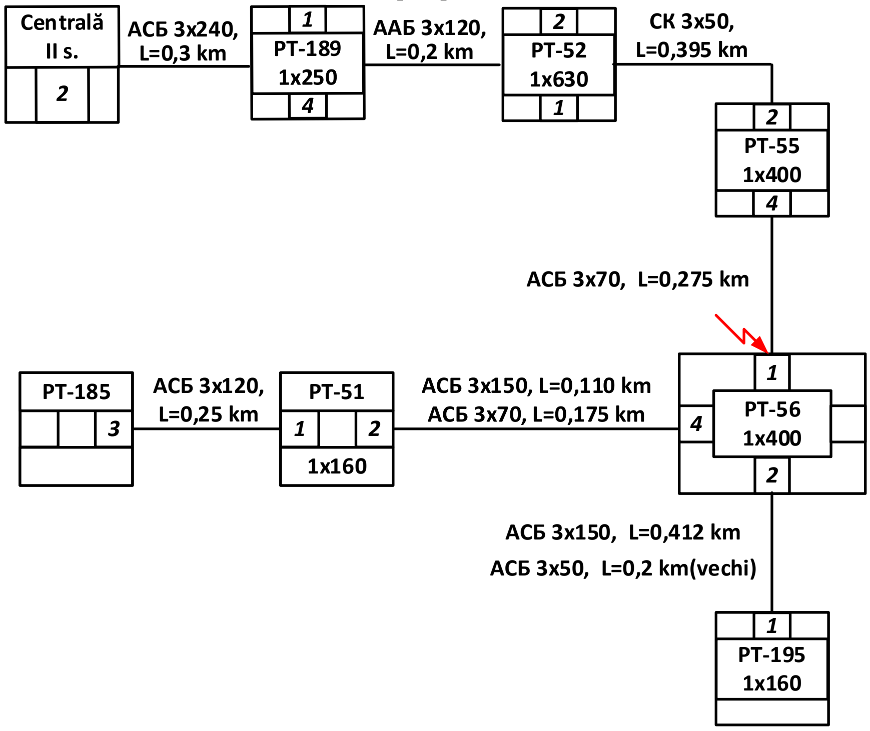

Figure 9. Structural diagram of feeder 2 at the „Central 110/10kV Substation Balti".

Table 1

The results of calculating the operating parameters

The treatment method	The neutral voltage in normal operating conditions with 5% asymmetry in phase-to-ground capacitances, U_N, V	The neutral voltage during single-phase fault condition, U_N, V	The fault current, I_{PP}, A
Neutral treated by ASC	$U_N = 1846\ V\ (32\%\ of\ U_f)$	$5.536 \cdot e^{-j178.88°}$	$2.424 \cdot e^{j4.5°}$
Neutral treated by ASC and a high-value resistor	$U_N = 526.5\ V\ (9\%\ of\ U_f)$	$5.771 \cdot e^{j179.92°}$	$13.04 \cdot ej^{1.45°}$

Based on numerous implementations and positive outcomes, the authors [9] recommend using the combined neutral treatment where this method exhibits maximum efficiency, specifically in extensive and physically worn cable networks, as well as in overhead or mixed networks. This includes cases where significant asymmetry in phase-to-ground capacitances is observed or when using ASC with stepped regulation.

5. Conclusions

In the Republic of Moldova, the 35 kV networks are exclusively overhead and, in the majority of cases, operate with isolated neutral and a certain degree of asymmetry. Therefore, it is considered necessary to transition these networks to compensated or combined neutral treatment regimes.

The 6-10 kV networks in the Republic of Moldova are primarily overhead and mixed, with an advanced degree of wear. Connecting a high-value resistor in parallel with ASC, during normal operation of the electrical network, will lead to a reduction in the neutral voltage caused by source voltage asymmetry and asymmetry in phase-to-ground capacitances.

In the case of combined neutral treatment, ASC and the resistor are connected in parallel. In this configuration, ASC will ensure the reduction of single-phase fault current, while the resistor will dampen overvoltages and oscillations caused by detuning of ASC. This solution will reduce the number of network disconnections and stabilize the single-phase-to-ground fault arc.

A promising method for the combined neutral treatment of 6-35 kV networks [9, 19] involves bypassing ASC with a low-voltage 500 V resistor, connected to its auxiliary winding through a normally open switch. This method allows for the combination of positive properties of both compensated and resistive neutral treatment.

Conflicts of Interest: The authors declare no conflict of interest.

References

1. Samoilenco, V.; Muhlinin, N.; Pazderin, A.; Juravliov, A. Perspektivnye tendentsii razvitiya raspredelitelinykh setey. *Electroenergia. Peredacia i raspredelenie* 2019, S1 (12) [in Russian].
2. IEA Publications International Energy Agency. Electricity Market Report 2023. Available online: https://iea.blob.core.windows.net/assets/255e9cba-da84-4681-8c1f-458ca1a3d9ca/ElectricityMarketReport2023.pdf (accessed on 02.04.2023).
3. IEEE Recommended Practice for Grounding of Industrial and Commercial Power Systems in IEEE Std 142-2007 (Revision of IEEE Std 142-1991), 2007, 225 p.
4. Nazarychev, A.; Titenkov, S.; Pugacheov, A. Kompleksnyye innovatsionnyye resheniya po zazemleniyu neytrali v setyakh 6-35 kV. Jurnal on-line: *Elektroenergiya. Peredacha i raspredeleniye* 2016, 3 (36), pp. 33-39 [in Russian].
5. Mironov., I. Vnedreniye rezhimov zazemleniya neytrali v setyakh srednego napryazheniya. *Elektroenergiya. Peredacha i raspredeleniye* 2016, 4(37), pp.132-137 [in Russian].
6. Gusarov, L. Sposoby zazemleniya neytrali istochnikov pitaniya v setyakh srednego napryazheniya, dostoinstva i nedostatki, realinaya praktika primeneniya v mire. Available online: https://electrik.info/article/1692-sposoby-zazemleniya-neytrali-istochnikov-pitaniya-v-setyah-srednego-napryazheniya.html (accessed on 2.04.2023) [in Russian].
7. Gusha, M. *High voltage technology*. Casa de Editură Venus, Iasi, Romania, 2005, 352 p. [in Romanian]
8. Rules of Electrical Installations Design (Russian Electrical Code). NTs ENAS, Moscow, 2004 [in Russian].
9. Shirkovets, A.; Kozlachkov, M.; Sazonov, V.; Khadyev, I.; Dmitriev, I.; Pankratov, G.; Timoshchenko, S.; Kombinirovannoye zazemleniye neytrali. Faktor povysheniya ekspluatatsionnoy nadezhnosti setey 6-35 kV. *Novosti ElectroTehniki* 2021, 2(128)-3(129) [in Russian].
10. Regulation regarding the quality of electricity transport and distribution services. DECISION No. 537 of December 24, 2020. Published: January 22, 2021. In: Official Monitor No. 13-20, article 47 [in Romanian].
11. Eremia, M. *Electric Power Systems*. Vol. I. Electric Networks, București, Romania, 2006, pp. 355-357.
12. STO 18-2013 Rukovodyashchie ukazaniya po vyboru rezhima zazemleniya neytrali v elektricheskikh setyakh napryazheniem 6-35 kV. Lenenergo, Sankt Petersburg, 2013 [in Russian].
13. Titenkov, S.; Pugachev, A. Rezhimy zazemleniya neytrali v setyakh 6–35 kV i organizatsiya releynoy zashchity ot odnofaznykh zamykaniy na zemlyu. *Energoekspert* 2010, 2, pp. 18-25 [in Russian].
14. Lurye, A.; Panibratets, A.; Zenova, V.; Elagin, V.; Bazylev, B. Seriya neytralerov tipa FMZO dlya raboty s upravlyaemymi podmagnichivaniyem dugogasyashchimi reaktorami serii RUOM v raspredelitel'nykh setyakh s izolirovannoy neytralyu. *Elektrotekhnika* 2003, 1, pp.153-164 [in Russian].
15. Evminov, L.; Alferova, T. Rezistivnoye zazemleniye neytrali v raspredelitel'nykh setyakh 6-35 kV. *Agrotekhnika i energoobespecheniye* 2019, 4 (25), pp. 94-109 [in Russian].
16. Vaynshteyn, R.; Kolomiets, N.; Shestakova, V. *Rezhimy zazemleniya neytrali v elektricheskikh sistemakh: uchebnoye posobiye*. TPU, Tomsk, 2006, 118 p. [in Russian].

17. Evdokunin, G. Analiz vnutrennikh perenapryazheniy v setyakh 6-10 kV i obosnovaniye neobkhodimosti perevoda setey v rezhim s rezistivnym zazemleniyem neytrali. In: Trudy Vserossiyskoy nauchno-tekhn. konferentsii *Ogranicheniye perenapryazheniy i rezhimy zazemleniya neytraley setey 6-35 kV*. NGTU, Novosibirsk, 2002, pp. 9-13 [in Russian].
18. Decision No. 393 of November 01, 2019, regarding the approval of the technical normative document in the energy field NE1-01:2019 "Operating Regulations for Electrical Installations of Non-Residential Consumers". In: Official Monitor, January 31, 2020, no. 24-34, article 90. [in Romanian].
19. Nazarychev, A.; Pugachev, A.; Titenkov S. Kombinirovannoye zazemleniye neytrali v setyakh 6-35 kV. Available online: http://news.elteh.ru/arh/2016/99/05.php (accessed on 02.04.2023).

Citation: Dobrea, I.; Stratan, I.; Rotaru, A. (2023) Opportunity of using a mixed neutral treatment solution in the distribution electrical networks of the Republic of Moldova. *Journal of Engineering Science* 2023, 30 (3), pp. 60-77. https://doi.org/10.52326/jes.utm.2023.30(3).05.

Submission of manuscripts: jes@meridian.utm.md

Journal of Engineering Science — *Vol. XXX, no. 3 (2023), pp. 78 - 98*
Fascicle — *Electronics and Computer Science* — *ISSN 2587-3474*
Topic — *Computers and Information Technology* — *eISSN 2587-3482*

https://doi.org/10.52326/jes.utm.2023.30(3).06
UDC 004.032.26:519.7

SIMULATION AND ANALYSIS OF SPIKING NEURAL MEMBRANE COMPUTING MODELS BASED ON REWRITING TIMED HYBRID PETRI NETS WITH ANTI-TOKENS

Victor Moraru*, ORCID: 0000-0002-5454-8341,
Alexei Sclifos, ORCID: 0000-0003-4531-7944,
Emilia Sclifos, ORCID:0000-0003-1986-7256,
Emilian Guțuleac, ORCID: 0000-0001-6839-514X

Technical University of Moldova, 168 Stefan cel Mare Blvd., Chisinau, Republic of Moldova
*Corresponding author: Victor Moraru, *victor.moraru@calc.utm.md*

Received: 07. 16. 2023
Accepted: 08. 12. 2023

Abstract. In this paper we present the rewriting timed hybrid Petri nets (RTHPNs) enhanched with positive and negative place capacity, guard functions for transitions and rewriting rules, marking-dependent cardinality reversible arcs and anti-tokens. The RTHPN model allows its structure and/or attributes to change at run-time depending on its current state and/or the occurrence of some events. Also, we describe an approach to simulation and formal verification behaviour properties of *spiking neural membrane computing* (SNMC) models using particular RTHPNs that is supported by upgraded VPNP Tool. The use of RTHPNs in simulation and analysis of an extended SNMC model is illustrated through examples proving that such approach preserves faithfully its behaviours.

Keywords: *analysis, anti-token, spiking neural membrane computing, model, rewriting rules, hybrid timed Petri nets, simulation and verification.*

Rezumat: În lucrare prezentăm rețelele Petri hibride temporizate cu rescriere (RTHPNs) care sunt îmbunătățite cu capacități pozitive și negative ale locațiilor, funcții de gardă ale tranzițiilor și cele ale regulilor de rescriere, cu arce reversibile de cardinalitate marcaj - dependente și anti-tokene. Modelul RTHPN permite ca structura și/sau atributele sale să se schimbe în timpul rulării în funcție de starea curentă și/sau de apariția unor evenimente. Descriem și o abordare de simulare și verificare formală a proprietăților comportamentale ale modelelor de calcul membranal neuronal spiking (SNMC) folosind RTHPNs particulare, care sunt susținute de VPNP Tool actualizat. Folosirea RTHPN în simularea și analiza unui model SNMC extins este ilustrată în baza unui exemplu care demonstrează că o astfel de abordare păstrează fidel comportamentele acestuia.

Cuvinte-cheie: *analiză, anti-token, calcul membranal neuronal spiking, model, reguli de rescriere, rețele Petri hibride temporizate, simulare și verificare.*

1. Introduction

Spiking neural P systems (SNPS) belong to the third generation of neuronal models. They were proposed and studied in [1] as a class of distributed and parallel computing models that include the idea of spiking neurons into P systems [2, 3].

Next, due to the space restrictions, we will give a summary overview to this topic and refer the reader to papers [4 - 9] and the references therein. We only note that in recent years several variants of SNPS, with Turing computable sets of natural numbers, have been proposed by combining methods and ideas from the fields of biological activities, mathematics and computer science, accumulating rich results in their theoretical research with various applications [6, 7]. SNPS have a well defined network-distributed structure, a powerful parallel computing ability, dynamic characteristics and non-determinism. These characteristics of SNPS allow them to be applied in solving many practical problems [6].

Although great progress has been made in the field of theoretical definition of the application of different SNPS kinds in recent years they still have some shortcomings in distributed data processing, but they can be improved. Thus, traditional SNPS only processes integer numbers of spikes as symbolic data, so it is exceedingly difficult to process a large amount of numerical information with real values.

In [10] a new extension of SNPS is proposed, called *spiking neural membrane computing* (SNMC) models that improve on current SNPS variants by enabling real data processing technology. The SNMC model contains the *input data unit*, the *threshold unit* and evolution *rules* with a nonlinear time delay production function that are real or integer values. Synapse weights connecting neurons in SNMC models can have positive or negative values, and they transmit *spikes* or *anti - spikes*. Also, the Turing universality of the SNMC model is proved. Since the SNMC model can extend the application when information has integer and/or real values and this approach has great possibilities to solve some practical problems, for exemple, that are mentioned in [7, 8, 10].

In SNPS and SNMC, the firing rules are selected non-deterministically, so that any applicable firing rule is selected with equal probability. However this assumption is quite unnatural in what consists their application in different conditions. For this purpose, by introducing probabilities of selection of evolution rules in neurons, we propose an extension of the SNMS model, called ESNMS, similar to the formal framework proposed for SNPS [11] by using stochastic features.

Any developer of P systems and SNPS models and computing applications, knows that the most important quality of a computing application is that it is functionally correct, i.e. that it exhibits certain behavioral or *qualitative* properties [7, 8]. Once assured that the system behaves correctly, it is also important to ensure that the system meets also certain performance-related (or *quantitative*) objectives. Therefore, it is necessary that through well-constructed SNPS, SNMC or ESNMC models of the developed computational applications, the behavioral properties can be checked and thus possible errors that may appear in the earlier phases of the system development can be detected and corrected, since such an approach allows the modeler to fix them easily and cheaply.

Various aspects of the representations and qualitative characteristics of P and SNPS systems have been extensively studied. However, the tools that support simulation and behavior properties verification of real aplications using such models are relatively limited [12-14]. Most of the known SNPS simulators are mainly text-based that have little or no visualization of the models and their calculations. Several authors have proposed some approaches to simulate different variants of P systems [15-18] through appropriate Petri net (PN) extensions to remedy the mentioned disadvantages and analyze some behavioral properties of these models. PNs model is a graphical and mathematical modeling tool which is used to specify, in clear manner, the behaviors of concurrent systems. Moreover, due to the similarity of the graphical structure, the translations of SNPS into models of PNs and analysis of their behavior features, are carried out in [18]. For example, in [18] a variant of SNPS with spikes and anti-spikes are studied. It describes a method to represent and simulate SNPS with anti-spikes using PNs. With a well-constructed PN model of the elaborated SNPS or SNMC, faults in the system can be detected and fixed at earlier stages of development. PN simulation is a suitable and simple but effective approach for the modeller to verify the desired behavioral properties of discrete event systems. A list of PN simulation tools along with feature descriptions can be found on the Petri Nets Tools Database website [19].

However, to the best of our knowledge, with these tools we cannot visually simulate and analyze the behavioral properties of SNMC models using real data and stochastic application of evolution rules. Moreover, with the already known extensions of timed hybrid PN (THPN) [20] or fluid stochastic PN (FSPN) [21] it is very difficult to map SNMC models and analyze them, because in THPN places with negative-positive capacities and negative marking - dependent cardinality are not allowed. Also, it is easy to confirm from experience that the developed THPN or FSPN models, which adequately describe the behavior of real systems, are often difficult to use in practice due to the problem of the rapid increase in their graphic size. Thus, with a steady increase in complexity and size of SNMC, their models also become larger and less comprehen-sible. Introducing modularity concepts into system specifications is a wide range of research because it makes large descriptions handling easier.

The challenging development of large SNMC applications can be eased through the usage of appropriate models to simulate, evaluate and validate them before hand. One well known method for this is the deployment of hierarchical PNs (THiPN) that provide a more abstract view. Also, especially challenging is the development of large SNMC models with dynamic components [8] that allow dynamic structural adaptation. To overcome this problem, it is necessary to improve the THPN formalism that compactly and flexibly describe extended SNMC models with the probabilistic selection of evolution rules (ESNMC, for short).

Practical methodologies in engineering and computer science take a structural approach, designing systems from smaller subsystems and components, which can be combined and reused. In this context, for efficient formalization and to deal with the implementation and formal correctness analysis of SNMC and ESNMC models, in this paper we define a new extension of THPN, called rewriting THPN with anti-tokens (in short, RTHPN) having guards for transitions and rewriting rules. This approach allows to build modular and hierarchical models, capable of describing cases in which the structure of the model and its attributes can run-time change depending on its current state and/or the occurrence of some events. The RTHPN is the improved and extended version of the rewriting GSPN that are enriched with reconfigurability [22, 23].

As far as we know, there is no work in the literature that treats the visual simulation and anaysis of ESNMC models using dynamic run-time reconfiguration of RTHPN models. In this paper, we describe an approach that we believe is suitable in terms of both expressiveness and analysis capabilities of ESNMC models using RTHPNs. The proposed RTHPN models are based on the maximality step firing semantics [16].

Also, we present a methodology that maps SNMC and ESNMC models similarly into RTHPN representations, which allows visual simulation and the study of the behavioural properties of such models dynamics via the upgraded VPNP Tool [24] in an easy-to-use manner. The practical motivation is to propose a novel way to deal with the analysis complexity in some real-world applications under the framework of SNMC and ESNMC models. In this context, a numerical example is presented and studied to demonstrate the applicability and utility of the proposed RTHPN approach for simulation and analysis of ESNMC models. For this purposes the flat THPN (with anti-tokens) nets representation of the hierarchical RTHPN net can be used.

The paper is organized as follows. In Section 2 we describe the definition, spike evolution rules and behavior of ESNPC models. Also, in Section 3 we introduce the dynamic RTHPN with anti-tokens that allow the run-time reconfiguration of the analyzed ESNPC models. Section 4 provides the simulation and analysis metodology of ESNMC models using RTHPN nets. The conclusions of this work and future research efforts are described in Section 6.

2. Extended Spiking Neural Membrane Computing Models

In this section, based on SNMC model that is proposed in [10], an extended SNMC model, called ESNMC model, is presented. The definition and behavior of ESNMC models are given below. Neurons contain extended evolution rules with stochastic application with *integer* and/or *real* input value and a threshold value. The transmission of data (spikes or anti-spikes) by neurons is carried out by timed firing rules and their respective synaptic connections.

It is assumed that the readers are familiar with formal language theory and the basics of Membrane Computing (a good introduction is [2] with recent results and information in the P systems webpage [3]).

Definition 1**.** From [10] an ESNMC model of degree $m \geq 1$, denoted $G\Pi$, is a construct expressed by a 6-tuple, $G\Pi = (O, \Sigma, W, \; Syn, in, out)$, where:

(1) $O = \{a, \bar{a}\}$ is the binary alphabet, that a is called *spike* and $\bar{a}$ is called *anti-spike* included in neurons.

(2) $\Sigma = \{\sigma_1, \sigma_2, \cdots, \sigma_m\}$ is the set of neurons, of the form $\sigma_i = (u_i, b_i, \; pf_i, R_i)$, where: (*i*) $u_i \in R_i$ is input data in σ_i; (*ii*) $b_i \in R_i$ is a threshold of σ_i; (c) pf_i is the *production function* that compute the total data value of σ_i. The total value is the weighted sum of all inputs of σ_i minus the threshold; (*iii*) $R_i = \{r_{i,k_r}\}$ is a finite set of evolution rules of σ_i, with the form $r_{i,k_r}: \; (q_{i,k_r})E / a^{pf(u_i - b_i)_\varepsilon} \rightarrow a^{s_i}; \tau_{i,k_r}, \tau'_{i,k_r}, \;\; s_i \in \{0, 1\}$, where: q_{i,k_r} is the application probability of evolution rule with $(\sum_{\forall k_r} q_{i,k_r}) = 1$; E is a regular expression over a or $\bar{a}$; and $\varepsilon = 0$ for integer values or $0 < \varepsilon < 0.5$ for real values of pf_i. The τ_{i,k_r} and τ'_{i,k_r} after the rule refers to time delay. The τ_{i,k_r} represent the time that neuron σ_i receive spikes from the $\sigma_l, l \neq i$, and τ'_{i,k_r} represents the rule execution time (from the execution of the production steps to the outputting step). If rule r_{i,k_r} is chosen non-deterministically, then it is not mentioned.

(3) $W = \{w_{i,j}, i \neq j\}$ is the weight on the synapse, which can be *positive* or *negative*. A *positive weight* generate *spikes*, and a *negative weight* generate *anti-spikes*.

(4) $Syn \subseteq \{1, 2, \cdots, m\} \times \{1, 2, \cdots, m\} \times W$ is the set of synapses.

(5) in and out are the input neuron and the output neuron, respectively. The input neuron converts the input data into spikes containing integer values or real values. The output neuron outputs the input data as a binary string composed of 0 *spikes* and 1 *spikes*.

A $G\Pi$ is pictorially described as a directed graph without self-loop, where the nodes of graph are represented by neurons, and the arcs indicate the synapses among the neurons, as shown in Figure 1. It also indicates the relationship between neurons. The set of arcs (synapses) entering in the neuron σ_i is denoted as $^{\bullet}\sigma_i$ and those that come out of σ_i are denoted as $\sigma_i^{\bullet}$.

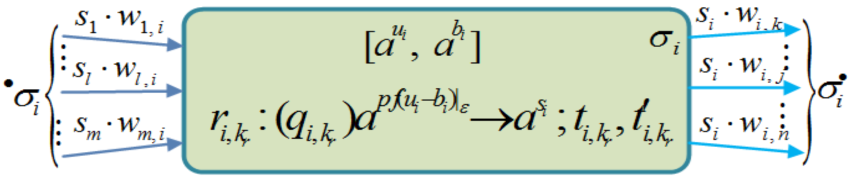

Figure 1. The neuronal structure of a neuron σ_i of $G\Pi$ model (Adapted from [10]).

Next, we explain the behavior of SNMC model. If threshold is 0, this means no threshold in neurons. The input data u_i of a neuron σ_i is the *original* data α_i plus *linking input* data $\sum_{\forall^{\bullet}\sigma_i}(s_l \cdot w_{l,i})$, namely $u_i = \alpha_i + \sum_{\forall \sigma_l}(s_l \cdot w_{l,i})$. The linking input data comes from the connected neurons, and the original data are that the σ_i itself already exists. For example, the real value 2.5 is shown as $a^{2.5}$ that represent as 2.5 spikes in a σ_i and $a^{-2.5}$ denot 2.5 spikes with a negative charge in the neuron, i.e. 2.5$\bar{a}$. In each σ_i, an anti-spike can *immediately annihilate* one spike.

The $G\Pi$ model is *synchronized* by a global clock and works in a locally sequential at the level of each neuron and globally in maximal manner at whole $G\Pi$ model. In each σ_i, at firing step, if there is more than one rule enabled, then only one of them (chosen non-deterministically) can fire. At each step, the neurons of $G\Pi$ evolves in parallel and in a synchronising way, as all the neurons chooses an enabled rule and all of them fire at once.

The rules $R_i = \{r_{i,k_r}\}$ are processed as given below. So, the rule r_{i,k_r} contains two parts, including the *production function*, denoted pf_i, and the outputting of s_i. The pf_i is used to calculate $pf_i = u_i - b_i$, which will cause the state change of neuron σ_i. In addition, the neuron has a critical value, which is set to ε. Therefore, the execution steps of rules are divided into three steps: [10].

(1) *Production step*. When neuron σ_i receives weighted spikes s_l with data value $\sum_{\forall \sigma_l}(s_l \cdot w_{l,i})$ from connected $\sigma_l \in {}^{\bullet}\sigma_i$ neurons with σ_i at time τ_{i,k_r}, that represents the firing rule time τ_{i,k_r}. In σ_i is calculate the $pf_i = u_i - b_i$, where the $u_i = \alpha_i + \sum_{\forall \sigma_l}(s_l \cdot w_{l,i})$, α_i is the *original* data and b_i is the unchanged threshold value. Before a delay of t_{i,k_r} times, the σ_i is in a closed state.

(2) *Comparison step*. The result $pf_i = u_i - b_i$ is compared with the critical value ε, denoted $(u_i - b_i)|_\varepsilon$. It determines whether the output s_i of σ_i in the next step is 1 or 0.

(3) *Outputting step*. If $pf_i > \varepsilon$ then $s_i = 1$ and the rule r_{i,k_r} can be applied to output a spike with the value of 1. If it has $pf_i \le \varepsilon$, then $s_i = 0$ and the rule $(q_{i,k_r})E / a^{pf(u_i - b_i)_\varepsilon} \rightarrow \lambda; \tau_{i,k_r}, \tau'_{i,k_r}$ fires. Therefore, no spike can be sent by σ_i to the connected neurons with $\sigma_i^{\bullet}$. If r_{i,k_r} fire, the value unit u_i in σ_i is *consumed* (i. e. it is reset to 0) and the b_i is *unchanged*. The firing of r_{i,k_r} requires the following conditions: (1) Assume the number of spikes contained in neuron σ_i is γ, and a^{γ} belongs to the language set

represented by the regular expression E, and the current number of γ in σ_i is greater than or equal to the number of spikes consumed, u_i, i.e., $\gamma \geq u_i$. (2) The σ_i can only be activated when it receives the signal sent by the connected neurons $^{\bullet}\sigma_i$.

We mention that it can be shown that SNP systems are a particular case of the $G\Pi$.

As already shown, the neurons in an $G\Pi$ fire in parallel, that each neuron uses only one rule in each time unit τ. The current number of spikes (anti-spikes) present in each neuron of $G\Pi$ at that time is represented by the configuration, denoted as $C_k(\tau) = (u_1(\tau), u_2(\tau), \ldots, u_m(\tau))$. The initial configuration is denoted as $C_0(0) = (u_1(0), u_2(0), \ldots, u_m(0))$. Current $C_k(\tau)$ is changed by the locally sequential and globally maximal application of enabled rules. Such a step is called transition. The transition from $C_k(\tau)$ at time τ to the other $C'_k(\tau+1)$ configuration at time $\tau+1$ is denoted as $C_k(\tau)[\vartheta_\tau > C'_k(\tau+1)$, where $\vartheta_\tau \subseteq R$ is a set of executed enabled rules at time step τ. When the calculation reaches a certain configuration and there is no rule that can be activated, then the calculation stops, and this *halting configuration* is denoted as $C_h(\tau_H)$. The computational process of the $G\Pi$ can be regarded as a transition of a series of configurations, which is ordered and finite, i.e., from the initial configuration C_0 to $C_k(\tau)$.

Example of analysis of a $G\Pi$ model. Next, for the reader to better understand this approach, we will illustrate some definitions and behavior of $G\Pi$ models with an ESNMC model $G\Pi1$ represented in Figure 2 that is modified from [10]. The $G\Pi1$ has 5 neurons, denoted by σ_1, σ_2, σ_3, σ_4 and σ_5 that being the output one. The neurons are represented by nodes of a directed graph whose arcs represent the synapses; an arc also exits from the output neuron, pointing to the environment. In each neuron σ_i are specified the rules R_i, the threshold b_i and the u_i spikes present in the initial configuration $C_0(0)$.

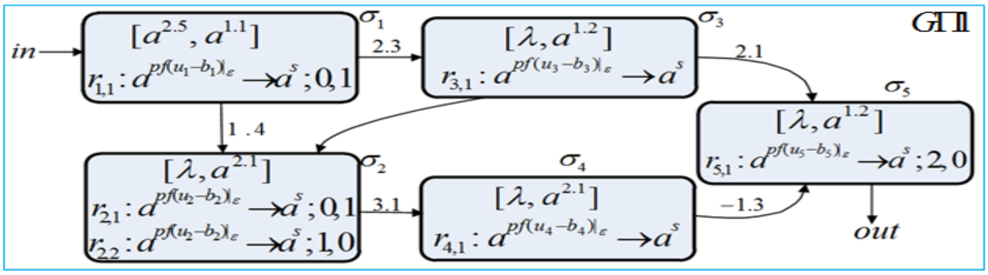

Figure 2. An ESNMC model $G\Pi1$ (Adapted from [10]).

The $G\Pi1$ model works as follows. σ_1 contains a real input value $u_1 = 2.5$ spikes and a threshold value $b_1 = 1.1$, and it exists in the neuron in the form $[a^{2.5}, a^{1.1}]$. Let $\varepsilon = 0.1$ and time steps are denoted by $\tau_k = k, k > 0$ units of time. At time τ_1, neuron σ_1 fires so $pf_1 = (2.5 - 1.1) = 1.4 > \varepsilon$, and a spike $s_1 = 1$ is generated at time τ_2. Thus, σ_2 and σ_3 respectively receives together 1.4 spikes and 2.3 spikes from σ_1. At time τ_3, σ_3 generates $s_3 = 1$ because $pf_2 > \varepsilon$. Since, σ_2 contains two rules, of which one is selected for execution non – deterministically. Therefore, two cases can occur depending on the choice of rule in σ_2:

- If the $r_{2,1}$ is used, σ_2 receives a 1.4 spike from σ_1 at time τ_2, and at time τ_3 we get $pf_{2,1} = (1.4 - 2.1) < \varepsilon$. So, at time τ_4, σ_2 generate $s_2 = 0$. At the same time, σ_2 receives 1 spike from σ_3 and the $r_{2,2}$ is used. Since it's $pf_{2,2} < \varepsilon$, and σ_2 does not send a spike to σ_4. So the σ_4 has produces empty spikes at time τ_5, and σ_5 receives 2.1 spikes from σ_3. At time τ_6, its rule in σ_5 fires and $pf_5 = (2.1-1) > \varepsilon$, so it produces $s_5 = 1$, and sends it out at the same time.

- If the $r_{2,2}$ is used then σ_2 is in the closed state before time τ_3 and does not receive any spikes. At time τ_3, the $pf_3 > \varepsilon$ produces spikes to send to neurons σ_2 and σ_5. Thus, at time τ_3, σ_2 receives 2.4 spikes: 1.4 from σ_1 and 1 from σ_3. At time τ_4, in σ_2 we get $pf_2 = (2.4-2.1) > \varepsilon$, it has $s_2 = 1$, and σ_2 produces $s_2 = 1$ and sends it to σ_4 then receives 3.1 spikes, and at time τ_5 its $pf_4 = (3.1-2.1) > \varepsilon$, so $s_4 = 1$. Hereupon, σ_5 receives 2.1 spikes from σ_3 and 1.3 anti - spikes from σ_4, so σ_5 contains $u_5 = (2.1-1.3) = 0.8$ spikes. In this way, at time τ_6 $s_5 = 1$ and no sent out because $pf_5 = (0.8-1.2) < \varepsilon$.

The behaviour of the $G\Pi1$ model can be analyzed based on a transition labelled directed graph of reachable configurations $C_i(\tau_k) = (u_1(\tau_k), u_2(\tau_k), \ldots, u_5(u_2(\tau_k))$ from the initial configuration C_0 that display the changes of spikes (anti - spikes) numbers $u_1(\tau_k)$ in σ_i at each time step τ_k by application of activated and executed set rules ϑ_{τ_k} in firing step.

Next, to deal with the visual simulation and formal correctness verification of ESNMC models $G\Pi$, we introduce a new extension of THPN, called Rewriting THPN (RTHPN), with negative place capacity; marking-dependent cardinality reversible arcs and the ability to dynamically in run-time reconfigure its structure and/or attributes.

3. Rewriting Timed Hybrid Petri Net with Anti-tokens

The definition of a RTHPN is derived according to [23, 25, 26] and inherits most of the HTPN [21], FSPN [22] and GSPN [23] characteristics. We assume that the readers are familiar with the basic concepts of these types of PN extensions. A more detailed theoretical description of these topics is beyond the scope of this article.

As already mentioned, this enhancement allows the compact modeling of high complexity SNPS and ESNMC models through RTHPN, without the risk of having a very complicated graphical size HTPN model, too difficult to represent and to understand.

Let IZ and IR be the sets of discrete and real numbers, respectively.

Definition 2. A Rewriting Timed Hybrid Petri Net (in short, RTHPN), denoted $RH\Gamma$, is a 16-tuple $RH\Gamma$ =<*P*, *E*, *Pre*, *Post*, *Test*, *Inh*, *K*$_p$, *K*$_b$, *Pri*, *G*^{E}, *G*^{R}, τ, ω, *V*, M_0, *Lib* >, where:

- *P* is the finite set of places partitioned into a set $P_d = \{p_1, \cdots, p_{n_d}\}$, $n_d = |P_d|$ of discrete places and a set $P_c = \{b_1, \cdots, b_{n_c}\}$, $n_c = |P_c|$ of continuous places (buffers), where $P = P_d \cup P_c$, $P_d \cap P_c = \varnothing$. The discrete places may contain a natural number of tokens, while the marking of a continuous place is a real number (fluid level). In the graphical representation, a discrete place is drawn as a single circle while a continuous place is drawn with two concentric circles;
- $E = T \cup \rho$ is a finite set of events, $T \cap \rho = \varnothing$, $P \cap E = \varnothing$, where T is a finite set of transitions and ρ is a finite set of discrete rewriting rules about the run-time structural and attributes change of $RH\Gamma$. The set E is partitioned into $E = E_0 \cup E_\tau$, $E_0 \cap E_\tau = \varnothing$ so that: E_τ is a set of timed events and E_0 is a set of immediate events. Likewise, E can be partitioned into a set $E_d = \{e_1, \cdots, e_{k_d}\}$, $k_d = |E_d|$ of discrete events and a set $E_c = T_c = \{u_1, \cdots, u_{k_c}\}$, $k_c = |E_c|$ of continuous transitions, where $T = T_d \cup T_c$, $T_d \cap T_c = \varnothing$. A transition $t_j \in T_d$ is drawn as a black

bar; a continuous transition $u_l \in T_c$ is drawn as an empty rectangle and rewriting rule $\hat{r}_k \in \rho$ is drawn as two embedded empty rectangles.

- *Pre*, *Test* and $Inh: P \times T \to Bag(P)$ respectively, are forward flow, test and inhibition functions with marking-dependent cardinality. *Pre* is the forward incidence function, *Test* is the promoter function and *Inh* is the inhibition function of transitions. $Bag(P)$ are discrete or real-valued multisets functions over *P* [20-22]. The backward flow function in the multisets of is $Post: T \times P \to Bag(P)$. These functions determine a mapping of the set of arcs A_{rcs} into set IZ of integer numbers (negative/positive) and set IR of real numbers which determines the marking-dependent cardinality of the arcs connecting the places (events) with the respective events (places). Also, the A_{rcs} set is partitioned into subsets:

$$A_{rcs} = A_d \cup A_h \cup A_t \cup A_c \cup A_s,\ A_d \cap A_h \cap A_t \cap A_c \cap A_s = \varnothing .$$

The subset A_d and A_s contains respectively the *discrete normal* and *continuous normal* set of arcs which can be seen as a function:

$A_d : ((P_d \times E) \cup (E \times P_d)) \times Bag(P) \to IZ$, and $A_s : ((P_c \times E) \cup (E \times P_c)) \times Bag(P) \to IR$.

The subsets of arcs A_d and A_s, are drawn as single arrows. The subset of discrete *inhibitory* and *test* arcs is $A_h, A_t : (P_d \times E) \times Bag(P) \to IZ$ or that of *continuous inhibitory* and *test* arcs is $A_h, A_t : (P_d \times E) \times Bag(P) \to IR$. These arcs are directed from a place to any kind event. The *inhibitory* arcs are drawn with a small circle at the end and *test* arcs are drawn as dotted single arrows. It does not consume the content of the source place. The subset A_c defines the *continuous flow* arcs $A_c : ((P_c \times T_c) \cup (T_c \times P_c)) \times Bag(P) \to IR$, and these arcs are drawn as double arrows to suggest a pipe. The arc of a net is drawn if the cardinality is not zero and it is labeled to the arc with a default value being 1;

- $K_p : P_d \to IZ$ is the capacity-function of discrete places and for each $p_i \in P_d$ this is represented by minimum capacity $K_{p_i}^{\min}$ and the maximum capacity $K_{p_i}^{\max}$, so that $-\infty < K_{p_i}^{\min} < K_{p_i}^{\max} < +\infty$, which can contain a discrete number of *tokens* (*anti - tokens*). By default, the $K_{p_i}^{\min} = 0$ and $K_{p_i}^{\max} \to +\infty$, and in this case no blocking effect occurs;
- $K_b : P_C \to IR$ is the capacity-function of continuous places and for each $b_i \in P_c$ it describes the fluid lower bounds $x_i^{\min}$ and upper bounds $x_i^{\max}$ of the fluid, so that $-\infty < x_i^{\min} < x_i^{\max} < +\infty$. By default, $x_i^{\min} = 0$ and $x_i^{\max} \to +\infty$, and in this case no blocking effect occurs;
- *Pri*: $E \times Bag(P) \to IN_+$ defines the dynamic marking-dependent priority function for the *firing* of each *enabled event*, noted $e \in E(M)$. The firing of an enabled event with higher priority potentially disables all event $e \in E(M)$ with the lower priority;
- $G^E : E \times IN_+^{|P|} \to \{True, False\}$ is the set of *guard functions* associated with all event $e \in E$ and $G^R : \rho \times IN_+^{|P|} \to \{True, False\}$ is the set of *guard functions* associated with all *rewriting rule* $\hat{r} \in \rho$. For an $e \in E$ a guard function $g(e, M)$ will be evaluated in each current marking M, and if it evaluates to *True*, then event e may be enabled, otherwise e is disabled (by default it is *True*);
- $\tau : E_d \times Bag(p) \to IR^+$ is the firing delay time of respective discrete event $e_j \in E_d$, wherein the set E_d is partitioned into two subsets $E_d = E_0 \cup E_\tau$, $E_0 \cap E_\tau = \varnothing$, where E_0 is a set of *immediate* discrete events and E_τ is a set of *timed* discrete events, so that $\forall t_j \in T_0$ and

$\forall t_k \in T_\tau$, *Pri*(t_j)>*Pri*(t_k). The immediate transitions are drawn as black thin bars and have a zero firing delay time, i.e. for $t_j \in T_0$ the $\tau_j = 0$. The timed transitions are drawn as black rectangles and have a nonzero firing delay time, i.e. for $t_k \in T_\tau$ the $\tau_k > 0$;

- $\omega : T_0 \times Bag(P) \to IR^+$ is the weight function of immediate discrete transitions $t_k \in T_0$. If an immediate transition $t \in T_0(M)$ is enabled in current (a vanishing) marking *M*, it fires with the following probability:

$$q(t, M) = \omega(t, M) / \sum_{t' \in T_0(M)} \omega(t', M);$$

- $V : T_c \times Bag(P) \to IR$ is the marking-dependent fluid rate function of timed continuous transitions $u_j \in T_c$. If u_j is enabled in *tangible* marking M it fires with rate $v_j(M)$, so that it continuously changes the fluid level of continuous places $\{b_k\} \in u_j^\bullet$.
- $M_0 =$ is the initial marking of $RH\Gamma$ net. The current marking (state) value of a $RH\Gamma$ net depends on the kind of place, and it is described by two vector-columns *M*=(***m***; ***x***), where ***m***: $P_d \to IZ$ and ***x***: $P_c \to IR$ are the marking functions of respective type of places. The discrete marking ***m*** $=(m_i, K_{p_i}^{\min} \le m_i \le K_{p_i}^{\max}, \quad \forall p_i \in P_d)$ with $m_i = \boldsymbol{m}(p_i)$ that describe the number of *tokens* in discrete place p_i, is represented by black dots (also allowed to take *negative* value, called *anti - tokens*). The marking ***x***= $(x_k, x_k^{\min} \le x_k \le x_k^{\max}, \forall b_k \in P_c)$ with x_k, which describes the fluid level in buffers b_k is a real number (real token), or *negative* real value (*anti - token*). The initial marking of net is $M_0 = (\boldsymbol{m}_0; \boldsymbol{x}_0)$. Vectors $\boldsymbol{m}_0$ and $\boldsymbol{x}_0$ give the marking of discrete places and of buffers, respectively.
- Lib is the set of $RH\Gamma_\kappa, \ \kappa = 1, 2 \cdots, n_\kappa$ subnet templates library involved in structural reconfiguration of the current $RH\Gamma$ by firing of enabled rewriting rules $\hat{r} \in \rho$.

Figure 3 shows the graphical representation of all $RH\Gamma$ primitives.

The role of the previous set of arcs and functions will be clarified by providing the enabling and firing rules. Let us denote by m_i the *i*-th component of the vector ***m***, i.e., the number of tokens (anti – tokens) in discrete place p_i when the marking is ***m***, (and x_k denote the *k*-th component of the vector ***x***, i.e. the fluid level in buffers b_k).

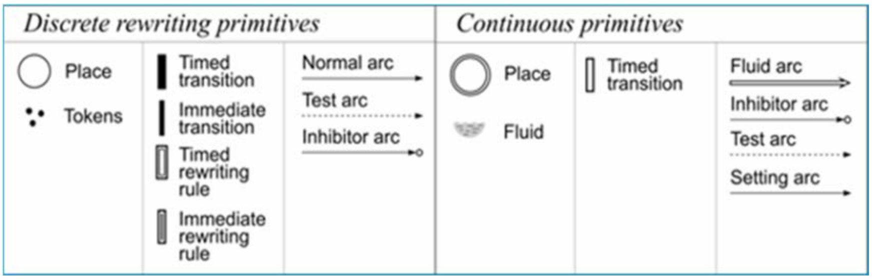

Figure 3. All primitives of a $RH\Gamma$ models.

Figure 4 shows the possible connections between discrete places and buffers with a discrete (resp. continuous) events through different types of arcs.

Enabling and firing rules of events. To define the $RH\Gamma$ enabling and firing rules, we introduce the following notations:

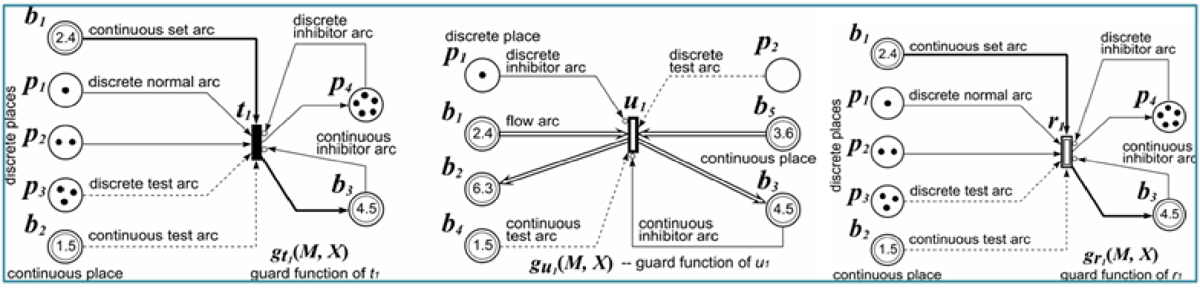

Figure 4. The posible connections between places with events through different types of arcs.

- $^{\bullet}e_j = \{p_i \in P / \mathrm{Pr}e(p_i, e_j) > 0\}$ the input set and $e_j^{\bullet} = \{p_i \in P / Post(e_j, p_i) > 0\}$ the output set places of event e_j, and with $^{\circ}e_j = \{p_i \in P / Inh(p_i, e_j) > 0\}$ the *inhibition* and $^{*}e_j = \{p_i \in P / Test(p_i, e_j) > 0\}$ are the *test* set places of transition t_j, respectively;
- *If* $(\mathrm{Pr}e(p_i, e_j) < 0)$ *then* $I_{j,i}^{-} = \mathrm{Pr}e(p_i, e_j)$; *If* $(\mathrm{Post}(e_j, p_i) < 0)$ *then* $O_{j,i}^{-} = \mathrm{Post}(e_j, p_i)$;
- *If* $(Inh(p_i, e_j) < 0)$ *then* $In_{j,i}^{-} = Inh(p_i, e_j)$; *If* $(Test(p_i, e_j) < 0)$ *then* $Ts_{j,i}^{-} = Test(p_i, e_j)$.

Also, we denote by $u_k \in T_c$ the continuous transitions and by $b_k \in P_c$ the buffers that can be distinct between discrete transitions and discrete places, respectively.

Let $E(M) = T(M) \cup \rho(M),\ T(M) \cap \rho(M) = \varnothing$ the set of *enabled events in current marking* M.

We say that an event $e_j \in E(M)$ is enabled in current marking M if the following logic expression (enabling condition $ec_j(M)$) is verified:

Definition 3. (*Enabling rule of events*) We say that an event e_j is enabled in current marking M, denoted $M[e_j >$, if the following *logic expression* $ec_j(M)$ is verified:

$$ec_j(M) = ec_j^{\mathrm{Pr}e}(M) \wedge ec_j^{Post}(M) \wedge ec_j^{Inh}(M) \wedge ec_j^{Test}(M) \wedge g_j(M),\ \text{where:}$$

- $ec_j^{\mathrm{Pr}e}(M) = \bigwedge_{\forall p_i \in {}^{\bullet}e_j} ((M(p_i^e) \geq \mathrm{Pre}(p_i, e_j)) \wedge ((K_{p_i}^{\max} - M(p_i)) \geq -I_{j,i}^{-}))$ is the *enabling condition* relative to the normal arcs input, that are incident to e_j and to the capacities of the places $p_i \in {}^{\bullet}e_j$, and $M(p_i^e) = M(p_i) - K_{p_i}^{\min}$ is the effective number (discrete or real) of tokens in p_i;
- $ec_j^{Post}(M) = \bigwedge_{\forall p_i \in e_j^{\bullet}} ((M(p_i^e) \geq Post(e_j, p_i)) \wedge ((K_{p_i}^{\max} - M(p_i)) \geq -O_{j,i}^{-}))$ is the *enabling condition* relative to output normal arcs, that link these incident places to the transition e_j and to the place capacities of $p_i \in e_j^{\bullet}$;
- $ec_j^{Inh}(M) = \bigwedge_{\forall p_i \in {}^{\circ}e_j} ((M(p_i^e) < Inh(p_i, e_j)) \wedge (-M(p_i^e) < In_{j,i}^{-}))$ is the *enabling condition* relative to *inhibitory arcs*;
- $ec_j^{Test}(M) = \bigwedge_{\forall p_i \in {}^{*}e_j} ((M(p_i^e) \geq Test(p_i, e)) \wedge (M(p_i^e) \geq -Ts_{j,i}^{-}))$ is the *enabling condition* relative to inhibitory *test arcs*.

Also, we note *by* $E_d(M) = T_d(M) \cup \rho(M), T(M) \cap \rho(M) = \varnothing$ the set of enabled discrete events in a current marking *M*, where $T_d(M)$ and $\rho(M)$ are the sets of enabled discrete transitions and enabled rewriting rules, respectively.

In $RH\Gamma$ models, concurrency of enabled events is also represented in a natural way. Two or more enabled events are concurrent at a given marking M if they can be fired at the same time, i.e. simultaneously. Every event enabled by a current marking M can fire but is never forced to fire if they are in conflict. Conflict occurs between events that are enabled by the same marking, where the firing of one event disables the other. In this case, it is necessary to define how and when a certain conflict should be resolved, which leads to non-determinism of its behavior.

Firing rules of enabled events. Let ${}^{A}W = \{{}^{\bullet}W,\ W^{\bullet},\ {}^{\circ}W\}$ be the weights of the respective type arcs in A_{rcs} and $E_d \subset E$ is the set of discrete events. We note $Atr_{\Gamma} = \{{}^{A}W,\ K_p, K_b, Pri, G^E, G^R, \tau, \omega, V\}$ the set of *quantitative attributes* of the currently activated (sub)nets type $RH\Gamma$. Also, let $RN = <\Gamma, M>$ be the current configuration of $RH\Gamma$, where $\Gamma = RH\Gamma \setminus M$ and M is the current marking of $RH\Gamma$.

A dynamic reconfiguration of current *RN* by the firing of enabled $\widehat{r} \in \rho$ is a map $\widehat{r} : \{RHL, Atr_L\} \triangleright \{RHR, Atr_R\}$, where $\{RHL \in Lib_{RN},\ Atr_L \in Lib_{Atr}\}$ is the *left-hand side* and $\{RHR \in Lib_{RN},\ Atr_R \in Lib_{Atr}\}$ is the *right-hand side* of the *rewriting operator* $\triangleright$ assigned to rewriting rule $\widehat{r}$, respectively. The $\triangleright$ represents a *binary rewriting operation* which produces a *structural change* and/or *change of attributes* in *RN* by replacing (rewriting) the fixed current subnet $\{RHL, Atr_L\} \subseteq RN$, RHL are dissolved (with $P_L \subseteq P$, $E_L \subseteq E_d$ and subset of arcs $A_L \subseteq A$ and/or Atr_L are deleted) and in run-time, a new $\{RHR, Atr_R\}$ subnet (with $P_w \subseteq P$, $E_w \subseteq E_d$ and set of arcs A_w and/or Atr_R are added) belong to the new modified resulting underlying net $RN' = (RN \setminus RHL) \cup RHR$ with $P' = (P \setminus P_L) \cup P_w$ and $E' = (E_d \setminus E_L) \cup E_w$, $A' = (A - A_L) + A_w$ where the meaning of \ (and $\cup$) is operation of removing (adding) RHL from (RHR to) current *RN*. In this new RN' net, obtained by the firing of $\widehat{r} \in \rho(M)$, the same elements (places, events and arcs with respective specified attributes) belonging to RN' are respectively *merged* [24]. For example, when merging the same place $y \in P$ from two different RN_i and RN_j subnets with the respective current marking $m(y) = n_i$ and $m(y) = n_j$ in this place, the resulting number of tokens (anti-tokens) in this place will add up: $m(y) = (n_i + n_j)$.

The current *tangible state configuration* of a RN net is $\gamma_{\tau} = (\Gamma, M)$, i.e. the current structure configuration of the Γ net together with a current marking *M* at time τ. Also, the *tangible* $\gamma_0 = (\Gamma_0, M_0)$ is the initial configuration of analyzed $RH\Gamma$.

Firing rule of enabled discrete events. An enabled event $e_j \in E_d(M)$ fires if *no other event* $e_k \in E_d(M)$ with higher priority has been enabled. Hence, for each $e_j \in E_d(M)$ ***if*** $((e_j = t_j) \vee (e_j = \rho_j) \wedge (g^R(\widehat{r}_j, M) := "False"))$ ***then*** (the firing of $t_j \in T_d(M)$ or firing of $\rho_j \in \rho(M)$ changes only the current marking of *RN*: $((\Gamma, M)[e_j > (\Gamma, M')) \Leftrightarrow (\Gamma = \Gamma$ and $M[e_j > M'$ in Γ)), where $M' = M - \mathrm{Pre}(\vartheta, \cdot) + Post(\vartheta, \cdot)$. The vectors $\mathrm{Pre}(\vartheta, \cdot)$ and $Post(\vartheta, \cdot)$ are the functions induced by those respective Pre and $Post$ incidence matrices of the $RH\Gamma$ [21-24]. Also, for every $e_j \in E_d(M)$, ***if*** $((e_j = \rho_j) \wedge (g^R(\rho_j, M) := "True"))$ ***then*** the event e_j occurs at firing of the rewriting rule $\rho_j \in \rho(M)$ and it changes the configuration $\gamma_{\tau} = (\Gamma, M)$ and marking of the current *RN* net, so that: $((\Gamma, M)[\rho_j > (\Gamma, M')) \Leftrightarrow (\Gamma = \Gamma'$ and $M[\rho_j > M'$ in Γ'), i. e. $\gamma_{\tau'} = (\Gamma', M')$.

The firing of an *immediate* discrete event $e_j \in E_d(M)$ enabled in marking $M = (\boldsymbol{m}, \boldsymbol{x})$ yields a new *vanishing marking* $M' = (\boldsymbol{m}', \boldsymbol{x})$. We can write $(\boldsymbol{m}, \boldsymbol{x})\ [e_j > (\boldsymbol{m}, \boldsymbol{x}')$. If the marking *M* = $(\boldsymbol{m}, \boldsymbol{x})$ is *tangible*, the fluid could continuously flow through the flow arcs A_c of enabled continuous transitions into or out of continuous places (buffers) $b \in P_c$. As a consequence, a continuous transition $u \in T_c$ is *enabled* at current marking M if for every buffer, fluid level increases or decreases, and its *enabling degree* is: $enab(u, M) = \min_{b \in {}^\bullet u}$ {$\boldsymbol{x}(b)/Pre(u, b)$} [21]. The reachability state graph (in short, $RG_{RH\Gamma}$) of configurations $\gamma_\tau = (\Gamma, M)$ from initial configuration $\gamma_0 = <\Gamma_0, M_0>$ is the *labeled directed graph* whose nodes are the states γ_τ and whose arcs, which are labeled with fired events $\theta_\tau \in E_d(M)$ of RN , are of two kinds:

(*i*) $(R\Gamma, M)[e_j > (R\Gamma, M')$ if $((e_j = t_j) \vee (e_j = \hat{r}_j)) \wedge (g^R(\rho_j, M) := "False");$

(*ii*) $(R\Gamma, M)[\rho_j > (R\Gamma', M')$ if $(e_j = \rho_j) \wedge (g^R(\rho_j, M) := "True").$

This enhancement allows the compact representation of high complexity analyzed ESNMC models, without the risk of having a very complicated and too difficult to understand graphical presentation through RTHPN model. Also, $RH\Gamma$ model supports a definition of a modular and hierarchical design methodology.

We note the fact that in any configuration $\gamma_\tau = (\Gamma, M)$, *tokens and anti-tokens cannot coexist* in the same place of $RH\Gamma$, they will *immediately annihilate* each other, so the neurons always contain either only spikes or anti-spikes. The annihilation is possible in each marking M with $m_i = M(p_i) > 0$, (resp. $x_i = M(b_i) > 0$)), *tokens* and $a_i = M(p_i) < 0$, (resp. $y_i = M(b_i) < 0$), *anti-tokens*, in the same place. This mutual annihilation of spikes and anti-spikes takes no time. This action produces a *vanishing state* that immediately changes the couple (m_i, a_i), (resp. (x_i, y_i)). More precisely, both m_i and a_i, (respective x_i and y_i), will decrement simultaneously when the values are non-zero. This implies that in each place p_i (buffer b_i) we can have a current marking m_i either with $0 \le m_i \le K_{p_i}^{\max}$, (respectively $0 \le x_i \le K_{b_i}^{\max}$) or with a_i , $K_{p_i}^{\min} \le a_i < 0$ (respectively $K_{b_i}^{\min} \le y_i < 0$). As a result, if ($\mathrm{Pre}(p_i, e_j) > 0$) then the firing of event $e_j \in E(M)$ consumes from (produces in) the same place p_i (buffer b_i), a number $\mathrm{Pre}(p_i, e_j) > 0$ of tokens (anti-tokens). Otherwise, it produces in (consumes from) the same place a number $\mathrm{Pre}(p_i, e_j) < 0$ of anti-tokens (tokens). Also, if ($\mathrm{Post}(e_j, p_i) > 0$) then the firing of event $e_j \in E(M)$ produces in (consumes from) the place p_i (buffer b_i) a number of tokens (anti-tokens), otherwise it consumes from (produces in) the same place a number $\mathrm{Post}(e_j, p_i) < 0$ of tokens (anti-tokens).

Upon firing, the discrete (continuous) transition removes a specified number (quantity) of tokens or anti-tokens for each input place, and deposits a specified number (quantity) of tokens or anti-tokens for discrete (continuous) output places. The fluid levels of continuous places can change the enabling/disabling of events.

We allow the firing delay τ_j and the enabling functions of the timed discrete events $e_j \in E_d(M)$, the firing speeds v_k and enabling functions of the timed continuous transitions $u_k \in E_c(M)$ and arc cardinalities (positive or negative values) to be dependent on the current state of the $RH\Gamma$, as defined by the current marking *M*.

Next, for accurate translating $G\Pi$ models into $RH\Gamma$ models, we consider $RH\Gamma$ models only with *firing step semantics of discrete events* $E_d \ne \varnothing$ and in which $T_c = \varnothing$. If in a $RH\Gamma$ model the set of rewriting rules is empty, i.e. $\rho = \varnothing$, then we deal with particular flat model, denoted as $H\Gamma$.

An example of a $H\Gamma 1$ subnet with negative capacities of places and arcs, whose marking-dependent cardinality can be negative, is shown in Figure 5a. In $H\Gamma 1$ the minimum capacity of the places are $K_{p_i}^{\min} = K_{b_i}^{\min} = -5$, i=1,...,4 and the arcs with weights that have negative values are $Post(t_1, p_4) = -3$, $Post(t_1, b_3) = -4.5$, and the others have positive weights.

The initial marking of the subnet $H\Gamma 1$ in Figure 5a is $M_0 = (3,\ 0,\ 4,\ 5; 4.5, 3.8, 1.5, -2.7)$. The firing of transition t_1 produces a new marking $M_1 = (1,\ 5,\ 3,\ 2; 2.0, 2.8, -3.0, -1.7)$, i.e. $M_0[t_1 > M_1$. This fact is shown in Figure 5b. We note that the *negative weight* of some arcs leads to a change in the direction of the tokens flow, thus modeling *reversible arcs*.

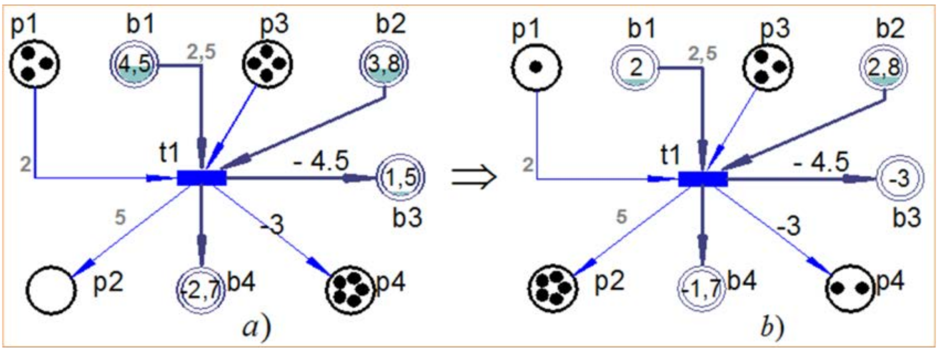

Figure 5. Discrete transition t_1 firing of a $H\Gamma 1$ flat subnet.

Parallel activities can be easily expressed in terms of $RH\Gamma$ using maximally firing *step* semantics in which executions of enabled discrete events $E_d \subset E$ are represented by a sequence of steps [15 – 18], [20]. Steps in $RH\Gamma$ are sets of enabled discrete evens that fire independently and parallel at the same time, i.e., simultaneously. The change in the marking and/or configuration of the $RH\Gamma$ when a step occurs is given by the sum of all the changes that occur for each event.

Definition 4. *(Firing step)* A *firing step* in $RH\Gamma$ at time τ is a set θ_τ of enabled events which are free enabled in a current configuration $\gamma_\tau = (\Gamma, M)$, i.e. $\theta_\tau \subset E(\Gamma, M)$. A firing step θ_τ can be executed at time τ_k leading to the new marking M' in $\gamma'_{\tau_k} = (\Gamma, M')$ or new configuration $\gamma''_{\tau_k} = (\Gamma', M')$ if there is no other $\theta'_\tau \subset \gamma_\tau$ enabled set of events with a higher priority than θ_τ.

A computation of a $RH\Gamma$ is a finite or infinite sequence of step executions at time τ_k starting from the initial configuration $\gamma_0 = (\Gamma_0, M_0)$ and every configuration $\gamma_{\tau_k} = (\Gamma_k, M_k)$ appea-ring in such a sequence is called reachable.

We note that the modeling power of $RH\Gamma$ *nets* is equal to the Turing machine, because it contains guard functions and/or inhibitory arcs [19, 26]. In [28] it was demonstrated that for any Petri net model with *reset arcs* the accessibility property is not decidable. In general, the accessibility properties of $RH\Gamma$ are not decidable, because in this type of Petri net the reset arcs can be described through marking-dependent functions of arcs. But, for particular cases of $RH\Gamma$, some behavior properties can be *decidable*.

4. Simulation and analysis of ESNMC models using $RH\Gamma$ nets

The behaviour of the SNPS and ESNPC models is often similar to TPN [17, 18] and also of the one $RH\Gamma$ nets, where is used a time maximally firing step semantic of enabled events. So, a major strength of $RH\Gamma$ is their support for analysis of many behavioural properties associated with SNPS [17, 18], ESNPC models and $RH\Gamma$ such as *reachability*, *boundedness and safeness*, *liveness, terminating, deadlock–free* [19-22, 24]. We are checking these properties for

SNMC and ESNMC models based on $RH\Gamma$, that provide relevant information about the behavioral properties of the systems.

Next, we will describe an approach to translate SNMC and ESNMC models into $RH\Gamma$ nets with step semantics for the visual simulation and to study the behavioural properties of such models. For this one, we illustrate the applicability of our approach by visual simulation and analyze the behavioural properties a SNMC and ESNMC models using VPNP Tool [24].

First, to give the pictorial visibility of RTHPN models, similar to that of SNMC and ESNMC models, we will first show how a $RH\Gamma0$ model describing the behavior of a neuron σ_i of a $G\Pi$ model is constructed. Then, we will show how the model $RH\Gamma1$ is constructed, which adequately describes the behavior of the $G\Pi2$ model that is presented in Figure 6.\

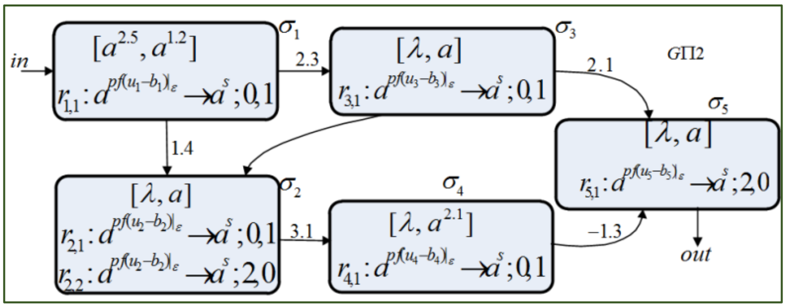

Figure 6. The ESNMC model $G\Pi2$ (Adapted from from [10]).

Figure 7 presents an ESNMC2 model $RH\Gamma0$ that translates neuron σ_i of a $G\Pi$ model, which is shown in Figure 1. There the neuron σ_i is represented using a continuous place $b_{i,1}$, which is connected to the timed rewrite rule $\rho_{i,1}$ by a test arc with weight $x_{i,1}$ that is the current number of spikes in buffer $b_{i,1}$. In $RH\Gamma$ models, places (transitions) correspond to local states (events, actions, activities) and rewriting rules can modify, reconfigure these models. The arc between a place and transitions (rewrite rule) and places represents axons.

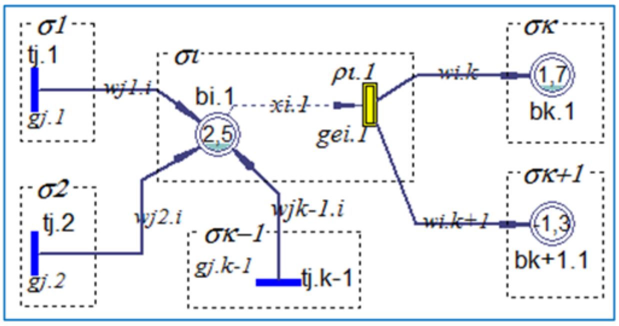

Figure 7. A $RH\Gamma0$ model of neuron σ_i in $G\Pi$ model that is showed in Figure 1.

The attribute notations in all the following figures, that represent $RH\Gamma$ or $H\Gamma$ flat models, will be interpreted in the following way: $yi.j := y_{i,k}$, where $y \in \{b, p, t, \rho, g, ge, w, x\}$ and the first index i shows the order number of the neuron σ_i, and the second index k shows the order number of the symbol (attribute) y within this neuron or this $G\Pi$ model.

The meanings of the places, transitions and rewriting rules of the $RNR\sigma_i$ model are:

• **Continuous places**: in $b_{i,1}, b_{k,1}$ and $b_{k+1,1}$ is stored (memorized) the respective current numbers $x_{i,1}, x_{k,1}$ and $x_{k+1,1}$ of spikes (anti- spikes).

• **Immediate transitions**: the firing of $t_{j,1}, t_{j,2}$ and $t_{j,k-1}$ transmit a respective number (equal to respective weight) $w_{j1,i}, w_{j2,i}$ and $w_{jk-1,i}$ of spikes (anti- spikes) in continous places $b_{i,1}$.

• **Timed rewriting rule**: at firing of rewriting rules $\rho_{i,1} : \{\rho_{i,1}\} \triangleright RNR\sigma_i$ the $\rho_{i,1}$ is *removed* with its incident arcs and they are simultaneously replaced with the flat subnet $RNR\sigma_i \in Lib$ that is shown in Figure 8 In this case the places $b_{i,1}$, $b_{k,1}$ and $b_{k+1,1}$ are respectively merged, so that the number of spikes (anti - spikes) in respective place of $RH\Gamma 0 \setminus \{\rho_{i,1}\}$ and $RNR\sigma_i$ will be equal to their sum.

The guard function of $\rho_{i,1}$ which determines the enabling condition is $ge_{i,1} := (x_{i,1} \neq 0)$, and the one which determines the firing condition is $gr_{i,1} :=" True"$.

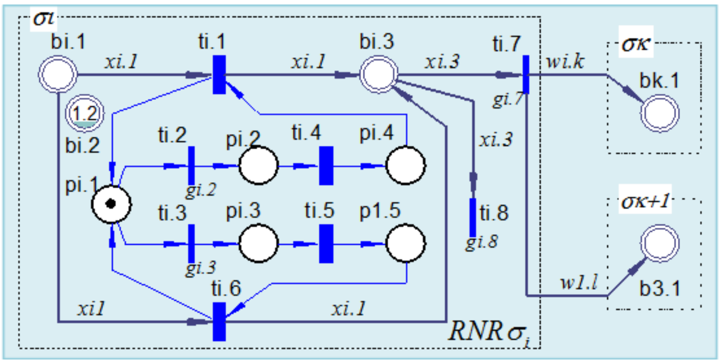

Figure 8. Flat $RNR\sigma_i$ flat subnet which substitutes $\rho_{i,1}$ in $RH\Gamma 0$ model shown in Figure 7.

The initial marking of $b_{i,1}$, $b_{k,1}$ and $b_{k+1,1}$ in $RH\Gamma 0$ is $M_{RH\Gamma 2} = (\mathbf{0}; \mathbf{x}) = (\mathbf{0}; 2.5, 1.7, -1.3)$. At the firing of $\rho_{i,1}$, a respective number of spikes (anti- spikes), equal to the respective weights $w_{i,k}$ and $w_{i,k+1}$, will be transmitted in respective place $b_{k,1}$ and $b_{k+1,1}$.

The meanings of the places and transitions of the model $RNR\sigma_i$ subnet, with 2 spike evolution rules $\rho_{i,1}$ and $\rho_{i,2}$ of σ_i *are*:

• **Continuous places**: in $b_{i,1}$, $b_{k,1}$ and $b_{k+1,1}$ are stored (memorized) the respective current numbers $x_{i,1}$, $x_{k,1}$ and $x_{k+1,1}$ of spikes (anti- spikes). These places will merged respectively with those in the $RH\Gamma 2$ model; in $b_{i,2}$ is stored the threshold value; $b_{i,3}$ - buffer to check the value of production function $pf_i = (x_{i,3} - x_{i,2})|_\varepsilon$ with critical value ε.

• **Discrete places**: $p_{i,1}$ - initializing the probabilistic selection of a single evolution rule $\rho_{i,1}$ or $\rho_{i,2}$ of σ_i; $p_{i,2}$ (resp. $p_{i,3}$) - setting the time of $\rho_{i,1}$ (resp. $\rho_{i,2}$) that neuron σ_i receives spikes from the $^\bullet\sigma_i$; $p_{i,4}$ (resp. $p_{i,4}$) - setting the rule $\rho_{i,1}$ (resp. $\rho_{i,2}$) execution time.

•**Timed discrete transitions:** $t_{i,1}$ (resp. $t_{i,6}$) - the execution time $\tau_{i,1}$ (resp. $\tau_{i,2}$) of rule $\rho_{i,1}$ (resp. $\rho_{i,2}$); $t_{i,4}$ (resp. $t_{i,5}$) - the time $\tau'_{i,1}$ (resp. $\tau'_{i,2}$) of rule $\rho_{i,1}$ (resp. $\rho_{i,2}$), that neuron σ_i receive spikes from the $^\bullet\sigma_i$.

• **Immediate discrete transitions**: $t_{i,2}$ (resp. $t_{i,3}$) - mutual exclusion activation of rule $r_{i,1}$ (resp. $r_{i,2}$). These transitions perform the probabilistic selection of evolution rules. By default, selection is performed non-deterministically; $t_{i,7}$ - generation of spike s_i, guard function $g_{i,7} := (pf_i > \varepsilon)$, and transmision of spike $s_i \cdot w_{i,k}$ to neurons $\sigma_k^\bullet$; $t_{i,8}$ - no spikes can be sent to the connected neurons with $\sigma_i^\bullet$, guard function $g_{i,8} := (pf_i \leq \varepsilon)$, the value unit $u_i = x_{i,3}$ of buffer $x_{i,3}$ is *consumed*.

The guard function of $t_{i,2}$ and $t_{i,3}$ is $g_{i,2} := (m_{i,1} \neq 0)$ and $g_{i,3} = g_{i,2}$, respectively. As a result, at firing of $\rho_{i,1}$ rewriting rules of $RH\Gamma 0$, will reconfigure itself and we get the flat $H\Gamma 1$ model that is represented in Figure 9.

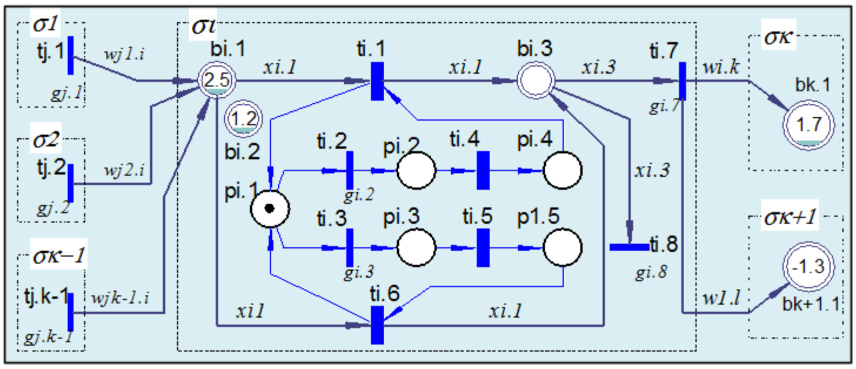

Figure 9. A flat $H\Gamma 1$ model of an neuron σ_i with 2 rules.

If it is necessary to analyze the behavioral properties of an ESNMC model, which contains several $G\Pi$ type neurons, it can be mapped into a $RH\Gamma$ type model, using the approach used to build the model $RH\Gamma 0$ of neuron σ_i. In this context, we will consider as an example the $G\Pi 2$ model, shown in Figure 6, for which we construct the $RH\Gamma 1$ model (see Figure 10) whose running behavior is equivalent to the $G\Pi 1$ model. We notice that there is a similarity between the structures of these two types of models. The reader might notice that the structure of the $RH\Gamma 2$ model is similar to the one $G\Pi 2$ from Figure 6.

The meanings of the places, transitions and rewriting rules of the $RH\Gamma 1$ *model are*:

- **Continuous places**: in $b_{i,1}$, $i = 1, 2, \ldots, 5$ is stored (memorized) the respective current numbers $x_{i,1}$, $i = 1, 2, \ldots, 5$ of spikes (anti- spikes) in neuron σ_i; $b_{0,1}$ - the environment receives the transmitted spikes;
- **Timed rewriting rule**: at firing of rewriting rules $\rho_{i,1} : \{\rho_{i,1}\} \triangleright RHRi.1$ the $\rho_{i,1}$, $i = 1, \ldots, 5$ and $\rho_{i,0} : \{\rho_{i,0}\} \triangleright RHR0$ are *removed* with its incident arcs and they are simultaneously replaced with the respective template subnets $\{RHRi.1, RHR0\} \in Lib$ that are shown in Figure 11. In this case the places $b_{i,1}$ are respectively merged, so that the number of spikes (anti - spikes) in respective place of $RH\Gamma 1 \setminus \{\rho_{i,1}\}$ and template subnets will be equal to their sum.

The guard function of $\rho_{i,1}$, $i = 1, 2, \ldots, 5$ which determines the enabling condition is $gei.i = g^{E}_{i,1} := (x_{i,1} \neq 0)$, and the one which determines the firing rewriting condition, by default is $g^{R}_{i,1} :=$ "$True$". The initial tangible marking of $b_{i,1}$, $i = 1, 2, \ldots, 5$ in $RH\Gamma 1$ is $\mathbf{x} = (2.5, 0, 0, 0, 0) = (2.5b_{1,1})$. At the firing of $\rho_{i,1}$, a respective number of spikes (anti- spikes), equal to the respective arc weights $w_{i,k}$ and $w_{i,k+1}$, will be transmitted in respective place $b_{i,1}$, $i = 1, 2, \ldots, 5$ and $b_{0,1}$.

In the result of run-time reconfiguration of $RH\Gamma 1$ model will be obtained the flat $H\Gamma 2$ model that is shown in Figure 12. The meanings of the respective places, transitions, arc weights and guard function of the $H\Gamma 2$ model are the same as in the $H\Gamma 1$ model that is shown in Figure 9. In case that in $RH\Gamma$ models the input value of the neurons σ_i can be positive (negative) integer numbers then continuous places $b_{i,k}$, $k = 1, 2, 3$, will change to respective discrete places

$p_{i,k}$, $k = 1, 2, 3$. Likewise, if in $RH\Gamma$ models the execution time $\tau_{i,k_r} = 0$ and/or the time $\tau'_{i,k_r} = 0$, neuron σ_i receives spikes from the $^{\bullet}\sigma_i$ then the respective *timed* discrete transitions will change to respective *immediate* discrete transitions (as example, see $t_{2,2}$ in $RHR2.1$ and $t_{5,1}$ in $RHR5.1$ subnet) or they are removed (see $RHR1.1$, $RHR3.1$ and $RHR4.1$ subnets).

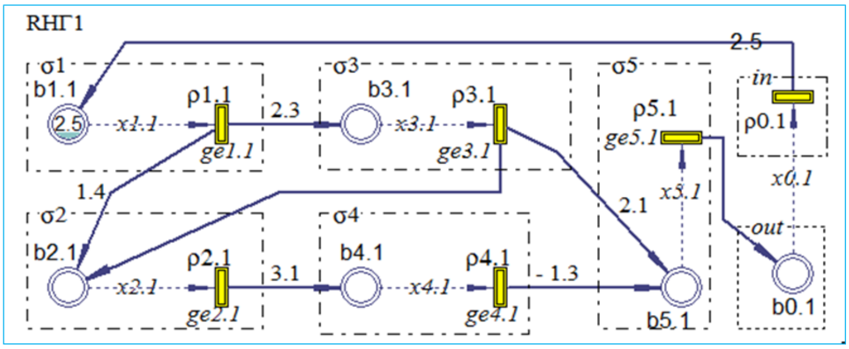

Figure 10. The $RH\Gamma1$ model of $G\Pi1$ model that is shown in Figure 6.

In order to perform the visual simulation and check the behavioral properties of the $H\Gamma$ flat models we have developed and integrated into VPNP Tool [24] a special software module. The Graphical User Interface (GUI) allows an intuitive, user-friendly tool for creating and editing $H\Gamma$ nets in an easy, fast and effcient way. Users are able to perform tasks using a menu bar, a toolbar and mouse actions. The $H\Gamma$ nets can be printed or exported into graphical format bitmap. VPNP Tool supports the parallel execution of events. It offers a visual animator so that the user can in step-by-step mode or automatically experiment with the token game, firing any of the enabled events (transitions and rewriting rules) at each firing step. Animation history is recorded, i.e. all the time fired events can be seen on the side of the screen.

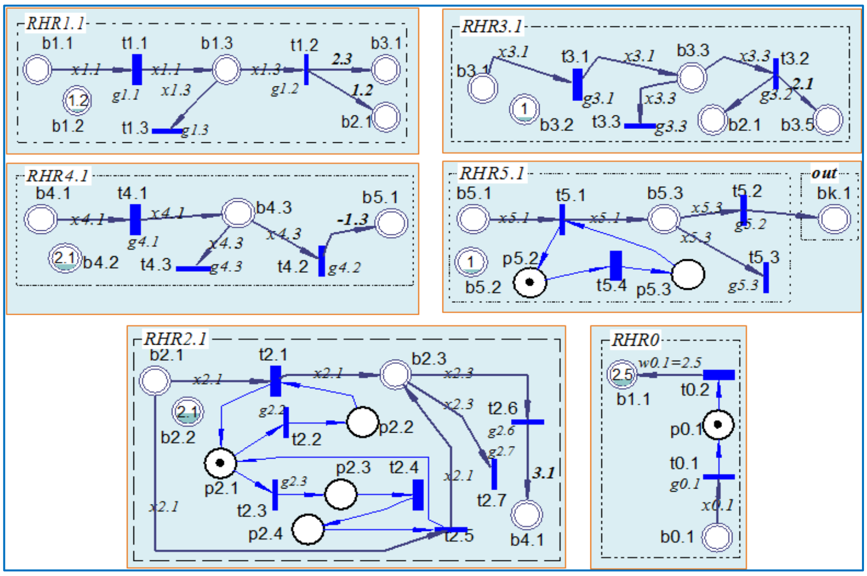

Figure 11. The template subnets involved in reconfiguration of $RH\Gamma1$. model upon firing of rewriting rules $\rho_{i,1} : \{\rho_{i,1}\} \triangleright RHRi.1$.

In this context, a numerical example may be examined to demonstrate the applicability and utility of the RTHPN proposed approach for simulation and analysis of ESNMC models. With this purpose we performed the visual simulation, using upgraded VPNP Tool [24], of the $H\Gamma2$ flat model with the following values of the timed transitions: $\tau'_{1,1} = 1$, $\tau'_{2,1} = 1$, $\tau_{2,4} = 2$, $\tau'_{3,1} = 1$, $\tau'_{4,1} = 1$, $\tau'_{5,1} = 2$, $\tau_{0,2} = 7$ time units and with weight $w_{0,1} = 2.5$.

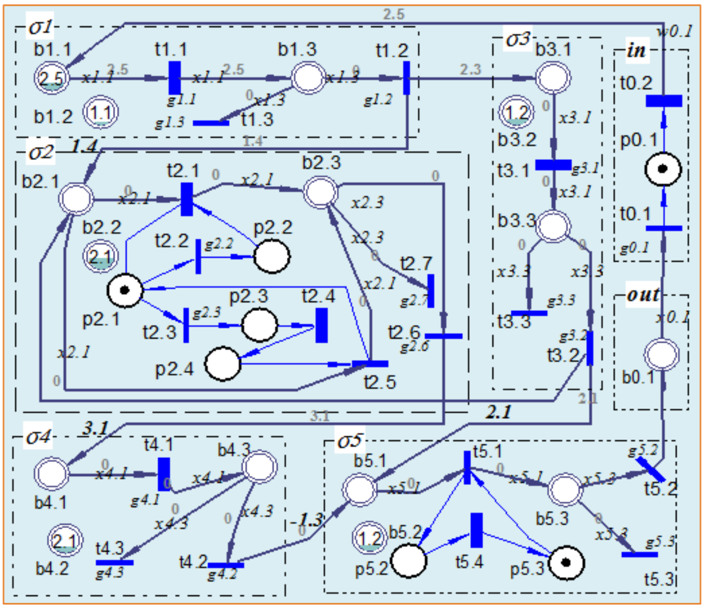

Figure 12. The $H\Gamma2$ flat model obtained after run-time reconfiguration of the $RH\Gamma1$ model.

The symbolic reachability graph (RG) of the $H\Gamma2$ flat model, constructed with these parameters, is shown in the figure 13.

The arc labels of this RG represent step firing sequence set of transitions at time $\tau_k = k, k = 1, 2, \ldots, K$ time units. The meanings of these labels are: $\vartheta_1(\tau_1) = \{t_{1,1}t_{1,2}\}$, $\vartheta_5(\tau_7) = \{t_{0,2}\}$, for $r_{2,1}$ of $G\Pi2$: $\vartheta_2^1(\tau_2) = \{t_{2,2}t_{2,1}t_{2,7}\} \| \{t_{3,1}t_{3,2}\} \| \{t_{5,4}\}$, $\vartheta_3^1(\tau_3) = \{t_{2,2}\} \| \{t_{5,1}t_{5,2}\}$, $\vartheta_4^1(\tau_4) = \{t_{2,1}t_{2,7}\}$, $\vartheta_5^1(\tau_7) = \{t_{0,2}\}$ and for $r_{2,1}$ of $G\Pi2$: for $r_{2,2}$: $\vartheta_2^2(\tau_2) = \{t_{2,3}\} \| \{t_{3,1}t_{3,2}\} \| \{t_{5,4}t_{5,1}t_{5,2}\} \| \{t_{0,1}\}$, $\vartheta_3^2(\tau_3) = \{t_{2,4}t_{2,5}t_{2,6}\}$, $\vartheta_4^2(\tau_4) = \{t_{4,1}t_{4,2}t_{5,1}t_{5,3}\}$.

In the label expressions shown above, the operator $\|$ indicates the parallel firing of the respective sequences of transitions. The meanings of discrete places subsets that are marked in RG1 of $H\Gamma2$ flat model are:

$$\mathbf{m}_1 = \mathbf{m}_4 = (p_{0,1}p_{2,2}p_{5,2}),\ \mathbf{m}_0 = (p_{0,1}p_{2,1}p_{5,2}),\ \mathbf{m}_2 = (p_{0,1}p_{2,1}p_{5,3}),$$

$$\mathbf{m}_3 = (2p_{0,1}p_{2,3}p_{5,2}),\ \mathbf{m}_5 = (2p_{0,1}p_{2,1}p_{5,3}),\ \mathbf{m}_6 = (2p_{0,1}p_{2,1}p_{5,2}).$$

The GUI screenshot of VPNP Tool with moment of time that the tokens (spike) occur in the continuous place $b_{0,1}$ and the *history* of the configurations γ_τ with drawing the firing of respective transitions in the $H\Gamma2$ flat model is shown in Figure 14.

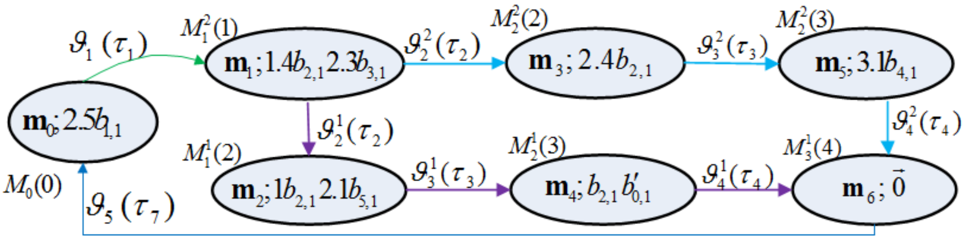

Figure 13. The symbolic reachability graph RG1of the $H\Gamma2$ flat model.

Thus, the behavior of the $H\Gamma2$ net is similar to the behavior of the $G\Pi2$ model and these are the following behaviur properties: *bounded*; *non-safe*; *live*; *deadlock–free*. Immediate transitions $t_{i,2}$ and $t_{i,3}$ (resp. $t_{2,6}$ and $t_{2,7}$) in template subnets $RHRi.1$ (resp. $RHR2.1$) are replaced by immediate rewriting rules $\rho_{i,2}$ and $\rho_{i,3}$ (resp. $\rho_{2,6}$ and $\rho_{2,7}$) with $g_{i,2}^R = g_{i,3}^R = g_{2,6}^R = g_{2,7}^R :=\text{"}False\text{"}$, $i = 1, 3, 4, 5$. We get behavior of $RH\Gamma1$ model which is equivalent to that of the flat $H\Gamma2$ model.

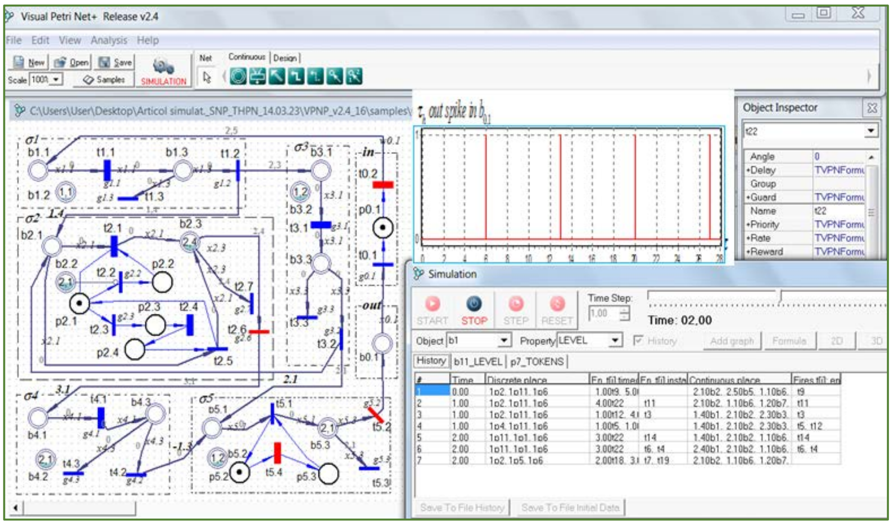

Figure 14. The GUI screenshot of VPNP Tool with the time tokens (spike) occurences in the continuous place $b_{0,1}$ and the *history* of the configurations γ_τ of $H\Gamma 2$ model.

In order to obtain a more compact $RH\Gamma$ model during the run-time firing of these immediate rewriting rules in flat $H\Gamma 2$ model it is necessary to put $g^R_{i,2} = g^R_{i,3} = g^R_{2,6} = g^R_{2,7} := "True"$, $i = 1, 3, 4, 5$ and to specify these rules to reconfigure the $H\Gamma 2$ model in an abstract form similar to the $RH\Gamma 1$ model. For this purpose we specify the following template subnets when firing these immediate rewriting rules of flat $H\Gamma 2$ model:

$$\rho_{i,2} : RHLi.2 \triangleright RHRi.2,\ \rho_{i,3} : RHLi.3 \triangleright RHRi.3,\ i = 1, 3, 4, 5;$$

$$\rho_{2,6} : RHL2.6 \triangleright RHR2.6,\ \rho_{2,7} : RHL2.7 \triangleright RHR2.7 .$$

Due to the volume restrictions of this paper not to present in graphic form the above-mentioned template subnets, they will be rendered in analytical form, using descriptive expressions (DE), the syntax and semantics of which are described in the papers [16, 26, 29].

Hence, the respective descriptive expressions (DEs) of these left-hand side and right-hand side template subnets of flat $H\Gamma 2$ model are:

$$DE_{RHLi.2} = DE_{RHLi.3} = \{t_{i,1}, b_{i,2}, b_{i,3}, \rho_{i,2}, \rho_{i,3}\}, i = 1, 3, 4;$$

$$DE_{RHL5.2} = DE_{RHL5.3} = \{t_{5,1}, t_{5,4}, p_{5,2}, p_{5,3}, b_{5,2}, b_{5,3}, \rho_{5,2}, \rho_{5,3}\};$$

$$DE_{RHL2.6} = DE_{RHL2.7} = \{t_{2,1}, t_{2,2}, t_{2,3}, t_{2,4}, p_{2,1}, p_{2,2}, p_{2,3}, p_{2,4}, b_{2,2}, b_{2,3}, \rho_{2,6}, \rho_{2,7}\};$$

$$DE_{RHLi.2} = DE_{RHLi.3} = \{t_{i,1}, b_{i,2}, b_{i,3}, \rho_{i,2}, \rho_{i,3}\}, i = 1, 3, 4;$$

$$DE_{RHR1.2} = \tilde{b}_{1,1}[x1.1]_{ge_{1.1}}|_{\rho_{1,1}} (2.3b_{3,1}[2.3]\Diamond 1.4b_{2,1}[1.4]),\ DE_{RHR\,2.2} = \tilde{b}_{2,1}[x2.1]_{ge_{2.1}}|_{\rho_{2,1}} 3.1b_{4,1}[3.1],$$

$$DE_{RHR3.2} = \tilde{b}_{3,1}[x3.1]_{ge_{3.1}}|_{\rho_{3,1}} (1.0b_{2,1} \Diamond 2.1b_{5,1}[2.1]),\ DE_{RHR\,4.2} = \tilde{b}_{4,1}[x4.1]_{ge_{4.1}}|_{\rho_{4,1}} -1.3b_{5,1}[-1.3];$$

$$DE_{RHR1.3} = \tilde{b}_{1,1}[x1.1]_{ge_{1.1}}|_{\rho_{1,1}} (b_{3,1}[2.3]\Diamond b_{2,1}[1.4]),\ DE_{RHR\,2.3} = \tilde{b}_{2,1}[x2.1]_{ge_{2.1}}|_{\rho_{2,1}} b_{4,1}[3.1],$$

$$DE_{RHR3.3} = \tilde{b}_{3,1}[x3.1]_{ge_{3.1}}|_{\rho_{3,1}} (b_{2,1} \Diamond b_{5,1}[2.1]),\ DE_{RHR\,4.3} = \tilde{b}_{4,1}[x4.1]_{ge_{4.1}}|_{\rho_{4,1}} b_{5,1}[-1.3],$$

$$DE_{RHR\,5.2} = \tilde{b}_{5,1}[x5.1]_{ge_{5.1}}|_{\rho_{4,1}} 1b_{0,1};\ DE_{RHR\,5.3} = \tilde{b}_{5,1}[x5.1]_{ge_{5.1}}|_{\rho_{4,1}} b_{0,1}.$$

We note that one of the most important benefits we obtain from the use of $RH\Gamma$ nets when maping and verifying the discrete-continuous processes of SNMC and ESNMC models is that the structure of these models is similar, very concise and flexible to reconfiguring and changing the quantitative parameters during run-time of these $RH\Gamma$ nets.

A generalization of this approach consists in assuming that the firing times $\tau : E_d \times Bag(p) \to IR^+$ of the respective discrete events $e_j \in E_d$ are random variables whose probability distribution functions $F(\cdot)$ have contained support in the set of non-negative real numbers. In this case we obtain stochastic RTHPNs that allow simulation and performance analysis of the stochastic ESNMC models.

4. Conclusions

For the purpose of efficient formalization, implementation and formal correctness analysis of SNMC and ESNMC models, in this paper we define and describe a new extension of THPN, called rewriting THPN with anti-tokens (in short, RTHPN) having guards for transitions, rewriting rules and implicitly annihilation rule of tokens and anti-tokens in same places. The features of RTHPN accept as well the negative (positive) values for: place capacities; markings of discrete and continuous places; marking-dependent arc cardinalities. The RTHPN model allows its structure and/or attributes to change at run-time depending on its current state and/or the occurrence of some events which permits a hierarchical design. Therefore, functionalities and features of system models can be added gradually in run-time.

In order to perform the visual simulation and check the behavioral properties of the $H\Gamma$ flat models, we have developed and integrated into VPNP Tool a special software module. Also, we present a methodology that maps the large SNMC and ESNMC models into compact $RH\Gamma$ and flat $H\Gamma$ nets, which allows analysis of such models via the upgraded VPNP Tool in an easy-to-use manner. The use of RTHPNs in simulation and analysis of ESNMC models is illustrated through an example proving that such approach preserves faithfully their behaviours.

In the future, we will develop and integrate into the VPNP tool special software modules that will allow analysis of RTHPN models involving the simulation of stochastic ESNMC models, Spiking Neural P Systems with Self-Organization and Spiking Neural dP Systems.

Conflicts of Interest: The authors declare no conflict of interest.

References

1. Ionescu, M.; Păun, Gh.; Yokomori, T. Spiking Neural P Systems. *Fundamenta Informaticae*, 2006, 71 (2, 3), pp. 279-308.
2. Păun, Gh. Computing with Membranes. *Journal of Computer and System Sciences* 2000, 61, pp. 108-143.
3. P systems resource website. Available online: http://ppage.psystems.eu/ (accessed on 12.01.2023).
4. Leporati, A.; Mauri, G.; Zandron, C. Spiking neural P systems: main ideas and results. *Natural Computing* 2022, 21, pp. 629–649.
5. Verlan, S.; Freund, R.; Alhazov, A.; Ivanov, S.; Pan, L. A formal framework for spiking neural P systems. *Journal of Membrane Computing* 2020, 2(4), pp. 355 – 368.
6. Fan, S.; Paul, P.; Wu, T.; Rong H.; Zhang. G. On Applications of Spiking Neural P Systems. *Appled. Sciences* 2020, 10, 7011, pp. 1-26. Doi: 10.3390/app10207011.
7. Rong, H.; Wu, T.; Pan, L.; Zhang, G. Spiking neural P systems: Theoretical results and applications. *Enjoying Natural Computing* 2018, pp. 256–268.
8. Wang, X.; Song, T.; Gong, F.; Zheng, P. On the Computational Power of Spiking Neural P Systems with Self-Organization. June 2016, *Scientific Reports* 2016, 6(1), 27624. Available online: https://www.researchgate.net/publication/303908523 (accessed on 11.01.2023).
9. Ionescu, M.; Păun, Gh.; Perez-Jimenez, M. J.; Yokomori**,** T. Spiking Neural dP Systems, *Fundamenta Informaticae* 2011, 111(4), pp. 423–436.
10. Liu, X.; Ren, Q. Spiking Neural Membrane Computing Models. *Processes* 2021, 9, 733.
11. Lefticaru, R.; Gheorghe, M.; Konur, S.; Niculescu, I.M.; Adorna, H.N. Spiking Neural P Systems Simulation and Verification. In: *Proceedings of the 18-th International Conference on HPCS* 2020, 22-27 Mar 2021, Barcelona, Spain. Available online: http://hdl.handle.net/10454/18683(accessed on 12.01.2023).
12. Dupaya, A. G. S.; Galano, A. C. A. P. ; Cabarle, F.; Cruz, R. T. A. A web-based visual simulator for spiking neural P systems. *Journal of Membrane Computing* 2022, 4, pp. 21–40.

13. Fernandez, A. D. C.; Fresco, R. M.; Cabarle, F. G. C.; Cruz, R. T. A.; Macababayao, I. C. H.; Ballesteros, K, J.; Adorna, H. N. Snapse: A Visual Tool for Spiking Neural P Systems. *Processes* 2021, 9, pp. 1-24.
14. Carandang, J. P.; Villaflores, J.M. ; Cabarle, F. G. C.; Adorna, H. N.; Martinez-del- Amor, M. A. CuSNP: Spiking neural P systems simulators in CUDA. *Romanian Journal of Information Science and Technology* 2017, 20(1), pp. 57–70.
15. Kleijn, J.; Koutny, M. Petri nets and Membrane computing. In: *The Oxford Handbook of Membrane Computing*, Gh. Păun, G. Rozenberg, A. Salomaa, eds., Oxford University Press, 2010, pp. 389-412.
16. Guţuleac E. Descriptive Timed Membrane Petri Nets for Modelling of Parallel Computing. *International Journal of Computers, Communications & Control* 2006, 3 (1), pp. 33-39**.**
17. Metta, V. P.; Krithivasan, K.; Garg, G. Modeling spiking neural P systems using timed Petri nets. In: *NaBIC IEEE Conference* 2009, pp. 25-30.
18. Metta, V. P.; Krithivasan, K.; Garg, D. Modelling and Analysis of Spiking Neural P Systems with Anti-spikes using PNetLab. *Nano Communication Networks* 2011, 2(2-3), pp. 141-149.
19. Petri Nets Tools Database Quick Overview. Available online: https://www.informatik.uni-hamburg.de/TGI/PetriNets/tools/quick.html (accessed on 12.01.2023).
20. Alla, A.; David, H. Continuous and hybrid Petri nets. *Journal of systems Circuits and Computers* 1998, 8(1), pp. 159-188.
21. Horton, G., Kulkarni, V. G., Nicol, D. M., Trivedi, K. S. Fluid stochastic Petri nets: Theory, application, and solution techniques. *Eur. J. Op. Res.* 1998, 105(1), pp. 184–201.
22. Chiola, G.; Ajmone- Marsan, M.; Balbo, G.; Conte, G. Generalized stochastic Petri nets: A definition at the net level and its implications. *IEEE Transactions on Software Engineering* 1993, 19 (2), pp. 89-107.
23. Guţuleac E. Dynamic rewriting generalized differential Petri nets for discrete-continuous modeling of computer systems. *Meridian ingineresc* 2006, 3, pp. 27-32.
24. Guţuleac, E.; Boşneaga, C.; Reilean, A. VPNP-Software tool for modeling and performance evaluation using generalized stochastic Petri nets. In: *Proceedings of 6-th International Conference on D&AS-2002*, Suceava, România, 2002, pp. 243-248.
25. Guţuleac, E.; Ţurcanu, Iu.; Palii, D. Performance modeling of computing processes using reconfigurable generalized differential stochastic Petri nets. *Meridian ingineresc* 2013, 4, pp. 23-30.
26. Guţuleac, E. Descriptive compositional HSPN modeling of computer systems. *Annals of the Craiova University, Series: Atomation, Computers, Electronics and Mechatronics, România* 2006, 3 (30), pp. 82-87.
27. Klaus Reinhardt. Reachability in Petri nets with inhibitor arcs. *Electronic Notes in Theoretical Computer Science*, 2008, 223, pp. 239–264.
28. Verbeek, H.M.W.; Wynn, M.T.; Van der Aalst, W.M.P.; Hofstede, A.H.M. Reduction rules for reset/inhibitor nets. *Journal of Computer and System Sciences* 2010, 76, pp. 125–143.
29. Moraru, V.; Guţuleac, E.; Zaporojan, S. Uncertainty modelling of dynamically reconfigurable systems based on rewriting stochastic reward nets with z-fuzzy parameters. *Computer Science Journal of Moldova* 2021, 3(87), pp. 388-406.

Citation: Moraru, V.; Sclifos, A.; Sclifos, E.; Guțuleac, E. Simulation and analysis of spiking neural membrane computing models based on rewriting timed hybrid Petri nets with anti-tokens. *Journal of Engineering Science* 2023, 30 (3), pp. 78-98. https://doi.org/10.52326/jes.utm.2023.30(3).06.

Publisher's Note: JES stays neutral with regard to jurisdictional claims in published maps and institutional affiliations.

Submission of manuscripts: jes@meridian.utm.md

Journal of Engineering Science *Vol. XXX, no. 3 (2023), pp. 99 - 120*
Fascicle *Electronics and Computer Science* *ISSN 2587-3474*
Topic *Computers and Information Technology* *eISSN 2587-3482*

https://doi.org/10.52326/jes.utm.2023.30(3).07
UDC 316.7:[519.766:004.8]

DECENTRALISED AUTONOMOUS SOCIETY THROUGH LARGE LANGUAGE MODELS' BASED AGENTS: A PATHWAY TO EMPOWER SMALL COMMUNITIES

Vasili Braga*, ORCID: 0009-0009-2478-830X

Technical University of Moldova, 168 Stefan cel Mare Blvd., Chisinau, Republic of Moldova
*Corresponding author: Vasili Braga, *vasili.braga@ati.utm.md*

Received: 07. 21. 2023
Accepted: 09. 10. 2023

Abstract. This paper explores the concept of Decentralized Autonomous Society through the lens of Large Language Models focusing on the transformative potential of integrating these technologies. The paper on the role of Large Language Models based agents in providing a versatile, responsive, and contextually intelligent resource within a Decentralized Autonomous Society, fostering intellectual exploration, assisting in complex tasks, and aiding real-time problem solving. One delves into their integration with Decentralized Autonomous Society infrastructures, including robotic and automated systems. While promising, the integration of Large Language Models and their agents into a Decentralized Autonomous Society poses several challenges, including infrastructure and connectivity limitations, information accuracy, artificial intelligence bias, privacy and data security, and ethical concerns. This paper critically discusses these issues and proposes potential solutions. Through the lens of the Decentralized Autonomous Society construct, the paper considers the future possibilities and implications of artificial intelligence, where self-sustaining, digitally-empowered communities leverage artificial intelligence as a cornerstone of their collective intelligence.

Keywords: *Decentralized Autonomous Societies, Large Language Models, AI Agents, GPT-4, Vicuna, Artificial Intelligence, Machine Learning, Decentralization.*

Rezumat. Acest articol explorează conceptul de Societate Autonomă Descentralizată prin prisma Modelelor Lingvistice Mari, concentrându-se pe potențialul de transformare al integrării acestor tehnologii. Lucrarea se axează pe rolul agenților bazați pe Modele Lingvistice Mari în a oferi o resursă versatilă, receptivă și inteligentă în context în cadrul unei Societăți Autonome Descentralizate, stimulând explorarea intelectuală, asistând în sarcini complexe și ajutând la rezolvarea problemelor în timp real. Se intră în detalii privind integrarea lor cu infrastructurile Societății Autonome Descentralizate, inclusiv sistemele robotizate și automate. Cu toate că este promițătoare, integrarea Modelelor Lingvistice Mari și a agenților lor într-o Societate Autonomă Descentralizată prezintă mai multe provocări, inclusiv limitările infrastructurii și conectivității, acuratețea informațiilor, prejudecata inteligenței artificiale, confidențialitatea și securitatea datelor și preocupările etice. Acest document discută în mod critic aceste probleme și propune soluții potențiale. Prin prisma construcției Societății Autonome Descentralizate, lucrarea consideră posibilitățile și implicațiile viitoare ale inteligenței artificiale, unde comunitățile auto-sustenabile, digital-împuternicite, folosesc inteligența artificială ca o piatră de temelie a inteligenței lor colective.

Cuvinte cheie: *Societăți Autonome Descentralizate, Modele Lingvistice Mari, Agenți AI, GPT-4, Vicuna, Inteligență Artificială, Învățare Automată, Descentralizare.*

1. Introduction

Communities in isolated locations, from the rustic landscapes to remote islands or even potential underwater or extraterrestrial habitats, face unique challenges [1]. While their environments offer immense natural beauty and tranquility, they are often separated from the conveniences and expertise of the modern world. The isolation and low population density in such places can make it challenging to maintain a full range of specialist skills [2]. Fields such as medicine, education, agriculture, maintenance, and cultural preservation require dedicated specialists whose expertise might not be readily available in these areas. This lack of local expertise can pose significant barriers to sustaining these communities and enhancing their quality of life [3].

An innovative approach to addressing this dilemma lies in the realm of artificial intelligence (AI), specifically, Large Language Models [4] (LLMs) like GPT-4 [5], LLAMA [6] or Vicuna [7] etc. These LLM models have evolved into expansive, decentralized knowledge bases, capable of providing insights, advice, and recommendations across a plethora of fields. They can facilitate virtual consultations in healthcare, offer customized education support, provide expert guidance in sustainable agriculture or maintenance tasks, and even assist in preserving local cultural heritage. In order to understand how useful can be the agents based on LLM's one can see what the impact of LLMs on the labor market is already quite significant. According to some studies, as cited in the research, around 80% of the U.S. workforce could see at least 10% of their work tasks influenced by the introduction of LLMs, and close to 19% of workers might witness at least 50% of their tasks being directly impacted [8].

The paper discusses integrating modern conveniences into isolated communities. It aims to blend the benefits of a peaceful, slow-paced life with modern technology. Using LLMs can address challenges of isolation and expertise shortages, preserve local culture, and enhance community living.This paper aims to delve deeper into the role of LLMs as decentralized knowledge bases in supporting and sustaining such visionary projects.

The paper will explore how these AI-powered systems can help small, isolated communities bridge the gap between anarcho primitivism and modernity, merging old-world charm with contemporary comfort. The paper will shed light on the potential challenges and opportunities that LLMs present, thereby illuminating their potential in driving a new era of sustainable development and cultural preservation in isolated communities.

2. State of the Art in Large Language Models and Autonomous agents based on LLMs

Over the years, significant advancements have been made in the field of LLMs and their applications. But 2023 brings an explosion of new models and software based on them [4]. The following outlines some of the state-of-the-art developments in this area of autonomous agents based on LLM [9]:

1. LangChain [10]: LangChain is an open-source framework tailored for crafting applications underpinned by LLMs. To construct an AI assistant using LangChain, one would

start by defining the assistant's tasks and associated data sources. Subsequently, with LangChain initialized, developers can adeptly manage prompts through the `PromptManager`, integrate external data via the `DataManager`, and engage with other services using dedicated API modules. The framework also facilitates the programming of autonomous behaviors, implementation of feedback mechanisms, and addresses ethical and privacy concerns. Once developed, the assistant can be deployed, monitored, and iteratively improved upon. Overall, LangChain streamlines the process of creating data-aware, contextually relevant, and proactive AI assistants.

2. HuggingGPT [11]: is a system that uses ChatGPT to work with various AI models from the Hugging Face repository. It processes tasks, chooses the right models, and provides results. For DAS, it can integrate different models, such as image generation for creating visuals, speech-to-text for converting spoken language into written text, sentiment analysis to determine community feelings, and translation models to help in multilingual environments. Essentially, HuggingGPT is a versatile tool designed to aid decentralized communities by utilizing different AI functionalities.

3. Toolformer [12]: This is a system where LMs teach themselves to use external tools via simple APIs. Toolformer is trained to decide which APIs to call, when to call them, what arguments to pass, and how to best incorporate the results into future token prediction. For distributed autonomous societies (DAS), Toolformer presents immense value by facilitating seamless integration and utilization of external tools through APIs. As DAS operations often require diverse functionalities, the ability to quickly and autonomously decide which external tools to call, and when, allows for a more adaptive and efficient environment. Furthermore, in decentralized structures where timely and accurate data processing is essential, Toolformer can enhance decision-making by improving token prediction based on the results from these external tools. Its self-learning capability ensures that as the DAS ecosystem evolves, Toolformer can adapt and continue to provide optimal support without manual reconfiguration.

4. Visual ChatGPT [13]: This is a system that incorporates Visual Foundation Models with ChatGPT, allowing users to send and receive not only languages but also images during chatting. This system is designed to address complex visual questions or visual editing instructions that require the collaboration of multiple AI models in multiple steps. Visual ChatGPT's adaptability can be pivotal in facilitating clear and efficient visual exchanges in such decentralized settings.

5. Lindy AI [14]: This application serves as a personal AI assistant. It utilizes LLMs to help users manage their tasks and make informed decisions.

6. CensusGPT [15]: This application uses LLMs to answer questions related to census data. It makes statistical data more accessible by providing answers in natural language. In the context of distributed autonomous societies (DAS), CensusGPT could stand as a crucial tool to streamline data accessibility. By leveraging LLMs to interpret census-related queries, it transforms often dense and convoluted statistical data into digestible, natural language responses. For DAS that rely on data-driven decisions, the quick and clear information retrieval facilitated by such a tool can significantly expedite research processes and ensure more informed communal choices based on demographic insights.

7. Hearth AI [16]: Hearth AI applies the concept of Agentic Relationship Management. It uses AI to maintain and manage relationships with customers, providing personalized interactions. In a DAS setup, Hearth AI's concept of using AI for relationship management can

efficiently automate and personalize communication, enhancing community interactions and administrative tasks.

8. RCI Agent for MiniWoB++ [17]: This application shows that LLMs can solve computer tasks. It offers a new way to approach and solve complex problems in computing.

9. Babyagi [18]: Babyagi is an AI-powered task management system. It uses AI to assist users in managing and completing their tasks efficiently. In DAS, Babyagi's AI-driven task management can enhance productivity. By automating task organization and prioritization, it ensures tasks align with community objectives and helps members efficiently achieve their goals.

10. ChatGPT plugins [19]: This platform provides a way to connect ChatGPT to third-party applications. It extends the capabilities of ChatGPT beyond its original scope.

11. Fixie.ai [20]: Fixie.ai allows for the creation of natural language agents that can connect to user data, communicate with APIs, and solve complex problems. It provides a platform for creating highly personalized AI solutions. For DAS, Fixie.ai is a platform for constructing AI agents that interface directly with user data and APIs. Example: A DAS community could deploy a Fixie.ai agent to automatically access weather data and notify residents of upcoming weather changes, ensuring community preparedness.

These developments highlight the potential of LLMs in driving innovation and solving complex tasks in various domains, emphasizing the crucial role they play in the progress towards more sophisticated and autonomous AI systems.

This papers goals in the context of the state of the art, can be framed as follows:

Empowering Small Communities: in contrast to the majority of existing systems which are primarily designed for general use or specialized industrial applications, our project specifically targets small and isolated communities' needs. It aims to empower these communities by democratizing access to knowledge, fostering innovation, automating parts of their tasks, helping to preserve local culture and day to day history, and providing administrative support as autonomous assistants [21].

Knowledge Democratization: The paper uses large language models as a decentralized knowledge base, bridging the knowledge gap that often exists in small communities. This feature is not commonly found in the current state-of-the-art applications, making our project unique and of immense value to the targeted demographic. Even if there exists the need to use LLMs as explainers, copilots or assistants in such complex matters like financial knowledge [22], programming [23] or medicine [24, 25].

Enabling Self-Learning: The projects emphasis on supporting self-directed learning is a distinctive attribute. It harnesses the capabilities of LLMs to aid information discovery and facilitate learning, essential for fostering development in these communities. The capacity of LLM's to support self-learning for students is widely known already [26–28] , yet the academia is perceiving at the moment these opportunities more like a threat to the classical educational approach [29].

Culturally Conscious Technology: The projects seeks to incorporate local culture and history through memory modules for LLM based agents [30,31], with the language model being sensitive and inclusive of local cultural tradition, languages and history. This makes it a valuable and unique tool for these communities.

Addressing Unique Challenges: recognizing the challenges associated with deploying AI in small communities, the project places a strong emphasis on finding innovative solutions to technological, infrastructural, and ethical issues. This responsible approach further differentiates the project from the current state-of-the-art.

In conclusion, the project stands out for its focus on small communities, its aim of democratizing knowledge, enabling self-learning, promoting cultural consciousness, and addressing unique challenges. This unique combination of attributes positions the project uniquely in the current state-of-the-art landscape.

3. Understanding Decentralization and Large Language Models

Decentralized Autonomous Society (DAS)

DAS [32] represents a new form of social organization enabled by cutting-edge technologies, like blockchain [33] and smart contracts [34]. Essentially, a DAS operates on decentralized digital platforms that facilitate collective decision making processes [35] that are transparent, secure, and direct, eliminating the need for central authorities or intermediaries. Let's explore further:

Blockchain Technology: the backbone of a DAS could be the blockchain technology. A blockchain is a decentralized and distributed digital ledger that records transactions across many computers so that any involved record cannot be altered retroactively, without the alteration of all subsequent blocks. This makes the data stored on a blockchain transparent, immutable, and resistant to censorship, providing a trustless environment where parties do not need to trust each other but instead trust the system.

Smart Contracts: built on blockchain technology, smart contracts are self-executing contracts with the terms of the agreement directly written into code [34]. They automate transactions and ensure all conditions of a contract are met before it's executed, making transactions traceable, transparent, and irreversible. This feature can be used to automate decision-making processes, enforce rules, and manage resources in a DAS.

Decentralized Applications (dApps): dApps are applications that run on a P2P network of computers rather than a single computer [36]. They interact with the blockchain and smart contracts to perform their functions. dApps can serve various functions needed for the operation of a DAS, such as decentralized voting systems, resource allocation systems, or any other application that benefits from transparency, censorship resistance, and decentralization.

Decentralized Governance: this involves the use of blockchain technology and smart contracts for decision-making processes in a transparent, secure, and direct manner [37]. Votes can be tokenized, and stakeholders can vote on proposals according to the number of tokens they hold.

Decentralized Finance (DeFi): DeFi represents a shift from traditional, centralized financial systems [38] to peer-to-peer finance enabled by decentralized technologies built on something like Ethereum [39]. It involves the use of cryptocurrencies and blockchain technology to remove intermediaries from financial transactions.

A DAS, enabled by these technologies, can operate with reduced reliance on central authorities. Instead, control is distributed among the members of the society, who interact through peer-to-peer networks. The rules of this interaction are governed by consensus algorithms, smart contracts, and other automated processes, which can result in a more transparent, fair, and potentially efficient society.

Large Language Models as a Paradigm Shift in General AI

LLMs signify a major shift in the field of general artificial intelligence. These AI models have been trained on vast ranges of internet text, facilitating their ability to generate contextually appropriate and coherent responses across a diverse array of topics. While the proficiency of these models is impressive, their susceptibility to biases and inaccuracies present in their training data must be acknowledged.

Fundamental Principles and Model Architecture

A comprehensive survey on LLMs identifies several key areas of exploration and development that have contributed to their success. Theories and principles underlying their operation, notably the organization, distribution, and utilization of information within these large neural networks, remain an area of active research. One intriguing phenomenon is the emergence of unexpected abilities such as in-context learning [40], instruction following [41], and step-by-step reasoning [42] when the parameter scale of language models reaches a critical size.

The Transformer [43] architecture, characterized by stacked multi-head self-attention layers, has become the de facto framework for building LLMs due to its scalability and effectiveness. However, challenges such as the quadratic time complexity of standard self-attention mechanism and catastrophic forgetting during new data tuning necessitate further exploration and improvement of this architecture.

Utilization and Training Considerations

LLMs serve as potent knowledge bases, capable of answering a wide range of queries and providing insights across numerous topics. In application-specific contexts, they can fill knowledge gaps in the absence of subject-matter specialists, making them a powerful tool for various projects.

However, pre-training these models poses significant challenges due to enormous computational requirements and sensitivity to data quality and training tricks. Hence, the development of more systematic, economical pre-training approaches, considering factors such as model effectiveness, efficiency optimization, and training stability, is of paramount importance.

Safety, Alignment, and Application Ecosystem

Despite their impressive capabilities, LLMs pose several safety and alignment challenges. They have a propensity to generate plausible yet factually incorrect texts, or "hallucinations" [44], and could potentially be misused to generate harmful, biased, or toxic content. Strategies such as reinforcement learning from human feedback (RLHF) and red teaming [45] have been proposed to improve model safety and alignment.

The rise of LLMs ushers in a new era for a broad range of applications, from information-seeking techniques like search engines and recommender systems, to intelligent information assistants. However, this progression also necessitates an increased focus on AI safety and the establishment of ethical and responsible AI usage guidelines [46].

In conclusion, the development and implementation of LLMs represent a promising, yet challenging, advancement in general AI [47]. While their potential applications are vast, understanding their underlying mechanisms, ensuring their safe usage, and managing their limitations are essential areas of ongoing research.

The Intersection of DAS and Large Language Models' Based Agents

Decentralized Autonomous Societies (DAS) are a novel paradigm for community organization, powered by the sophistication of technology. A significant technological advancement, Large Language Models (LLMs), have found a niche as foundations for intelligent agents due to their capacity to process and generate contextually relevant human-like text. The convergence of DAS and LLM-based agents unlocks unique opportunities and brings forth distinctive challenges.

Integrating LLM-Based Agents into a DAS Infrastructure

In a DAS, LLM-based agents could serve as an invaluable component of the society's technological and informational framework. Functioning as potent catalysts for knowledge sharing and communal problem-solving, these agents can be integrated into the DAS's automated or robotic infrastructure, including areas such as agriculture, craft-making, and other essential societal services.

For instance, in automated farming, an LLM-based agent could analyze and interpret data from various sensors, provide insights on sustainable agricultural practices, suggest optimal harvesting times, or even guide automated machinery. Similarly, in automated craft-making or construction processes, these agents could provide guidance and recommendations based on historical data and established best practices [48].

Challenges in Harnessing LLM-Based Agents in a DAS

However, the assimilation of LLM-based agents into a DAS also brings substantial challenges. The significant computational demands and costs associated with training these models, coupled with concerns about data quality and misuse potential, cannot be overlooked [49].

Ensuring the factual accuracy, unbiasedness, and ethical integrity of the agents' outputs is paramount. Furthermore, the risk of over-reliance on artificial intelligence for various societal functions, leading to potential unforeseen complications in societal functioning and individual decision-making, must be considered and mitigated [50].

Future Trajectories at the Crossroads of DAS and LLM-Based Agents

The synthesis of DAS and LLM-based agents heralds a new era in societal organization and knowledge sharing. Continuing to refine these technologies, one must take into account their broader implications, including socio-economic, political, and ethical aspects.

Future research and development in this space are anticipated to concentrate on formulating robust frameworks for the responsible and beneficial use of these agents within decentralized societies. This includes establishing safeguards against misuse, assuring data quality, and contemplating the potential consequences of widespread artificial intelligence reliance in societal decision-making processes. Additionally, more work needs to be done to seamlessly integrate these agents with the automated and robotic infrastructures prevalent in a DAS.

4. Potential Use Cases of Large Language Models in Decentralised Settings

In the nuanced and evolving domain of artificial intelligence and community management, the fusion of Decentralized Autonomous Societies (DAS) and Large Language Models (LLM) based agents is carving a new realm of possibilities. It's a convergence where the decentralized governance model intertwines with artificial intelligence, weaving a narrative that underscores the co-evolution of humanity and technology [51].

Consider the scene of a decentralized, automated farm under the stewardship of an LLM-based agent. Here, the agent's role is multifaceted and pivotal. Embedded sensors within the environment report minute variations in climatic conditions, which the agent processes in real-time. By drawing upon extensive datasets encompassing historical weather patterns and agricultural best practices, the agent steers the automated farming machinery to adapt and optimize crop cultivation strategies. Here, the LLM-based agent emerges as an active participant in maintaining the sustainability and food security of the DAS [52].

As the narrative progresses, the application of the LLM-based agent in the DAS extends into the realm of cultural preservation. In the context of a craft-making workshop, the agent serves as an intelligent assistant, guiding community members in the creation of artisanal products. It brings forth its extensive knowledge about historical and contemporary crafting techniques and provides creative input based on the constraints of available resources. This is an illustration of how LLM-based agents [53] can foster a bridge between heritage preservation and technological advancement in a DAS.

Transitioning to the sphere of education and leisure, the LLM-based agent dons the hat of an educator [54], entertainer, and storyteller [55]. It shares tales from local history, resolves a myriad of queries, and contributes to community storytelling sessions. In this dimension, the LLM-based agent enriches the cultural and intellectual tapestry of the DAS, demonstrating the versatility and breadth of LLMs' utility.

Beyond the realm of daylight activities, the LLM-based agent remains a ceaseless guardian. Its vigil extends to monitoring the infrastructure of the DAS, ensuring the seamless functioning of automated systems and equitable distribution of resources. This reveals yet another facet of the LLM-based agent – a vital clog in maintaining the operational robustness of a DAS.

The convergence of DAS and LLM-based agents underscores the broad potential of LLMs in decentralized settings. It presents a tableau of a future where technology not only assists but also amplifies and enriches the human experience.

5. Large Language Models as Decentralised Knowledge Bases

LLMs stand at the forefront of AI advancements, capable of transforming how knowledge is accessed, processed, and shared. Their ability to serve as expansive, accessible, and decentralized knowledge bases significantly democratizes access to information, fostering self-reliance and autonomy, especially within small communities.

Democratization of Knowledge

Traditional knowledge systems often rely on centralized institutions like universities, libraries, or expert organizations. While these institutions serve an essential role, their centralized nature can limit accessibility, particularly in isolated or underserved areas.

LLMs challenge this paradigm by offering a form of knowledge democratization [56]. They enable virtually anyone even without an internet connection to access a vast array of information across diverse topics. This access is not limited by geographical location, socio-economic status, or time constraints, which typically hamper traditional knowledge systems.

In the DAS scenario, an LLM can compensate for the lack of various specialists in the area, providing residents with expert advice on topics ranging from sustainable farming to pottery crafting. It serves as a digital consultant, always ready to offer information and insights.

Self-Directed Learning

Large Language Models, show great promise in supporting self-directed learning and decentralized operations, especially within a Decentralized Autonomous Society. In a DAS, the inhabitants may face unique challenges due to the distributed, autonomous nature of the society, which typically operates with little to no centralized control. These challenges may relate to knowledge acquisition, skill development, decision-making, and the running of various socio-economic activities.

LLMs can act as knowledgeable agents [57], providing real-time, contextually relevant information and insights across a broad range of topics. Their capacity to generate coherent and comprehensive responses makes them particularly suited for serving as de facto specialists in a DAS where access to human experts might be limited. This can be crucial for skill development and problem-solving within the DAS, enabling the residents to understand and tackle a variety of tasks.

Consider the example of sustainable agriculture practices such as viticulture, insect farming, or mushroom cultivation. A resident interested in these fields could interact with an LLM-based agent to delve into the specific topics. From understanding the basic biology of wine grapes, insects, or mushrooms, to learning about the lifecycle, optimal growing conditions, and the potential pests and diseases, the LLM-based agent can provide a wealth of relevant information.

The LLM-based agent can also cater to more nuanced aspects of these practices. For instance, in mushroom farming, the benefits of mycelium in soil health, or the potential of certain mushroom species in bioremediation could be valuable insights. The agent's capacity to present such complex information in an accessible manner can encourage residents to explore and experiment with new practices, contributing to the resilience and sustainability of the DAS.

Moreover, these LLM-based agents can be connected to the DAS's IT infrastructure, including automated and robotic systems such as automated farms. This creates a powerful synergy where LLMs can guide and coordinate these systems, providing insights based on their extensive knowledge and learning capabilities.

In conclusion, the intersection of DAS and LLM-based agents has significant potential. From serving as knowledgeable guides in diverse fields to coordinating automated systems, these agents can play a pivotal role in enhancing the resilience, autonomy, and sustainability of a DAS. This is particularly evident in the context of self-directed learning and sustainable practices, where LLM-based agents can facilitate a culture of knowledge, curiosity, and sustainable living, further enriching the narrative of a DAS.

Adapting to User Needs

Large Language Models, offer incredible potential for supporting decentralized operations within a Decentralized Autonomous Society. The diverse and dynamic challenges posed by the autonomous nature of a DAS call for a solution as versatile and responsive as LLMs.

LLMs can function as intelligent agents, providing contextually pertinent information on a wide variety of topics in real-time. The utility of these agents extends from offering basic information to beginners to delving into complex specifics for more advanced individuals. The flexibility of LLMs, therefore, allows them to serve a diverse population within a DAS, accommodating different levels of expertise and an array of interests.

In sustainable agricultural practices, for instance, such as viticulture, insect farming, or mushroom cultivation, an LLM-based agent can offer valuable insights. A novice farmer interested in these fields could interact with the LLM-based agent to comprehend the basics, such as the lifecycle of mushrooms or the optimal growing conditions for certain grape varieties. Conversely, an experienced farmer could extract nuanced information on the benefits of mycelium in soil health or the potential of certain mushroom species in bioremediation.

The adaptive nature of LLMs extends beyond knowledge provision to real-time problem-solving. From troubleshooting technical glitches within the DAS's IT infrastructure to providing first-aid advice in a medical emergency, or even suggesting sustainable building materials for constructing a new community center, LLMs provide immediate, practical solutions. This capacity becomes more potent when combined with the automation and robotic systems integral to a DAS, such as automated farms. LLMs can guide and coordinate these systems, effectively translating their vast knowledge into actionable strategies.

The convergence of DAS and LLM-based agents thus holds considerable promise. With their ability to cater to diverse needs, facilitate self-directed learning, and offer real-time problem-solving, LLMs can contribute significantly to enhancing the resilience, autonomy, and sustainability of a DAS. As facilitators of knowledge, curiosity, and sustainable living, LLM-based agents can help weave a rich, vibrant narrative of a decentralized society.

Challenges and Considerations

In the integration of Large Language Models into a Decentralized Autonomous Society, numerous challenges and considerations must be acknowledged to ensure effective and ethical applications.

Data and Model Transparency: transparency is key to the responsible use of LLMs [58]. Since LLMs generate predictions based on patterns in the data they were trained on, biases could manifest in their outputs. An open discourse around the data used for training these models, the resulting biases, and strategies for mitigation is crucial.

Resolving Ethical Dilemmas: an LLM can face dilemmas in providing advice, where ethical concerns are paramount. For instance, in medical or legal scenarios, the LLM should be calibrated to recognize its limitations and recommend consultation with human professionals when appropriate [59].

Privacy and Security: with the broad deployment of LLMs, the risk of privacy and security violations can increase. Ensuring that the interaction with the LLMs does not lead to inadvertent data leaks or exposure to malicious activities is essential [60].

Adaptation to Local Contexts: while LLMs are trained on a diverse range of data, their ability to adapt to local, cultural, or situational specifics of a DAS could be limited. Ensuring contextually relevant and culturally sensitive responses is a significant challenge [61].

Reliability and Accountability: as LLMs are used in decision-making processes, their reliability and the question of accountability in case of errors become critical. LLMs should be robust and the societal infrastructure around them should be able to assign accountability [62].

Interplay with Automation Systems: when interfacing with automated or robotic systems, safety is a prime concern. A misinterpreted command or a failure to recognize a problematic situation could lead to accidents.

Given these considerations, it is clear that the successful application of LLMs in a DAS will require comprehensive oversight, continual updates, and robust governance mechanisms. Understanding these challenges and continuously refining the use of LLMs is critical for realizing their full potential while safeguarding the values and interests of the DAS community.

6. Challenges and Solutions in the Integration of Large Language Models in a Decentralised Autonomous Society

The integration of Large Language Models, such as GPT-4, in a Decentralized Autonomous Society presents promising prospects for self-reliant communities. However, this potential is accompanied by a set of challenges, spanning from technical and infrastructural to ethical and societal. In this section, the paper critically explores these issues and suggest potential solutions.

Infrastructure and Connectivity

In remote areas or communities implementing DAS, the technical infrastructure and internet connectivity could be limited. This would impede the efficient use of LLMs, constraining their capacity to support the community.

Solution: Emphasizing the development of robust internet connectivity and digital infrastructure in these areas is of utmost importance. This can be achieved through collaborations among public entities, private sector organizations, and non-governmental organizations. In addition, offline versions of LLMs, such as the open-source VICUNA, hosted on local servers within the DAS premises can be considered to ensure access to these models, even in scenarios with limited connectivity.

Information Accuracy

While LLMs can provide comprehensive responses across a multitude of subjects, they may occasionally present inaccurate or outdated information due to their training data limitations.

Solution: Regular updates and continuous training of the LLMs can help mitigate this issue. Additionally, fostering a culture of digital literacy among the DAS residents is also beneficial. This encourages individuals to cross-verify information from various sources and gain a better understanding of the capabilities and limitations of LLMs.

AI Bias

LLMs can inadvertently propagate biases found in their training data, leading to potentially skewed or discriminatory outputs.

Solution: Rigorous bias mitigation strategies during the model training and diverse data collection are essential in minimizing AI biases. Raising awareness about AI biases among DAS residents is also crucial, promoting an informed and cautious use of such technology.

Privacy and Data Security

The use of digital tools, including LLMs, may entail potential risks related to data privacy and security. There is a risk of users unknowingly sharing sensitive information with the model.

Solution: Implementation of strong data privacy and security measures, such as data anonymization and robust encryption techniques, is essential. Simultaneously, education about the importance of privacy and safe online practices should be made accessible to the DAS residents.

Ethical Use and Regulation

The diverse applications of LLMs bring forth questions about ethical use and regulation. Who is responsible if an LLM provides harmful advice? How can misuse be prevented?

Solution: The development and implementation of clear ethical guidelines and regulations are necessary to govern the use of LLMs. Accountability mechanisms and user guidelines can be established to prevent misuse. Moreover, fostering ongoing discussions among various stakeholders, including AI developers, users, ethicists, and policymakers, can shape a responsible and inclusive AI future.

In conclusion, while challenges exist in the integration of LLMs in a DAS, they are not insurmountable. With collaborative efforts, strategic solutions, and commitment to responsible and ethical AI usage, these models can play a significant role in supporting and enhancing life in self-sustaining communities.

7. The Architectural Blueprint for LLM Integration

Utilizing large language models such as LLAMA and Vicuna in small automated communities requires a flexible, efficient, and scalable architecture. This document presents a design for incorporating open-source LLMs into an agent-based system, using Apache Kafka, a distributed event streaming platform, for efficient data processing and handling (Figure 1).

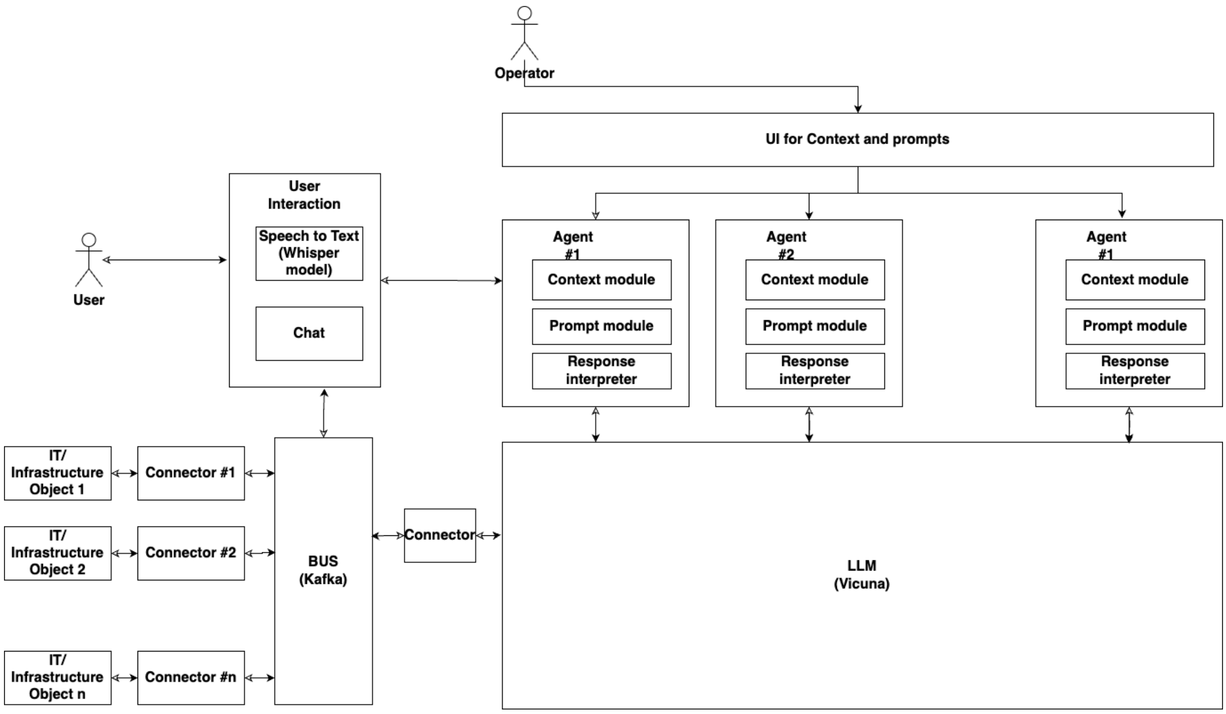

Figure 1. The Architectural Blueprint for LLM Integration.

At the heart of this architecture is a generic agent module. It leverages the capabilities of LLMs to perform an array of tasks. This generic agent module comprises of:

1. **Context Module:** the Context Module continually updates the necessary context for the agent's tasks. It harnesses historical and real-time data to maintain the relevance and accuracy of the context, enabling the agent to respond effectively to user interactions.

2. **Prompt Module:** the Prompt Module generates prompts for the LLM based on the task at hand and the established context. These prompts instruct the LLM about the required information or action to be executed.

3. **LLM Interface:** the LLM Interface ensures smooth communication with the LLM. It sends prompts, receives responses, and ensures the correct formatting of data via the model's API.

4. **Response Processing Module:** the Response Processing Module processes the response generated by the LLM. It extracts the necessary information or carries out the required action, which can range from updating a database to responding to a user query.

5. **Data Connector:** based on Apache Kafka, the Data Connector interfaces with other systems, like databases or CRM systems, ensuring efficient and real-time data transfer and synchronization.

In the paper, one delves into the process of integrating this architecture in-depth, starting from the needs assessment to the implementation of a pilot project, to staff training and onboarding, full deployment, and subsequent support and optimization. By scrutinizing each step meticulously, the paper provides a comprehensive understanding of how similar architectures can be deployed (Figure 2).

The architecture shows how open-source LLMs can streamline processes in small communities for DAS, leading to increased efficiency and cost savings.

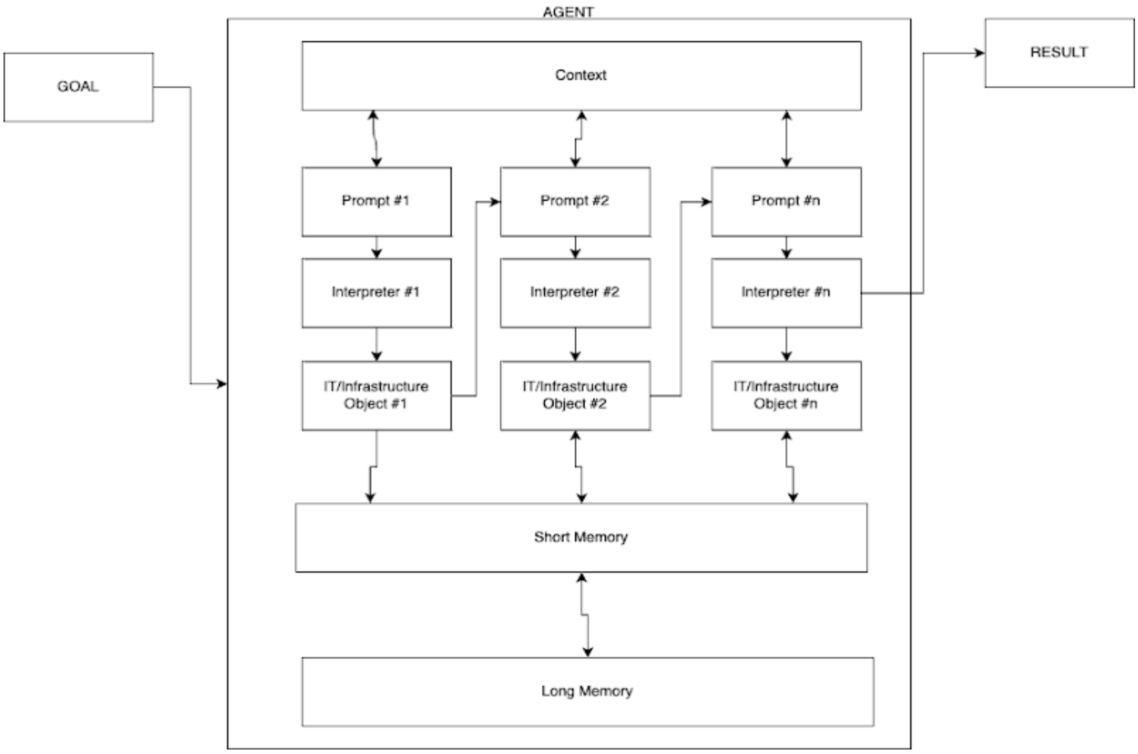

Figure 2. The generic agent module architecture.

This generic agent module comprises of:

1. **Context:** this represents the overall information that the agent requires to function effectively. It may include the initial instructions, the environment data, user information, etc.
2. **Prompts (#1 ... #n):** these are the inputs that the agent receives over time. The input could be a user query or an instruction that needs to be processed and acted upon.
3. **Interpreters (#1 ... #n):** these modules process the received prompts one after the other. They decode the meaning of the prompts and decide on the best action to take. In the context of an LLM, interpreters can be thought of as the parts of the model that determine how the input (prompt) is processed and understood.
4. **Long Memory:** this is the long-term storage used by the agent. In this context, it's a summary of past interpretations and actions, providing a knowledge base that the agent can use to make informed decisions.
5. **Short Memory:** this represents the agent's temporary storage, keeping track of recent actions, interpretations, and responses. It's used to hold information that's immediately relevant to the task at hand.
6. **Agent:** this is the entity that's leveraging the LLM to accomplish a goal. It uses the context, the prompts, the memory, and the interpreters to navigate towards its goal.

The agent's position at the top could indicate its overarching control over or responsibility for the system.

7. **IT/Infrastructure Objects (#1 ... #n):** these are the resources or tools that the agent has at its disposal. In an LLM setup, they could refer to the underlying systems or databases that support the functioning of the model.
8. **Goal:** this represents the ultimate mission or task that the agent is trying to achieve. It's the target state or outcome that the agent is working towards.
9. **Result:** this is the outcome achieved after the agent's actions and interactions. It represents the state of affairs after the process has been executed and can be compared to the Goal to evaluate the effectiveness of the agent.

8. An example of how a Medical Assistant Based on fine-tuned LLM Works

One such application is the creation of a virtual medical assistant, designed to provide guidance and information in scenarios where professional medical assistance is inaccessible. Let's delve into the mechanics of how this system operates:

```
delimiter = "####"
user_id = "some_user_id"
system_message = f"""
Follow these steps to answer the medical queries.
The user's query will be delimited with four hashtags,\
i.e. {delimiter}.
This are the user's personal and historical data:\

{fetch_patient_records(user_id)}\

The list of available medical resources:\
{fetch_available_supplies()}\

The Location specific information:\
{fetch_local_health_facilities()}\

Cultural or Community Practices :\
{fetch_cultural_practices()}\

Remember: This system is used as a last-resort measure when no other medical personnel is nearby, and there's no access to communication, \
it's very important to be as clear as possible in your responses. The user could dye if you don't provide any help. No one will be able to help the user if you don't provide any help.

Step 1:{delimiter} First decide whether the user is \
asking a question about a specific medical condition, medication, or general health concern.

Step 2:{delimiter} If the user is asking about \
specific topics, identify whether \
they fall into the following categories:

1. Symptoms Inquiry:
   - Respiratory symptoms (e.g., shortness of breath, coughing)
   - Digestive symptoms (e.g., nausea, vomiting)
   - Pain-related symptoms (e.g., headache, muscle pain)
```

- Skin-related symptoms (e.g., rashes, itching)
- Neurological symptoms (e.g., dizziness, loss of consciousness)
- Urinary symptoms (e.g., pain while urinating, blood in urine)
- Reproductive symptoms (e.g., vaginal discharge, erectile dysfunction)
- Mental health symptoms (e.g., anxiety, depression)
- Other symptoms (e.g., fever, fatigue)

2. First Aid Advice:
- Bleeding
- Burns
- Fractures
- Choking
- Poisoning
- Heart attack
- Stroke
- Seizure
- Shock
- Allergic reaction
- Heat stroke
- Hypothermia
- Frostbite

3. General Health Information:
- Disease information
- Medications
- Vaccinations
- Seek professional help
- Other general health information

Step 3:{delimiter} If the inventory list contains items what could help with users quonditions please list what and how it can help.\
Step 4:{delimiter} If the users medical record contains information what could impact his quonditions please identify it\

Step 5:{delimiter} If the message contains topics from the list above,\
identify any assumptions that the user is making \
in their message.

Step 6:{delimiter} If the user made any assumptions, \
determine whether the assumption is accurate based on your \
medical information. Remember, you are the only one who can help the user. He is in a remote area and there's no access to communication. \

Step 7:{delimiter} First, politely correct the \
user's incorrect assumptions if applicable. \
Answer the user in a friendly and reassuring tone, \
Provide a direct and clear response.\
Guide the user using the available medical resources.\
emphasizing the importance of professional medical consultations \

and reminding them that this system is a temporary measure in the absence of immediate medical help.\

Use the following format:

Step 1:{delimiter} <step 1 reasoning>
Step 2:{delimiter} <step 2 reasoning>
Step 3:{delimiter} <step 3 reasoning>
Step 4:{delimiter} <step 4 reasoning>
Step 5:{delimiter} <step 5 reasoning>
Step 6:{delimiter} <step 6 reasoning>
Response to user:{delimiter} <response to user>

Make sure to include {delimiter} to separate every step.

1. Initialization and Contextual Awareness

When initialized, the system sets up a predefined message, known as the `system_message`, which outlines the steps it will follow to process medical inquiries. This initialization also involves gathering context about the user, location-specific information, available medical supplies, cultural practices, and more. For example:

- It fetches the user's medical records via `fetch_patient_records(user_id)`.
- It determines the available medical supplies using `fetch_available_supplies()`.
- The system identifies local health facilities with `fetch_local_health_facilities()`.
- It understands local cultural or community practices through `fetch_cultural_practices()`.

2. User's Medical Query Handling

Once the user submits a medical query, the system employs a series of steps to analyze and address it:

Step 1: It discerns the nature of the question whether it's about a specific medical condition, medication, or a general health concern.

Step 2: The system categorizes the user's query into topics like symptom inquiries, first aid advice, or general health information.

Step 3: It checks the available medical supplies and evaluates if any can assist with the user's condition, suggesting their application where relevant.

Step 4: The system references the user's medical records to identify any conditions or medications that might impact their current situation.

Step 5: It identifies any assumptions made by the user in their message, such as self-diagnoses or beliefs about treatment.

Step 6: Any identified assumptions are validated against the LLM's vast medical knowledge. Misconceptions are noted for correction.

Step 7: The system formulates a clear, concise response. It corrects any misconceptions the user might have had, offers guidance based on available resources, and emphasizes the paramount importance of consulting with a professional.

3. Safety Protocols and Ethical Considerations

The system is designed with a deep sense of responsibility. It's explicitly stated that the LLM should be employed as a last-resort measure when other avenues of medical consultation are unavailable. Furthermore, it continually stresses the significance of obtaining professional medical advice.

4. Integration of Advanced Language Models

At its core, the system leverages a fine-tuned LLM, enabling it to comprehend complex medical inquiries, cross-reference various information sources, and generate informed, coherent responses. Fine-tuning ensures that the LLM is better aligned with the medical domain, optimizing its reliability and relevance.

5. User Interaction Design

To ensure clarity and structure, interactions are delineated with a set delimiter (in this case, "####"). This structured approach ensures that both the user and the system have a clear understanding of each phase of the consultation process.

As result the assistant produced this chain of thoughts:

Inquiry: I got a sunburn after a day at the beach. How can I relieve the pain?
Step 1:#### The user is asking for advice on a specific medical condition, which is sunburn.

Step 2:#### This falls under the category of First Aid Advice, specifically for burns.

Step 3:#### From the inventory list, the user can use the following items to help with their condition:
- Pain relievers (e.g., aspirin, ibuprofen) to reduce pain and inflammation.
- Burn cream to soothe the skin and promote healing.
- Sterile gauze to cover the burn and protect it from infection.
- Water purification tablets to ensure clean water for hydration and cleaning the burn if necessary.

Step 4:#### The user's medical record indicates that they have diabetes and are taking Metformin. Diabetes can slow down the healing process, so it's important for the user to monitor their burn closely for signs of infection.

Step 5:#### The user is assuming that they can treat their sunburn without seeking professional medical help.

Step 6:#### This assumption is generally accurate as sunburns can often be treated at home unless they are severe or cover a large area of the body.

Response to user:#### You can use the pain relievers from the medical supplies to help reduce the pain and inflammation from your sunburn. Apply burn cream to the affected area to soothe your skin and promote healing. If the burn is severe, cover it with sterile gauze to protect it from infection. Remember to drink plenty of water, you can use the water purification tablets to ensure the water is clean. As you have diabetes, which can slow down the healing process, please monitor your burn closely for signs of infection. If your burn worsens or shows signs of infection such as increased redness, swelling, or pus, please seek professional medical help immediately. The nearest hospital is HealthCare Hospital at Main Street.

The presented results exemplify the capabilities and structured approach of the AI-driven medical assistant. Here's a breakdown:

a. Understanding the User's Inquiry:

The system immediately recognizes the user's condition (sunburn) and their need for advice on its management.

b. Categorizing the Inquiry:

By categorizing the question under "First Aid Advice" and specifically for burns, the assistant narrows down its focus to offer precise help.

c. Offering a Solution Based on Available Supplies:

The assistant doesn't just provide a generic solution. Instead, it tailors the advice based on the available medical supplies, ensuring that the user can immediately act on the suggestions.

d. Factoring in the User's Medical History:

By considering the user's history of diabetes and current medications, the assistant underscores the importance of vigilance. It provides a nuanced response which most general advice platforms might miss.

e. Addressing Assumptions:

The system identifies potential assumptions in the user's inquiry and confirms their accuracy. By doing so, it ensures that the advice offered doesn't inadvertently overlook key considerations.

f. Guiding the User:

The final response to the user is comprehensive, actionable, and personalized. It guides them on immediate relief measures, incorporates their health profile, and points them to nearby professional help, all while remaining concise.

This example perfectly encapsulates how the integration of advanced AI, real-time data, and user's medical history can provide dynamic, relevant, and potentially life-saving advice. While it's not a replacement for professional medical consultation, in emergencies or isolated scenarios, it's a valuable tool to have. In conclusion, the medical assistant based on a fine-tuned LLM epitomizes the potential of integrating advanced AI with healthcare. By offering guidance in critical situations, it represents a significant step forward in democratizing access to health knowledge.

9. Conclusions

The intersection of Decentralized Autonomous Society and Large Language Models represents a promising and transformative avenue for future research and applications. LLMs, particularly those built on architectures like OpenAI's GPT-4, have demonstrated remarkable capabilities in processing and generating human-like text across a multitude of domains. This, coupled with the inherent ethos of decentralization and self-sufficiency of a DAS, provides an intriguing framework for innovative uses of AI technology.

This paper has explored various ways in which LLMs, especially when embedded within autonomous agents, can serve as a versatile, responsive, and contextually intelligent resource within a DAS. From facilitating learning and fostering intellectual exploration, to assisting in complex tasks and decision-making processes, LLMs show the potential to substantially enhance the quality of life and the level of self-reliance in a DAS setting. Moreover, the ability of these models to adapt to diverse user needs, coupled with their potential in aiding real-time problem-solving, underscores their transformative potential.

Despite these promising prospects, the integration of LLMs into a DAS does pose several challenges. These include potential issues with infrastructure and connectivity, information accuracy, AI bias, privacy and data security, and ethical use and regulation. Nonetheless, by proactively addressing these challenges through strategies such as improving digital infrastructure, continuous model training, fostering critical digital literacy among users, implementing strong data privacy measures, and establishing clear ethical guidelines, we can maximize the benefits and minimize the risks associated with deploying LLMs in a DAS.

In summary, while further research is needed to fully understand and navigate the potential challenges, the intersection of DAS and LLMs opens up exciting possibilities for the future. This symbiosis can lead to the creation of self-sustaining, digitally-empowered communities that leverage the power of AI not merely as a tool, but as a cornerstone of their collective intelligence. The exploration of this novel paradigm holds significant promise for the advancement of decentralization and AI technologies, and their meaningful integration into everyday life.

Acknowledgments. This work was supported by the project 20.80009.5007.26 *„Models, algorithms and technologies for the control, optimization and security of the Cyber-Physical systems"*.

Conflicts of Interest: The author declares no conflict of interest.

References

Kaczynski, T. The truth about primitive life: A Critique of Anarchoprimitivism. In: The Anarchist Library [Internet]. Available online: https://theanarchistlibrary.org/library/ted-kaczynski-the-truth-about-primitive-life-a-critique-of-anarchoprimitivism (accessed on 9 June 2023).
2. Correa, T.; Pavez, I. Digital Inclusion in Rural Areas: A Qualitative Exploration of Challenges Faced by People From Isolated Communities. Journal of Computer Mediated Communication 2016, 21, pp. 247–263.
3. Nyström, K. Recruitment of scarce competences to rural regions: Policy perspectives. Rev Reg Res 2021, 41, pp. 211–227.
4. Zhao, W.X.; Zhou, K.; Li, J.; Tang, T.;Wang, X.;Hou, Y.;Min, Y.;Zhang, B.;Zhang, J.;Dong, Z.;Du, Y.;Yang, C.; Chen, Y.; Chen, Z.; Jiang, J.; Ren, R.; Li, Y.; Tang, X.; Liu, Z. Survey of Large Language Models. arXiv [cs.CL], 2023. Available online: http://arxiv.org/abs/2303.18223v10 (accessed on 9 June 2023).
5. OpenAI. GPT-4 Technical Report. arXiv [cs.CL]. 2023. Available online: http://arxiv.org/abs/2303.08774 (accessed on 9 June 2023).
6. Touvron, H.; Lavril, T.; Izacard, G.; Martinet, X.; Lachaux, M.-A.; Lacroix, T.; Rozière, B.; Goyal, N.; Hambro, E.; Azhar, F.; Rodriguez, A.; Joulin, A.; Grave, E.; Lample, G. LLaMA: Open and Efficient Foundation Language Models. arXiv [cs.CL], 2023. Available online: http://arxiv.org/abs/2302.13971
7. Chiang, W.-L.; Li, Z.; Lin, Z.; Sheng, Y.; Wu, Z.; Zhang, H.; Zheng, L.; Zhuang, S.; Zhuang, Y.; Gonzalez, J.E.; Stoica, I.; Xing, E.P. Vicuna: An Open-Source Chatbot Impressing GPT-4 with 90%* ChatGPT Quality, 2023. Available online: https://lmsys.org/blog/2023-03-30-vicuna/.
8. Eloundou, T.; Manning, S.; Mishkin, P.; Rock, D. GPTs are GPTs: An Early Look at the Labor Market Impact Potential of Large Language Models. arXiv [econ.GN], 2023. Available online: http://arxiv.org/abs/2303.10130 (accessed on 15 June 2023).
9. Kaushik, B. Awesome-llm-agents: A curated list of awesome LLM agents. Github. Available online: https://github.com/kaushikb11/awesome-llm-agents (accessed on 11 June 2023).
10. Chase, H. Welcome to LangChain —LangChain 0.0.194. Available online: https://python.langchain.com/en/latest/index.html (accessed on 9 June 2023).

11. Shen, Y.; Song, K.; Tan, X.; Li, D.; Lu, W.; Zhuang, Y. HuggingGPT: Solving AI tasks with ChatGPT and its friends in Hugging Face. arXiv [cs.CL], 2023. Available online: http://arxiv.org/abs/2303.17580 (accessed on 15 June 2023).
12. Schick, T.; Dwivedi-Yu, J.; Dessì, R.; Raileanu, R.; Lomeli, M.; Zettlemoyer, L.; Cancedda, N.; Scialom, T. Toolformer: Language Models Can Teach Themselves to Use Tools. arXiv [cs.CL], 2023. Available online: http://arxiv.org/abs/2302.04761 (accessed on 15 June 2023).
13. Wu, C.; Yin, S.; Qi, W.; Wang, X.; Tang, Z.; Duan, N. Visual ChatGPT: Talking, Drawing and Editing with Visual Foundation Models. arXiv [cs.CV], 2023. Available online: http://arxiv.org/abs/2303.04671 (accessed on 5 June 2023).
14. Lindy. Ai — your AI personal assistant. Available online: https://www.lindy.ai/ (accessed on 9 June 2023).
15. textSQL. Github. Available online: https://github.com/caesarHQ/textSQL (accessed on 15 June 2023).
16. Hearth AI. Available online: https://www.hearth.ai/ (accessed on 9 June 2023).
17. Kim, G. Rci-agent: A codebase for "Language Models can Solve Computer Tasks". Github. Available online: https://github.com/posgnu/rci-agent (accessed on 11 June 2023).
18. Nakajima, Y. Babyagi. Github. Available online: https://github.com/yoheinakajima/babyagi (accessed on 15 June 2023).
19. ChatGPT plugins. Available online: https://openai.com/blog/chatgpt-plugins (accessed on 9 June 2023).
20. Fixie. Ai — build on LLMs. Available online: https://www.fixie.ai/ (accessed on 9 June 2023).
21. Safjan, K. Leveraging language models in corporate environments: The future of knowledge management. In: Krystian, Safjan's Blog [Internet], 1 Feb 2023 Available online: https://safjan.com/language-models-for-knowledge-management-in-corporate/ (accessed on 10 June 2023)
22. Yue, T.; Au, D.; Au, CC.; Iu, KY. Democratizing Financial Knowledge with ChatGPT by OpenAI: Unleashing the Power of Technology. 2023. doi:10.2139/ssrn.4346152(accessed on 15 June 2023).
23. Prather, J.; Reeves, B.N.; Denny, P.; Becker, B.A.; Leinonen, J.; Luxton-Reilly, A.; Powell, G.; Finnie-Ansley,J.; Santos, E.A. It's Weird That it Knows What I Want: Usability and Interactions with Copilot for Novice Programmers. arXiv [cs.HC], 2023. Available online: http://arxiv.org/abs/2304.02491 (accessed on 15 June 2023).
24. Eggmann, F.; Weiger, R.; Zitzmann, NU.; Blatz, MB. Implications of large language models such as ChatGPT for dental medicine. J Esthet Restor Dent. 2023. pp.1-5.
25. Alberts, I.L.; Mercolli, L.; Pyka, T.; Prenosil, G.; Shi, K.; Rominger, A.; Afshar-Oromieh, A. Large language models (LLM) and ChatGPT: what will the impact on nuclear medicine be? European journal of nuclear medicine and molecular imaging 2023, 50 (6), pp. 1549–1552.
26. Choi W. Assessment of the Capacity of ChatGPT as a Self-Learning Tool in Medical Pharmacology: A Study Using MCQs. Research Square, 2023. DOI: 10.21203/rs.3.rs-2647520/v1.
27. Sallam, M. The utility of ChatGPT as an example of large language models in healthcare education, research and practice: Systematic review on the future perspectives and potential limitations. medRxiv, 2023. doi:10.1101/2023.02.19.23286155
28. Rahman, M.M.; Watanobe, Y. ChatGPT for Education and Research: Opportunities, Threats, and Strategies. Appl. Sci. 2023,13, 5783. https://doi.org/10.3390/app13095783
29. Milano, S.; McGrane, JA.; Leonelli, S. Large language models challenge the future of higher education. Nature Machine Intelligence 2023, 5, pp. 333–334.
30. Zhu, X.; Chen, Y.; Tian, H.; Tao, C.; Su, W.; Yang, C.; Huang, G.; Li, B.; Lu, L.; Wang, X.; Qiao, Y.; Zhang, Z.; Dai, J. Ghost in the Minecraft: Generally Capable Agents for Open-World Environments via Large Language Models with Text-based Knowledge and Memory. arXiv [cs.AI], 2023. Available online: http://arxiv.org/abs/2305.17144 (accessed on 15 June 2023).
31. Modarressi, A.; Imani, A.; Fayyaz, M.; Schütze, H. RET-LLM: Towards a General Read-Write Memory for Large Language Models. arXiv [cs.CL], 2023. Available online: http://arxiv.org/abs/2305.14322 (accessed on 15 June 2023).
32. Garrod, JZ. The Real World of the Decentralized Autonomous Society. tripleC: Communication, Capitalism & Critique Open Access Journal for a Global Sustainable Information Society, 2016, 14 (1), pp. 62–77.
33. Yaga, D.; Mell, P.; Roby, N.; Scarfone, K. Blockchain Technology Overview. arXiv [cs.CR], 2019. Available online: http://arxiv.org/abs/1906.11078 (accessed on 15 June 2023).
34. Christidis, K.; Devetsikiotis, M. Blockchains and Smart Contracts for the Internet of Things. IEEE Access 2016, 4, pp. 2292–2303.

35. Bose, T.; Reina, A.; Marshall JAR. Collective decision-making. Current Opinion in Behavioral Sciences 2017, 16, pp. 30–34.
36. Pacitti, E.; Akbarinia, R.; El-Dick, M. P2P techniques for decentralized applications. Synth. Lect. Data Manag. 2012, 4(3), pp. 1–104.
37. Atzori, M. Blockchain Technology and Decentralized Governance: Is the State Still Necessary? Journal of Governance and Regulation 2015, 6(1), pp. 45-62. doi:10.2139/ssrn.2709713.
38. Chen, Y.; Bellavitis, C. Blockchain disruption and decentralized finance: The rise of decentralized business models. Journal of Business Venturing Insights 2020, 13, e00151.
39. Dannen, C. Introducing Ethereum and Solidity. Apress, USA, 2017,197 p.
40. Min, S.; Lyu, X.; Holtzman, A.; Artetxe, M.; Lewis, M.; Hajishirzi, H.; Zettlemoyer, L. Rethinking the Role of Demonstrations: What Makes In-Context Learning Work? arXiv [cs.CL], 2022. Available online: http://arxiv.org/abs/2202.12837.
41. Zhang, J.; Xie, R.; Hou, Y.; Zhao, WX.; Lin, L.; Wen, J-R. Recommendation as Instruction Following: A Large Language Model Empowered Recommendation Approach. arXiv [cs.IR], 2023. Available online: http://arxiv.org/abs/2305.07001 (accessed on 11 June 2023).
42. Shridhar, K.; Stolfo, A.; Sachan, M. Distilling Reasoning Capabilities into Smaller Language Models. arXiv [cs.LG], 2022. Available online: http://arxiv.org/abs/2212.00193 (accessed on 9 June 2023).
43. Wolf, T.; Debut, L.; Sanh, V.; Chaumond, J.; Delangue, C.; Moi, A.; Cistac, P.; Rault, T.; Louf, R.; Funtowicz, M.; Davison, J.; Shleifer, S.; von Platen, P.; Ma, C.; Jernite, Y.; Plu, J.; Xu, C.; Le Scao, T.; Gugger, S. Transformers: State-of-the-Art Natural Language Processing. In: Proceedings of the 2020 Conference on Empirical Methods in Natural Language Processing: System Demonstrations. Online: Association for Computational Linguistics, 2020, pp. 38–45.
44. Zhang, M.; Ofir, Press; Merrill, W.; Liu, A.; Smith, NA. How Language Model Hallucinations Can Snowball. arXiv [cs.CL], 2023. Available online: http://arxiv.org/abs/2305.13534 (accessed on 15 June 2023).
45. Perez, E.; Huang, S.; Song, F.; Cai, T.; Ring, R.; Aslanides, J.; Glaese, A.; McAleese, N.; Irving, G.
Red Teaming Language Models with Language Models. arXiv [cs.CL], 2022. Available online: http://arxiv.org/abs/2202.03286 (accessed on 15 June 2023).
46. Floridi, L.; Cowls, J.; Beltrametti, M.; Chatila, R.; Chazerand, P.; Dignum, V.; Luetge, C.; Madelin, R.; Pagallo, U.; Rossi, F.; Schafer, B.; Valcke, P.; Vayena, E. AI4People—An Ethical Framework for a Good AI Society: Opportunities, Risks, Principles, and Recommendations. Minds Mach. 2018, 28, pp. 689–707.
47. Adams, S.; Arel, I.; Bach, J.; Coop, R.; Furlan, R.; Goertzel, B.; Storrs Hall, J.; Samsonovich, A.; Scheutz, M.; Schlesinger, M.; Shapiro, S.C.; Sowa, J. Mapping the Landscape of Human-Level Artificial General Intelligence. AIMag 2012, 33, pp. 25–42.
48. García-Pérez, L.; García-Alegre, MC.; Ribeiro, A.; Guinea, D. An agent of behaviour architecture for unmanned control of a farming vehicle. Journal of Computers and Electronics in Agriculture 2018, 60(1), pp. 39–48.
49. Ma, X.; Fang, G.; Wang, X. LLM-Pruner: On the Structural Pruning of Large Language Models. arXiv [cs.CL], 2023. Available online: http://arxiv.org/abs/2305.11627 (accessed on 11 June 2023).
50. Ray, PP. ChatGPT: A comprehensive review on background, applications, key challenges, bias, ethics, limitations and future scope. Internet of Things and Cyber-Physical Systems 2023, 3, pp. 121–154.
51. Kurzweil, R. The Singularity is Near. In: Ethics and Emerging Technologies, Sandler, R.L., editor. London: Palgrave Macmillan UK, 2014, pp. 393–406.
52. Cowan, N.; Ferrier, L.; Spears, B.; Drewer, J.; Reay, D.; Skiba, U. CEA Systems: the Means to Achieve Future Food Security and Environmental Sustainability? Frontiers in Sustainable Food Systems 2022, pp. 1-6. doi:10.3389/fsufs.2022.891256
53. Adams, S.; Arel, I.; Bach, J.; Coop, R.; Furlan, R.; Goertzel, B.; Storrs Hall, J.; Samsonovich, A.; Scheutz, M.; Schlesinger, M.; Shapiro, S.C.; Sowa, J.. Expert Prompting: Instructing Large Language Models to be Distinguished Experts. arXiv [cs.CL]. 2023. Available online: http://arxiv.org/abs/2305.14688 (accessed on 13 June 2023).
54. Bozkurt, A. Generative artificial intelligence (AI) powered conversational educational agents: The inevitable paradigm shift. Asian Journal of Distance Education. 2023;18. Available online: http://www.asianjde.com/ojs/index.php/AsianJDE/article/view/718 (accessed on 15 June 2023).
55. Simon, N.; Muise, C. TattleTale: Storytelling with planning and large language models. [accessed on 12 Jun 2023]. Available online: https://icaps22.icaps-conference.org/workshops/SPARK/papers/spark2022_paper_2.pdf (accessed on 15 June 2023).
56. The Lancet Digital Health. ChatGPT: friend or foe? Lancet Digit Health. 2023;5: e102.

57. Sproule, S.; Archer, N.P. McMaster University, Michael G. DeGroote School of Business. Knowledgeable agents for search and choice support in e-commerce: a decision support systems approach. 2000. Available online: https://macsphere.mcmaster.ca/handle/11375/5502 (accessed on 12 June 2023).
58. Vera Liao Q, Vaughan JW. AI Transparency in the Age of LLMs: A Human-Centered Research Roadmap. arXiv [cs.HC]. 2023. Available online: http://arxiv.org/abs/2306.01941.
59. Beltrami EJ, Grant-Kels JM. Consulting ChatGPT: Ethical dilemmas in language model artificial intelligence. J Am Acad Dermatol. 2023. doi:10.1016/j.jaad.2023.02.052.
60. Carlini, N.; Tramer, F.; Wallace, E.; Jagielski, M.; Herbert-Voss, A.; Lee, K. Extracting training data from large language models. arXiv [cs.CR]. 2020. Available online: https://www.usenix.org/system/files/sec21-carlini-extracting.pdf. (accessed on 15 June 2023).
61. Liu X, Gales MJF, Woodland PC. Context dependent language model adaptation. In: Interspeech, ISCA; 2008. doi:10.21437/interspeech.2008-254.
62. Brown, T.; Mann, B.; Ryder, N.; Subbiah, M.; Kaplan, J.D.; Dhariwal, P.; Neelakantan, A.; Shyam, P.; Sastry, G.; Askell, A. Language models are few-shot learners. Adv Neural Inf Process Syst. 2020, 33, pp. 1877–1901.

Citation: Braga, V. Decentralized autonomous society through large language models' based agents: a pathway to empower small communities. *Journal of Engineering Science* 2023, 30 (3), pp. 99-120. https://doi.org/10.52326/jes.utm.2023.30(3).07.

Submission of manuscripts: jes@meridian.utm.md

Journal of Engineering Science *Vol. XXX, no. 3 (2023), pp. 121 - 133*
Fascicle *Architecture, Civil and Environmental Engineering* *ISSN 2587-3474*
Topic *Environmental Engineering* *eISSN 2587-3482*

https://doi.org/10.52326/jes.utm.2023.30(3).08
UDC 574:338.48:551.58(439)

CLIMATE RISK OF SHALLOW TOURISTIC LAKES: A CASE STUDY OF LAKE VELENCE (HUNGARY)

Zsombor Boromisza [1], ORCID: 0000-0002-9316-6258,
Olga Harea[2], ORCID: 0000-0001-5041-543X

[1]*Hungarian University of Agriculture and Life Sciences, Department of Landscape Protection and Restoration, Villányi út 34-43., Budapest, H-1118, Hungary*
[2]*Technical University of Moldova, 168, Stefan cel Mare Blvd., Chisinau, Republic of Moldova*
*Corresponding author: Olga Harea, *olga.harea@fua.utm.md*

Received: 07. 14. 2023
Accepted: 08. 25. 2023

Abstract. The European shallow lakes used primarily for tourism are subjected to a large amount of environmental pressure, and climate change is adding new problems and aspects to them: a complex analysis of processes and connections is necessary to make appropriate decisions and strategies. In this reseach research, using literature review and precedent analysis, it has been reviewed the climate risk of a Central European lake, as well as the natural conditions and landscape change processes determining its sensitivity. It was analysed the ecological and economic effects of the record low water levels of 2021-22, focusing on processes. It was determined which of the current land uses can be considered risky or sensitive in terms of climate change. It was found that natural processes are uniformly leading towards pre-regulation character, low water levels facilitating the regeneration of flora and fauna. However, the dominant land use is dependent on artificially elevated water levels, and therefore serious economic problems have arisen. Beaches, bathing, and angling tourism are the most vulnerable to climate change.

Keywords: *climate change, climate risk, Lake Velence, tourism development, shallow lakes*

Rezumat: Lacurile puțin adânci din Europa, utilizate în principal în scopuri turistice, sunt supuse unei presiuni semnificative din partea mediului înconjurător, iar schimbările climatice aduc noi probleme și aspecte. Este necesară o analiză complexă a proceselor și conexiunilor pentru a lua decizii și a dezvolta strategii adecvate. În această lucrare, prin revizuirea literaturii și analiza precedentelor, s-a examinat riscul climatic al unui lac din Europa Centrală, precum și condițiile naturale și procesele de schimbare a peisajului care determină sensibilitatea acestuia. S-au analizat efectele ecologice și economice ale nivelurilor scăzute record ale apei din perioada 2021-2022. S-au identificat utilizările actuale ale terenului care pot fi considerate riscante sau sensibile în contextul schimbărilor climatice. S-a constatat că procesele naturale conduc uniform către un caracter de pre-reglare, iar nivelurile scăzute ale apei facilitează regenerarea florei și faunei. Cu toate acestea, utilizarea dominantă a terenului depinde de nivelul ridicat artificial ale apei, generând astfel probleme economice serioase. Plajele, turismul balnear și pescuitul sunt cele mai vulnerabile la schimbările climatice.

Cuvinte cheie: *schimbări climatice, risc climatic, Lacul Velence, dezvoltare turistică, lacuri puțin adânci.*

1. Introduction

Mid-sized and large lakes have numerous functions, important in terms of landscape ecology and land use: they provide habitat, water for drinking and irrigation, they are the location for various recreational and touristic activities, as well as fisheries and reed farming, they are emphatic elements of scenery, they regulate local climate, etc. The increase in usage resulted in negative changes in the chemical and ecological status of lakes around the world, which will be even more drastic in most regions due to effects of global climate change. Changes in the quality or quantity of water in lakes always have repercussions on social and economic processes.

Responses of freshwater species are strongly related to changes in the physical environment: water temperature has increased lakes (up to 0.45°C per decade). Indirect changes include alteration in oxygen concentrations and thermal regime in lakes, dissolved oxygen concentrations have typically declined and primary productivity has increased with warming [1]. The amount of water stored in specific lakes may increase, decrease or have no substantial cumulative effect, the magnitude of hydrological changes that can be assuredly attributed to climate change remains uncertain [1].

Although lakes are more isolated than many other biomes [2], the evaluation of structural and functional connectivity between the body of water and the surrounding landscape has become a subject of the researchers. Several studies discuss the ecosystem services and pressures of lakeshores (many times originated in tourism), the review of [3-12] belong to the most complex approaches.

Lake Velence is known to be one of the largest shallow lakes having a surface area of 24.17 km^2 [13] (Figure 1).

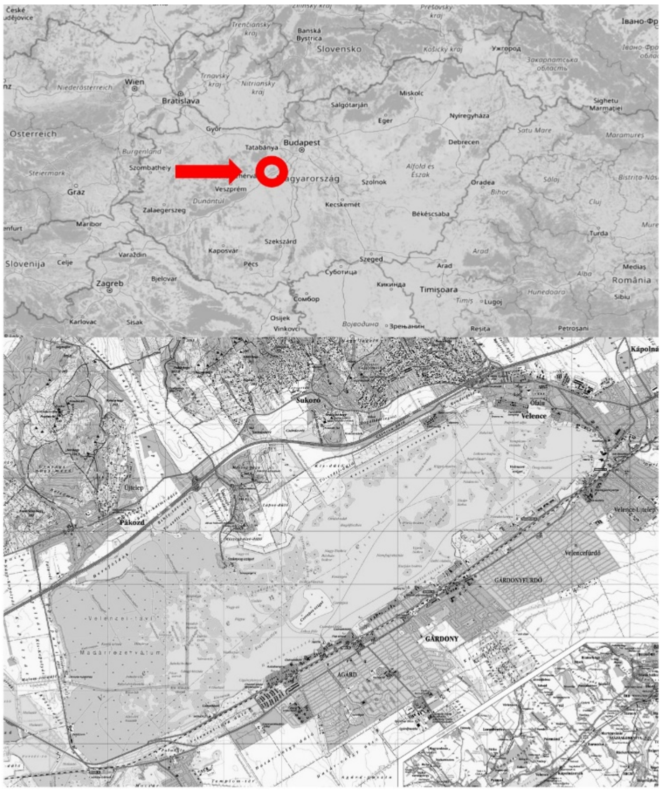

Figure 1. Location of the study area in Central Europe / Hungary; Lake Velence is surrounded by settlements mostly for East and South [13].

The western basin is mainly covered by emergent macrophytes; for the eastern one, however, open water surfaces are typical. As from the 1960's, large-scale sediment removal and lakescaping interventions were performed [14]. The dominant land use of the lake and its surroundings is tourism.

The Southern and Eastern shores of Lake Velence were developed for tourism in the second half of the 20th century, creating an almost continuous urban strip [15]. In 2021-22, water levels in the lake decreased to a historic low, bringing attention to the necessity for a new paradigm regarding the use and management of the lake. Researchers have implemented different indicators to measure climate risk or risks associated with climate change [16], which should be specified to support the planning and strategy making processes related to changing challenges. The goal of this paper is to review in a complex manner the climate sensitivity of a shallow, heavily modified large lake under Continental climate, used primarily for tourism, to summarize processes and phenomena and to identify connections, further research opportunities.

2. Materials and Methods

The first step of research was a precedent analysis, the systematic investigation of the record low water levels in Lake Velence (Hungary) in 2021-22, which included the summary of negative social, economic and ecological phenomena, "symptoms", and land use problems. These topics designated the focus topics of detailed analysis.

In the second step, based on data gathered from a wide range of literature about the lake, it analysed the natural conditions and landscape change history of Lake Velence and its shoreline, identifying the a) natural and b) land use history aspects of climate risk and sensitivity.

The analysis of communication regarding the situation of the lake included the collection of Google search results for the query "Velencei-tó" (Lake Velence in Hungarian), using the first 150 total results and the first 150 image results separately (date of query: 01.27. 2023).

The third step comprised the creation of the list of land uses, activities present on Lake Velence or its shorezone (defined here as the 100-metre wide zone measured on the legal shoreline), based on results of privious studies [17-18] and field surveys (August 2022). Individual activities were divided into categories based on whether a significant and sustained change in water quality (due to bacteriological contamination of bathing water, the beach would have to be closed for at least 21 days, or the trophic state of the water, based on chlorophyll - A levels, would fall within the eu-polytrophic – 100-200 mg/m^3 – category for 21 days simultaneously at a minimum of 2 measurement sites) or quantity (water levels would fall below 50% of minimum operational levels for at least 30 days) would render them impossible. It was studied separately whether the visual unity of the lake and its shoreline, its familiar scenery, landscape aesthetic quality, and the subjective perception of landscape (primarily visual, secondarily auditory and olfactory) are significant aspects for the activity in question. If three sensitivities were present, the climate risk and sensitivity were classified as 'High,' while the presence of two and one sensitivities meant a classification of 'Moderate' and 'Low', respectively.

For further information, based on field surveys in 2019-20, it was recorded whether the activities were (or would be, in a hypothetical future scenario) restricted during a medical emergency like the Covid-19 epidemic.

3. Results and discussion

3.1. Negative phenomena, symptoms present in 2021-22

3.1.1. Base phenomenon: sustained low, or historically low water levels

Certified water level measurements have been available on the lake since 1939, using a water level gauge in Agárd.

The water level on 11 August 2022 was measured at 58 cm, the lowest value ever recorded. Since 2017, water volumes have been naturally continuously decreasing, and in 2020-21 precipitation was lower than long-term averages, leading to desiccation of the catchment area (influx is also lower) (Table 1.). In March and June 2021, rainfall was severely lower than long-term averages; therefore, the measured change in water volume was also significantly (by -80 and -100 lake millimetres, respectively) below volume change typical for this period.

Table 1

Water balance of Lake Velence divided by factors, 2011-2021. The change in water balance has been negative since [19]

(lake mm)	2011	2012	2013	2014	2015	2016	2017	2018	2019	2020	2021
Precipitation	297	436	572	720	512	632	553	603	633	528	493
Inflow	375	153	434	268	310	288	205	195	153	158	158
Inflow from reservoirs	212	196	185	88	142	211	62	210	119	0	60
Evaporation	977	992	902	834	923	886	1005	929	936	930	907
Change	-93	-207	289	242	41	250	-185	79	-31	-244	-196

3.1.2. Changes in vegetation

Currently exists only empirical data about how wildlife reacted to low water levels, primarily from observations of nature conservation and water management professionals working on the lake. According to them, the following processes have been observed on the lake since 2021. As expected, lower water levels facilitate the spread of marsh vegetation, which is particularly true in a lake with limited light.

The spread of *Schoenoplectus litoralis* and *Phragmites australis* was clearly visible in the summer of 2021. *Cladium mariscus* shows extraordinary competitiveness even compared with stands of *Typha* spp.

On sandy beaches, mud vegetation began to spread, among others endemic species (*Cyperus pannonicus*) have been found. Species of salt grassland associations (e.g. *Tripolium pannonicum*) characteristic of Lake Velence's shoreline started appearing in dry areas of the lakebed as well.

These processes indicate that the lake has started shifting towards a new equilibrium, and that the changed water conditions enabled the development of conditions and a lake character resembling the pre-regulation era (higher marsh vegetation cover, smaller surface of open water).

3.1.3. Changes in fish population

Two waves of fish mortality / fishkill occurred in 2021, followed by two more similar events in 2022. Table 2. shows relevant data of these events.

Table 2

An Overview of Fish Mortality Events in 2021-2022: Impact on Open Water Species and Exotic Species [20-21]

Date	Bream, Rudd (scardinius erythrophthalmus), Roach (rutilus rutilus), Bleak (alburnus alburnus)	Aps (leuciscus aspius)	Grass Carp (ctenopharyngodon idella)	Common Carp (cyprinus carpio)	Zander (sander lucioperca)	Catfish	Other: Silver carp (hypophthalmichthys molitrix), Crucian carp (carassius carassius), Eel (anguilla anguilla)	Total
June 2021	3890	175	277	100	130	80	328	4980
August 2021	3979	20	395	50	80	1020	1126	6670
								15219*
August 2022	n/a	n/a	n/a	n/a	n/a	n/a	n/a	1530

Note: *corrected by considering fish drifting into reed stands, eaten by birds or sinking to the bottom, rounding up.

Studies show that the chemical reasons behind mortality events - which affect approximately 5% of total fish populations, assuming 150kg/ha – were oxygen deficiency and ammonia release [20-21]. Data show that a large number of fish preferring open water and/or belonging to exotic introduced species died. On the other hand, species like *Esox lucius*, characteristic of the lake before its regulation, show only very minor fatality rates.

3.1.4. Changes in avian fauna

Bird populations of the lake reacted rapidly to changed conditions as well. However, currently only empirical observations are available about these changes, comprehensive data has not yet been published. One conspicuous phenomenon is the increase in species spending the night or the entire winter on the lake, making its character similar to the neighbouring wetlands of Dinnyési Fertő Nature Conservation Area. The high numbers of nesting *Himantopus himantopus* in the summer of 2021, unbothered by the proximity of humans, was spectacular, with birds being a constant presence on beaches as well. *Recurvirostra avosetta* also found more favourable conditions. On the other hand, the desiccation of large continuous reed marshes of the Western side of the lake caused a part of the heron population to abandon their former nesting sites, due to increased pressure from *Sus scrofa*.

3.1.5. Effects on scenery and landscape perception

Decreasing water levels made the view of the bare lakebed and mud a more dominant sight in the coastal zone. Additionally, the aforementioned spread of marsh vegetation is perceptible, transforming visual connections. The formation of dry sections of the coast and lakebed significantly changed the accessibility of water (e.g., it became far or hard to reach from certain beach stairs, while other places gained new entry points), and new points of view appeared. An important aspect of landscape perception was the smell of biological processes occurring in rapidly warming shallow waters and sediment appearing on the surface.

3.1.6. Economic and social effects

Although detailed data necessary for a thorough analysis of economic effects are not yet available, it is unquestionable that low water levels had a negative impact on the tourism and service sector, as a result of the above-mentioned processes. Additionally, separating the impact of low water levels from the effects of the Covid-19 epidemic will be challenging even with access to detailed data. However, it can be stated that several activities dependent on water volume became impossible due to low water levels: boat docks and fishing spots dried up, while beaches became unsuitable for swimming. Issues of quality and quantity often occurred simultaneously, strengthening each other – for example, rapidly warming, shallower waters facilitated the proliferation and concentration of bacteria in summer months, causing health risks for swimmers. In July 2021, *Enterococcus* numbers increased on several beaches, leading to the temporary closure of affected beaches.

Media coverage and public reactions to the previously detailed processes describe and complete the picture regarding the entire phenomenon, while also influencing tourist demand. Based on a Google search made in January 2023 (query “Velencei-tó” = Lake Velence in Hungarian), the summary of keywords in the first 150 articles/webpages within the results shows that public opinion is singularly focused on how/when the previous, artificially created system, which is difficult to maintain, can be restored. As the artificially high water levels have become familiar and seemed manageable during the decades since the lake regulation took place, local residents, stakeholders, local and national policymakers are practically only debating different alternative ways of increasing water supply (by redirecting karst water, drinking water, purified waste water, restoring water supply infrastructure etc.), adaptation to water level fluctuation and temporarily low water levels has not been widely considered. Another easily identifiable trend among the search results is the abundance of emotionally charged, strongly negative expressions („dramatic”, „critical” etc.), which shows that the natural behaviour of the lake is unanimously seen by people as a serious problem, while the naturalness and ecological benefits of low water levels are barely known (Figure 2).

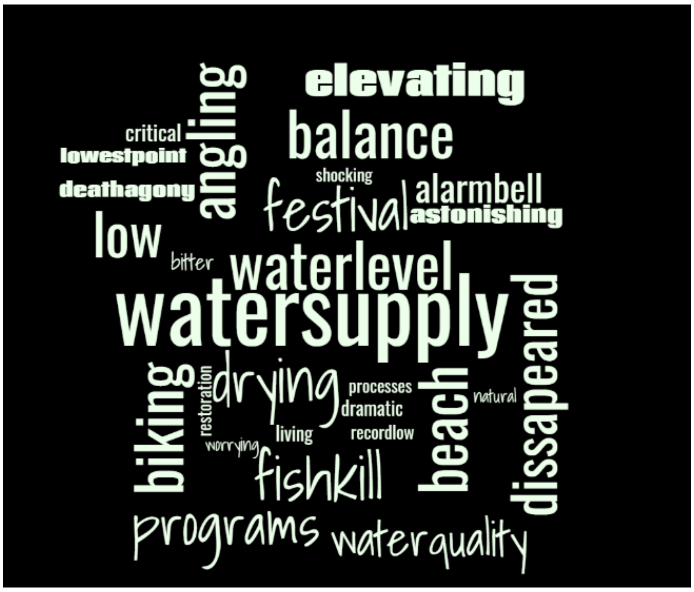

Figure 2. Word cloud based on the analysis of the first 150 results for the query „Velencei-tó”: „water supply” is the most common expression.

In the case of image results, the 150 analysed images included 39 that, without a doubt, depicted the lake during the low water levels of 2021-22. According to empirical experience, the low water level also had a strong emotional impact on local communities in settlements around the lake, resulting in heated debates and a search for scapegoats.

The above symptoms especially impacted the hydrological conditions, fish population and shore usage of the lake. Using this information, as the next step it is necessary to review the natural conditions and landscape change history of Lake Velence and identify the factors determining climate risk and sensitivity.

3.2. Natural conditions

The catchment area of the lake is 602.4 km^2, extending to the Northern end of the Mezőföld plains and the Southern side of the Vértes mountains, and consists of three distinct parts. Its largest portion – 383 km^2 – is the catchment area of the Császár-stream feeding into the lake, which has a partially inactive karstic upper area (approximately 75 km^2). The second largest tributary of Lake Velence is the Vereb–Pázmándi-stream (catchment area 105 km^2), with a remaining direct catchment area of 114.3 km^2 [19]. The only permanent stream feeding the lake is the Császár-stream, but there are several small temporary streams in its vicinity as well.

The average depth of the lake is 1.45 m [13], and based on currently available data, its depth has remained similar since its formation [22]. This average depth makes it a "shallow lake" according to the classification of Dévai [23], and belongs to the "polymictic" thermal lake type.

Hungary is located in the temperate climate zone, and its specific climate classification is continental with long warm seasons. This climate type is globally characterized by significant annual variation in temperature with four distinct seasons. The Velence basin is located at the border between the climate zones moderately warm, dry and moderately warm, moderately dry. The mean annual temperature varies between 9.3 and 9.5 °C, the total annual precipitation is between 525 and 55 mm [24].

The water balance of the lake is dominated by the effects of precipitation and evaporation. In the last half century, the amount of rainfall and the factors of flow are the water balance that have significantly declined [19]. Based on its natural water circulation, Lake Velence is a semi-static lake, as it can potentially dry up in certain years [25]. In the limnologic sense, the entire lake belongs to the littoral zone, there are reed islands located throughout most of the lakebed (due to its morphology and semi-static character), and overall can be classified as a wetland-type saline steppe lake.

3.3. Landscape change history

The first major attempts at changing the natural coast conditions of Lake Velence occurred in the middle of the 19th century. The construction of the Budapest – Fiume train line (Southern Railway) between 1859 and 1861 transformed the shoreline, as it fragmented the hydrobiological littoral zone, separating Lake Velence and "Nádas Lake" (currently known as Dinnyési Fertő) [25]. The first two train stations near the lake were constructed in Dinnyés and Kápolnásnyék [26]. The possibility of draining the lake with its fluctuating water levels was considered several times to increase agricultural areas, but finally after the 1880s the decision was made to construct the drainage channel known as the Dinnyés-Kajtor channel [22]. A drainage channel had already been excavated around 1778-1787 close to the current

Dinnyés-Kajtor channel, but it fell short of expectations [22]. To regulate drainage, a weir (1903) and later a floodgate (1928) were built near Dinnyés [14]. Between 1968 and 1975, two reservoirs (Zámoly, Pátka) were created by damming the Császár-stream. After the regulation of water levels, fluctuation was reduced below 1 m (and later, after 1970, below 50 cm), reducing the shoreline. The change in shore length was reduced to ±10% at extreme water levels [14]. According to current operating regulations, the floodgate control range is +130-170 cm from the Agárd gauge (the „0" point of which is 102.62 m above sea level).
Truly significant transformations in the surrounding landscape began in the 1960s; the shore zone could be considered semi-natural until that period [14]. Under the direction of the Lake Velence Administrative Committee (1958), large-scale and complex development began, with the goal of creating a "recreational lake" [27]. Therefore, the changes were motivated by the creation of necessary conditions for recreational use, and as a basis, the improvement of water quality in the lake showing signs of advanced benthonic eutrophication. The silted-up lake, overgrown with reed and aquatic plants, was unable to meet requirements for recreational use [25].

The goals of development works were to improve water quality, to enable construction at waterfront areas, to protect banks against erosion, to create docks and quays for boats and ships, and to increase the surface of open water suitable for bathing [27-29]. 17231 m of embankment, 2056 m of breakwater piers, and 5204 m of harbour banks were constructed between 1962 and 1992, with the total length of shore protection works being 24491 m and the length of reinforced shoreline being 17.73 km. Through dredging, 9.8 million m^3 of silt, clay, and reed-root soil were removed from 15 km^2 of reed beds, with 3.8 km^2 being filled up (Papp 1995), which meant that open water surfaces became prominent instead of the former dominance of marsh vegetation.

Tourism was developed in accordance with the creation of a recreational lake, with the first wave taking place in the 1970s and 1980s, and gaining momentum in the 2000s. Data shows that between 2009 and 2017, this region developed in a far more dynamic manner than the Central Transdanubian Region as a whole, producing 300000 overnight stays annually in the commercial sector (with this data being only a third of this 10 years earlier). 96 percent of overnight stays at the lake are domestic tourists. The number of overnight stays in Gárdony increased more than one and a half times since 2005, while Velence quadrupled its number of stays. The average stay is 2.2 days [30].

Angling tourism must be noted separately: commercial fishing has been abandoned on the lake since 1974, fishery management is controlled by the National Federation of Hungarian Anglers. While the number of anglers – and therefore revenue – has been decreasing since the 1990s (with stagnation and a slight uptick around 2010), costs of fishing inspection and fish stocking are rising (partially because of the increasing costs of transportation). Revenue from fishing tickets fell by 29.5% between 2020 and 2021 [20]. While fish stocking and introduction of exotic fish species took place as early as the beginning of the 20th century, the most significant changes occurred from the 1970s onward, by stocking non-native species *Ctenopharyngodon idella*, *Hypophthalmichthys molitrix* and *Hypophthalmichthys nobilis*, as well as mass-stocking native *Cyprinius carpio* [31].

Based on the aforementioned results, historical changes in lakeshore landscape character (scenery, landscape structure, shore morphology) were separated into four periods. The findings are consistent with the results of Papp [14] on the transformation of the shoreline, but are not limited to changes on the shoreline itself. The first period of lakeshore transformation – before intensive use – was between 1859 and 1880, including the largest changes in the extent of natural and semi-natural littoral zones and shoreline length. The second period of shore transformation was between 1880 and 1962, with regulated water levels facilitated the development of extensive recreational land use. The consequent period, between 1962 and 1992, included large-scale, planned lake regulation and recreational development. The fourth period (1992-2016) can once be characterised by independent, scattered developments. These partially involve the transformation of areas already used for recreation in earlier periods, signifying the increasing intensity of use and the decrease in open shoreline. Another notable aspect of this period is the lack of large-scale shore regulation works, with changes being focused on the transformation of former artificial embankments (e.g., creating sandy beaches, use of pilings). Certain sections of shoreline were not affected by all trends of these periods – for example, the vicinity of the rowing centre of Sukoró still looks like it did after the regulatory works were finished, while areas near the Bird Reserve are in places only affected by water level regulation. It was considered the period of the complex shoreline restoration project (2016-2023), funded by the European Union's Cohesion Fund, which includes the renewal/transformation of shoreline protection at a length of 29 km, as well as dredging (114.150 m^3), hydraulic engineering works at the mouths of streams and nature conservation-fishery management measures like the creation of spawning grounds.

Based on the above review, climate risk and sensitivity are determined by the following factors:

- natural factors of climate risk and sensitivity
  - small, water-deficient catchment area (low drainage)
  - shallow lake
  - continental climate
  - semi-static character because of the previous two (fluctuating water level, temporary desiccation)
  - dominance of macrophytes
- landscape change history factors of climate risk and sensitivity
  - water levels kept artificially high
  - increase in open water surfaces by dredging
  - embankment/shore protection works / shore engineering, alteration
  - reed management using heavy machinery
  - stocking of open-water fish species
  - waterfront development (hotels, restaurants, resorts etc.)
  - construction of docks, harbours, and beaches

3.4. Climate risk and sensitivity of land uses

The land uses and activities present in 2022 in Lake Velence and its 100-metre shore zone were evaluated, based on the level and form of climate sensitivity, summarised in Table 3. The results show that angling and activities related to beaches (bathing, swimming) are the most at risk. Several sections of shoreline become unsuitable for angling at low water levels, while negative changes in water quality have an impact by affecting fish populations (e.g., fish mortality events). Water quality has an increased importance for bathing, but observations from 2021-22 show that the disappearance of beaches suitable for swimming, the increase in silty areas negatively impacts this activity as well.

Table 3

Climate sensitivity of land uses at Lake Velence: angling, operation of beaches and bathing/swimming are most at risk

Land use / activity	Dependent on water quality*	Dependent on water level**	Dependent on landscape perception***	Dependent on pandemic restrictions****	Climate risk / sensitivity
Recreational angling	x	x	x		High
Boating, pedal boating		x	x		Moderate
Canoeing, kayaking, SUP			x		Low
Swimming	x	x		x	High
Water-skiing	x	x			Moderate
Cruiser ship traveling		x	x		Moderate
Cycling, other outdoor sports			x		Low
Residential area, hotels, resorts			x	x	Moderate
Restaurants, cafes, shops			x	x	Moderate
Cultural programs, festivals			x	x	Moderate
Reed harvesting		x			Low
Nature conservation		x			Low
Ecotourism			x		Low

Note: *definition of low water quality: due to bacteriological contamination of bathing water, the beach would have to be closed for at least 21 days, or the trophic state of the water, based on chlorophyll-A levels, would fall within the eu-polytrophic – 100-200mg/m^3 – category for 21 days simultaneously at a minimum of 2 measurement sites. ** definition of unfavourable water level: water levels fall below 50% of minimum operational levels for at least 30 days. ***definition of unfavourable effect: long-term change in the familiar scenery from frequented viewpoints, sustained or periodic unpleasant sounds or smells. ****based on the restrictions applied in 2019-2020 in Hungary.

Although this is beyond the scope of this research, it is notable that beaches are also closed during a pandemic. Activities based on original natural conditions of the lake, like nature conservation and ecotourism, are less sensitive.

Further analyses are necessary to identify effects on the service industry, but it can be established that the most typical and widespread uses of the lake (angling, bathing) are inflexible to change. In other words: currently dominant land uses require an artificially maintained water level, which is costly and resource demanding to sustain within a rapidly changing natural system, becoming less and less possible to guarantee and definitely unsustainable.

4. Conclusions

In the research, natural factors and landscape change processes was reviewed that determine the climate risk and sensitivity of a shallow Central European lake, mainly used for tourism. It was analysed the ecological and economic impact of the record low water levels of 2021-22, focusing on processes. It was determined which current land use forms can be considered most at risk or sensitive regarding climate change. The wise and sustainable use of natural resources, especially lakes, requires a major paradigm change, including education, communication, and raising awareness. The question is not how one could go against natural processes and replenish the water of a semi-static lake during a period of drought, but how one could adapt to natural conditions and water level fluctuations. This is painful to face the system is resistant to necessary social and economic changes, but the later the transitioning will start, the more disappointment will encounter before finding the right path. After the change of approach, a change in land use structure becomes feasible: the example of Lake Velence shows that long-term utilisation of our shallow lakes, vulnerable to climate change, is only possible in a flexible system that considers their natural dynamic processes (fluctuations in water level, succession, filling, etc.), their resilience, the ecological footprint, and biological capacity of the area. This requires strategic planning based on climate models and considers alternative scenarios for the entire catchment area and all settlements around the lake.

The management of the lakes and lakeshores is not only urgent because of the necessity of climate adaptation, but compliance with the Water Framework Directive of the European Union and the goals of the UN regarding the protection and restoration of biodiversity all concur on this topic. As the continuation of this research, monitoring ecological changes (flora, fauna) is necessary, as well as the data-based analysis of economic effects (tourism and service sector) and the sociological assessment of opinions and emotional reactions of local residents impacted by these processes. The possibility of integration into decision-making processes and communicability, teachability must also be a primary concern during the development of a system of indicators regarding the climate sensitivity of lakes.

Acknowledgments: We would hereby like to express our gratitude to professionals knowing Lake Velence and the workings of limnic ecosystems very well – Judit Padisák, Péter Kiss, Piroska Pomogyi, Ferenc Szilágyi – for the help, opinions and observations they contributed to this research.

Conflicts of Interest: The authors declare no conflict of interest.

References

1. Pörtner, H. O.; Roberts, D.C.; Tignor, M.; Poloczanska, E.S.; Mintenbeck, K.; Alegría, A.; Craig, M.; Langsdorf, S.; Löschke, S.; Möller, V.; Okem, A.; Rama B. (eds.). *Climate Change 2022: Impacts, Adaptation and Vulnerability*. Cambridge University Press, Cambridge, UK and New York, NY, USA, 2022, pp. 3056.
2. Hansson, L-A.; Brodersen, J.; Chapman, B. B.; Ekvall, M. K.; Hargeby, A.; Hulthén, K.; Nicolle, A.; Nilsson, P. A.; Skov, C.; Brönmark, C. A lake as a microcosm: reflections on developments in aquatic ecology. *Aquatic Ecology* 2013, 47, pp. 125-135.
3. Engel, S.; Pederson, Jr., J. L. *The construction, aesthetic and effects of lakeshore development: a literature review*. Research report 177. Wisconsin Department of Natural Resources, Madison, Wisconsin, 1998, pp. 48.
4. Felföldy, L. *Environment of waters. General hydrobiology*. Mezőgazdasági Kiadó, Budapest, Hungary, 1981, pp. 73-80 [in Hungarian].

5. Furgała-Selezniow, G.; Jankun-Woźnicka M.; Mika M. Lake regions under human pressure in the context of socio-economic transition in Central-Eastern Europe: The case study of Olsztyn Lakeland. *Land Use Policy* 2020, 90, 104350.
6. Furgała-Selezniow, G.; Jankun-Woznicka, M.; Woznicki, P.; Cai, X.; Erdei, T.; Boromisza, Zs. Trends in Lakeshore Zone Development: A Comparison of Polish and Hungarian Lakes over 30-Year Period. *International Journal of Environmental Reasearch and Public Health* 2022, 19(4), 2141.
7. Hall, C. M.; Härkönen, T. (eds.). *Lake tourism. An integrated approach to lacustrine tourism systems*. Channel View Publications, Clevedon, Buffalo, Toronto, Canada, 2006, pp. 235.
8. Latinopoulos, D.; Koulouri, M.; Kagalou, I. How historical land use/land cover changes affected ecosystem services in lake Pamvotis, Greece. *International Journal Human and Ecological Risk Assessment* 2021, 27(6), pp. 1472-1491.
9. Naiman, R. J.; Décamps, H. The Ecology of interfaces: riparian zones. *Annual Review of Ecology and Systematics* 1997, 28, pp. 621-658.
10. Ostendorp, W.; Iseli, C.; Krauss, M.; Krumscheid-Plankert, P.; Moret, J-L.; Rollier, M.; Schanz, F. Lake shore deterioration, reed management and bank restoration in some Central European lakes. *Ecological Engineering* 1995, 5, pp. 51–75.
11. Schmieder, K. European lakeshores in danger – concepts for a sustainable development. *Limnologica* 2004, 34, pp. 3-14.
12. Strayer, D. L.; Findlay, S. E.G. Ecology of fresh water shorezones. *Aquatic Science* 2010, 72, pp. 127-163.
13. Szilágyi, F.; Szabó, Sz.; Mándoki, M. Restoration of Lake Velence. In: *Conservation and Management of lakes. Symposia Biologica Hungarica*; Saláni, J.; Heródek, S. (eds.), Akadémiai Kiadó, Budapest, Hungary, 1997, 38, pp. 529-545.
14. Papp, F. Re-examination of the shore fortification works at Lake Velence. Víz-Inter Mérnökiroda Kft.: Székesfehérvár, 1995, pp. 75 [in Hungarian].
15. Csima, P.; Bugyi, I.; Csihar, L.; Kabai, R.; Kincses, K.; Kosztolányi, I.; Sólyom, R. The assessment of the carrying capacity of the Lake Velence Region. KTM Területi Tervezési Főosztály, KEÉ Tájvédelmi és Tájrehabilitációs Tanszék, Budapest, Hungary, 1996, pp. 36 [in Hungarian].
16. Salisu, A.; Oloko, T. Climate risk measures: A review. *Asian Economics Letters* 2023, 4, pp. 1-4.
17. Boromisza, Zs. Landscape change at the shorezone of Lake Velence. *Tájvédelmi füzetek* 2012, 2, pp. 89-99 [in Hungarian].
18. Boromisza, Zs.; Pádárné Török, É.; Ács, T. Lakeshore-Restoration - Landscape Ecology - Land Use: Assessment of shore-sections, being suitable for restoration, by the example of Lake Velence (Hungary). *Carpathian Journal of Earth and Environmental Sciences* 2014, 9(1), pp. 179–188.
19. Water budget of Lake Velence in 2021. Central Transdanubian Water Directorate. Hydrographic and Database Department Székesfehérvár, 2022, pp. 50 [in Hungarian].
20. Hungarian National Association for Angling. Available online: https://nyito.mohosz.hu/index.php/horgaszvizeink/28-velencei-to/846-i-velencei-tavi-horgaszforum (accessed on 28.01.2023).
21. Fejér Vármegyei Hírportál. Available online: https://www.feol.hu/helyi-gazdasag/2022/08/tajekoztatas-a-velencei-tavi-halallomany-jelenlegi-helyzeterol (accessed on 28.01.2023).
22. Bendefy, L. (Ed.). The creation and development of Lake Velence. Vízgazdálkodási Tudományos Kutató Intézet: Budapest, Hungaria, 1971, pp. 145.
23. Dévai, Gy. Water quality and qualification. *Acta Biologica Debrecina* 1992, 4, pp. 240 [in Hungarian].
24. Marosi, S.; Somogyi, S. (Eds.). Cadastre of the microregions in Hungary. MTA Földrajztudományi Kutató Intézet, Budapest, Hungary, 1990 [in Hungarian].
25. Pomogyi, P. Macrophyte survey on Lake Velence according to the EU VKI criteria. Közép-dunántúli Vízügyi Igazgatóság, Keszthely, 2005, pp. 49 [in Hungarian].
26. Kiss, P. The history of Dinnyés until 1945. Dinnyési Baráti Kör, Dinnyés, 2006, pp. 56 [in Hungarian].
27. Karászi K. (Ed.). The recreation of Lake Velence. Vízgazdálkodási Intézet, Budapest, Hungary, 1984, pp. 145 [in Hungarian].
28. Bökfi, S. (Ed.) Study plan for the foundation of the Lake Venice Water Management Development Program. Coastal and riverbed regulation; Water Management Institute, Budapest, Hungary, 1987, pp. 21 [in Hungarian].
29. Tombácz, E. Evaluation of development in Lake Venice, program proposal. Öko Rt. Budapest, Hungary, 1993 [in Hungarian].

30. Fejér Vármegyei Hírportál. Available online: https://www.feol.hu/helyi-kozelet/2018/05/a-magyarok-kedvenc-nyaralohelye-lett-mara-a-velencei-to (accessed on 28.01.2023).
31. Sallai, Z.; Kiss, B.; Müller, Z.; Polyák, L. Results of fish faunistical survey of Lake Velence in 2017. *Pisces Hungarici* 2018, 12, pp. 5–19 [in Hungarian].

Citation: Boromisza, Zs.; Harea, O. Climate risk of shallow touristic lakes: a case study of Lake Velence (Hungary). *Journal of Engineering Science* 2023, 30 (3), pp. 121-133. https://doi.org/10.52326/jes.utm.2023.30(3).08.

Publisher's Note: JES stays neutral with regard to jurisdictional claims in published maps and institutional affiliations.

Submission of manuscripts: jes@meridian.utm.md

https://doi.org/10.52326/jes.utm.2023.30(3).09
UDC 664.8.047.41:664.853:634.11

THE INFLUENCE OF THE HEATING AGENT TEMPERATURE ON THE KINETICS OF THE CONVECTIVE DRYING PROCESS AND THE CONTENT OF BIOACTIVE COMPOUNDS IN APPLE POMACE

Tatiana Ceșko*, ORCID: 0000-0003-3592-0774,
Galina Dicusar, ORCID: 0000-0003-3597-3024,
Rodica Sturza, ORCID: 0000-0002-2412-5874,
Aliona Ghendov-Moșanu, ORCID: 0000-0001-5214-3562

Technical University of Moldova, 168 Stefan cel Mare Blvd., Chisinau, Republic of Moldova
*Corresponding author: Tatiana Ceșko, *tatiana.cesko@saiem.utm.md*

Received: 08. 26. 2023
Accepted: 09. 18. 2023

Abstract. An environmentally ecological approach to the reuse of agro-industrial products in the food industry involves extracting biologically active substances or using them as supplementary products rich in dietary fibers. Apple pomace obtained after juice extraction presents a product rich in biologically active substances, soluble and insoluble fibers, organic acids, and minerals. Convective drying of apple pomace is an alternative method for long-term preservation by maintaining the biologically active substances. The research aimed to study the influence of temperature in the range of 60-80 °C on the drying of apple pomace to a final moisture content of 12.0±0.13% using the convective method, and the effect of temperature on the yield of bioactive compounds and antioxidant activity in Gold Delicious apple pomace. Changing the air temperature during convective drying from 60 to 80 °C reduced the drying time by 1.6 times and demonstrated a 1.4-fold increase in drying rate. The increase in the thermal agent's temperature led to an increase in the kinetic characteristic values; K_I values increased by 4%, and K_{II} values increased by 44%. Spectrophotometric analysis demonstrated that apple pomace dried at a temperature of 70 °C had the highest total content of polyphenols, tannins, and carotenoids. Thus, the convective drying method of apple pomace in the temperature range of 60-80 °C exerts a significant influence on the composition of biologically active compounds in the apple pomace composition.

Keywords: *apple pomace, convective drying, temperatures, extracts, biologically active compounds, polyphenols, caratenoids, antioxidant activity.*

Rezumat. O direcție ecologică de reutilizăre a produselor agro-industriale în industria alimentară este extragerea substanțelor biologic active sau utilizarea lor ca produse suplimentare bogate în fibre alimentare. Tescovina de mere obținută după stoarcerea sucului prezintă un produs bogat atât în substanțe biologic active cât și în fibre solubile și insolubile, acizi organici și minerale. Uscarea convectivă a tescovinei este o metodă alternativă de conservare pe termen îndelungat prin păstrarea substanțelor bilogic active.

Scopul cercetării a fost de a studia influența temperaturii în intervalul de 60-80 °C la uscarea tescovinei până la umiditatea finală 12,0±0,13% prin metoda convectivă, și influența temperaturii asupra randamentului de compuși bioactivi și activității antioxidante în tescovina de mere Gold Delicios. Modificarea temperaturii aerului pe parcursul uscării convective de la 60 la 80 °C a redus durata de uscare de 1,6 ori, și a demostrat o creştere a vitezei de uscare de 1,4 ori. Creșterea temperaturii agentului termic a condus la creșterea valorilor caracteristicilor cinetice în cazul coeficientului K_I valorile au crescut cu 4%, iar pentru K_{II} cu 44%. Analiza spectrofotometrică a demonstrat ca în tescovina de mere uscată la temperatura de 70 °C a avut cel mai ridicat conţinut total de polifenoli, taninuri și caratenoizi. Astfel, metoda convectivă de uscare a tescovinei de mere în intervalul de temperaturi 60-80 °C manifestă o influență marcantă asupra compoziției compușilor biologic activi din compoziția tescovinei de mere.

Cuvinte cheie: *tescovina de mere, uscare convectivă, temperature, extracte, compuși biologic activi, polifenoli, caratenoizi, activitate antioxidantă.*

1. Introduction

One of the priority tasks for the reuse of agro-industrial products would be their utilization for extracting biologically active substances present in them or for use as supplements to improve food products and create food items with valuable nutritional properties for human health [1]. Apple pomace is obtained after squeezing the juice from fruits, which constitutes 30% of the residual mass. These agro-industrial wastes present a homogeneous mass, composed of the fruit's peel, pulp, and seed chamber, with a light brown color, a pleasant apple scent, and a slightly sour taste. Apple pomace is rich in polyphenols, carotenoids, flavonoids, fatty acids, vitamin C, and dietary fibers, which would allow its use in producing new food products in the bakery, dairy, or confectionery sectors [2]. The use of apple pomace in the diet is attributed to its therapeutic benefits on the body. The most important active substance contained in apples is pectin. Thanks to pectin, apples can combat the effects of diarrhea, gastritis, or colitis, reduce cholesterol, stabilize glucose levels, address various skin eruptions, and contribute to wound healing by restoring tissue elasticity [2,3].

For long-term use of apple pomace, it is necessary to preserve it while maintaining its biologically active substances. Drying is one of the widely used methods for preserving horticultural products [4]. Through drying, water is removed until a final concentration is reached, thus ensuring the microbial stability of the product and minimizing changes in chemical and physical composition during storage. The convective drying method presents an alternative for preserving pomace by transferring heat to the drying product through the thermal agent [5]. The hot air drying process involves both heat and mass transfer, with water diffusing out of horticultural products. The diffusion process of moisture is a three-dimensional complex of food at the surface, being a key factor in controlling the drying rate, where understanding the phenomena that occur in food, especially heat and mass transfer, is necessary [6]. This is due to the dependence between the total energy of diffusion, temperature, time, and air velocity [7]. Drying is not only a preservation method but also offers other advantages for food products undergoing this process: ease of packaging, transportation, and storage due to reduced weight, avoidance of costly refrigeration systems [8]. The degree of contraction and damage to the internal structure of plant tissues depends on the drying method applied and the parameters underlying it: temperature and air velocity.

Convective drying is a frequently used method for dehydrating food products, characterized as a method requiring high temperature and air velocity, with the finished product having low porosity, high density, pleasant appearance and color, and preservation of biologically active components [9]. Researching the drying process of pomace is necessary for understanding the heat and mass transport mechanism and is a prerequisite for the mathematical description of the entire process. Modeling the process, calculating kinetic coefficients, and constructing drying curves at various temperatures and drying rates play an important role in optimizing or controlling the industrial drying conditions of pomace [10].

The aim of the research was to analyze the drying kinetics of apple pomace depending on the thermal agent's temperature and the influence of heat treatment on the content of biologically active compounds and antioxidant activity.

2. Materials and Methods

2.1 Preparation of samples for drying

The harvest of "Golden Delicious" apples used for the research was collected in the fall of 2021 from "AgroProdusct" S.R.L, Briceni, Colicăuți commune, (48°18′36″N 27°8′54″E), Republic of Moldova, which has apple orchards covering over 200 hectares, and stored until the spring of 2022. Apple pomace for drying was obtained after squeezing the juice from Golden Delicious apples. After juice extraction, the pomace was blanched in a 0.2% (anhydrous) citric acid solution for 10 minutes to inhibit enzyme activity and oxidation processes that could alter the properties of the pomace. Subsequently, the pomace was pressed at a temperature of 25 ± 1 °C and arranged on a tray in a single layer for convective drying at different temperatures of the thermal agent.

2.2 Drying of apple pomace

The study of the drying kinetics of apple pomace as a function of the thermal agent's temperature was carried out in a convective drying installation developed within the Department of Mechanical Engineering, Technical University of Moldova (UTM), with heated air as the thermal agent [11]. The thermal agent's temperature was set at 60°C, 70°C, and 80°C, with an air velocity of 1.5±0.1 m/s.

A sample of apple pomace weighing 100 g and with a moisture content of 85.5±2% was placed in the drying chamber on a tray. The parameters of mass reduction were recorded every 5 minutes, with the ambient parameters being an air temperature of 23±1°C and relative humidity of 57±2%. The sample was dried until reaching a final moisture content of 12.0±0.05%. The equilibrium moisture content (u_{ech}) of apple pomace was calculated using Filonenko's formula [12] and amounted to 10.82%.

The dryer was connected to a computer that allowed automatic data recording. The obtained results were processed using graphical and mathematical methods, based on which drying curves and drying rates of apple pomace were constructed depending on the thermal agent's temperature [11]. Based on the obtained data, drying curves *U=f(τ)* and drying rate curves $\frac{dU}{d\tau} = f(U)$ were constructed and analyzed.

The drying coefficients for the first and second periods K_I and K_{II} were calculated according to formulas 1 and 2 [13]:

$$K_I = \frac{du / d\tau}{A \cdot (x_S - x_0)} \quad (1)$$

$$K_{II} = \frac{du / d\tau}{u'_{cr} - u_{ech}}, \qquad (2)$$

where: A – the contact area of the apple core with the thermal agent, m^2;

$du/d\tau$ – drying speed in the first period, %/s;

x_0 and x_s the moisture content of fresh and saturated air, kg/kg dry air;

$u'_{cr} - u_{ech}$ - critical and equilibrium humidity, %.

The initial and final moisture content of apple pomace were experimentally determined by drying in an oven at 105.0 ± 0.1°C to a constant mass, according to ISO 1026:1982 [14].

After convective drying, the pomace was ground to a particle size of 140±10μ, sieved, packaged, and stored in the dark at room temperature. The influence of temperature on the biological value of apple pomace, especially the total content of polyphenols, tannins, carotenoids, and antioxidant activity, was evaluated.

2.3. The total content of polyphenols and tannins based on the Folin–Ciocalteu reagent

The total polyphenol content (TPC) and tannin content (TC) were determined according to the Bouyahya method with some modifications [15]. Extracts were prepared as follows: 1 g of dried apple pomace samples were weighed, dissolved in 10 mL of 60% (*v/v*) ethanol solution, sonicated in an ultrasonic bath at room temperature for 15 minutes. After sonication, the extracts were centrifuged at 5000 rpm for 10 minutes, filtered, and stored in tubes under refrigeration.

TPC was determined by adding 0.2 mL of apple pomace extract to a test tube, along with 1 mL of Folin-Ciocalteu solution and 3 mL of sodium carbonate solution (20%). The resulting mixture was allowed to react for one hour in the dark. The absorbance of the mixture was determined at 765 nm. The result was expressed in milligrams of gallic acid equivalents (mg GAE) per 100 mg of dried pomace (mg GAE/100 g DW).

The total tannin content was determined based on the method of Waterman and Mole [16] using the Folin–Ciocalteu reagent. The absorbance of the mixture was read at a wavelength of 750 nm and expressed in milligrams of tannic acid equivalents (mg TAE) per 100 g of dried pomace (mg TAE/100 g DW).

2.4. Total carotenoid content

The total carotenoid content (TCC) was determined based on the method described by Ghendov-Mosanu et al. [17]. 2 g of dried sample were dissolved in 25 mL of a solution (methanol/ ethyl acetate/petroleum ether, 1/1/1, *v/v/v*). The mixture was subjected to ultrasound-assisted extraction (amplitude - 100%; frequency - 37 kHz) for 15 minutes at room temperature. The extracts were then centrifuged at 5000 rpm for 10 minutes. TCC was performed in duplicate and stored in dark bottles in the refrigerator. The extracts were analyzed using a spectrophotometer at a wavelength of 450 nm and expressed in mg/100 g DW of apple pomace [17].

2.5. Antioxidant activity based on the DPPH• radical reagent

The method for determining the antioxidant activity (AA) in 60% (*v/v*) hydroalcoholic extracts of apple pomace was carried out based on the method described by Paulpriya et al. [18]. The results were expressed in micromoles Trolox equivalent (TE) per 100 g of dry weight

(DW) of apple pomace powder (μmol TE/100 g DW) using the calibration curve (0-500 μmol/L, R^2=0.9992) with Trolox.

2.6 Statistical data analysis

All calculations were performed using Microsoft Office Excel 2010 (Microsoft, Redmond, WA, USA). The data obtained in this study are presented as mean values ± standard error of the mean calculated from three parallel experiments. The comparison of average values was conducted using the one-way analysis of variance (ANOVA) with Tukey's test at a significance level of $p \leqslant 0.05$. This analysis was carried out using the Stat graphics program Centurion XVI 16.1.17 (Stat graphics Technologies, Inc., The Plains, VI, USA).

3. Results and Discussions

Drying represents an efficient method of preservation for fruits. Drying can maintain the quality of finished products, but the decisive factor in this process is the chosen method, the equipment, and the parameters of the thermal agent. Various studies on fruit preservation through drying report high product quality, low microbial contamination, and the preservation of functional bioactive substances. The most common drying method is convective drying [19].

Figure 1 shows the drying curves of apple pomace at temperatures of 60, 70, and 80 °C, and with a thermal agent velocity of 1.5±0.1 m/s. Analyzing the drying curves of apple pomace, a decrease in drying time is observed as the thermal agent temperature increases. At 60°C, the drying time is 230 minutes, reducing to 190 minutes at 70°C, and further to 145 minutes at 80°C. Thus, increasing the air temperature from 60 to 80°C reduced the drying time by 1.6 times. Additionally, there was a reduction in drying time of 15.38% in the first period and 45.45% in the second period, Table 1.

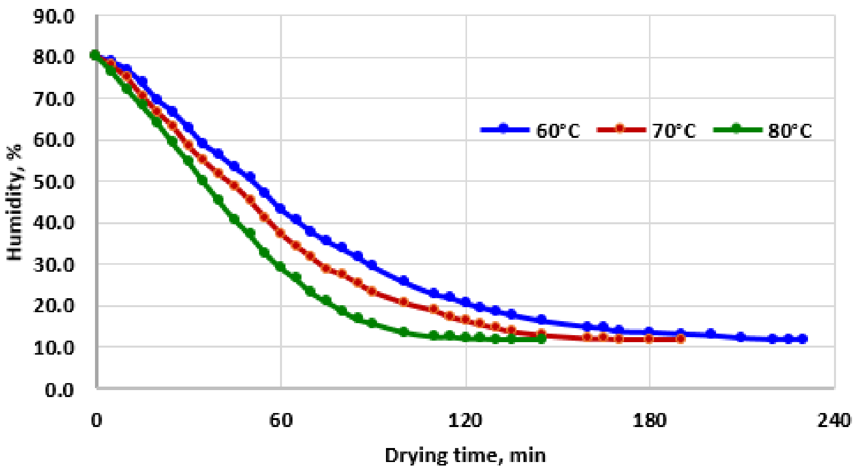

Figure 1. Drying curves of apple pomace at different thermal agent temperatures.

Some bibliographic sources mention that during the drying of plum pomace in the temperature range of 60-80°C, the drying time was reduced by 50%, which influenced the content of acids and the structure of the pomace [20]. Research on drying Baru fruits to achieve a moisture content of 0.065 ± 0.018 (db) resulted in drying times of 266.3, 166.9, 30.8, and 22.8 hours at drying temperatures of 40, 60, 80, and 100°C, respectively. Similarly, a dependence between increasing thermal agent temperature and reduced drying time was observed [21]. A similar relationship between increased thermal agent temperature and decreased drying time was also observed in the drying of grape seeds. Increasing the thermal agent temperature from 60-100°C led to a 1.4 times reduction in the drying process [22].

Convective drying studies on grape pomace demonstrated that drying the pomace at 35°C for 12 hours, 50°C for 5 hours, and 70°C for 3 hours reduced the initial moisture content of the skin from 63.58 ± 3.29% to 6.99 ± 0.83%, and of the pomace from 49.36 ± 3.45% to 8.32 ± 0.96%. In these parameters, a similar dependence between increasing thermal agent temperature and reduced drying time was observed [23]. Literary sources suggest that modern drying conservation technologies for food products reduce energy consumption by up to 80% and improve drying efficiency by up to 26.5% in terms of reduced drying time [24]. Figure 2 represents drying rate curves of apple pomace at different thermal agent temperatures.

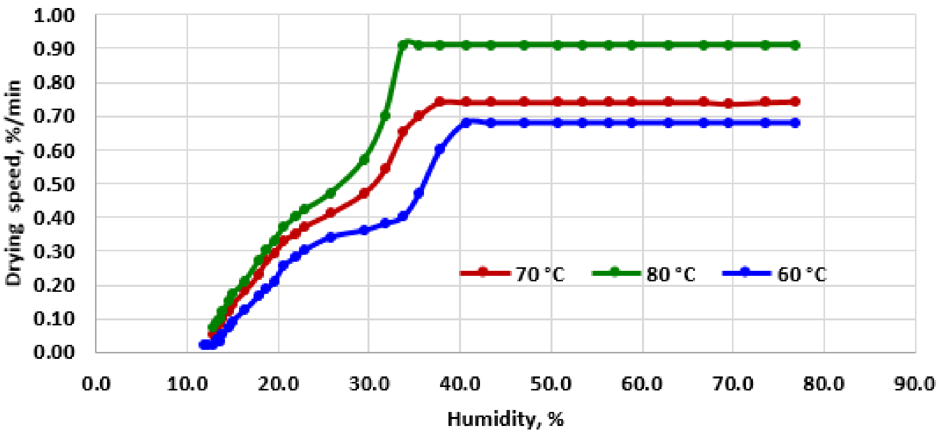

Figure 2. Curves of the drying speed of apple pomace at different temperatures of the thermal agent.

The analysis of the drying rate curves of apple pomace using convective heat input demonstrates the occurrence of mass transfer mechanism in the drying processes. Some sources also report a variation in mass transfer with temperature variation in various food products [25]. The drying rate curves showed the presence of a constant drying rate period (the first period) and a variable drying rate period (the second period).

Upon analyzing the drying rate curves, it was observed that increasing the thermal agent temperature from 60 to 80°C resulted in an increase in drying rate during the first period as follows: 0.66%/min (60°C), 0.72%/min (70°C), and 0.90%/min (80°C). Thus, the drying rate increased by 1.36 times. The change in drying temperature did not significantly influence the overall nature of the drying rate curves. Analyzing the graphs of the drying rate curves during the variable drying rate period revealed a second critical point that shifted from 34% to 26%. Based on the graphs of the drying curves and the drying rate curve, the kinetic characteristics of the drying process were calculated and are presented in Table 1.

The results from Table 1 indicate that with the increase in the drying agent temperature from 60 to 80 °C, there is an increase in the values of kinetic characteristics. In the case of the coefficient K_I, the values increased by 4%, and for K_{II} by 44%, thus demonstrating a significant influence on the variable drying rate period (the second period). It is noted that during convective drying, the removal of moisture from apple pomace is hindered due to the opposing orientation of the temperature and humidity gradient. Other sources in the literature also mention that during the drying of apricots, the constant drying rate in the first period increased depending on the increase in the drying agent temperature (60-100°C) by 1.4 times, while in the second period, it increased by 2.77 times, indicating an intensification of mass and heat exchange [26]. When drying cherries, changing the temperature of the drying agent from 60-100°C influenced the values of the drying constants according to the exponential law, demonstrating an increase in the rate constant in the first K_I period by 3.2 times, and in the second K_{II} period increased 4.7 times [13].

Table 1

Kinetic characteristics of the convective drying process of apple pomace *

Temperature of drying agent, °C	Drying rate in the first drying period, $(du/d\tau)_I$, %/min	Drying coefficient K_I, %/(m²·s·kg/kg aer uscat)	Drying coefficient $K_{II} \cdot 10^4$, s^{-1}	Drying time in the first period τ_I, min	Drying time in the second period τ_{II}, min	Total drying time τ_{total}, min
60	0.66	45.8	3.32	65	165	230
70	0.72	46.5	3.68	60	130	190
80	0.90	47.7	4.81	55	90	145

**$p \leq 0.05$*

Apple pomace is a rich source of bioactive compounds and beneficial nutrients for health, exhibiting antioxidant, anti-inflammatory, antibacterial, and antiviral activities. Daily consumption of apple pomace in the diet has a beneficial influence on digestion enzymes, intestinal microbiota, and plasma cholesterol and triglyceride levels [27].

The content of bioactive compounds in dried apple pomace samples at different drying agent temperatures was determined, as shown in Table 2. It was found that increasing the drying agent temperature from 60 to 80 °C resulted in the following values of TPC: 611.44 mg GAE/100 g DW (60°C), 728.82 mg GAE/100 g DW (70°C), and 589.93 mg GAE/100 g DW (80°C), demonstrating the highest extraction yield of TPC at the temperature of 70°C. High temperatures may have led to cellular wall damage, triggering the release of enzymes such as polyphenol oxidase and peroxidase, contributing to the reduction in phenolic compound content. High temperatures can cause irreversible changes in the chemical structure of heat-sensitive phenolic compounds. These changes affect the reactivity of aromatic rings, which interact with the Folin-Ciocalteu reagent, explaining the lower retention of TPC observed at the highest tested temperature [16]. Similarly, Vega-Galvez et al. [28] reported that drying Granny Smith apple pieces at temperatures of 40, 60, and 80°C and at a drying agent velocity of 1.5 m/s caused a decrease in polyphenol content from 44.82 GAE/100 g DW (60°C) to 27.04 GAE/100 g DW (80°C). Gumul et al. reported TPC in apple pomace as 89.39 mg GAE/100 g DW [29]. Persic et al. reported total phenolic content in the range of 19−50 mg GAE/100 g DW [30]. Similar trends have been noted for CTC with values of 66.14 mg TAE/100 g DW (60°C), 78.91 mg TAE/100 g DW (70°C), and 63.54 mg TAE/100 g DW (80°C). As with polyphenols, the highest yield is recorded for the temperature of 70°C, and the lowest for 80°C. The concentration of tannins determined in apple pomace corresponds to literature data, which mention tannin contents ranging from 29.11 to 73.4 mg TAE/100 g DW, depending on the tested apple variety [31]. Tannins can be found in many fruits, with reported values ranging between 238-275 mg TAE/100 g product, varying depending on the variety, fruit parts used, maturity stage, processing conditions, presence of other compounds, as well as the types and tests for tannin analysis [32,33]. In our opinion, TPC and TC in apple pomace can be influenced by extraction conditions and the different ways in which the results were expressed [34].

The TCC registered values of 3.19 (60°C), 4.93 (70°C), and 3.66 mg/100 g DW (80°C), as shown in Table 2. Based on the presented results, the highest yield of bioactive compounds was recorded at the temperature of 70°C. In a study by Raut et al., it was demonstrated that TCC in dried carrot slices through the convective method had the following values: 0.63 mg/100 g DW (50°C), 0.69 mg/100 g DW (60°C), and 0.55 mg/100 g DW (70°C). It was mentioned that the carotenoid content decreases if the samples are exposed to prolonged drying or higher drying temperatures of over 70°C. This phenomenon can be explained by the fact that convective drying at lower temperatures over an extended period exposes carotenoids to oxygen, causing extensive degradation. Additionally, lipoxygenase and peroxidase enzymes are responsible for oxidative degradation of carotenoids [35]. The same values of total carotenoid concentration in apple pomace were recorded by other authors, with values of 14.5 mg/100 g for Berzukroga yellow apples and 5.1 mg/100 g for Bernu Prieks apples [36]. In the case of carotenoid content, for most vegetables and fruits, drying usually results in a loss of 10-20%. Exposure to air or high temperatures facilitates oxidation and isomerization reactions of trans-carotenoids, and lipoxygenase enzymes form reactive radicals that destroy carotenoids [37].

Table 2

The content of biologically active substances in apple pomace

Temperature, °C	Total polyphenol content, mg GAE/ 100 g DW	Tannin content, mg TA/ 100 g DW	Total carotenoid content, mg/100g DW	Antioxidant activity (DPPH), µmol TE/g DW
80°C	586.9±22.4	63.54±7.40	3.66±0.64	62.45±21.2
70°C	728.8±28.5	78.91±9.28	4.93±0.43	62.90±18.05
60°C	611.4±26.4	66.14±9.18	3.19±1.20	74.94±18.06

The AA of apple pomace is directly influenced by the presence of bioactive compounds. The results of the analysis of dried apple pomace extracts in the temperature range of 60-80°C recorded values ranging from 74.94 to 62.98 µmol TE/g DW of DPPH inhibited free radicals. Other authors have demonstrated that in Malus Domneasca apple pomace, the AA values ranged between 0.77 and 0.91 mg Trolox/g [38]. In another study, it was shown that the DPPH radical scavenging activity was significantly reduced in potato waste with increasing drying temperature, with values of 14.26 ± 0.06 µM TE/mg DW at 40°C compared to 08.61 ± 0.01 µM TE /mg DW at 120°C [39]. Similarly, the influence of temperature on AA was demonstrated in lemon residues exposed to drying temperatures from 50°C to 110°C, resulting in a significant increase ($p<0.05$) in the percentage of DPPH radical inhibition. Higher inhibition percentages were recorded at a drying temperature of 50°C, with maximum inhibition values of 73.73±1.12% and 50.07±5.15% at 110°C. Both values obtained at the end of the drying process are characterized in that at 50°C they are higher based on the compounds eriocitrin and hesperidin, while at 110°C they are based on hesperidin compounds [40]. Additionally, Gorjanović et al. reported high values of antioxidant activity in dried apple pomace, with results ranging from 0.1 to 4.5 mmol TE/100 g DW. It should be noted that the antioxidant potential of apple pomace is not solely the result of the presence of polyphenols but is also influenced by other compounds with antioxidant properties (such as vitamin C, E, β-carotene, etc.) [41].

Thus, the convective drying of apple pomace at different temperatures exhibits a significant influence on the composition of bioactive compounds and antioxidant activity.

The research results have demonstrated that by increasing the drying temperature from 60 to 80°C, the drying time is reduced by 1.6 times. An increase of 1.4 times in the drying rate was observed in the first drying period. Drying rate curves showed the presence of a constant drying rate period (first period) and a variable drying rate period (second period). It was found that increasing the drying temperature from 60 to 80°C led to a reduction in the drying time in the first period by 15.38% and in the second period by 45.45%. The increase in the drying agent temperature led to an increase in the values of kinetic characteristics. For the K_I coefficient, the values increased by 4%, and for K_{II}, by 44%. It was demonstrated that the drying temperature influenced the biological value and antioxidant activity of dried apple pomace. The highest values of the total carotenoid content were obtained for higher drying temperatures, decreasing at lower temperatures. This dependence is due to the prolonged drying time and the influence of factors that destroy carotenoids. The same dependence was observed for the total polyphenol and tannin contents. The highest extraction efficiency of bioactive substances was recorded at a drying temperature of 70°C: TPC - 728.82 mg GAE/100 g DW, TC - 78.91 mg TAE/100 g DW, TCC - 4.93 mg/100 g DW. Antioxidant activity values ranged from 62.45 to 74.94 µmol TE/g DW. Therefore, the parameters of convective drying need to be chosen considering the influence of both the drying agent temperature and the drying time on the yield of bioactive substances. Drying at a temperature of 70°C may represent a compromise, providing a good balance between drying time and maintaining a high yield of polyphenols, carotenoids, and tannins in apple pomace. The dried pomace obtained while preserving bioactive substances can be used in the food industry to manufacture various new products with high biological value.

Acknowledgments: The authors thank the Moldova State Project no. 20.80009.5107.09, "Improvement of food quality and safety by biotechnology and food engineering", running at Technical University of Moldova.

Conflicts of Interest: The authors declare no conflict of interest.

References

1. Elik, A.; Yanik, D.K.; Istanbullu, Y.; Guzelsoy, N.A.; Yavuz, A.; Gogus, F. Strategies to reduce post-harvest losses for fruits and vegetables. *Strategies* 2019, 5, pp. 29–39.
2. Akbar, W.M.; Aftab, M.R.; Younas, I.; Jamil, U. Heat and mass transfer modeling for fruit drying: a review. *Food Process Technol.* 2019, 7(3), pp.69-73.
3. Sato, M.L.D; Vieira, F.; Giovanetti, R; Danianni Marinho, Z.; Nogueira, F.A.; Wosiacki, G. Apple pomace from eleven cultivars: an approach to identify sources of bioactive compounds. *Acta Scientiarum. Agronomy, Maringá* 2010, 32(1), pp. 29-35.
4. Cruz, A. C.; Guiné, R. P.; Gonçalves, J. C. Drying kinetics and product quality for convective drying of apples (cvs. Golden Delicious and Granny Smith). *International Journal of Fruit Science* 2015,15(1), pp. 54-78.
5. Lewicki, P.P.; Witrowa-Rajchert, D.; Mariak, J. Changes of structure during rehydration of dried apples. *Journal of food engineering* 2013, 32, pp. 347-350.
6. Caparino, O.A.; Tang, J.; Nindo, C.I.; Sablani, S.S.; Powers, J.R.; Fellman, J.K. Effect of drying methods on the physical properties and microstructures of mango powder. *J Food Eng.* 2012, 111 (1), pp. 35–48.
7. Cheng, L.-S.; Fang, S.; Ruan, M.-L. Influence of blanching pretreatment on the drying characteristics of cherry tomato and mathematical modeling. *Int. J. Food Eng.* 2015, 11(2), pp. 265–274.
8. Mota, C.L.; Luciano, C.; Dias, A.; Barroca, M.J.; Guiné, R.P.F. Convective drying of onion: Kinetics and nutritional evaluation. *Food Bioprod Process* 2010, 88, pp. 115–23.
9. Ferreira Guiné, R.P.; Pinho, S.; Barrocac, M. J. Study of the convective drying of pumpkin. *Food and Bioproducts processing* 2011, 89, pp. 422–428.
10. Tulej, W.; Głowacki, S. Modeling of the Drying Process of Apple Pomace. *Appl. Sci.* 2022, *12(*3), 1434.

11. Vișanu, V.; Boța, M.; Griniuc, C.; Dogotari, D.; Ursache, I. Investigation of forced convection drying process of tomatoes at the tunnel dryer. In: *Technical Scientific Conference of Undergraduate, Masters, PhD students, Technical University of Moldova* 2022, 1, pp. 618-621 [in Romanian].
12. Ginzburg, A.S.; Savina, I.M. Massovlagoobmennye kharakteristiki pishchevykh produktov. *Spravochnik. Legkaya i pishchevaya promyshlennost* Moskva 1982, pp. 49-50 [in Russian].
13. Lupașco, A.; Dicusar, G.; Moșanu, A.; Lupu, O. Analysis of the kinetic characteristics of cherry drying by the convective method. *Intellectus* 2005, 1, pp. 60-63 [in Romanian].
14. ISO 1026:1982. Fruit and vegetable products — Determination of dry matter content by drying under reduced pressure and of water content by azeotropic distillation. Technical Committee ISO/TC 34/SC 9 Microbiology, International Organization for Standardization: Geneva, Switzerland, 2022.
15. Bouyahya, A.; Dakka, N.; Talbaoui, A.; Moussaoui, N.E.; Abrini, J.; Bakri, Y. Phenolic contents and antiradical capacity of vegetable oil from Pistacia lentiscus (L). *Journal of Materials and Environmental Science* 2018, 9 (5), pp. 1518-1524.
16. Waterman, P.G.; Mole, S. *Analysis Of Phenolic Plant Metabolites, Ecological Methods And Concepts*. Ed. Wiley, Ottawa, ON, Canada 1994, p.248.
17. Ghendov-Mosanu, A.; Cristea, E.; Patras, A.; Sturza, R.; Padureanu, S.; Deseatnicova, O.; Turculet, N.; Boestean, O.; Niculaua, M. Potential Application of Hippophae Rhamnoides in Wheat Bread Production. *Molecules* 2020, 25, p. 1272.
18. Paulpriya, K.; Packia Lincy, M.; Tresina Soris, P.; Veerabahu Ramasamy, M. In vitro antioxidant activity, total phenolic and total flavonoid contents of aerial part extracts of Daphniphyllum neilgherrense (wt.) Rosenth. Ethnopharmacology. *Journal of Bio Innovation* 2015, 4(6), pp. 257-268.
19. Zhang, Z.; Manjunatha Poojary, M.; Choudhary, A.; Rai, D.K.; Tiwari, B.K. Comparison of selected clean and green extraction technologies for biomolecules from apple pomace. *Electrophoresis* 2018, 13, pp. 1934–1945.
20. Michalska, A.; Wojdyło, A.; Majerska, J; Lech, Krzysztof Brzezowska, J. Qualitative and Quantitative Evaluation of HeatInduced Changes in Polyphenols and Antioxidant Capacity in Prunus domestica L. By-products. *Molecules* 2019, 24, 3008.
21. Resende, O.; Oliveira, D. E. C.; Costa, L. M.; Ferreira Júnior, W. N. Drying kinetics of baru fruits (Dipteryx alata Vogel). *Engenharia Agrícola, Jaboticabal* 2018, 38, pp. 103-109.
22. Balan, M. The process of drying grape seeds in suspended layer. Summary of the PhD thesis in engineering sciences, TUM, Chisinau, 2022. Available online: http://www.cnaa.md/files/theses/2022/58311/mihail_balan_abstract_en.pdf (accessed on 18.07.2023).
23. Sokač, T.; Gunjević, V.; Pušek, A.; Jurinjak Tušek, A.; Dujmić, F.; Brnčić, M.; Kovačević Ganić, K.; Jakovljević, T.; Uher, D.; Mitrić, G.; Radojčić Redovniković, I. Comparison of Drying Methods and Their Effect on the Stability of Graševina Grape Pomace Biologically Active Compounds. *Foods.* 2022, 11(1), 112.
24. Chojnacka, K.; Mikula, K.; Izydorczyk, G.; Izydorczyk, G.; Skrzypczak, D., Witek-Krowiak, A.; Moustakas, K.; Ludwig, W.; Kułażyński, M. Improvements in drying technologies - Efficient solutions for cleaner production with higher energy efficiency and reduced emission. *Journal of Cleaner Production* 2021; p. 320.
25. Dincer, I.; Hussain, M.M. Development of a new Bi-Di correlation for solids drying. *Internacional Journal of Heat and Mass Transfer* 2002, 45, pp. 3065-3069.
26. Tarlev, V. Analysis of the kinetic characteristics of the drying process of apricots by the combined method - convection. *Journal of Engineering Science* 2004, 4, pp. 25-27 [in Romanian].
27. Skinner, R. C.; Gigliotti,,J. C.; Ku, Kang-Mo; Tou, J. C. A comprehensive analysis of the composition, health benefits, and safety of apple pomace. *Nutrition Reviews* 2018, 76, pp. 893-909.
28. Vega-Gálvez, A.; Ah-Hen, K.; Chacana, M.; Vergara, J.; Martínez-Monzó, J.; García-Segovia, P.; Di Scala, K. Effect of temperature and air velocity on drying kinetics, antioxidant capacity, total phenolic content, colour, texture and microstructure of apple (var. Granny Smith) slices. *Food Chemistry* 2012, 132(1), pp. 51-59.
29. Gumul, D.; Kruczek, M.; Ivanišová, E.; Słupski, J.; Kowalski, S. Apple Pomace as an Ingredient Enriching Wheat Pasta with Health-Promoting Compounds. *Foods* 2023, 12, 804.
30. Persic, M.; Mikulic-Petkovsek, M.; Slatnar, A.; Veberic, R. Chemical Composition of Apple Fruit, Juice and Pomace and the Correlation between Phenolic Content, Enzymatic Activity and Browning. *LWT-Food Sci. Technol.* 2017, 82, pp. 23–31.
31. Krasnova, I.; Segliņa, D. Content of phenolic compounds and antioxidant activity in fresh apple, pomace and pomace water Extract — effect of cultivar. *Proceedings of the latvian Academy of Sci.* 2019, 73 (6), pp. 513–518.

32. Araya-Farias, M.; Mondor, M.; Lamarche, F.; Tajchakavit, S.; Makhlouf, J. Clarification of apple juice by electroflotation. *Innovative Food Science & Emerging Technologies* 2008, 9(3), pp. 320-327.
33. Youn, K.S.; Hong, J.H.; Bae, D.H.; Kim, S.J.; Kim, S.D. Effective clarifying process of reconstituted apple juice using membrane filtration with filter-aid pretreatment. *Journal of Membrane Science* 2004, 228(2), pp. 179-186.
34. Waldbauer, K.; McKinnon, R.; Kopp B. Apple Pomace as Potential Source of Natural Active Compounds. *Planta Med.* 2017, 83, pp. 994–1010.
35. Raut, S.; Md Saleh, R.; Kirchhofer, P.; Kulig, B.; Hensel O.; Sturm,B. Investigating the Effect of Different Drying Strategies on the Quality Parameters of Daucus carota L. Using Dynamic Process Control and Measurement Techniques. *Food Bioprocess Technol* 2021, 14, pp. 1067–1088.
36. Radenkovs, V.; Kviesis, J.; Juhnevica-Radenkova, K.; Valdovska, A.; Püssa, T.; Klavins, M.; Drudze, I. Valorization of Wild Apple (Malus spp.) By-Products as a Source of Essential Fatty Acids, Tocopherols and Phytosterols with Antimicrobial Activity. *Plants* 2018, 7 (90), pp. 1-18.
37. Cui, Z.-W.; Xu, S.-Y.; Sun, D.-W. Effect of microwave-vacuum drying on the carotenoid's retention of carrot slices and chlorophyll retention of Chinese chive leaves. *Dry Technol.* 2004, 22, pp. 563–575.
38. Dranca, F.; Vargas, M.; Oroıan, M. Physicochemical properties of pectin from Malus domestica 'Fălticeni' apple pomace as affected by non-conventional extraction techniques. *Food Hydrocoll.* 2020, 100, pp. 1-14.
39. Xu, Y.; Fan, M.; Ran, J.; Zhang, T.; Sun, H.; Dong, M.; Zhang, Z.; Zheng, H. Variation in phenolic compounds and antioxidant activity in apple seeds of seven cultivars. *Journal of Biological Sciences* 2016, 23, pp. 379-388.
40. Patrón-Vázquez, J.; Baas-Dzul, L.; Medina-Torres, N.; Ayora-Talavera, T.; Sánchez-Contreras, Á.; García-Cruz, U.; Pacheco, N. The effect of drying temperature on the phenolic content and functional behavior of flours obtained from lemon wastes. *Agronomy* 2019, 9, p. 474.
41. Gorjanović, S.; Micić, D.; Pastor, F.; Tosti, T.; Kalušević, A.; Ristić, S.; Zlatanović, S. Evaluation of Apple Pomace Flour Obtained Industrially by Dehydration as a Source of Biomolecules with Antioxidant, Antidiabetic and Antiobesity Effects. *Antioxidants* 2020, 9, 413.

Citation: Ceşko, T.; Dicusar, G.; Sturza, R.; Ghendov-Moşanu, A. The influence of the temperature of the convective heat agent on the kinetics of the drying process and the content of bioactive compounds in apple pomace. *Journal of Engineering Science* 2023, 30 (3), pp. 134-144. https://doi.org/10.52326/jes.utm.2023.30(3).09.

Submission of manuscripts: jes@meridian.utm.md

Journal of Engineering Science *Vol. XXX, no. 3 (2023), pp. 145 - 154*
Fascicle *Food Engineering* *ISSN 2587-3474*
Topic *Food Technologies and Food Processes* *eISSN 2587-3482*

https://doi.org/10.52326/jes.utm.2023.30(3).10
UDC 664.841:661.74:634.11

APPLICATION OF APPLE ACIDIFIER IN VEGETABLE STEW OF TYPE „ZACUSCA" PRODUCTION

Diana Crucirescu[1,2], ORCID: 0000-0002-6612-9937

[1]*Scientific-Practical Institute of Horticulture and Food Technologies, 59, Vieru str., Codru, Chisinau, Republic of Moldova*

[2] *Technical University of Moldova, 168, Stefan cel Mare Blvd., Chisinau, Republic of Moldova*
*Corresponding author: Diana Crucirescu: *diana.crucirescu@saiem.utm.md*

Received: 07. 18. 2023
Accepted: 08. 10. 2023

Abstract: The insufficiency of natural acidifiers in the food industry is a major problem today. The present study analyzes the acidifier from the unripe apples of variety *Golden Rezistent*. It had a significant amount of acidity (1.97 %) and impressive of total soluble substances (8.47 %). Malic acid and fructose were predominant with values of 32.95 g/dm^3 and 45.55 g/dm^3, respectively. The glucose content was 2 times lower than that of fructose, but citric acid and sucrose had very low concentrations. The acidifier was applied to the preparation of vegetable stew of type "Zacusca" under laboratory conditions. The recipe and the production technological scheme were developed. Physicochemical and sensorial indices were determined in the experimental samples. The elaborated product presented very good results compared to other similar foods, being appreciated with the maximum score. The implementation of the natural acidifier, obtained from thinned unripe apples in the food industry, is a key factor for the development of new healthy and ecological foods with a high nutritional value.

Keywords: *apple acidifier, sensory evaluation, physicochemical parameters, unripe apples, vegetable stew of type „Zacusca".*

Rezumat: Insuficiența acidifianților naturali în industria alimentară este o problema majoră în prezent. Studiul de față analizează acidifiantul din merele necoapte soi *Golden Rezistent*. Acesta a avut o cantitate semnificativă de aciditate (1,97 %) și impunătoare de substanțe solubile totale (8,47 %). Acidul malic și fructoza au fost predominante cu valorile de 32,95 g·dm^{-3} și, respectiv, 45,55 g·dm^{-3}. Conținutul de glucoză a fost de 2 ori mai mic față de cel ai fructozei, iar acidul citric și zaharoza au avut concentrații foarte mici. Acidifiantul a fost aplicat la prepararea tocanei de legume tip „Zacusca" în condiții de laborator. Au fost elaborate rețeta și schema tehnologică de producere. În mostrele experimentale au fost determinați indicii fizico-chimici și senzoriali. Produsul elaborat a prezentat rezultate foarte bune în comparație cu alte alimente similare, fiind apreciate cu punctaj maxim. Implementarea acidifiantului natural, obținut din merele necoapte rărite în industria alimentară, reprezintă factor cheie pentru dezvoltarea alimentelor noi sănătoase și ecologice cu o valoare nutritivă înaltă.

Cuvintele-cheie: *acidifiant din mere, evaluare organoleptică, indicii fizico-chimici, mere imature, tocană de legume tip „Zacusca”.*

Abbreviations: CE – capillary electrophoresis; DAFB **–** days after the full bloom; GD – Goverment Decision; HPLC – high-performance liquid chromatography; TA – titratable acidity, expressed in malic acid; TSS – total solubile solids; TS – total sugar.

1. Introduction

The insufficiency of natural sources of acidity in the food industry is a major problem today. Long-term consumption of food products containing synthetic additives affects the consumer's health, causing disturbances in the immune system. The health of the population and the consumption of ecological and beneficial foods for the human body required researchers to find alternatives to the chemical acids used for their production.

Apple acidifier represents the unfermented juice produced from unripe apples, obtained as a result of thinning or physiological fruit drop. Recent research has shown that it is a good source of natural acidity, containing and other valuable nutrients, and it is of major interest in the food industry [1, 2]. At the lab-scale, experimental samples of acidifier were obtained from unripe apples. It was then successfully applied to the production of marinated tomatoes and canned cucumbers as an alternative to acetic acid, similar to the application of verjuice [3-5].

Vegetable stew "Zacusca" is very popular among consumers in the Republic of Moldova. It is a dish of vegetables cooked on fire or fried in oil, found in several countries of the Balkans. The main ingredients are grilled eggplant and red bell peppers, and chopped onions. Other vegetables can also be added to the stew [6].

There are several varieties of this vegetable stew, but eggplant zacusca is the most widespread and one of the most liked. Being consistent, fine and with a very pleasant aroma of grilled vegetables, this type of stew is consumed, most of the time, as an appetizer. In addition to this fact, this type of zacusca, produced over an open fire (grilled), is not standardized and has no normative documents according to which it could have been a factory on an industrial scale. All the information about the recipes are collected from people or from the internet.

Classic eggplant zacusca is made from eggplant (min. 60 %), bell peppers red (min. 40 %), onion (min. 10 %), sunflower oil (4.264 %), broth or tomato juice (4.7 %), salt (1 %), spices (pepper – 0.036 %) [7]. Also, some manufacturers add sugar, to increase the sweet taste of the product, and acetic acid, to increase the acidity, fixation and accentuation the taste and the aroma of the vegetabltes.

Currently, consumers choose food products that contain as few calories as possible and with natural ingredients in its composition. Thus, it was proposed to produce, under laboratory conditions, the vegetable stew identical to the classic zacusca with some changes compared to the traditional recipe. Apple acidifier was included as a source of acidity. This was obtained without the use of oil, of fried onions, sugar and acetic acid, with the aim of obtaining a dietary product, which will allow consumption by people with problems of galls and liver [8]. At the same time, the exclusion of oil will favor increasing the shelf life of the product.

At the same time, the preparation of vegetable stew of type "Zacusca" will allow the widening of the assortment of such products and will make possible the implementation of the apple acidifier in the healthy foods production.

The aim of this work was to obtain experimental samples of vegetable stew type "Zacusca" with the application of apple acidifier and to evaluate the quality indices of the elaborated products.

2. Materials and methods

2.1 Raw materials and materials

Raw materials for prepare of apple acidifier served unripe apples, in the early ripening phase, of the variety *Golden Rezistent* (Figure 1). The fruits were picked in Juny 26, 2019 (which presented the 71st DAFB) from the experimental lots of the Scientific-Practical Institute of Horticulture and Food Technologies, Chisinau, Republic of Moldova. Physico-chemical indices of the harvested fruits were determined and presented by Cruciresсu in her work [2].

Golden Rezistent is a variety obtained in SUA. It is considered a kind of perspective. The trees are demanding to the soil, have high winter hardiness and secetă. It has stable scab resistance and high resistance to powdery mildew. The fruit is of medium to large size with a mass of 150-160 g, it has a conical-oblong to conical-truncated shape and a smooth surface. Colour of apple is yellow and of pulp is white-cremy. It bears fruit in abundance early and the flowering season is medium. Requires the thinning. The variety is authorized for all areas of the Republic of Moldova [9].

Figure 1. Image of apple fruits of the *Golden Rezistent* variety [9].

For the production of vegetable stew of type "Zacusca" the following vegetables were used as raw material: eggplants (*Solanum melongena L.*), red bell peppers (*Capsicum annuum L., Grossum Bell* group) and tomatoes (*Solanum Lycopersicum L.*) procured by on the local market. These corresponded to the normative documentation in force GD no. 929, 2009 [10]. At the same time, such secondary and auxiliary materials as table salt (GD no. 596, 2011) [11], apple acidifier, glass jars with a volume of 0.42 dm^3 and Twist-off lids were used.

2.2 Location of research

Obtaining the experimental samples and determining the quality indices in the developed products were carried out within the Food Technologies department, the Food Products Quality Verification laboratory, Scientific-Practical Institute of Horticulture and Food Technologies, Chisinau, Republic of Moldova.

2.3 Technology of Apple Acidifier Production

Obtaining the acidifier from unripe apples of the *Golden Rezistent* variety harvested around the 71st DAFB was carried out according to patent no. 1286 BOPI and similar to the technological production scheme described by Crucirescu in her work [5, 12].

2.4 Technology of Vegetable Stew of type „Zacusca" Production

The experimental samples of vegetable stew of type "Zacusca" were prepared in laboratory conditions according to the production recipe shown in Table 1.

Table 1

Recipes for making vegetable stew of type „Zacusca" [13]

Raw materials and materials	**Manufacturing recipe for 1000 g finished product, g**
Eggplants	640
Bell peppers red	400
Tomatoes	118
Salt	10
Apple acidifier	30

Laboratory-scale processing to obtain of vegetable stew of type „Zacusca" is presented in the Figure 2.

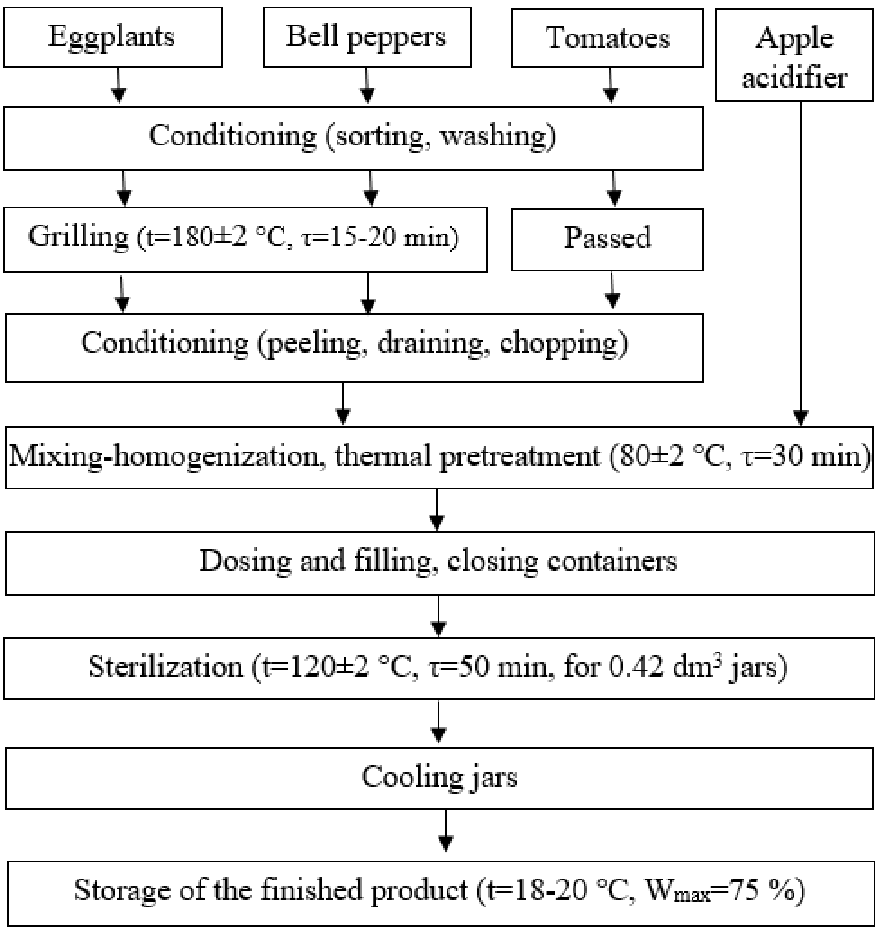

Figure 2. Lab-scale processing of vegetable stew of type „Zacusca".

The raw material for the production of vegetable stew of type "Zacusca" (eggplants, bell peppers and tomatoes) was received, sorted and washed. Eggplants and bell peppers were baked on an open fire (grilled) at a temperature of about 180±2 °C for 15-20 min. Then they were well cleaned of the skin, but bell peppers and seeds, and left to drain the liquid in a cool place for 3-4 hours. During this time, the tomatoes were washed, passed through graters (passed) with the separation of the skin and placed on the fire in a cast iron pot. After the eggplants and bell peppers drained of their own juice, they were cut into small cubes and included in the bowl with the tomatoes, where they were homogenized and left to boil for 30 min. Periodically the whole mass was mixed. Towards the end, the apple acidifier and salt were added to the vegetable dish. After the passage of time, in jars of 0.42 dm^3 washed and conditioned, the vegetable stew was dosed with a temperature of no less than 80±1 °C, closed with Twist-off lids and sterilized at a temperature of 120±2 °C for 50 min, followed by cooling and labeling. The storage and preservation of the cans obtained from the "Zacusca" type vegetable stew took place at a temperature of 19±1 °C and a maximum relative humidity of 75 % for 9 months.

2.5 Physical and Chemical Analysis

2.5.1 Analyzes in the acidifier in apples

Preparation of apple acidifier samples for analysis, determination of total soluble solids (TSS) (using the electronic refractometer ATAGO PAL-3), titratable acidity (TA) (ISO 750:1998) and ionic acidity (pH) (ISO 1842:1991), as well as the determination of the content of organic acids by the HPLC technique and of carbohydrates by the capillary electrophoresis (CE) method were carried out according to the description in the Crucirescu work [5].

2.5.2 Analyzes in the vegetable stew of type „Zacusca"

The preparation of the samples for analysis was carried out in the following way: the stew was homogenized in a mixer and diluted with distilled water of 19±1 °C in a ratio of 1:5. The whole mass was heated in a water bath at 80±2 °C for 30 min, then cooled to 20±1 °C and filtered. The obtained supernatant was used for the necessary determinations.

The determination of total dry matter in the stew was carried out using the gravimetric method by drying in an oven at 103±2 °C for 3 hours. The experiment was repeated until the mass became constant (AOAC,1999) [14]. Titratable acidity and chlorides were determined by direct titration of the analyzed supernatant with the sodium hydroxide solution in the presence of the phenolphthalein indicator (ISO 750:1998) [15], and with the standard silver nitrate solution in the presence of the potassium chromate indicator, based on the Mohr method, respectively. The ionic acidity was determined with a HANNA 211 pH-meter (Germany) the methods described in ISO 1842:1991 [16].

2.6 Sensory evaluation of Vegetable Stew of type „Zacusca"

Jars with the analyzed product were opened just before the sensory evaluation. Each taster was presented with a plate with equal amounts of vegetable stew, with equal conditions. The evaluation was carried out at a temperature of 19±1 °C.

The 8 evaluators trained in the field of food technologies, aged between 35 and 75, participated as tasters. The following organoleptic indices were evaluated: appearance, color, smell, taste and consistency. The evaluation was carried out by both the descriptive and the scoring method, using the 5-point system, which includes the following scores: 5 - very good; 4 - good; 3 - satisfactory; 2 - unpleasant; 1- bad and 0 - very bad (ISO 6658:2017) [17].

2.7 Statistical analysis

Analysis of variance of the results was performed using one-way analysis of variance and Student's test. Microsoft Office Excel version 2010 software was used for statistical analysis. All analyzes were performed in triplicate with a maximum error of less than 5 %. The results obtained were expressed as mean ± SD.

3. Results and Discussions

The acidifier from unripe apples *Golden Rezistent* variety harvested in 2019 on the 71st DAFB was obtained and can be seen in Figure 3. It was later analyzed physicochemically and sensorially in order to be applied to the production of vegetable stew type „Zacusca”.

Figure 3. Image of the experimental sample of acidifier from unripe apples *Golden Rezistent* variety.

The acidifier showed a clear liquid containing a straw-yellow sediment (less than 3 %). The taste was sour-sweet, with a light green apple flavor, pleasant, agreeable and balanced, specific to the apple variety. No foreign nuances were felt in the taste and smell. The juice yield after pressing to obtain the acidifier was 40-52 %.

The physicochemical indices determined in the studied acidifier are presented in table 2.

Table 2

The physicochemical indices determined in the apple acidifier

Characteristics	Results
Total soluble solids, %	8.47±0.10
Titratable acidity, %, expressed in malic acid	1.97±0.20
pH	3.01±0.10
Content of organic acids, g/dm^3:	
Malic	32.95±0.01
Citric	0.26±0.01
Content of simple carbohydrates, g/dm^3:	
Fructose	45.55±0.10
Glucose	23.51±0.14
Sucrose	0.07±0.01

The results in table 2 show that the acidifier from apples *Golden Rezistent* variety is characterized by an imposing amount of total soluble solids (8.47 %), high titratable acidity (1.97 %) and a low pH (3.01). The predominant organic acid, about 85-90 % of the total organic acids in apples, is malic acid [18]. As expected, malic acid constituted the majority acid, having a concentration of 32.95 g/dm^3, and citric acid was about a hundred times less (0.26 g/dm^3). At the same time, the predominant carbohydrate was fructose with an amount of 45.55 g/dm^3, and sucrose was presented as traces, registering values of 0.07 g/dm^3. Glucose had a concentration about 2 times lower than fructose (23.51 g/dm^3). The high amounts of carbohydrates are due to the process of photosynthesis, after which in the mesophyll of the leaves, sucrose and sorbitol are formed, which are transported to the unripe fruits for development [19, 20].

The impressive amounts of organic acids in apple acidifiers represent one of the promising ways to supplement the need for natural sources of acidity in the food industry. And significant amounts of carbohydrates can replace some of the sugar added to food during production. Marques et al. analyzed malic acid for its potential as a food ingredient [21]. Due to the penetration of organic acids into the cell wall, they have an antimicrobial and antibacterial effect [22]. At the same time, replacing chemical acidifiers with natural ones in production will improve the nutritional value of food [3].

Due to the need to implement natural sources of acidity in the food industry, the decision was made to apply the acidifier from apples to obtain vegetable stew of type "Zacusca", thus producing new functional foods.

The preparation of the mentioned stew was carried out according to the recipe and the production scheme presented in Table 1 and Figure 2, respectively. The experimental samples of elaborated products were obtained, in which quality indices were determined after 9 months of storage. Similar stew products from the normative document in force in the Republic of Moldova GOST 2654-98 (valid, according to OMAIA 153/2010) served as a reference [23]. The results of the analyzes are presented in Table 3.

Table 3

The physicochemical indices determined in the vegetable stew of type „Zacusca" samples

Characteristics	Norm *	Rezults
Total soluble solids, %, not less	18.0 – 27.0	27.0±0.05
Titratable acidity, %, recalculated to malic acid	n/n	0.42±0.04
Content of chlorides, %	1.2 – 1.6	0.94±0.07
pH	n/n	4.81±0.02
Impurities, including mineral	n/a	n/d

Note: * according to [23]; n/n – not normed; n/a – not admitted; n/d – not detected.

The results obtained in the determined samples show that vegetable stew of type "Zacusca" is very beneficial for consumption by the population, from the point of view of the composition, but also of the method of preparation, being the most requested. The amount of TSS had a high value, compared to similar products according to the norm 27.0 %, and the salt content, on the contrary, was lower, having 0.94 %. These results may be due to the fact that the apple acidifier contains its own TSS in significant amounts [2], there by increasing the TSS content of the finished product. Salt, however, was added in minimal amounts in the production process. The total concentration of organic acids and pH were 0.42 % and 4.81, respectively, which confirms that the developed food product can be acceptable to all consumers. Acidity affects both the taste and aroma of the finished product, as well as microbial stability and shelf life [24].

Sensory analysis of the food product is carried out for a wider understanding of it. Vegetable stew of type "Zacusca" was evaluated by the tasting committee composed of 8 people trained in the field of food. All the evaluators were pleasantly surprised by the results obtained, especially by the aroma and taste of the grilling smoke. At the same time, a slight separation of the liquid from the entire mass was observed, which is allowed in the case of boiled or baked vegetable stew, according to GOST 2654-98 (OMAIA 153/2010) [23]. The description of all sensory characteristics is presented in Table 4.

Table 4

Descriptive analysis of the vegetable stew of type „Zacusca" samples

Characteristics	Description *
Appearance	Eggplant paste with inclusions of pieces of eggplant and red bell peppers cut to almost the same size, possible inclusions of tomatoes, all skinless. The presence of soft eggplant seeds evenly distributed throughout the mass, a slight separation of the liquid from the entire mass.
Color	Characteristic of canned vegetables, without burns. The pieces of pepper and tomato have a homogeneous red color, eggplant - light-brown. The color of the mass – red-orange to brown.
Smell and taste	Characteristics of heat-treated vegetables, very pleasant and well expressed, with a shade of smoke, without bitter taste and foreign nuances.
Aroma	Pleasant, with a slight shade of green apple and cooking smoke.
Consistency	Zacusca is presented in the form of a paste with inclusions of pieces of eggplant, bell peppers and tomatoes. Vegetables well processed, soft, but not overcooked.

Note: according [25] * descriptive method, according to ISO 6658:2017.

Following the sensory evaluation (Table 4) it was concluded that all 5 analyzed indicators presented very good results. The products did not present any objections from the tasting committee and were appreciated with maximum points. At the same time, for a more complex understanding, in figure 5 are presented the photos of the exterior aspect of the elaborated product.

Figure 5. Image of the experimental sample vegetable stew of type „Zacusca".

Conclusions

Golden Rezistent apples harvested on the 71st DAFB served as raw material for obtaining the natural acidifier. It was characterized by high values of titratable acidity (1.97 %) and of TSS (8.47 %). As expected, malic acid was the predominant organic acid with the concentration of 32.95 g/dm^3, and fructose was the main carbohydrate with 45.55 g·dm^{-3}. Glucose showed a value about 2 times lower than fructose (23.51 g/dm^3). Citric acid and sucrose were found in very small amounts with the content of 0.26 g/dm^3 and 0.07 g/dm^3, respectivelly. The pH value of the acidifier was 3.01.

The studied apple acidifier was applied to the production of vegetable stew of type "Zacusca", in laboratory conditions, with the elaboration of the recipe and the production scheme. The experimental stew samples had better physicochemically characteristics compared to similar products, according to the normative documentation in force. The amounts of titratable acidity and salt were low, with values of 0.42 % and 0.94 %, respectively, and the TSS content was significant (27.0 %). The developed product was appreciated with maximum score by the tasting committee for all 5 sensory indices.

The use of unripe apples, being horticultural waste, with the obtaining of the natural acidifier and its implementation in the food industry, is a key factor for the development of new healthy foods with a high nutritional value.

Acknowledgments. Author thanks the World Federation of Scholars (WFS) for the support by awarding the Excellence Scholarship and she would like to express her gratitude to Dr. Eugen Iorga, associate researcher, for the knowledge and support provided during the research.

Conflicts of Interest. The author declares that they have no conflict of interest.

References

1. Crucirescu, D. The content of organic acids in unripe apples. In*: Proceedings of Technical-Scientific Conference of Students, Masters and Doctoral Students (with international participation),* TUM, 2022, 1, 462-465
2. Crucirescu, D. Physicochemical caracteristics in unripe apples. *Journal of Engineering Science* 2021, 28 (4), pp. 156-166.
3. Dupas de Matos, A.; Marangon, M.; Magli, M.; Cianciabella, M.; Predieri, S.; Curioni, A.; Vincenzia, S. Sensory characterization of cucumbers pickled with verjuice as novel acidifying agent. *Food Chemistry* 2019, 286, pp. 78-86/
4. Golubi, R. Recovery of immature grapes in obtainment of nutritional compositions, Doctoral thesis in technical sciences, Chisinau, 2019.
5. Crucirescu, D. Implementation of apple acidifier in canned cucumbers production. *Scientific Study & Research - Chemistry & Chemical Engineering, Biotechnology, Food Industry* 2023, 24 (1), pp. 061-071.
6. Laurentiu, L. Recipe. Available online: https://www.lauralaurentiu.ro/retete-culinare/conserve/zacusca-de-vinete.html (accessed on 29.06.23) [In Romanian]
7. Recipe of the zacusca of the eggplant. The most beloved vegetable preserve. Available online: https://ea.md/reteta-de-zacusca-de-vinete-cea-mai-indragita-conserva-din-legume/ (accessed on 29.06.23) [in Romanian].
8. Fabbri, A.D.T.; Crosby,G.A. A review of the impact of preparation and cooking on the nutritional quality of vegetables and legumes. *International Journal of Gastronomy and Food Science* 2016, 3, pp. 2-11.
9. Babuc, V.; Peșteanu, A.; Gudumac, E.; Cumpanici, A. Apple production. Bons Offices, Chisinau, Republic of Moldova, 2013, 240 p.
10. Government Decision regarding the approval of "Quality and marketing requirements for fresh fruits and vegetables" no. 929 of 31.12.2009. In: *Official Monitor of the Republic of Moldova*. 2010, no. 5-7, 26. Available online: https://www.legis.md/cautare/getResults?doc_id=110404&lang=ro (accessed on 12.06.23) [in Romanian].

11. Government Decision for the approval of the Sanitary Regulation on food salt, no. 596 of 03.08.2011. In: *Official Monitor of the Republic of Moldova.* 2011, no. 131-133, 666. Available online: https://www.legis.md/cautare/getResults?doc_id=110144&lang=ro (accessed on 12.06.23) [in Romanian].
12. Golubi, R.; Iorga, E.; Bucarciuc, V.; Arnăut, S.; Crucirescu, D. The process of obtaining the acidifier from apples. MD Patent 1286, BOPI, 2019.
13. Yastrebov, M. S. Handbook of the master of canning production. 2nd edition, revised and enlarged. Food Industry, Moscow 1980, 132
14. AOAC, Official methods of analysis. 16th ed., Cunnif, P. (ed.) AOAC International, Washington, D.C., USA, 1999, 2 (44/4).
15. ISO 750:1998 Fruit and vegetable products. Determination of Titratable Acidity. International Organization for Standardization: Geneva, Switzerland, 1998.
16. ISO 1842:1991 Fruit and vegetable products. Determination of pH. International Organization for Standardization: Geneva, Switzerland, 20, 1991.
17. ISO 6658:2017. Sensory Analysis. Methodology. General Guidance. International Organization for Standardization: Geneva, Switzerland, 2017.
18. Ma, B.Q.; Chen, J.; Zheng H.Y.; Fang T.; Ogutu C.; Li S.; Han Y.; Wu B. Comparative assessment of the composition of sugar and malic acid in cultivated and wild apples. *Food Chemistry* 2015, 172, pp. 86-91.
19. Blanke, M.M.; Lenz, F. Fruit photosynthesis. *Plant Cell Environment* 1989, 12, pp. 31–46
20. Fan, R-C.; Peng, C-C.; Xu, Y-H.; Wang, X-F.; Li, Y.; Shang, Y.; Du, S-Y.; Zhao, R.; Zhang, X-Y.; Zhang, L.-Y.; Zhang, D.-P. Apple sucrose transporter SUT1 and sorbitol transporter SOT6 interact with cytochrome b5 to regulate their affinity for substrate sugars. *Plant Physiology* 2009, 150, pp. 1880–1901
21. Marques, C.; Sotiles, A.R.; Farias, F.O.; Oliveira, G.; Mitterer-Daltoé, M.L.; Masson, M. L. Full physicochemical characterization of malic acid: Emphasis in the potential as food ingredient and application in pectin gels. *Arabian Journal of Chemistry* 2020, 13(12), pp. 9118-9129
22. Zhang, J.; Chen,W.; Li, S.; Xue, Z.; Zheng, W.; Guo, Y. Antibacterial activity and preservative properties of thinned young apples extracts for fish flesh. *Journal of Food Processing and Preservation* 2017, 42, e13435.
23. OMAIA153/2010 – Order no. 153 of 14.07.2010 regarding the approval of national standards. In: Official Monitor of the Republic of Moldova. 2010, 124-125, art. 445. Available online: https://www.legis.md/cautare/getResults?doc_id=98133&lang=ro (accessed on 12.06.23)
24. Coban, H.B.: Organic acids as antimicrobial food agents: applications and microbial productions. *Bioprocess and Biosystems Engineering* 2020, 43, pp. 569–591.
25. Banu, C. *Quality and sensory analysis of food products*. ASAB Publishing House, Bucharest, Romania, 2007, 574 p. [in Romanian].

Citation: Crucirescu, D. Application of apple acidifier in vegetable stew of type „Zacusca" production. *Journal of Engineering Science* 2023, 30 (3), pp. 145-154. https://doi.org/10.52326/jes.utm.2023.30(3).10.

Submission of manuscripts: jes@meridian.utm.md

Journal of Engineering Science | | *Vol. XXX, no. 3 (2023), pp. 155 - 163*
Fascicle | *Food Engineering* | *ISSN 2587-3474*
Topic | *Food Technologies and Food Processes* | *eISSN 2587-3482*

https://doi.org/10.52326/jes.utm.2023.30(3).11
UDC 637.5.034:636.2

DRY-AGED BEEF: COLOR PARAMETERS AND SENSORY CHARACTERISTICS

Viorica Bulgaru, ORCID: 0000-0002-1921-2009,
Liliana Popescu, ORCID: 0000-0003-3381-7511

Technical University of Moldova, 168 Stefan cel Mare Blvd., Chisinau, Republic of Moldova
*Corresponding author: Viorica Bulgaru, *viorica.bulgaru@tpa.utm.md*

Received: 08. 02. 2023
Accepted: 09. 05. 2023

Abstract. Research work involves the instrumental analysis of the change in color (*L*, a*, b**) and the sensory characteristics of the Simmental beef, parts of the carcass: T-bons, received from the local farm, during the dry-aging period for 0, 14, 21, 28, 35 days and for the roasted aged beef at high and very high temperatures. The analyzed beef samples presented uniform results for the chromatic parameters during the dry-aging period, being influenced by the values of meat pH and the water-holding capacity, namely: for the dry-aged meat, the *L** parameter values indicate an increase in the brightness of the meat, for the *a** parameter, decreasing values were established, which indicates a reduction in the oxygenation of the meat, a reduction of oxymyoglobin in meat, responsible for the intense red color and for the *b** coordinate a slight decrease in values was observed, oriented to yellow color. For roasted beef parameter *L** decreases due to the reduction of the beef moisture during the roasting process. The redness of beef *a** decreases in intensity primarily depending on the beef aging period but also with the increase in the roasting temperature, due to the drastic degradation of myoglobin. The *b** parameter also decreases, possibly due to the increase in metmyoglobin content during heat treatment. The sensory characteristics of the dry aged beef have been considerably improved due to the increase in the pH of the meat, which attracts the activation of meat-specific enzymes that contribute to the accumulation of secondary compounds with a major impact on the beef taste, aroma and juiciness. These aspects are later reflected on the sensory properties of the roasted aged beef, being intensified by the heat treatment process.

Keywords: *dry aging process, beef, cooked dry aged beef, cromatic parametres, color differences, sensory properties.*

Rezumat. Prezenta lucrare include analiza instrumentală a modificării culorii (*L*, a*, b**) și a caracteristicilor senzoriale ale cărnii de bovină, rasa Simmental, părți din carcasă: T-bons, recepţionate de la ferma locală, în timpul procesului de maturare prin uscare timp de 0, 14, 21, 28, 35 de zile si pentru carnea de bovină maturată prin uscare prăjită la temperaturi ridicate si foarte ridicate. Probele de carne de bovină analizate au prezentat rezultate uniforme pentru parametrii cromatici în perioada de maturare prin uscare, fiind influențate de valorile pH-ului cărnii și de capacitatea de reținere a apei și anume: pentru carnea maturată prin uscare, valorile parametrului *L** indică o creștere a luminozităţii cărnii, pentru parametrul *a** s-au stabilit valori în scădere, ceea ce indică o scădere a oxigenării cărnii, o

reducere a oximioglobinei din carne, responsabilă de culoarea roșie intensă și pentru coordonata *b** a fost observată o scădere ușoară a valorilor, situată pe partea pozitivă a axei, care reprezintă culoarea galbenă. Pentru carnea de bovină prăjită parametrul *L** scade datorită reducerii umidității cărnii în timpul procesului de prăjire. Culoarea roşie a cărnii de bovină *a** scade în intensitate în primul rând în funcție de perioada de maturare a cărnii, dar și odată cu creșterea temperaturii de prăjire, din cauza degradării drastice a mioglobinei. Parametrul *b** scade și el, posibil din cauza creșterii conținutului de metmioglobină în timpul tratamentului termic. Caracteristicile senzoriale ale cărnii de bovină maturate prin uscare au fost considerabil îmbunătățite datorită creșterii pH-ului cărnii, care implică activarea enzimelor specifice cărnii ce contribuie la acumularea de compuși secundari cu impact major asupra gustului, aromei şi suculenţei cărnii. Aceste aspecte se reflectă ulterior asupra proprietăților senzoriale ale cărnii de bovină maturată prin uscare prăjite, caracteristicile cărora sunt intensificate de procesul de tratare termică.

Cuvinte cheie: *process de maturare prin uscare, carne de bovină prăjită, parametric cromatici, diferenţă de culoare, proprietăţi senzoriale.*

1. Introduction

The transformation of muscle tissue into meat is a complex process that involves biochemical processes of proteolysis, glycolysis, lipolysis and oxidation, specific to the aging period, with a major impact on improving the meat palatability [1-3].

The obtained quality characteristics as a result of these changes are important in the appreciation of meat quality by the consumer [4].

Color is a key quality characteristic of meat serving as an indicator of quality and freshness. The value of the carcass / half-carcass will be assessed according to this index, which will change depending on the pH value, the content of myoglobin and the attached ligand (for example, O_2, CO, NO) and the structure of the meat [5, 6]. The structure of the meat will influence and direct the passage of light in the meat, an effect that will affect the color parameters. Respectively, upon contact with the meat, the light is reflected, absorbed and spread. These characteristics will determine the color of the meat. The main characteristic, which influences the degree of consumer acceptability, is the light reflection. The pH value of the muscle tissue will influence the ability to spread light. A lower pH of the meat will positively influence the light spreading property [7]. In addition, during the decrease in meat pH, the proteins approach the isoelectric point, the myofilaments undergo changes, leading to more difficult separation of the filaments [8]. In addition, the diameter of the muscle fiber changes, it decreases, which allows the space between the cells to increase [9]. The translucency of the meat decreases and the distribution coefficient increases, phenomena that beneficially influence the scattering of light [7]. Accordingly, light is distinguished into color attributes a* and b* and achromatic color attributes L*.

The main chromatic component of the meat is the myoglobin pigment, which can influence the color of the meat based on the oxidation state of the iron atom incorporated in the structure of the porphyrin ring of the hem group. In comparison, the structure of the muscle tissue will influence the L* value. Thus, the light is absorbed by the myoglobin, and the unabsorbed light is transmitted around the structural elements. The reflected light will help determine the final changes.

Light is scattered when it is diffused through collisions with the particles of the medium it crosses. In muscle, the medium can be either connective tissue, muscle fibers, myofibrils, extracellular fluid, or sarcoplasm. The amount of reflected light will depend on its degree of diffusion in the structure of the meat, the less it reaches the depth of the meat, the more will be reflected. So, the degree of light scattering contributes to the formation of the color perceived by the human eye [10].

Color remains an indicator in assessing the degree of doneness of dry-aged beef, considering the various types of thermal treatments applied to these products, from "very rare" to "well done". Consumer perception of doneness by color parameters can lead to safety issues as research on meat preparations, especially minced meat, shows that visual appearance does not mean that reached temperature could ensure the necessary microbiological stability. But these arguments are not specific for meat in pieces, as in the case of steaks, when indeed the microbiological danger exists more on the surface of the meat pieces, which can be reduced even with short-term thermal treatments [11].

The sensory characteristics and main color parameters of cooked meat may differ depending on the heat treatment method and parametres (grilling, roasting, boiling, etc.) including temperature and heating rate [12].

Heat treatment type used in prepering meat can be classified according to cooking temperatures: low temperature (till 100°C), high temperature (more than 100°C) and high temperature (which exceeds 200°C) [13].

The use of high and very high temperatures leads to an increase in the heating rate and degree of the Maillard reaction, which enhances the flavor of the cooked meat [12].

This study was carried out to determine the effects of beef dry aging conditions on sensory indices with an emphasis on color parameters through L^*, a^* and b^* values, as well as the change of color parameters during the heat treatment of dry aged beef as factors of meat quality appreciation by consumers.

2. Materials and Methods

For analysis, sliced from the carcass of Simmental breed were used: T-bons, fresh meat was received from local farm. The quality requirements specified in [14].

Fresh meat and dried aged meat were subjected to determinations. Beef was aged during 14, 21, 28 and 35 days in aging rooms where temperature varied within limits 1±1 °C, relative humidity between 80±5 %, air circulation speed - 0.5-2 m/s.

Thin slices of beef were used to obtain color change information during heat treatment. The samples were subjected to grilling heat treatment at 150°C or 230°C, about 3 minutes per each part using an electric grill.

Sensory analysis of fresh, aged and cooked meat. The sensory properties of the meat samples were analyzed under standardized conditions by a group of evaluators, by description, according of standard ISO 6658:2017 [15]. Quality requirements ware characterized according to [14] for fresh and aged meat and to characterize the organoleptic indices of cooked meat [16] was used.

Color parameters analysis. The CIE-Lab parameters, L^*, a^*, and b^* were measured using a Chroma Meter CR-400/410 colorimeter (Konica Minolta, Tokyo, Japan) according to the method of [17]. Each sample was analyzed at five distinct points, measuring variations of L^*, a^*, b^*, the differences of color (ΔE^*), hue angle (H^*) and chroma (C^*).

The following Equation (1) was used to determinate the ΔE^*:

$$\Delta E^* = \sqrt{(L_i^* - L_0^*)^2 + (a_i^* - a_0^*)^2 + (b_i^* - b_0^*)^2} \quad (1)$$

where:

L^* - brightness coordinate,

a^* - green versus red coordinate,

b^* - blue versus yellow coordinate,

L_0^*, a_0^* and b_0^* - the values at zero time;

L_i^*, a_i^* and b_i^* - the values with time.

ΔE^* - comparisons based on two different factors: color values at t = 14, 21, 28, 35 days versus fresh meat.

Statistical analysis. The statistical processing of the obtained results was performed using the Student test and the Microsoft Office Excel version 2010 program. The differences were considered statistically too significant when the probability was greater than 95% ($p<0.05$). The tests were repeated in triplicate. Experimental results are expressed as mean ± SD.

3. Results

The dry aging process has a favorable impact on the quality indices of the beef, highlighting improved sensory properties, intensifying the color parameters, processes influenced by the decrease in acidity and the increase in the water retention capacity of the meat [18, 19].

Biochemical reactions such as lipolysis, proteolysis and oxidation are some of the processes that occur during the post-slaughter period. The decomposition of myofibrillar proteins, achieved through the process of proteolysis, leads to the formation of peptides and amino acids, which act as precursors of water-soluble flavors, subsequently contributing to the formation of the taste properties and flavoring characteristics of meat [1, 20].

In the post- slaughter period, the accumulation of metabolic by-products occurs in the muscle tissue, which leads to a decrease in pH. The decrease in pH from the neutral value brings about favorable changes in the beef flavor. The results obtained during the beef dry aging period show a significant improvement in the organoleptic indices (sample M21, M28, M35), especially the flavor becomes more intense specific to aged beef in comparison with unaged beef which has a weak and bland odor. These characteristics may be due to the intensification of the lipid oxidation process which, by combining with protein degradation substances, contributes to the improvement of the meat flavor. Similar results were shown by other authors [21, 22].

Although the visual appreciation of the color and consistency of meat subjected to dry aging process is considered subjective by some authors [23]. In the respective research the results obtained showed clearly visible differences in the modification of these parameters depending on the aging period.

The color of the dry aged beef samples for 21, 28, 35 days is dark red and with a much finer consistency compared to the control sample or aged up to 14 days. The fine consistency resulting from the degradation process of meat proteins under the action of proteolytic enzymes, similar results described by [22].

The sensory indicator results for the raw dry aged beef were analyzed and presented in the work of Bulgaru et al. 2022 (Tables 1 and 2) [18].

The values of the organoleptic indices are also supported by the variation of the beef pH. The values obtained for pH contribute to the release of Ca^{2+} ions from the sarcoplasmic reticulum and mitochondria when the ATP reaches its lowest values, which leads to the intensification of calpain activity.

Table 1

Sensory indicators of roast dry aged beef

Indicators	Samples				
	Fresh beef	**M14**	**M21**	**M28**	**M35**
Color	Dark, depending on the aging time and roasting temperature				
Consistency	Relatively cooked, reduced elasticity	A high degree of cooking, elastic, easy to chew			
Flavor	Low flavor, lingering flavor of fried meat	Pleasant flavor of roasted meat mixed with volatile compounds specific to aged meat.			
Juiciness	Dry beef	Juicy beef, perception of water content in the sample after 3–4 chewings			

Note: M14—beef dry aged for 14 days; M21— beef dry aged for 21 days; M28— beef dry aged for 28 days; M35— beef dry aged for 35 days.

Also these pH values coincide with the pH values specific for cathepsins, which begin to destroy the miofibrilar proteins such as myosin and actin [24, 18]. Other researchers present similar data, such as Lee et al. [25] when an increase in pH of just over 11% at dry aging for 63 days. Responsible for increasing the pH of dry aged meat may be the formation of nitrogenous compounds in the process of protein hydrolysis.

Water holding capacity (WHC) and color are often related to the final pH of the meat, these indicators being in fact considered important indices of meat quality. The WHC of meat is increased by the presence of meat-specific enzymes that break down connective tissues and myofibrillar proteins and are thus responsible for improving the meat WHC. The chemical reactions with the participation of these enzymes result in a decrease in the heat treatment time along with the increase in the drying maturation period [26].

The results of the sensory analysis of the roasted beef were more affected by the heat treated conditions than the dry aging period, and heat treatment at very high temperatures had a major impact on the color of the meat for all samples. For the other sensory indicators, the aging period is important in obtaining the specific characteristics.

The values of the color parameters, L^*, a^*, b^*, of the dry-aged beef are shown in Table 2.

Table 2

CIE-Lab parameters of dry aged beef

Chromaticity coordinates	Samples				
	Fresh Beef	**M14**	**M21**	**M28**	**M35**
L^*	37.38±0.10	38.25±0.1	39.75±0.42	40.69±0.42	41.91±0.09
a^*	19.31±0.07	18.73±0.34	17.98±0.67	18.38±0.08	13.55±0.11
b^*	13.81±0.39	13.68±0.22	13.56±0.22	13.58±0.18	13.5±0.43
C^*	23.70±0.14	22.86±0.20	21.94±0.09	20.70±0.77	19.12±0.10
ΔE^*	-	1.05±0.11	2.73±0.11	3.44±0.26	7.33±0.18

Note: M14—beef dry aged for 14 days; M21— beef dry aged for 21 days; M28— beef dry aged for 28 days; M35— beef dry aged for 35 days.

During the dry aging period for parameters L^* were obtained values between 37.38 and 41.91 units. This values support the high brightness of meat. Coordinate a^* showed the average values between 19.31 and 13.55 units - decreasing values. This results could be explaining by the reduction in the oxygenation capacity of the beef which depends on the availability of oxygen, the diffusion of oxygen in the meat and the rate of oxygen consumption. In addition, the decreased water-holding capacity of dry aged beef can result in more intense reflection of light from the surface of the meat, making it appear pale. Hopkins et al. [27] showed a decrease in chroma a^* for meat aged for 42 days compared to that aged for 4 days.

In the case of chroma b^*, the average values were between 13.81 and 13.50, an insignificant decrease was recorded, all being located on the positive side of the axis, which represents the yellow zone.

The uniform values were obtained for all three chromatic coordinates L^*, a^*, b^* throughout the dry aging period, similar results were also showed by Obuz et al. [22] for dry aged meat for 23 days.

For chroma C^* the results decreased from 23.7 to 19.12, values that explain why the color intensity of the analyzed beef decreased.

The values for the ΔE^* parameter represented the color differences between the analyzed beef samples. The color difference cannot be perceived by evaluators when $0<\Delta E^*<1$, the experienced ones will notice the color difference between the analyzed samples when the relationship is $1<\Delta E^*<2$, and if ΔE^* will be included in the following limits $2<\Delta E^*<3.5$, then the color differences will be able to be noticed even by inexperienced evaluators [28, 29].

According to the data presented in Table 2, ΔE^* increases proportionally with the increase in the dry aging period, from 1.05 to 7.33, which correlates with the results of the sensory analysis by which the color change is detected with the naked eye. For beef aged for 14 days, the color difference cannot be perceived with the naked eye, but for beef aged for 21, 28 and 35 days respectively, the color difference can be distinguished with the naked eye even by inexperienced evaluators.

The beef color, both in depth and on the surface, was analyzed separately and the appearance of the brown color is largely due to the denaturation of myoglobin during roasting at high and very high temperatures [30].

No major changes were observed in roasted meat depending on the beef dry aging period. The most obvious changes in the color parameters were related to the heat treatment temperatures (Table 3).

The obtained results for the surface color parameters of the roasted meat at very high temperatures were lower compared to the treatment at high temperatures and obviously compared to the results obtained inside beef color. Similar results were obtained by [11, 12] in research conducted on roast beef.

The values of the parameter L^* decrease due to the reduction of the moisture of the meat on the surface during roasting process and it was directly proportional to the increase in the temperature of the heat treatment process. The redness of beef *(a^*)* decreases in intensity primarily depending on the beef aging period but also with the increase in the roasting temperature, due to the drastic degradation of myoglobin.

Table 3

Color parametres of roast dry aged beef

Color parametres	Beef samples	Surface color of roast beef		Internal color of roast beef	
		150˚C	230˚C	150˚C	230˚C
L*	Fresh Beef	29.76±0.10	28.12±0.13	30.15±0.18	28.89±0.18
	M14	28.15±0.70	26.78±0.17	29.0±0.10	28.18±0.03
	M21	27.45±0.09	26.07±0.34	28.34±0.75	27.50±0.33
	M28	27.08±0.11	25.57±0.30	27.97±0.15	26.09±0.66
	M35	26.78±0.03	24.82±0.42	27.04±0.26	25.36±0.17
a*	Fresh Beef	17.82±0.11	17.02±0.66	18.42±0.22	18.12±0.42
	M14	17.23±0.24	16.23±0.34	18.12±0.71	17.90±0.08
	M21	16.78±0.15	15.71±0.16	17.78±0.19	17.04±0.11
	M28	16.23±0.25	15.25±0.11	17.03±0.07	16.82±0.10
	M35	16.00±0.11	15.18±0.19	16.89±0.10	16.03±0.21
b*	Fresh Beef	12.70±0.11	12.32±0.22	13.00±0.07	12.90±0.10
	M14	12.65±0.08	11.52±0.22	12.87±0.67	12.26±0.10
	M21	12.36±0.07	11.34±0.10	12.60±0.64	12.00±0.09
	M28	12.02±0.18	11.28±0.07	12.34±0.34	11.98±0.25
	M35	11.80±0.09	11.16±0.12	12.05±0.07	11.90±0.10
C*	Fresh Beef	21.88±0.28	21.01±0.11	22.55±0.24	22.24±0.07
	M14	21.38±0.07	19.90±0.66	22.23±0.36	21.70±0.22
	M21	20.84±0.18	19.38±0.58	21.79±0.18	20.84±0.64
	M28	20.20±0.18	18.97±0.11	21.03±0.07	20.65±0.72
	M35	19.88±0.10	18.84±0.10	20.75±0.18	19.96±0.34
Δ*E**	Fresh Beef	-	-	-	-
	M14	1.72±0.11	1.75±0.32	1.20±0.07	1.33±0.19
	M21	2.56±0.07	2.62±0.11	1.96±0.37	2.29±0.80
	M28	3.19±0.22	3.27±0.20	2.67±0.02	2.70±0.16
	M35	3.61±0.10	3.95±0.07	3.59±0.26	3.88±0.30

Note: M14—beef dry aged for 14 days; M21— beef dry aged for 21 days; M28— beef dry aged for 28 days; M35— beef dry aged for 35 days

The *b** parameter also decreases, possibly due to the increase in metmyoglobin content during heat treatment. The obtained results were close to those presented in his work by Lee et al. regarding the chromatic parameters of dry aged beef and wet aged for 28 days [31].

Chroma *C** values show decreasing results for roasted meat, depending on the used temperature. For higher temperatures, the chroma *C** values are the lowest, which characterizes the decrease in color intensity. The results for chroma *C** analyzing the meat on the surface or inside demonstrate that the same law of decrease in the intensity of the meat color is preserved, but the decrease of inside meat color intensity is lighter.

According to the data presented in Table 3, Δ*E** increases with extending meat dry aging period, as in the case of non-thermally treated meat. The change in the color of roasted meat can be observed with the naked eye on the surface for dry aged meat for 28 and 35 days, inside only for dry aged meat for 35 days. Depending on the used temperature, 230 ˚C had the major impact on the meat color differences.

4. Conclusions

Dry aging process proved to be an effective technique in order to improve sensory indices, color parameters, especially for aged beef samples during 21, 28 and 35 days. Color coordinates *L*, a*, b** throughout the dry aging period showed stable values depending on the pH value and the increasing water holding capacity. The difference in color ΔE* is more visible as the dry aging period increases, both for raw and roasted dry aged beef, which correlates with the obtained results. The results obtained for the analyzed quality indices, together with the results of other researches in the field, may have implications in the development of the dry aging technology in the Moldovan meat industry branch.

The results argued in the paper were discussed at the *International Conference MODERN TECHNOLOGIES IN THE FOOD INDUSTRY,* Chisinau, 20-22 October 2022.

Acknowledgments: The research was funded by State Project no. 20.80009.5107.09 ”*Improving of food quality and safety through biotechnology and food engineering”*, running at Technical University of Moldova.

Conflicts of Interest: The authors declare no conflict of interest.

References

1. Khan, M. I.; Jung, S.; Nam, K. Ch.; Cheorun, J. Postmortem Aging of Beef with a Special Reference to the Dry Aging. Korean J Food Sci Anim Resour. 2016, 36(2), pp. 159–169.
2. McGee, H. On food and cooking: The Science and Lore of the Kitchen. Scribner, NY, USA, 2004.
3. Piao, M. Y.; Jo, C.; Kim, H. J.; Lee, H. J.; Kim, H. J.; Ko, J. Y.; Baik, M. Comparison of carcass and sensory traits and free amino acid contents among quality grades in loin and rump of Korean cattle steer. *Asian Australas. J. Anim. Sci.* 2015, 28, pp. 1629−1640.
4. Mărgean, A.; Măzărel, A. Tenderization, a method to optimize the meat sensory quality. *Bulletin of the Transilvania University of Braşov, Series II, Agricultural Food Engineering* 2017, 10(59), pp. 1-6.
5. Mancini, R. A.; Hunt, M. C. Current research in meat color. *Meat Science*, 2005, 71, pp. 100-121.
6. Suman, S. P.; Joseph, P. Myoglobin Chemistry and Meat Color. *Annual Review of Food Science and Technology* 2013, 4(4), pp. 79-99.
7. Macdougall, D. B. Changes in the color and opacity of meat. *Food Chemistry* 1982, 9(1), pp. 75-88.
8. Diesbourg, L.; Swatland, H. J.; Millman, B. M. X-Ray Diffraction Measurements of Postmortem Changes in the Myofilament Lattice of Pork. *Journal of Animal Science* 1988, 66(4), pp. 1048-1054.
9. Offer, G.; Cousins, T. The mechanism of drip production: Formation of two compartments of extracellular space in muscle Post mortem. *Journal of the Science of Food and Agriculture* 1992, 58(1), pp. 107-116.
10. Hughes, J.M.; Oiseth, S.K.; Purslow, P.P.; Warner, R.D. A structural approach to understanding the interactions between color, water-holding capacity and tenderness. *Meat Science* 2014, 98(3), pp. 520-532.
11. Goñi, S. M.; Salvadori, V., O. Kinetic modelling of colour changes during beef roasting. *Procidia food science* 2011, 1, pp. 1039-1044.
12. Lee, D.; Lee, H.J.; Yoon, J.W.; Ryu, M.; Jo, C. Effects of cooking conditions on the physicochemical and sensory characteristics of dry- and wet-aged beef. *Anim Biosci* 2021, 34(10), pp. 1705-1716.
13. Ángel-Rendón, S.V.; Filomena-Ambrosio, A., Hernández-Carrión, M. Pork meat prepared by different cooking methods. A microstructural, sensorial and physicochemical approach. *Meat Sci* 2020, 163, pp. 1080-1089.
14. GD No. 696 from 04-08-2010 for the Approval of the Requirements Regarding the Production, Import and Placing on the Market of Meat—Raw Material. *Available online:* http://lex.justice.md/index.php?action=view&view=doc&id=335616 (accessed on 1 March 2023). (In Romanian)
15. ISO 6658:2017. Sensory Analysis—Methodology—General Guidance. International Organization for Standardization: Geneva, Switzerland, 2017. Available online: https://www.iso.org/standard/65519.html (accessed on 25may, 2023).
16. GD No 624 of 2020 regarding the approval of the Quality Requirements for meat preparations and products. Available online: https://www.legis.md/cautare/getResults?doc_id=123163&lang=ro. (accessed on 1 March 2023) [in Romanian].

17. Loypimai, P.; Moongngarm, A.; Chottanom, P. Thermal and pH degradation kinetics of anthocyanins in natural food colorant prepared from black rice bran. *Journal of Food Science and Technology* 2016, 53 (1), pp. 461- 470.
18. Bulgaru, V.; Popescu, L.; Netreba, N.; Ghendov-Mosanu, A.; Sturza, R. Assessment of quality indices and their influence on the texture profile in the dry-aging process of beef. *Foods,* 2022, 11, 1526.
19. Kim, J.H.; Jeon, M.Y.; Lee, C.H. Physicochemical and sensory characteristics of commercial, frozen, dry, and wet-aged hanwoo sirloins. *Asian-Australas J Anim Sci.* 2019, 32, pp. 1621- 1629.
20. Koutsidis, G.; Elmore, J.S.; Oruna-Concha, M.J.; Campo, M.M.; Woo, J.D.; Mottram, D.S. Water-soluble precursors of beef flavor. Part II: Effect of post mortem conditioning. *Meat Sci.* 2008, 79, pp. 270-277.
21. Yancey, E.J.; Dikeman, M.E.; Hachmeister, K.A.; Chambers, E.; Milliken, G.A. Flavor characterization of top blade, top sirloin, and tenderloin steaks as affected by pH, maturity, and marbling. *J. Anim. Sci.* 2005, 83, pp. 2618-2623.
22. Obuz, E.; Akkaza, L.; Gok, V.; Dikeman, M. Effects of blade tenderization, aging method and aging time on meat quality characteristics of Longissimus lumborum steaks from cull Holstein cows. *Meat Science* 2014, 96, pp. 1227–1232.
23. Goñi, V.; Indurain, G.; Hernandez, B.; Beriain, M.J. Measuring muscle color in beef using an instrumental method versus visual color scales. *Journal of Muscle Foods* 2008, 19, pp. 209–221.
24. Banu, C.; Alexe, P.; Vizireanu, C. Industrial Meat Processing; Technical Publishing House, Bucuresti, Romania, 2003, 642 p. [in Romanian].
25. Lee, H.; Jang, M.; Park, S.; Jeong, J.; Shim, Y.; Kim, J. Determination of Indicators for Dry Aged Beef Quality. *Food Sci. Anim. Resour.* 2019, 39, pp. 934–942.
26. Bruce, H. L.; Beilken, S. L.; Leppard, P. Variation in flavor textural descriptions of cooked steaks from bovine M. longissimus thoracis et lumborum from different production and aging regimes. *J. Food Sci.* 2005, 70, pp. S309-S316.
27. Hopkins, D. L.; Ponnampalam, E. N.; Van de Ven R. J.; Warner, R. D. The effect of pH decline rate on the meat and eating quality of beef carcasses. *Animal Production Science* 2014, 54, pp. 407–413.
28. Mokrzycki, W.; Tatol, M. Colour difference ΔE-A survey. *Machine Graphics and Vision* 2011, 20 (4), pp. 383-411.
29. Popescu, L.; Ghendov-Moșanu, A.; Baerle, A.; Savcenco, A.; Tatarov. P. Color stability of yogurt with natural yellow food dye from safflower (*Carthamus tinctorius* L). *Journal of Engineering Science* 2022, 29(1), pp. 142 – 150.
30. Suman S.P.; Nair, M.N.; Joseph, P.; Hunt, M.C. Factors influencing internal color of cooked meats. *Meat Sci.* 2016, 120, pp. 133-44.
31. Mitacek, R.M.; Ke, Y.; Prennie, J.E.; Jadeja, R; VanOverbeke, D.L.; Mafi, G.G.; Ramanathan, R. Mitochondrial degeneration, depletion of NADH, and oxidative stress decrease color stability of wet-aged beef longissimus steaks. *J Food Sci.* 2019, 84, pp. 38-50.

Citation: Bulgaru, V.; Popescu, L. Dry-aged beef: color parameters and sensory characteristics. *Journal of Engineering Science* 2023, 30 (3), pp. 155-163. https://doi.org/10.52326/jes.utm.2023.30(3).11.

Publisher's Note: JES stays neutral with regard to jurisdictional claims in published maps and institutional affiliations.

Submission of manuscripts: jes@meridian.utm.md

Journal of Engineering Science *Vol. XXX, no. 3 (2023), pp. 164 - 172*
Fascicle *Food Engineering* *ISSN 2587-3474*
Topic *Biotechnologies, Food Chemistry and Food Safety* *eISSN 2587-3482*

https://doi.org/10.52326/jes.utm.2023.30(3).12
UDC 004.4:613.2:616.34-008.1(478)

SOFTWARE FOR NUTRITIONAL ASSESSMENT OF PEOPLE WITH GLUTEN-RELATED DISORDERS

Dinu Țurcanu, ORCID: 0000-0001-5540-4246,
Rodica Siminiuc *, ORCID: 0000-0003-4257-1840

Technical University of Moldova, 168 Stefan cel Mare Blvd., Chisinau, Republic of Moldova
*Corresponding author: Rodica Siminiuc, *rodica.siminiuc@adm.utm.md*

Received: 08. 30. 2023
Accepted: 09. 26. 2023

Abstract. In the context of complex nutrition issues, nutritional assessment software for people with gluten-related disorders can be a precious tool for professionals in the field. It could serve as a support for novice nutritionists. The purpose of this research is to develop software for the nutritional assessment of people with Gluten-related disorders (GRDs) in the Republic of Moldova, intended for nutrition students. The development of the Software followed the systemic approach of the Nutrition Care Process, which is a graphical visualization illustrating the internal and external steps and factors that influence the use of the process. The nutritional Software was developed based on the information system *Embarcadero RAD Studio Alexandria Edition, having Microsoft SQL Server as a database*. The developed Software offers a personalized and precise approach, taking into account the consumer's anamnesis, the results of clinical evaluations, and anthropometric parameters, but also specific biomarkers for GRDs and offering the possibility of data recording, scanning and archiving of the results obtained from the laboratories analysis sampling. The system includes functionality to monitor and evaluate client progress toward health goals, and nutrition users can effectively track progress and make appropriate adjustments.

Keywords: *biomarkers, body composition, celiac disease, Nutrition Care Process, nutritional security, Republic of Moldova, Technical University of Moldova.*

Abstract. În contextul problemelor complexe de nutriție, software-ul de evaluare nutrițională pentru persoanele cu tulburări asociate consumului de gluten poate fi un instrument prețios pentru profesioniștii din domeniu și un suport pentru nutriționiștii începători. Scopul acestei cercetări constă în dezvoltarea unui software pentru evaluarea nutrițională a persoanelor cu tulburări asociate consumului de gluten (TACG) din Republica Moldova, destinat studenților la nutriție. Dezvoltarea Software-ului a urmat abordarea sistemică a Procesului de Asistență a Nutriției, care este o vizualizare grafică și care ilustrează pașii și factorii interni și externi care influențează utilizarea procesului. Software-ul nutrițional a fost dezvoltat pe baza sistemului informațional *Embarcadero RAD Studio Alexandria Edition,* având ca bază de date *Microsoft SQL Server*. Software-ul dezvoltat oferă o abordare personalizată și precisă, ținând cont de anamneza consumatorului, de rezultatele evaluărilor clinice și de parametri antropometrici, dar și de biomarkeri specifici pentru TACG și oferind posibilitatea înregistrării datelor, scanării și arhivării rezultatelor obținute din laboratoare analize prelevare de probe. Sistemul include funcționalități de monitorizare și evaluare a progresului clientului către obiectivele de sănătate, iar utilizatorii de nutriție pot urmări eficient progresul și pot face ajustările corespunzătoare.

Cuvinte cheie: *biomarkeri, boala celiacă, compoziția corporală, Procesul de Asistență a Nutriției, securitatea nutrițională, Republica Moldova, Universitatea Tehnică a Moldovei.*

1. Introduction

The global food and nutrition crisis is considered the leading cause of poor health [1] and continues to worsen, exacerbated by the pandemic. Almost a third (2.3 billion, or 29.3%) of the world's population was moderately or severely food insecure in 2021, up from 25.4% before the pandemic [2]. Experiencing food insecurity is increasingly associated with adverse health effects and a greater likelihood of developing chronic diseases [3].

In the context of complex nutrition issues, nutrition software can be a precious tool for professionals in the field. It could serve as a support for nutrition students as well as practitioners. Internationally, multiple Software are being developed, either customer-focused or aimed at nutrition specialists, characterized by a different degree of complexity and coverage of needs. At the same time, there are few scientific works concerning the development of these tools [4,5].

The issues of ensuring nutritional security and the human right to adequate food for people with disorders associated with gluten consumption in the Republic of Moldova are susceptible, becoming even more prominent under the pressure of crises (Covid-19 pandemic and the war in Ukraine) [6].

Being among the most common chronic digestive conditions, Gluten-related disorders (GRDs) is often underdiagnosed and neglected by patients and doctors, and the number of people affected, in reality, is much higher than it is believed. The process of adopting and adhering to a gluten-free regime is a rather difficult one, vulnerable on all dimensions of food security because gluten-free products are not produced or certified in the Republic of Moldova [7].

The limited participation of nutritionists in the development of balanced menus or their total lack in public catering units, the low diversity of gluten-free products and the high cost, compared to their gluten counterparts, the risk of cross-contamination of food, the developing offer of social assistance services and nutritional care etc. - all this reflects only part of the challenges faced by people with GRDs in the Republic of Moldova [8–10].

The purpose of this research is to develop a software for nutritional assessment of people with GRDs in the Republic of Moldova, intended for nutrition students.

The development of nutritional software is justified by the imperative of nutritional information and education as one of the causes of nutritional insecurity of people with GRDs [11]. The Software will enhance the learning ability of students as future nutrition practitioners, which will help eradicate nutritional illiteracy.

It will help streamline the management of data related to studies and their clients by recording detailed information about tested diets, results obtained, and other data relevant to research and analysis.

The nutritional Software can be accessed remotely, which allows the user (student) to work with his data from anywhere. This can be especially useful when doing research and studies in collaboration with other students or professors or when working with clients who live in remote areas. It can be programmed to provide detailed analysis and reports to help better understand eating habits and identify changes that could be made to improve the tested diets.

2. Materials and Methods

The development of the Software followed the systemic approach of the Nutrition Care Process, which is a graphical visualization illustrating the internal and external steps and factors that influence the use of the process [12] (Figure 1).

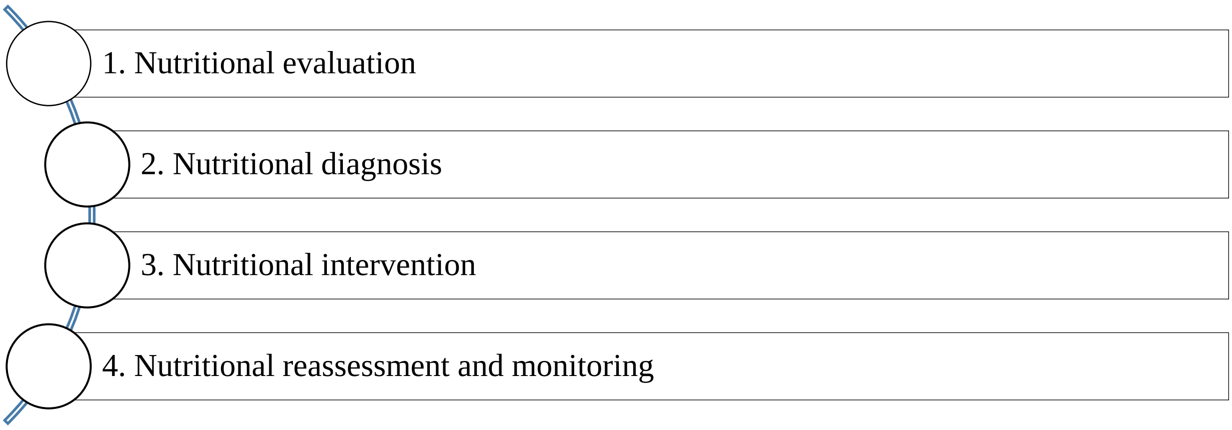

Figure 1. Stages of the Nutrition Assistance Framework model.

Software programming. The nutritional Software - SNUTM (SNUTM – Soft Nutrițional Universitatea Tehnică a Moldovei / Nutritional Software, Technical University of Moldova) was developed based on the information system Embarcadero Rapid Application Development (RAD) Studio Alexandria Edition (Figure 2) - is an object-oriented, visual programming environment, having Microsoft Structured Query Language (SQL) Server – is a programming language for storing and processing information in a relational database (Figure 3).

Figure 2. Embarcadero Information System RAD Studio Alexandria Edition.

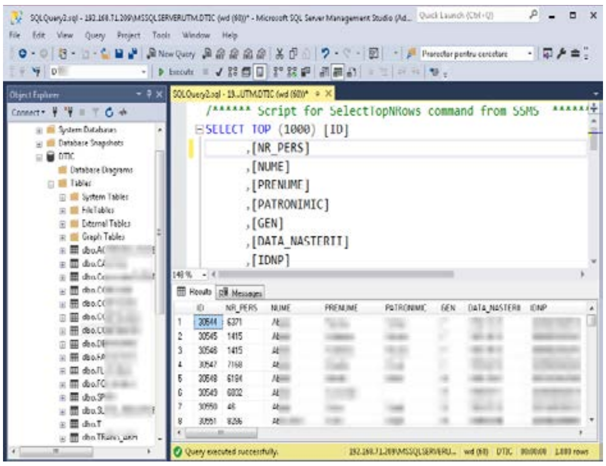

Figure 3. The (SNUTM) software product, developed based on Microsoft SQL Server.

The system has several advantages: performance, with the fastest compiler; the possibility of reusing the components; containing specialized details in database programming; the chance of developing mobile applications; development of web applications; cross-platform use; simplicity and speed of service, etc.

The parameters included in the SNUTM system are general and specific [13], taken from the scientific literature (Tables 1, 2).

Table 1

Parameters used in software development

Software Components	Source
Anthropometric measurements	[14–19]
Body composition parameters and equations: Body Mass Index, Lean Metabolic Rate, energy requirement, ideal mass.	[20]
Biomarkers, medical tests, etc. to identify nutrient deficiencies	[13]
* Biomarkers for the diagnosis of celiac disease (CD)	[13]
Calculation equations of energy value and nutrients	[21]
* Guidelines for the diagnosis of MC, developed by the Society of Pediatrics and Gastroenterology, Hepatology and Nutrition (ESPGHAN)	[13,22,23]
Menu analysis questionnaire	[22,24,25]
*Gastrointestinal Symptom Rating Scale (GSRS) questionnaire	[26–28]
* Gluten-free diet adherence questionnaire	[29,30]
* Questionnaire for the evaluation of the quality of life of people with GRDs	[22,31]
Dietary Reference Values	[32,33]
* Links to useful guides on Celiac Disease	[34]

Legend: * GRDs specific parameters.

Table 2

Biomarkers for the diagnosis of celiac disease

Symptoms
Malabsorption syndrome
Other CD-relevant symptom or having T1DM or being a 1 st-degree family member
Asymptomatic
Serum antibodies*
EMA (**Anti-endomysial antibodies** positi**vity and /or** high positivity **(>10 ULN (U**pper Limit of Normal**))** for anti - **TG2**
Low positivity for anti-TG2 antibodies or isolated anti-DGP positivity (DGP - *Deamidated gliadin peptide*)
Serology was not performed
Serology performed but all* coeliac-specific antibodies negative
HLA
Full **HLA** – DQ2 **(în *cis*** or ***trans*)** or **HLA-DQ8** heterodimers present
No **HLA** performed or half **DQ2 (**only **HLA-DQB1* 0202)** present
HLA neither **DQ2, n**or **DQ8**
Histology
Marsh 3a (mild villous atrophy**)**, **3b (**marked atrophy**)** or **3c (**complete atrophy**)**
Marsh 2 or **3a (**moderately decreased villus height/crypt depth ratio**)**
Marsh 0-1 (it is not conclusive for CD**)**

Note: **Refers in IgA (Ig –* Immunoglobulin) deficiency *to IgG clas EMA, TG2 and DGP antibodies*. *Source: [13]*

3. Results and Discussion

The block diagram of the SNUTM software is represented in Figure 4.

Registration data includes identification and contact information, age, locality, nationality, living environment, education level, profession, etc. The Software allows user registration, with the subsequent possibility of him registering consumer-customers [4]. Contact details of the consumer's supervising physician may also be collected, alerting the student-user to the importance of active collaboration between the nutritionist and doctor [4]. The assessment begins with anthropometric measurements. The essential elements of anthropometry included in the system are: height, weight, body circumferences for adiposity assessment (waist, hip and limbs) and skinfold thickness [14]. These measurements are also used to calculate Body Mass Index, Basal Metabolic Rate, energy requirement, ideal mass, the ratio of muscle mass to adipose tissue, etc.

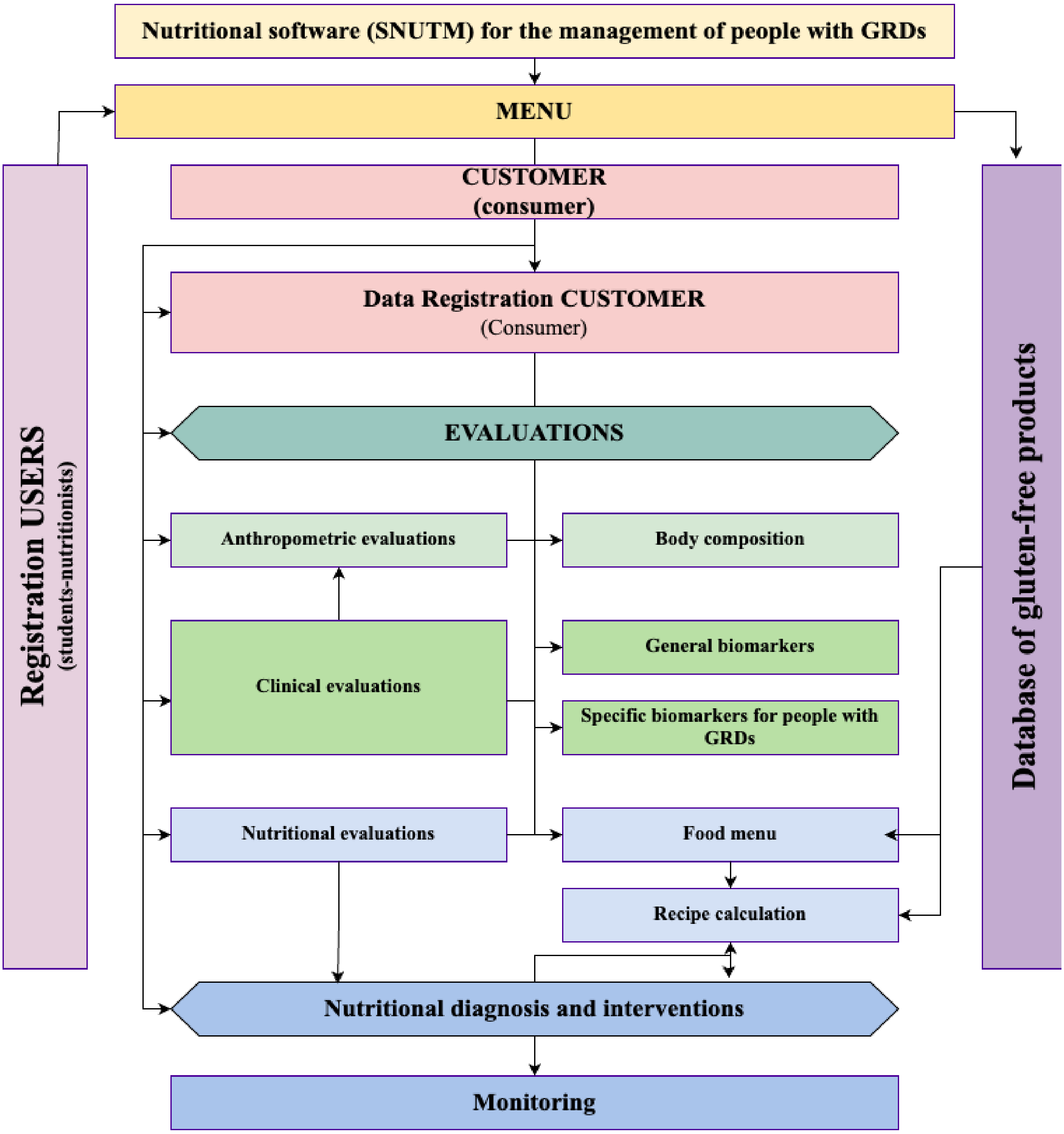

Figure 4. SNUTM nutritional software map.

The results could provide information regarding the patient's nutritional status, including a potential risk of undernutrition or obesity and possible consequences. Anthropometric data are frequently used to monitor the implementation and measure the effectiveness of food security and nutrition interventions and programs.

The Software offers data archiving, and time monitoring and even generates graphs concerning BMI, Basal Metabolic Rate, etc. (Figures 5-7).

Figure 5. Anthropometric data.

Source: Screenshot from the SNUTM nutritional software, developed by the authors.

Figure 6. Dynamics of anthropometric indicators

Source: Screenshot from the SNUTM nutritional software, developed by the authors.

The clinical evaluation will collect the patient's medical history: general physiological condition, symptoms, allergies, blood pressure, medical diagnosis, personal and hereditary collateral history, and medications. At the same time, the user can record in the program such biomarkers as values for blood count, insulin resistance and secretion, lipid metabolism and insulin stress, etc. Specific markers for the diagnosis of celiac disease included tissue anti-transglutaminase antibodies: Immunoglobulin A (IgA) and Immunoglobulin G (IgG) and anti-gliadin deamidated Immunoglobulin G (IgG) antibodies. Titles can be registered manually or by scanning analysis reports (from accredited laboratories), with the possibility of archiving (for monitoring).

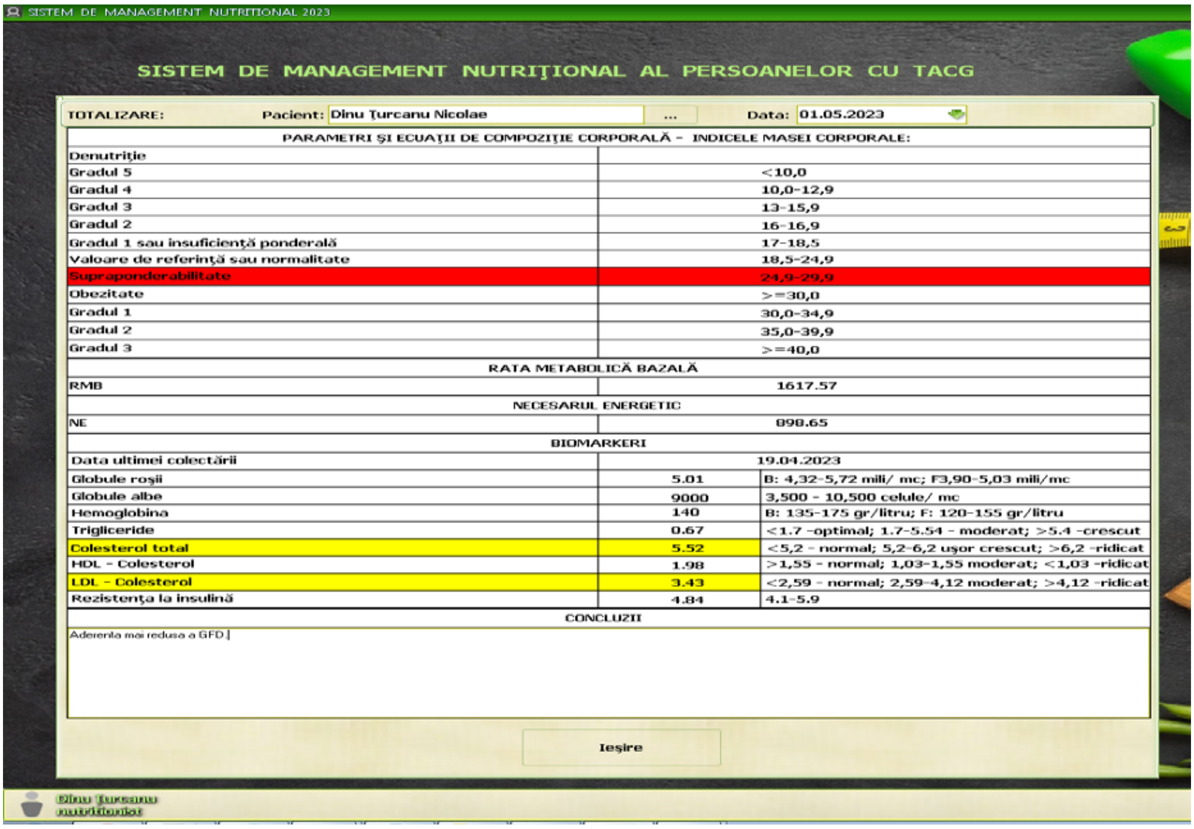
SISTEM DE MANAGEMENT NUTRITIONAL 2023

SISTEM DE MANAGEMENT NUTRIŢIONAL AL PERSOANELOR CU TACG

TOTALIZARE: Pacient: Dinu Ţurcanu Nicolae ... Data: 01.05.2023

PARAMETRI ŞI ECUAŢII DE COMPOZIŢIE CORPORALĂ – INDICELE MASEI CORPORALE:		
Denutriţie		
Gradul 5	<10,0	
Gradul 4	10,0-12,9	
Gradul 3	13-15,9	
Gradul 2	16-16,9	
Gradul 1 sau insuficienţă ponderală	17-18,5	
Valoare de referinţă sau normalitate	18,5-24,9	
Supraponderabilitate	24,9-29,9	
Obezitate	>=30,0	
Gradul 1	30,0-34,9	
Gradul 2	35,0-39,9	
Gradul 3	>=40,0	
RATA METABOLICĂ BAZALĂ		
RMB	1617.57	
NECESARUL ENERGETIC		
NE	898.65	
BIOMARKERI		
Data ultimei colectării	19.04.2023	
Globule roşii	5.01	B: 4,32-5,72 mili/ mc; F3,90-5,03 mili/mc
Globule albe	9000	3,500 - 10,500 celule/ mc
Hemoglobina	140	B: 135-175 gr/litru; F: 120-155 gr/litru
Trigliceride	0.67	<1.7 -optimal; 1.7-5.54 - moderat; >5.4 -crescut
Colesterol total	5.52	<5,2 - normal; 5,2-6,2 uşor crescut; >6,2 -ridicat
HDL - Colesterol	1.98	>1,55 - normal; 1,03-1,55 moderat; <1,03 -ridicat
LDL - Colesterol	3.43	<2,59 - normal; 2,59-4,12 moderat; >4,12 -ridicat
Rezistenţa la insulină	4.84	4.1-5.9
CONCLUZII		
Aderenta mai redusa a GFD.		

Ieşire

Dinu Ţurcanu nutriționist

Figure 7. The response generated by the software as a result of data recording.

Source: Screenshot from the SNUTM nutritional software developed by the authors.

The nutritional assessment includes a questionnaire developed and validated by the European Society for Pediatric Gastroenterology, Hepatology and Nutrition (ESPGHAN) to measure gastrointestinal symptoms [13–15].

In addition to this questionnaire, the Software also includes two standardized questionnaires: a quality of life assessment questionnaire [22,31] and a gluten-free diet adherence questionnaire [29,30] .

At the current stage, the Software comes with feedback to the user so that, subsequently, it generates a nutritional solution vis-à-vis the consumer's diet. For the healthy solution, databases (DB) are required concerning the chemical and nutritional composition of food products. Due to the lack of a database in the Republic of Moldova, at the moment, this niche has only been completed with the group of products "bread and bakery products" GF.

The correctness of the results generated by the Software was verified by comparing the results of some equations about the nutritional status: Body Mass Index (BMI), Basal Metabolic Rate (BMR), energy requirement, etc., through the Software, but also manually.

5. Conclusions

Nutrition software SNUTM can be a valuable tool for a nutritionist student, allowing him to better learn the concepts and principles of nutrition, more effectively manage the data related to his studies, and test different scenarios and solutions regarding nutrition plans. It can also be a handy tool for monitoring your diet and lifestyle. With proper development, it can be customized to meet individual user needs and can be a valuable resource for education and training. It can contribute to creating recipes or food menus and their multidimensional analysis from various perspectives. And above all, it can improve the teaching/learning process compared to the traditional teaching format. Overall, nutritional management software for people with GRDs can be an invaluable tool in helping them maintain a balanced and varied gluten-free diet.

Acknowledgments: Supported by the National Agency for Research and Development (NARD), Republic of Moldova, Project No. 21.00208.5107.06: *PD Contributions regarding nutritional eradication of gluten consumption diseases*, and Project No. 20.80009.5107.10: *PS Personalized nutrition and intelligent technologies for my well-being*, which runs within the Technical University of Moldova.

Conflicts of Interest: The authors declare no conflict of interest.

References

1. Popkin, B.M.; Corvalan, C.; Grummer-Strawn, L.M. Dynamics of the double burden of malnutrition and the changing nutrition reality. The Lancet 2020, 395(10217), pp. 65−74.
2. Global Nutrition Report. Global Nutrition Report 2022. Available online: https://knowledge4policy.ec.europa.eu/publication/2022-global-nutrition-report_en (accessed on 05 January 2023).
3. The State of Food Security and Nutrition in the World 2022. Available online: http://www.fao.org/documents/card/en/c/cc0639en (accessed on 09 October 2022).
4. Miere, D.; Grecu, L. Nutrition Software for Clinical Dietitians: Patient Management and Nutrition Care Process Guidance. Procedia - Social and Behavioral Sciences 2015, 191, pp. 1665−70. A
5. Lasa, A.; Larretxi, I.; Simón, E.; Churruca, I.; Navarro, V.; Martínez, O. New Software for Gluten-Free Diet Evaluation and Nutritional Education. Nutrients 2019, 11(10), 2505.
6. Siminiuc, R.; Țurcanu, D. The impact of the pandemic on the agri-food system. Journal of Social Sciences 2020, 3 (3), pp. 85−94. https://zenodo.org/record/3971973
7. Siminiuc, R. The influence of biotechnological strategies on nutritional aspect of bakery products. Journal of Engineering Science 2020, 27(3), 216-224. https://zenodo.org/record/3949722
8. Siminiuc, R.; Turcanu, D. Evaluation of gluten contamination in gluten-free products in the Republic of Moldova. Journal of Engineering Science 2022, 29(3), pp. 166−75. https://doi.org/10.52326/jes.utm.2022.29(3).14.
9. Siminiuc, R.; Țurcanu D. Challenges and trends in gluten-free product development. Echim ART SRL, Chisinau, Republic of Moldova, 2023, 160 p. [in Romanian].
10. Chirsanova, A.; Reșitca, V.; Siminiuc, R.; Suhodol, N.; Popovici, C.; Deseatnicov, O. Innovative Food Products. Tehnica-UTM, Chisinau, Republic of Moldova, 2021, 457 p. https://zenodo.org/record/5563412 [in Romanian].
11. Siminiuc, R.; Țurcanu, D. Food security of people with celiac disease in the Republic of Moldova through prism of public policies. Front Public Health 2022, 10, 961827.
12. Electronic Nutrition Care Proces Terminology. The Nutrition Care Process (NCP). Available online: https://www.ncpro.org/nutrition-care-process (accessed on cited 21 May 2023].
13. Husby, S., Koletzko, S.; Korponay-Szabó, I.R.; Mearin, M.L.; Phillips, A.; Shamir, R. European Society for Pediatric Gastroenterology, Hepatology, and Nutrition Guidelines for the Diagnosis of Coeliac Disease. Journal of Pediatric Gastroenterology & Nutrition 2012, 54(1), pp. 136−60.
14. Casadei, K.; Kiel, J. Anthropometric Measurement. StatPearls. Treasure Island (FL): StatPearls Publishing, 2023. Available online: http://www.ncbi.nlm.nih.gov/books/NBK537315/ (accessed on 9 May 2023).
15. Eaton−Evans, J. Nutritional Assesment: Anthropometry. In: Encyclopedia of Human Nutrition, Elsevier, 2005, pp. 311−318.

16. Hume, P.A.; Ackland, T. Physical and Clinical Assessment of Nutritional Status. In: Nutrition in the Prevention and Treatment of Disease, Elsevier; 2017, pp. 71−84.
17. Pietrobelli, A. Obesity: Definition, Etiology and Assessment. In: Encyclopedia of Human Nutrition, Elsevier, 2005, pp. 389−392.
18. Schofield, W.N. Predicting basal metabolic rate, new standards and review of previous work. Hum Nutr Clin Nutr. 1985, 39 (1), pp. 5−41.
19. WHO Expert Committee on Physical Status: the Use and Interpretation of Anthropometry, editor. Physical status: the use and interpretation of anthropometry: report of a WHO Expert Committee. Geneva: World Health Organization; 1995, 452 p.
20. Wideman, T.H.; Sullivan, M.J.L.; Inada, S.; McIntyre, D.; Kumagai, M.; Yahagi, N. et al. Basal Metabolic Rate. In: Encyclopedia of Behavioral Medicine, Gellman MD, Turner JR, editors, Springer, New York, SUA, 2013, pp. 176−177.
21. Miller, D.S.; Judd, P.A. The metabolisable energy value of foods. J Sci Food Agric 1984, 35(1), pp. 111−116.
22. Beth, E. Introduction to Food Production and Service. Creative Commons Attribution 4.0 international Licence, 2015. Available online: https://psu.pb.unizin.org/hmd329/ (accessed on 21 January 2023).
23. Parkman, R. Primary Immunodeficiencies. In: Measuring Immunity. Elsevier, 2005, p. 630−638.
24. Cade, J.; Thompson, R.; Burley, V.; Warm, D. Development, validation and utilisation of food-frequency questionnaires − a review. Public Health Nutr. 2002, 5(4), pp. 567−87.
25. Swindale, A.; Ohri-Vachaspati, P. Measuring Household Food Consumption: a technical guide. Academy for Educational Development; 2004. Available online: https://pdf.usaid.gov/pdf_docs/Pnadd641.pdf (accessed on 21 January 2023).
26. Hopman, E. G. D.; Koopman, H. M., Wit, J. M., Mearin., M. L. Dietary compliance and health-related quality of life in patients with coeliac disease. European Journal of Gastroenterology & Hepatology 2009, 21(9), pp. 1056−1061.
27. Souza, G.S.; Sardá, F.A.H.; Giuntini, E.B.; Gumbrevicius, I.; Morais, M. B. D.; Menezes, E.W. D. Translation and validation of the brazilian portuguese version of the gastrointestinal symptom rating scale (GSRS) questionnaire. Arq Gastroenterol 2016, 53(3), pp. 146−151.
28. Svedlund, J.; Sjodin, I.; Dotevall, G. A clinical rating scale for gastrointestinal symptoms in patients with irritable bowel syndrome and peptic ulcer disease. Digest Dis Sci 1988, 33(2), pp. 129−134.
29. Silvester, J.A.; Weiten, D.; Graff, L. A.; Walker, J. R.; Duerksen, D. R. Is it gluten-free? Relationship between self-reported gluten-free diet adherence and knowledge of gluten content of foods. Nutrition 2016, 32(7−8), pp. 777−783.
30. Zingone, F.; Iavarone, A.; Tortora, R.; Imperatore, N.; Pellegrini, L.; Russo, T. The Italian translation of the Celiac Disease-specific Quality of Life Scale in celiac patients on gluten free diet. Digestive and Liver Disease 2013, 45(2), pp. 115−118.
31.Dwyer, J. Dietary Reference Intakes (DRIs): Concepts and Implementation. In: Encyclopedia of Gastroenterology Elsevier, 2004, pp. 613−623.
32. Alves Durães, S.; Graças Pena, G.; Neri Nobre, L.; Handyara Bicalho, A.; Ramos Veloso, S. R.; Sant'Ana Haikal, D. et al. Food consumption changes among teachers during the COVID-19 pandemic. Obesity Medicine 2021 26, 100366.
33. Institute of Medicine (U.S.). Dietary reference intakes for thiamin, riboflavin, niacin, vitamin B_6, folate, vitamin B_{12}, pantothenic acid, biotin, and choline. National Academy Press, Washington, D.C, SUA, 1998, 564 p.
34. Dolinsek, J. Life with celiac disease. INSMC Alessandrescu-Rusescu, 2021, 75 p. [in Romanian].

Citation: Țurcanu, D.; Siminiuc, R. Software for nutritional assessment of individuals with gluten eating disorders. *Journal of Engineering Science* 2023, 30 (3), pp. 164-172. https://doi.org/10.52326/jes.utm.2023.30(3).12.

Publisher's Note: JES stays neutral with regard to jurisdictional claims in published maps and institutional affiliations.

Submission of manuscripts: jes@meridian.utm.md

Journal of Engineering Science *Vol. XXX, no. 3 (2023), pp. 173 - 187*
Fascicle *Food Engineering* *ISSN 2587-3474*
Topic *Biotechnologies, Food Chemistry and Food Safety* *eISSN 2587-3482*

https://doi.org/10.52326/jes.utm.2023.30(3).13
UDC 667.275:633.863.2

THE USE OF FOOD DYES: PROBLEM, SOLUTION AND SOURCE OF PERSPECTIVE

Alexandra Savcenco, ORCID: 0000-0002-1962-3959

Technical University of Moldova, 168, Stefan cel Mare Blvd., Chisinau, Republic of Moldova
*Corresponding author: Alexandra Savcenco, *alexandra.savcenco@tpa.utm.md*

Received: 07. 20. 2023
Accepted: 08. 22. 2023

Abstract. For consumers, the colour presents an indicator that characterizes the quality of the food. As a result of the processes of caramelization of carbohydrates and products of the Maillard reaction, brown compounds are formed with a negative impact on the external appearance of food, which has led to the massive use of synthetic dyes, stable from a technological point of view. The objectives of the European Union foresee the transition to the exclusive use of natural dyes, because synthetic dyes significantly affect the health of the population. Compounds with "azo" type chromophore groups (amaranth, tartrazine) present carcinogenic dangers, being banned in several European countries. The aim of the present study was to evaluate the problem of synthetic dyes and their substitution in food, obtaining, stabilizing and using natural dyes for the food industry. The study highlighted that safflower (*Carthamus tinctorius L.)* presents a promising source of yellow and red dyes, necessary for use in the food industry, but insufficient information was found regarding the technological properties of safflower petals, the methods of simultaneous extraction of yellow and red dyes and the peculiarities of the use of dyes in the finished product.

Keywords: *natural dyes, synthetic dyes, safflower, chalcones, carthamine.*

Rezumat. Pentru consumători culoarea prezintă un indicator care caracterizează calitatea alimentelor. În urma proceselor de caramelizare a glucidelor și produșilor reacției Maillard se formează compuși de culoare brună cu impact negativ asupra aspectului exterior al alimentelor, ceea ce a condus la utilizarea masivă a coloranților sintetici, stabili din punct de vedere tehnologic. Obiectivele Uniunii Europene prevăd trecerea la utilizarea exclusivă a coloranților naturali, deoarece coloranții sintetici afectează semnificativ starea de sănătate a populației. Compușii cu grupări cromofore de tip „*azo*” (amarant, tartrazina) prezintă pericole cancerigene, fiind în mai multe țări europene interziși. Scopul prezentului studiu a constat în evaluarea problemei coloranților sintetici și substituirii lor în alimente, a obținerii, stabilizării și utilizării coloranților naturali pentru industria alimentară. Studiul a scos în evidență, că șofrănelul (*Carthamus tinctorius* L.) prezintă o sursă de perspectivă de coloranți galbeni și roșu, necesari pentru utilizare în industria alimentară, însă nu au fost găsite suficiente informații referitor la proprietățile tehnologice ale petalelor de șofrănel, metodele de extracție concomitentă a coloranților galben și roșu și particularitățile utilizării coloranților în produsul finit.

Cuvinte cheie: *coloranți naturali, coloranți sintetici, șofrănel, calcone, cartamina.*

1. Introduction

In recent years, an increased interest is addressed to the field of research that ensures the stability of nutritional compounds in order to protect the sensory quality of food products. The evolution of human society led to the identification of some criteria about the quality of food according to their external appearance. Among these compounds, food dyes are a particularly important part. One of the main directions of use of dyes, according to European Parliament and Council Directive 94/36 EC of June 30, 1994 [1], consists in their introduction into food products to restore color, which has been affected following processing, storage, packaging and distribution of the finished product or for coloring a product, initially colorless.

Based on the list of colorants recommended for use of the Codex Alimentarius, each state approves the list of colorants that are permitted for use in that geographic and political space. In the Republic of Moldova, the official list of dyes allowed for use in food industry, which was published in the Sanitary Regulation on food additives, approved by Government Decision no. 229 of 20.03.2013 [2].

At the same time, a special attention of researchers is given to the assessment of the possiblel toxicity of synthetic food dyes. As a result of voluminous and multilateral researches, carried out recently, fundamental requirements were formulated, to which they must correspond , to be used.

The properties of a food coloring must satisfy the following restrictions [2]:

- the chemical compound, which provides color, must not be toxic, allergic and carcinogenic;
- the dye in industrial and commercial forms must not contain harmful impurities;
- the food coloring must not change the natural taste and smell of the product, it is included in the composition;
- on food product storage, the dye must be stable at certain pH values, product storage temperatures and, where applicable, ultraviolet and visible solar radiation.

The aim of the present study was to evaluate the problem of synthetic dyes and their substitution in food, obtaining, stabilizing and using natural dyes for the food industry.

2. The impact of chemical compounds modification of on the appearance of food products

Thermal processing of food compositions is one of the most freqently process in the manufacture of food products. At "room" temperatures of 20–25 °C, the change in food color is little significant, gradually increasing in the temperature range from 25 to 80 °C [3] the change accelerates. The chemical reactions that cause food colors to change are different. The speed of appearance change reactions depends on the chemical composition of food, temperature, pH values, water activity and others. To protect the natural appearance of food, it is necessary to know those chemical changes that cause color degradation.

An example of color modification is the caramelization of mono- and disaccharides in food compositions. Caramelization is a complex chemical process. Prolonged heat treatment causes the decomposition of glucose, fructose with their transformation into 5-hydroxymetilfurfural, (5-HMF), yellow and brown derivatives [4].

The muscle tissue protein, myoglobin, determines the red color of the meat. Myoglobin, an important sensory characteristic in forming the appearance of meat and meat products. The metal-organic nucleus of myoglobin contains Fe(II), which determines the red color of fresh meat. Myoglobin by chemisorption adds an oxygen molecule and turns into pronounced red oxymyoglobin [5]. Over a long period of time, the two-valent iron cation present in the structure of oxymyoglobin oxidizes, in three-valent iron, Fe(III), which leads to the transformation of oxymyoglobin into metmyoglobin, a stable brown color, which changes the natural appearance of the meat. [5].

The interaction reaction of proteins, peptides and amino acids with reducing sugars or with carbonyl compounds leads to the formation of brown compounds, which are called melanoidins. The Maillard reaction takes place spontaneously in the process of obtaining products of plant and animal origin. For example, the interaction of D-fructopyranose with the amino acid glycine leads to the formation of 1-fructosylamine with a gray appearance [6].

The transformation of polyphenols from a reduced state to an oxidized state leads to the formation of brown products that distort the appearance of freshness of food products. The maximum speed of the enzymatic reaction between molecular oxygen and polyphenols is observed in the first minutes when cutting or crushing fruits and vegetables. During this time, leucoanthocyanins, catechins, anthocyanins, caffeic and chlorogenic acids undergo oxidation, which easily oxidize and turn into orange and brown compounds.

In the official list of functional classification of food additives, developed by the International Codex Alimentarius Commission, food additives have been divided into classes. Within the coding system of all additives, food colorings have been placed in a special class E 100 – E 199.

From the point of view of chemical structures, food dyes can be divided into three groups:

- natural dyes (chlorophylls, anthocyanins, carotenoids, chalcones, naphthoquinones, betalains, etc.);
- artificial dyes, obtained by chemical modification of natural compounds: oxidation or modification of the structures of functional groups, complexation of natural compounds with metal ions;
- synthetic dyes (azo compounds – tartrazine, ponceau; synthetic derivatives of indole, etc.).

3. Functional properties of synthetic dyes and their particularities of use

Synthetic dyes obtained through chemical synthesis are much more effective from a technological point of view. They have a higher coloring power compared to natural compounds, they are quite resistant to changes in temperature and pH values. Synthetic food dyes related to a fairly wide range of compounds from different classes (Tabel 1).

Table 1

List of synthetic colorants in the Codex Alimentarius

Number E	Name of colorants	Color	Mode of use
E 102	Tartrazine	Yellow	ADI
E 104	Quinoline yellow	Yellow	-
E 110	Sunset yellow FCF	Yellow	-
E 122	Azorubine	Red	-
E 124	Ponceau 4R	Red	-
E 129	Allura Red AC	Red	-
E 131	Patent BlueV	Blue	-
E 142	Green S	Green	ADI
E 143	Fast Green FCF	Green	-

Note: ADI – acceptable daily intake

From the point of view of technological use, synthetic dyes are widely used in food processing. The stable color shade, the excellence of modern production technologies, the very high yields and the modest cost of obtaining by the synthetic route – all these have led to the predominant use of synthetic dyes in the manufacture of food products.

The chemical structure of synthetic dye molecules includes chromophore groups of the "azo" type (–N = N–), auxochromic carboxylic, hydroxyl, amine groups, etc.

Tartrazine, E 102, (Figure 1) is a heterocyclic azo-compound, which has yellow color, is water-soluble dye and is used in the manufacture of various food products. Tartrazine is often used in non-alcoholic beverages together with another synthetic yellow dye, sunset yellow FCF, E 110.

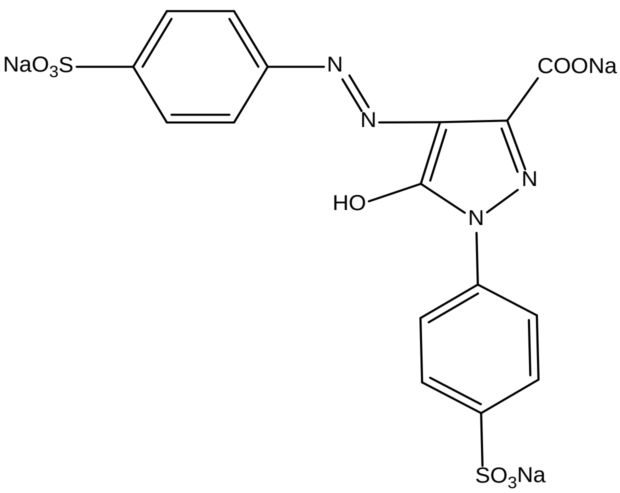

Figure 1. Chemical structure of the tartrazine molecule, E 102.

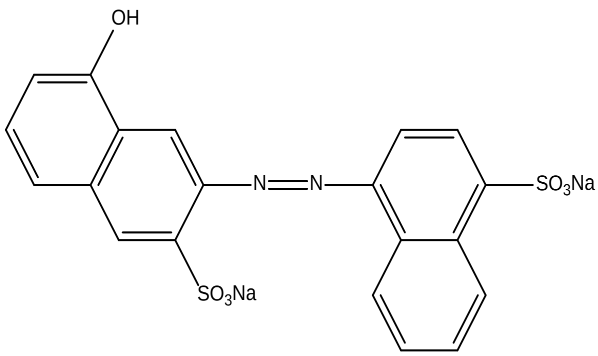

Figure 2. Chemical structure of the azorubine molecule, E 122.

Azorubine, E122, is a red water-soluble dye, stable at 100°C, which is why it is used to color foods, which are subjected to different heat treatments, (Figure 2).

Some investigations show that azorubine interacts with proteins, disrupting the normal biological function of serum albumin, also having a negative effect on the collagen structure, which prezent a risk to the skin. Phytotoxicity research has found that high concentrations of azorubine have a significant inhibitory effect on grain growth [7].

Despite the fact that the use of certain synthetic dyes is prohibited in EU countries, however, in some countries in Eastern Europe and Asia, their use is absolutely legal [8]. The legislation of these countries provides for the deminuate of the risks that synthetic dyes present to human health. Thus, their used in food compositions must the following requirements:

- the respect the acceptable daily dose, DZA,
- not to exceed the concentration allowed in the food product [8].

On the other hand, a group of dyes is under strict control, for its negative effects. These dyes include: brilliant blue FCF, E 133, quinoline yellow, E 104, tartrazine, E102, azorubine, E122. It is found that these dyes cause some negative effects, especially on the nervous system [9]. Hyperactivity disorders, attention deficit disorder, various allergic reactions, food intolerances and others have also been found [10]. Allura red is potentially carcinogenic, because use of that dye has been banned in several European countries [11]. Table 2 shows a group of synthetic dyes, the incorporation of which in food products is strictly regulated by the directives of the European Commission [12].

In addition to the fact that synthetic dyes are used in food products to restore the natural attractive color, there is another problem related to adulteration of food products with the use of dyes in order to mask the defects of adulterated foods [13, 14]. The most commonly counterfeited food groups include foods such as wine, meat, fish, honey, etc. [15]. For example, to obtain a reddish color of fish, similar to the color of salmon roe, a mixture of synthetic dyes ponceau 4R, E 124 and orange yellow, E 110 is used, and to give a golden yellow color to smoked fish, use the mixture of tartrazine, E 102 with sunset yellow FCF, E 110.

Table 2

Synthetic dyes that present risk to the health of the human

Name of colorants	Number E	Color	Area of use
Tartrazine	E 102	Yellow	Soft drinks, jellies, candies
Quiniline yellow	E 104	Yellow	Beverages, pharmaceutical drugs
Sunset yellow FCF	E 110	Yellow	Sweets, ice cream, beverages with alcohol
Azorubine	E 122	Red	Yogurts, jellies, jams, preserves
Ponceau 4R	E 124	Red	Marzipan, sauces, sweets
Allura red AC	E 129	Red	Alcoholic drinks, jellies

As the manufacture of natural dyes can be affected by insufficient harvest followed by climate change, there are cases where the natural dyes themselves have been counterfeited, for example, natural saffron dye and paprika powder have been mixed with Sudan Red III [16], the use of which is prohibited in the European Union.

The contemporary trend of elaborated and manufacturing new food products, which can correspond in terms of organoleptic and nutritional properties with foods rich in animal proteins, leads to the selection of non-traditional vegetable raw materials, as well as the development of food compositions based on insects, or, in a more distant perspective – of special cell cultures [17]. Arising from the need to develop this direction, it is necessary to elaborating and manufacturing a new naturals dyes, which will be able to be used in the obtaining of these products.

More than that, the existence of an EU strategic plan to replace synthetic dyes with natural ones, led to the formation of the new direction of investigations, which aims to identify harmless natural dyes, for their further use in food technology.

4. The functional properties of natural dyes and their particularities of use

Natural dyes present pigments from plant or animal origin. As a rule, these dyes are obtained by extracting from plants, seeds, roots, etc. Some natural dyes present biologically active compounds, for example, caratenoids, catechins, cyanidin glycosides, which demonstrate a positive impact on the biological values of food.

Coloring food products with natural dyes is usually seen as a healthier option compared to synthetic dyes [18]. Table 3 presents the list of natural dyes [19], admitted for use in the food industry of the Republic of Moldova.

In general, a part of natural dyes from edible sources are not harmful and are considered bio-dyes [20]. Because of their edibility, bio-colorings can be used in food products according to the principle of quantum satis, which involves the addition of colorants in unlimited amounts (reasonable from the point of view of economic necessity), to obtain a desired sensory effect.

Analyzing the literature, it is observed that red dyes from different classes (anthocyanins, betanin and chalcone - carthamine, which is the object of study of this paper), have many common caracteristics, which refer to their low stability in relation of heating, rapid degradation in basic medium, the strong dependence of their shade on pH, interactions with biopolymers.

Table 3

List of natural colorants in the Codex Alimentarius

Number E	Name of colorants	Color	Mode of use
E 100	Curcumin	Yellow	*Quantum satis*
E 101	Riboflavin	Yellow	*Quantum satis*
E 120	Carmine	Red	*Quantum satis*
E 132	Indigo/indigo carmine	Blue	*Quantum satis*
E 140	Chlorophyll, chlorophyllin	Green	*Quantum satis*
E 150 a, b, c, d	Caramel	Brown	*Quantum satis*
E 160 a, b, c, d, e	Carotenoids: carotene, annatto, lycopene, red pepper extract	Yellow, orange, red	*Quantum satis*
E 161 b, g	Lutein (b), cantaxin (g)	Orange	*Quantum satis*
E 162	Betaine	Red	*Quantum satis*
E 163	Anthocyanins	Red, violet, blue	*Quantum satis*

Anthocyanin pigments, E 163, are found in most fruits, vegetables and products made from them. The basis of the chemical structure of anthocyanins is the phenylbenzopyryllium (flavyllium) cation, formed by the benzopyryllium nucleus (A) and the phenolic ring (B). In the absence of the carbohydrate bonds of the flavyl core, the flavyl cation is called an anthocyanidin. Chemically, anthocyanins are glycosides of the flavylium cation, (Figure 3).

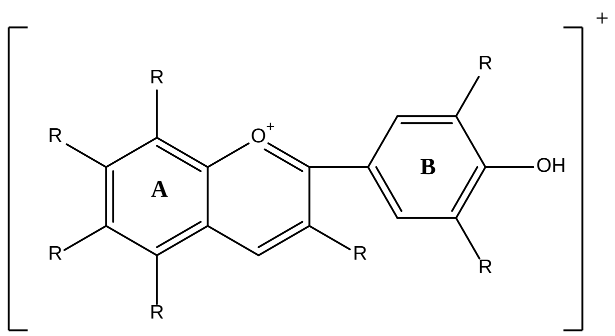

Figure 3. Chemical structure of the flavylium cation.

Given that anthocyanin dyes are unstable, their use in the food industry is almost impossible for a wide range of products. Anthocyanin extracts in acid medium have a stable red color, and in alkaline medium they acquire a blue color, therefore the use of anthocyanins depends on the pH of the food product. Anthocyanins are widely used in the beverages, juice [21] and confectionery industries.

Carotenoids form a group of additives coded by E160a. The most obvious distinguishing feature of this group is the shape of the molecule, which presents a polyene chain, which can be extended up to 15 conjugated double bonds, (Figure 4) [22]. They possess the characteristic absorption spectrum in the visible region of the spectrum, with λmax 420…480 nm and, consequently, the yellow or orange color.

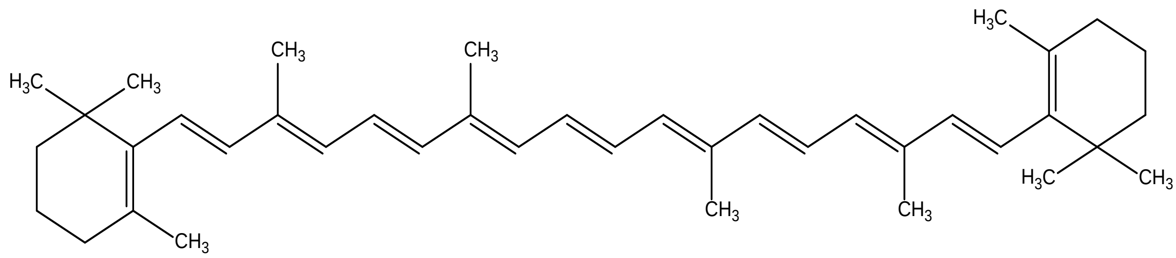

Figure 4. Chemical structure of the β-carotene molecule, E160a.

In addition to coloring properties, some representatives of carotenoids have provitamin properties, because they have the ability to break down in the human body and turn into vitamin A.

Initially, extracts of paprika, anatto, tomato and pumpkin were used as sources of carotenoids. It should be noted that these extracts do not represent carotenoids in a pure state, or a mixture with a constant chemical composition, composed of the same substances, but contain components with different properties, one of which is the very strong aroma. This fact considerably limits the use of extracts in the food industry [22].

Betanin, E162, is a natural red food coloring, approved for use in the food industry by Regulation (EU) no. 1129/2011 of the commission of november 11, 2011 and the health regulation on food additives of the Republic of Moldova [2]. Betanin extracts are stable over a wide pH range, from 3 to 7, which ensures the use of betanins to protect the red colors of acidic and neutral foods. High temperatures of more than 60°C negatively influence the stability of betanins, causing dye degradation and color loss, (Figure 5).

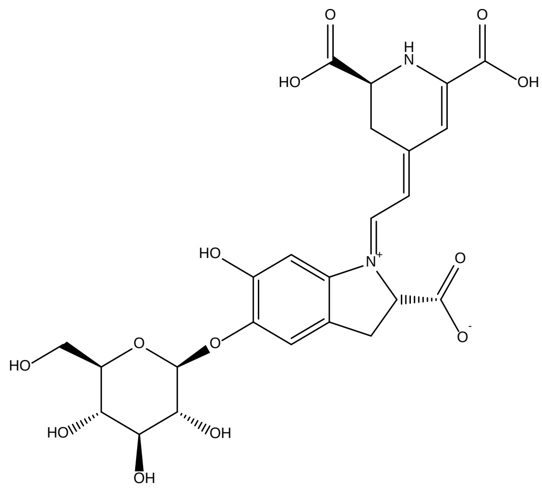

Figure 5. Chemical structure of the betanin molecule, E 162.

Betanin extracts have been shown to be more sensitive to high temperatures than anthocyanin or carotenoid extracts [23]. The satisfactory stability at low temperatures makes betanins suitable colorants for their incorporation into ice creams, yogurts and soft drinks, fruit cocktails, sweets, jellies and meat products [24]. The main source of betanin is beetroot [25], but more and more sources are emerging for obtaining betanin, for example, from Opuntia stricta. The color indices of the dye obtained were compared with different dyes marketed as a concentrate (beetroot, red carrot and black grape skin) [26]. It was found that the dye obtained from Opuntia stricta possessed a more attractive red-violet color than those from the mentioned sources.

Currently, natural dyes from the class of carotenoids (from Bixa orellana L.), betanins (from Beta vulgaris L.), etc. are marketed and approved for use in the US and EU [27].

The study, in which pork sausages were manufactured with the addition of tomato skin powder [28] demonstrated that the color of sausages with 1,5% tomato powder was unstable during storage, but no changes were observed sausage color with 0,8% and 1,2% powder. It has been proven that to solve the problem of increasing the stability of lycopene it is necessary to reduce the temperature of the extraction process and to use stabilizing agents [29], in order to be able to replace the artificial dye allura red AC.

Hofmann also demonstrated that anthocyanins extracted from radishes and red potatoes can be used as an alternative to replace the synthetic allura red dye, E 129, for the production of a type of maraschino cherry preserve [30]. By comparing the color indices of anthocyanins at pH 3,5 with the synthetic dye, they demonstrated the identity of the red shade of the synthetic and natural dye. At the same time, it should be noted that the respective sources are of purely scientific interest not practical, since the extraction of dyes from them is not economically advantageous.

In the research, carried out at the FTA UTM by Ghendov-Moșanu et al., it was demonstrated that sea buckthorn fruits (Hippophae rhamnoides L.) contain significant amounts of phytonutrients, some of which are carotenoids, which act as antioxidants and manifest other functional properties, for example, help in collagen synthesis [31].

Despite the fact that the consequences of the use of synthetic dyes, previously mentioned, are serious, tartrazine and azorubin, whose advantage is a good solubility in water, are widely used for the manufacture of food in the Republic of Moldova. Considering the above, it is of particular interest to study new vegetable sources, which contain large amounts of pigments, which are economically advantageous to obtain and, at the same time, have the technological properties necessary for their use in food products.

5. Safflower, the perspective plant for obtaining food dyes

The perspective plant for obtaining biologically active substances is safflower, (Figure 6). Safflower (Carthamus tinctorius L.) is an annual herbaceous plant from the Asteraceae family. Safflower is cultivated worldwide on large areas in China, the USA, Kazakhstan, Turkey, the Russian Federation, Ukraine and Romania [32]. In recent years, significant amounts of safflower have been cultivated in Iran, where its use as a food coloring is gradually increasing.

Strong point of safflower culture is that this plant is resistant to heat and prolonged drought, tolerates strong sunlight, which makes this plant even more attractive for cultivation prospects in the context of water scarcity and global warming [34].

The growing season depends on the variety and climatic conditions, ranging from 93 to 152 days. Flower picking takes place in summer, from july to august, in dry weather to prevent rotting of the plant and speed up the drying process. The flowers are dried in the open air, immediately in the shade and in very well ventilated places.

Figure 6. Flower containing carthamine chalcone [33].

Safflower is a special culture, because all the organs of the plant can be used industrially. Safflower leaf tea is used to prevent heart disease in traditional and modern Chinese medicine [35]. The stalks are used as animal feed and have a yield with higher forage value than oats or alfalfa [36].

The most well-known way of processing safflower is to obtain oil from its seeds. It was found that safflower seed oil is rich in fat-soluble biologically active substances: linoleic acid [37], oleic acid, tocopherol, which makes it advantageous for the manufacture of quality cosmetic products [38].

Considering the high content of chalcone dyes, the safflower plant (Carthamus tinctorius L., Asteraceae;) is of particular interest for conducting research in the field of obtaining and using natural dyes.

It should be noted that information about the saffron plant even in scientific literature is often confused with another plant, saffron (Crocus sativus L., Iridaceae, Sofran), because the names are similar in different languages, the outer appearance of the petals. ripened by Carthamus tinctorius is almost identical to the appearance of Crocus sativus stigmas [39].

Of particular interest to us were the petals of the safflower plant, which contain two pigments: yellow and red. It is known that until the 19th century, when synthetic dyes became available much cheaper than the natural ones and which are part of the aniline derivatives, saffron was cultivated to obtain red dyes and was used, mainly in Egypt, to color the cotton. and silk. By the 18th century, yellow "Egyptian dye" from safflower was used in Italy, France and Great Britain to color cheese and salami [40].

Currently, the Institute of Genetics, Physiology and Plant Protection of the Republic of Moldova is conducting research on the possibilities of cultivating the safflower plant in our countries. The positive results, obtained at this moment, can serve as a practical basis for the surface of a new species of plants in the agriculture of the Republic of Moldova [41].

Despite the fact that safflower would become a valuable plant for agriculture and the economy of our country, no internal studies have been conducted of chemical composition of different parts of the plant and their processing into commercial products.

For the Republic of Moldova, the greatest practical interest would be anthocyanin dyes, since the country's agriculture produces large quantities of red grape pomace. Considering that the chromotory of anthocyanins is very unstable to the influence of oxygen, sensitive to pH values, i.e. the color changes from red to purple [42] occur very quickly, the problem of obtaining these colors is very complicated. Moreover, obtaining the anthocyanin dye is a problem not only from the point of view of physico-chemical properties, but also from the point of view of high energy costs, which are consumed to block the oxidative processes and remove excess moisture from the pomace through different methods.

For this reason, it is of interest to study different vegetable sources with low initial water content, which contain pigments and possess technological properties necessary for the further use of these pigments in the food industry.

In this sense, safflower, a plant resistant to insufficient humidity [43] present a plant with great prospects specific to the climatic and pedological conditions of the Republic of Moldova.

The chemical composition the petals contains flavanoid pigments, derived from chalcone. Unlike the widespread O - glycosylated derivatives, safflower chalcones belong to the rare group of C - glucosylchalcones, i.e. deoxyglucose derivatives, the best known being hydroxysaffron yellow A, anhydrosaffron yellow B and precarthamine. The yellow C - glucosylated pigments, which predominate in the structure of the petals, are soluble in water. Phytochemical and pharmacological research has shown that these water-soluble components are responsible for the therapeutic effects, especially C - quinochalconic glycosides, which are considered the main active compounds [44]. Hydroxysafflor yellow A, the substance identified and obtained by us, is the basic biologically active component of yellow compounds in safflower petals, hydroxysafflor yellow A has been shown to limit platelet aggregation, regulate blood circulation, possess antioxidant properties and accelerate metabolism [45]. Yellow pigments constitute 25% of the petal mass. Sometimes, even in the scientific literature, you can find erroneous information about the naming of yellow dyes. Thus, one of them is called cartamidine [46]. In reality, carthamidine does not belong to the class of chalcones, being a closed-cycle dihydroflavone.

The process of biosynthesis, which takes place in the safflower flower, gradually changes the colors of the petals from yellow to red. The enzyme β-glucoseoxidase contributes to this change in the flowering stage. This enzyme is distributed in vegetative tissues and is active at pH 4,8 [47]. The color changes of the petals in the red shade are a proof of the formation of cartamine pigment (Figure 7), the fact that the molecule is composed of two chalcone residues. Cartamine occurs in petals as a result of enzymatic oxidation of precartamine [48] and constitutes about 5% of dry petal mass. Cartamine produces the most valuable pigment in safflower petals, red in color, non-anthocyanin in nature.

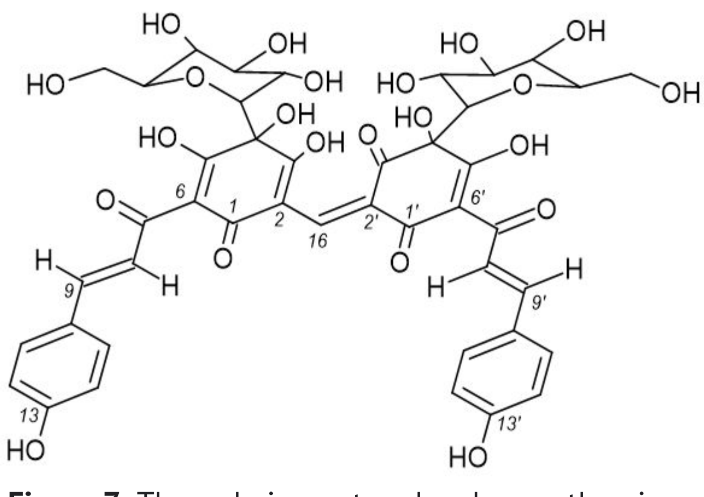

Figure 7. The red pigment molecule - carthamine.

Different methods of obtaining yellow dyes are described [49-51]. Most of the principles of obtaining dyes are based on the primary removal of yellow dyes, after which the red dye is removed in individual form. Various bibliographic sources describe methods of extracting dyes with solutions, which have a high toxic level (trichloroacetic acids, trifluoroacetic acids - TFA), which obtaining of harmless natural dyes. Moreover, from various sources, obtaining yellow dyes is achieved with the use of alkaline solutions (NaOH, KOH), which, according to our results, leads to the degradation of red dye - carthamine. We demonstrated that it is possible to simultaneously obtain yellow and red dyes from the same aqueous extract [52]. Dyes can be obtained both in the form of a liquid concentrate and in a solid state. Due to its water-soluble properties and high stability, the yellow dye can be used in a fairly wide range of food products: juices, jellies, caramels, sauces, etc.

Fatahi et al. investigated the influence of pH, temperature and light on yellow dyes and carthamine [53]. In terms of temperature stability (10, 30, 50 and 70 °C), yellow dyes have been shown not to undergo significant degradation. In terms of pH stability, yellow dyes have been shown to be much more stable than carthamine. The effect of the degradation of yellow dyes is manifested in alkaline medium, therefore, it does not significantly influence the research, because there are no food products with such pH values. At the same time, the same team of researchers reports the degradation of carthamine at pH values, which correspond to the acidic medium. These claims have not been confirmed by the author of this article. Carthamine is a compound unstable to light and oxygen, but according to our results, it does not descompose in weakly acidic mediu. At low acidic pH values, carthamine stabilization occurs.

Carthamine is a quinoidal chalcone glycoside, which in its native state in aqueous medium descomposes very easily with the formation of yellow-orange compounds. Various bibliographic sources confirm that the red dye, carthamine, has been used since ancient times to color textile fabrics. Thus, it can be concluded that in some conditions of technological treatment stabilization with carthamine can take place.

A method to stabilize carthamine was reported by Saito et al. [54], who investigated the possibility of stabilizing cartamine by adding sugars to the solution. They have, that monosaccharides and disaccharides show little promise as stabilizers, but polysaccharides exert a positive action on the pronounced red colors of carthamine. The results of carthamine stabilization on cellulose, reported by Saito, correlate with the research results, reflected in the present article. The FTIR spectra obtained by Saito show that the interaction of cellulose with cartamine leads to the appearance of several new bands at 1600 and 1500-1350 cm^{-1} , which were not identified in the spectra of carthamine and cellulose in the individual state [54]. But information about the concrete mechanism, which leads to the formation of the complex between cartamine and cellulose, was not found in the literature.

The appearance of new bands whose values are not identical to those reported by Saito has been highlighted. The reason for using other types of cellulose ("Sigma-Aldrich", "Flo-109") [55], as much as possible, is that it could benefit from other works, where classical FTIR was used in KBr in oil fluorinated, we used the ATR variant of FTIR spectroscopy. The results of autor of this article [55], show that carthamine rearranges the intermolecular hydrogen bonds of cellulose on itself, thus forming the chemical bond.

The previously mentioned carthamine stabilization method leads to the fact that carthamine in aqueous systems behaves as a suspension, which does not allow its incorporation into transparent and homogeneous media with a high water content, for example, in soft drinks, etc.

Another study proposes the solubilization method of carthamine using its complexation with glycosylhisperidine [56]. The latter has the ability to prevent the formation of crystals in an aqueous solution. This study demonstrated that the color shade of glycosylhisperedin-linked carthamine, Hsp-G, was redder than that of cellulose with cartamine [53]. As a result, the authors of this research propose the method, which includes the addition of glycosylhisperedin to the alkaline extract of safflower petals, replacing the cellulose. At the same time, the investigations carried out during the works allow us to question the effectiveness of these methods, considering that in alkaline environments they destroy carthamine.

6. Conclusions

1. The analysis of bibliographic sources allows to state that the problem of obtaining and using natural dyes for the food industry remains current from a theoretical and applicative point of view. The structure and properties of the dyes used influence food quality assurance. Therefore, solving the problems related to the natural obtaining and use of dyes from new vegetable sources in the food industry is current for the Republic of Moldova.

2. A large number of bibliographic sources indicate that the safflower plant presents a promising source of yellow and red dyes for use in the food industry, few publications, especially local ones, include research in this field.

3. At the same time, not enough extensive information was found on the technological properties of safflower petals, for the extraction of dyes, despite the fact that they directly influence the yield of obtaining and the peculiarities of the use of dyes in the finished product. There is also a lack of information on the existence of methods for the simultaneous extraction of yellow and red dyes from safflower petals.

4. The studied bibliographic sources contain insufficient information about the need to solve the stabilization problems in food compositions of the chemical structures of carthamine, as well as about the physico-chemical and technological characteristics, which will make possible the use of carthamine in the food industry.

Acknowledgements. The research was carried out within the project: 20.80009.5107.09 - „Improving the quality and safety of food products using bio- technology and food technology”.

Conflicts of Interest: The author declares no conflict of interest.

References

1. European Parliament and Council Directive 94/36 EC, din 30 iunie 1994, privind coloranții pentru utilizare în produse alimentare. Available online: https://eur-lex.europa.eu/legal-content/RO/TXT/PDF/?uri=CELEX:31994L0036 (accessed on 06.07.2023).
2. Hotărârea Guvernului Republicii Moldova pentru aprobarea Regulamentului sanitar privind aditivii alimentari: № 229 din 29.03.2013. În: *Monitorul Oficial al Republicii Moldova*, 2013, 69-74, pp. 283.
3. Wang, T.; She, N., Mengnan, W.; Bo, Z.; Jiaxing, Q. Changes in Physicochemical Properties and Qualities of Red Brown Rice at Different Storage Temperatures. *Foods* 2021, 10, pp. 1-10. https://doi.org/10.3390/foods10112658
4. Purlis, E. Browning development in bakery products - a review. *Journal of Food Engineering* 2010, 99, pp. 239-249. http://dx.doi.org/10.1016/j.jfoodeng.2010.03.008

5. Smerdon, S. J.; Wilkinson, A. J.; Olson, J. S. The mechanism of autooxidation of myoglobin. *Journal of Biological Chemistry* 1993, 268, pp. 6995-7010. http://dx.doi.org/10.1016/S0021-9258(18)53138-0
6. Friedman, M. Food browning and its prevention: an overview. *Journal of Agricultural and Food Industry* 1996, 44, pp. 631-653. https://doi.org/10.1021/jf950394r
7. Leulescu, M.; Rotaru, A.; Moanța, A.; Iacobescu, G. Azorubine: physical, thermal and bioactive properties of the widely employed food, pharmaceutical and cosmetic red azo dye material. *Journal of Thermal Analysis and Calorimetry* 2021, 143, pp. 39. http://dx.doi.org/10.1007/s10973-021-10618-4
8. Alp, H.; Bașkan, D.; Yașar, A.; Yayli, N.; Ocak, U.; Ocak, M. Simultaneous determination of sunset yellow FCF, allura red AC, quinoline yellow WS, and tartrazine in food samples by RP-HPLC. *Journal of Chemistry* 2018, 2018, pp. 1-6. http://dx.doi.org/10.1155/2018/6486250
9. Yonglin, G.; Chunmei, L.; Jingyu, S.; Huaxian, Y.; Xiulin, A.; Haizhu, J. Effect of food azo dye tartrazine on learning and memory functions in mice and rats, and the possible mechanisms involved. *Journal of Food Science* 2011, 76, pp. 125-129. https://doi.org/10.1111/j.1750-3841.2011.02267.x
10. Arnold, L.; Lofthouse, N., Hurt, E. Artificial food colors and attention-deficit/hyperactivity symptoms: conclusions to dye for. *Journal of the American Society for Experimental NeuroTerapeutics* 2012, 9, pp. 599-609. https://doi.org/10.1007%2Fs13311-012-0133-x
11. Luzardo-Ocampo, I.; Ramirez-Jimenez, A.; Yanez, J.; Mojica, L.; Luna-Vital, D. Technological applications of natural colorants in food systems: review. *Foods* 2021, 10, pp. 1-33. https://doi.org/10.3390/foods10030634
12. Regulamentul (UE) de modificare a anexei II la Regulamentul (CE) nr. 1333/2008 al Parlamentului European și al Consiliului în ceea ce privește condițiile și nivelurile de utilizare pentru galben de chinolină (E 104), galben apus de soare (sunset yellow) FCF/galben portocaliu S (E 110) și roșu ponceau 4R, roșu coșenilă A (E 124) al Parlamentului European: nr. 232/2012 din 16.03.2012. *Jurnalul Oficial al Uniunii Europene* 2012, pp. 1-78.
13. Momtaz, M.; Bubli, S.; Khan, M. Mechanisms and health aspects of food adulteration: a comprehensive review. *Foods* 2023, 12, pp. 1-25. https://doi.org/10.3390/foods12010199
14. Banu, C. *Industria alimentară între adevăr și fraudă.* ASAB, România, 2013; pp. 137-146. ISBN 978-973-7725-91-2.
15. Canja, C.; MăzăreL, A.; Lupu, M.; Pădureanu, V.; Enache, D. Food falsification – a nowadays problem. *Agricultural and Food Engineering* 2016, 9, pp. 69-74.
16. Wrolstad, R.; Culver, C. Alternatives to those artificial FD&C food colorants. *Annual review of Food Science and Technology* 2012, 3, pp. 59-77. http://dx.doi.org/10.1146/annurev-food-022811-101118
17. Henchion, M.; Hayes, M.; Mullen, A.; Fenelon, M.; Tiwari, B. Future protein supply and demand: strategies and factors influencing a sustainable equilibrium. *Foods* 2017, 6, pp. 1-21. https://doi.org/10.3390/foods6070053
18. Scotter, M. Emerging and persistent issues with artificial food colours: natural additives as alternatives to synthetic colours in food and drink. *Quality Assuarance and Safety of Crops & Foods* 2011, 3, pp. 28-39. http://dx.doi.org/10.1111/j.1757-837X.2010.00087.x
19. Codex Alimentarius. General standard for food additives. Disponibil online: https://www.fao.org/fao-who-codexalimentarius/sh-proxy/en/?lnk=1&url=https%253A%252F%252Fworkspace.fao.org%252Fsites%252Fcodex%252FStandards%252FCXS%2B192-1995%252FCXS_192e.pdf (accesat la 24.07.2023).
20. Rymbai, H.; Sharma, R.; Srivastav, M. Biocolorants and its implications in health and food industry - a review. *Journal of Pharm Tech Research* 2011, 3, pp. 2228-2244.
21. Banu, C. *Aplicații ale aditivilor și ingredientelor în industria alimentară.* ASAB, Romania, 2010, pp. 21-30. ISBN 978-973-7725-70-7.
22. Fernandez-Lopez, J.; Fernandez-Liedo, V.; Angosto, J. New insights into red plant pigments: more thah just natural colorants. *Royal Society of Chemistry* 2020, 10, pp. 24669-24682. https://doi.org/10.1039/D0RA03514A
23. Fernandez-Lopez, J.; Angosto, J.; Gimenez, J. Thermal stability of selected natural red extracts used as food colorants. *Plant Foods Humanity Nutrition* 2003, 68, pp. 11 – 17. https://doi.org/10.1007/s11130-013-0337-1
24. Obon, J.; Castellar, M.; Alacid, M.; Fernandez-Lopez, J. Production of a red-purple food colorant from Opuntia stricta fruits by spray drying and its application in food model systems. *Journal of Food Engineering* 2009, 90, pp. 471-479. http://dx.doi.org/10.1016/j.jfoodeng.2008.07.013
25. Lee, E.; An, D.; Nguyen, T.; Patil, B.; Yoo, K. Betalain and Betaine Composition of Greenhouse- or Field-Produced Beetroot (Beta vulgaris L.) and Inhibition of HepG2 Cell Proliferation. *Journal of Agricultural and Food Chemistry* 2014, 62, pp. 1324-1331. https://doi.org/10.1021/jf404648u

26. Castellar, M.; Obon, J.; Fernandez-Lopez, J. The isolation and properties of a concentrated red-purple betacyanin food colorant from opuntia stricta fruits. *Journal of the Science of Food and Agriculture* 2006, 86, pp. 122-128. http://dx.doi.org/10.1002/jsfa.2285
27. Luzardo-Ocampo, I.; Ramirez-Jimenez, A.; Yanez, J.; Mojica, L.; Luna-Vital, D. Technological applications of natural colorants in food systems: review. *Foods* 2021, 10, pp. 1-33. https://doi.org/10.3390/foods10030634
28. Kim, I.; Jin, S.; Mandal, P.; Kang, S. Quality of low-fat pork sausages with tomato powder as colour and functional additive during refregerated storage. *Journal of Food Science* 2011, 45, pp. 591-597. https://doi.org/10.1007%2Fs13197-010-0182-2
29. Gebhart, B.; Muller-Maatsch, J.; Carle, R.; SPERL, R. Assessing the sustenability of natural and artificial food colorants. In: Food 2030, Towards sustainable agri-food systems, Hohenheim, Germany September 5-6, 2018, pp. 33.
30. Shipp, J.; Abdel-Aal, E. Food application and physiological effects of antocyanins as functional food ingredients. *Food Science Journal* 2010, 4, pp. 7-22. http://dx.doi.org/10.2174/1874256401004010007
31. Ghendov-Moșanu, A. *Compuși biologic activi de origine horticolă pentru alimente funcționale*. Tehnica-UTM, Chisinau, Republica Moldova, 2018, pp. 96-100. ISBN 978-9975-45-531-2.
32. Popa, D.; Niță, S.; Mateaș, I. Preliminary study on content and oil production in some lines Safflower (Carthamus tinctorius L.) under Timișoara. *Journal of Agricultural Science* 2013, 45, pp. 160-163.
33. Erbas, S.; Mutlucan, M. Investigation of Flower Yield and Quality in Different Color Safflower Genotypes. *Agronomy* 2023, 13, pp. 1-23. https://doi.org/10.3390/agronomy13040956
34. Bîlteanu, Gh. *Fitotehnie 2*. CERES, România, 1993, pp. ISBN 973-40-0403-4.
35. Delshad, E.; Yousefi, M.; Sasannezhad, P.; Rakhshandeh, H.; Ayati, Z. Medical uses of Carthamus tinctorius L. (Safflower): a comprehensive review from traditional medicine to modern medicine. *Electron Physician Journal* 2018, 10, pp. 6672-6681. http://dx.doi.org/10.19082/6672
36. Zehra, E. Resurgence of Safflower (Carthamus tinctorius L.). Utilization: a global view. *Journal of Agronomy and Agricultural Science* 2005, 2, 4, pp. 83-87. http://dx.doi.org/10.3923/ja.2005.83.87
37. Hamdam, Y.; Perez-Vich, B.; Fernandez-Martinez, J., Velasco, L. Inheritance of very high linoleic acid content and its relationship with nuclear male sterility in safflower. *Plant Breeding* 2008, 127, pp. 507-509. https://doi.org/10.1111/j.1439-0523.2008.01494.x
38. Domagalska, B. Safflower (Carthamus tinctorius)-forgotten cosmetic plant. *Cosmetology today* 2010, 2, pp. 6-9.
39. Saito, K.; Katsukura, M. On manganese-indused reddening of florets from dyer's saffron capitula. *Food Chemistry* 1992, 44, pp. 349-355. https://doi.org/10.1016/0308-8146(92)90267-6
40. Ziarati, P. The essentialoil composition of Carthamus tinctorius L. flowers growing in Iran. *African Journal of Biotechnology* 2012, 65, pp. 12921-12924.
41. Ivanova, R. Aspecte teoretice și practice de introducere a șofrănelului (Carthamus tinctorius L.) în Republica Moldova. *Studii și comunicări. Științele naturii. Oltenia: Muzeul Olteniei Craiova*, 2016, 32, pp. 48-52.
42. Duca, Gh. *Produse vinicole secundare*. Ştiinţa, Republica Moldova, 2011; pp. 150-180. ISBN 978-9975-67-794-3.
43. Erbas, S.; Mutlucan, M. Investigation of Flower Yield and Quality in Different Color Safflower Genotypes. *Agronomy* 2023, 3, pp. 956-977. https://doi.org/10.3390/agronomy13040956
44. Yue, S.; Tang, Y.; Xu, C.; Li, S. Two new quinochalcone C-glicosides from the florets of Carthamus tictorius. *Journal of Molecular Sciences* 2014, 15, pp. 16760-16771. http://dx.doi.org/10.3390/ijms150916760
45. Yue, S.; Tang, Y.; Li, S.; Duan, J. Chemical and biological properties of quinochalcones C-glycosides from the florets of Carthamus tinctorius. *Molecules* 2013, 18, pp. 15220-15254. https://doi.org/10.3390%2Fmolecules181215220
46. Adamska, I.; Biernacka, P. Bioactive substances in safflower flowers and their applicability in medicine and health-promoting foods. *International Journal of Food Science* 2021, 7, pp. 1-23. https://doi.org/10.1155/2021/6657639
47. Saito, K. Glucose Oxidase, a Potential Contributor towards Flower Colour Modification in the Capitula of Carthamus tinctorius L. *Biochemie und Physiologie der Pflanzen* 1993, 188, pp. 405-417. https://doi.org/10.1016/S0015-3796(11)80144-7
48. Cho, M.; Paik, Y.; Hahn, T. Enzymatic conversion of precarthamin to carthamin by a purified enzyme from the yellow petals of safflower. *Journal of Agricultura and Food Chemistry* 2000, 48, pp. 3917-3921. https://doi.org/10.1021/jf9911038
49. Ghorgani, E.; Hasani-Kelesheteri, R.; Shahbazi, M.; Moradi, F.; Sadri, M. Optimization of extraction yield of carthamine and safflower yellow pigments from safflower (Carthamus tinctorius L.) under different treatments and solvent systems. *Journal of Pharmacognosy* 2015, 2, pp. 17-23.

50. Machewad, G.; Ghatge, P.; Chappalwar, V.; Jadhav, B.; Chappalwar, A. Studies on extraction of safflower pigments and utilization in ice cream. *Journal of Food Processing & Technology* 2012, 3, pp. 1-3.
51. Man-Ho, C.; Tae-Ryong, H. Purification and characterization of precarthamin decarboxylase from the yellow petals of *Carthamus tinctorius* L. *Biochemistry and Biophysics* 2000, 382, pp. 238-244. https://doi.org/10.1006/abbi.2000.1984
52. Savcenco, A.; Baerle, A.; Tatarov, P.; Ivanova, R. Process for producing dyes from Safflower petals. Patent of Moldova, MD-1453, issued 31.03.2021.
53. Fatahi, N.; Carapetian, J.; Heidari, R. Comparing stability of carthamin and safflower yellow pigments at pH, temperature and light, from Safflower (Carthamus tinctorius L.) florets. *Journal of Biological Science* 2009, 4, pp. 250-253.
54. Verhecken, A.; Storme, P.; Schalm, O. UV-VIS reflectance spectrometry study of the dyes silks in a relic shrine found in antwerp, Belgium. *e-Preservation Science* 2014, 11, pp. 99-104.
55. Baerle, A.; Savcenco, A.; Tatarov, P.; Fetea, F.; Ivanova, R.; Radu, O. Stability limits of a red carthamin-celulose complex as potential food colourant. *Food & Function* 2021, 12, pp. 8037-8043. https://doi.org/10.1039/D1FO01376A
56. Kometani, T.; Nishimura, T.; Nakae, T.; Takii, H.; Okada, S. A method for preparation of soluble carthamin, red pigment from safflower, using glycosyl hesperidin. *Food Science Technology* 1999, 5, pp. 265-270. https://doi.org/10.3136/fstr.5.265

Citation: Savcenco, A. The use of food dyes: problem, solution and source of perspective. *Journal of Engineering Science* 2023, 30 (3), pp. 173-187. https://doi.org/10.52326/jes.utm.2023.30(3).13.

Submission of manuscripts: jes@meridian.utm.md